Towards the Understanding of the Transient Behaviour and Sources of Variability on the Process Outcomes in Inertia Friction Welding



Luca Raimondi

Department of Mechanical, Materials, and Manufacturing Engineering
University of Nottingham

This dissertation is submitted for the degree of
Doctor of Philosophy

January 2021

Ai miei genitori, Luisa e Gianni, per avermi su(o)pportato tutti questi anni

(To my parents, Luisa and Gianni, who have supported me all these years)

Acknowledgements

I would like to extend my gratitude to my supervisors Dr. Chris Bennett, Prof. Dragos Axinte and Dr. Andres Gameros for their invaluable help and support over the last four years; to Dr. Peter Stevens, Dr. Christine Hannon and Dr. Andrew Walpole for the availability and support based on their vast technical knowledge of the subject; to Mrs. Cecilia Flores for the precious administrative support and great advices she provided in several occasions.

I am extremely thankful to Rolls-Royce Plc. and the Engineering and Physical Sciences Research Council (EPSRC) for the funding support received (Grant Ref. 15220152) that made this research possible and to the University of Nottingham for providing access to their facilities and equipment.

Finally, a big thank you goes to all my colleagues at the UTC for their help and friendship.

Abstract

The difficulty in creating high-quality joints in high-strength/high-temperature materials for aerospace applications fostered the interest in solid-state friction-based joining techniques. Among these, inertia friction welding (IFW) found numerous industrial applications to join axisymmetric components since highly repeatable and fully automated, does not require filler material, shielding gas or vacuum, produces a small heat-affected zone and is not affected by bulk melting. Two workpieces, one rotating and the other stationary, are pressed together and the frictional heat generated at the weld interface causes a localised plastic deformation and their junction.

IFW found large interest among researchers and several studies focused on the modelling of the thermo-mechanical evolution of the joint to predict the welding response to changes in process parameters. To cope with the complexity of the phenomena occurring during welding, these models usually rely on simplifications in term of weld geometry, alignment and interaction between the workpieces, machine behaviour, process loads and clamping conditions. In addition, despite many studies showed that dynamic effects can deeply affect the process evolution and the quality of the outcomes in manufacturing processes that share similarities with IFW, no study presented a satisfactory dynamic analysis of IFW.

To fill these research gaps, three main objectives were addressed: (i) development of a novel monitoring system for the in-process characterisation of the IFW machine that can act as a diagnostic tool; (ii) investigate the machine response to the process

conditions and assess the validity of the axisymmetric assumption conventionally adopted to study IFW; (iii) modelling the effect of the imperfect contact between the workpieces on the pressure distribution at the weld interface and the dynamic behaviour of the system.

The monitoring system developed is a significant step forward from the existing systems. In fact, the simultaneous measurement of complementary parameters related to the weld evolution provided a holistic view of the process that proved fundamental in giving physical meaning to the phenomena observed. From data extracted with a set of rundown tests and steel welds, a non-negligible relative runout between the headstock and tailstock was measured. The imperfect contact between the workpieces caused by the runout was correlated to a pressure variation in the circumferential direction at the weld interface and radial non-axisymmetric loads particularly evident in the initial stages of the process. These findings are important because not only differ from the idealised conditions conventionally assumed but also, when combined with the compliance of the machine, can foster a larger misalignment.

This research allowed to shed light on the actual interaction between the workpieces and point out that when local phenomena at the weld interface need to be evaluated, the traditional axisymmetric assumption can fail in providing realistic results. In addition, the versatility of the monitoring system makes it ideal as a research platform for further studies and tool to assess the equivalency of different machines.

Table of contents

List of figures xv

List of tables xxv

Nomenclature xxvii

1 Introduction 1

1.1 Background . . . 1

1.2 Research problem overview . . . 3

1.3 Aims and objectives of the study . . . 6

1.4 Thesis structure . . . 9

2 Literature review 11

2.1 IFW key features . . . 14

2.1.1 IFW process overview . . . 14

2.1.2 Process parameters and efficiency . . . 16

2.1.3 Weld phases . . . 19

2.1.4 Frictional behaviour . . . 20

2.2 IFW setup . . . 23

2.2.1 Evolution of IFW machines . . . 23

2.2.2 Tooling . . . 28

2.2.3 The measurement and monitoring of IFW systems 38
2.3 Dynamics of Rotating Systems 43
2.3.1 Modelling of rolling elements bearings 44
2.3.2 Modelling of bearing-rotor system in manufacturing application 45
2.4 Summary of the literature 51
2.5 Research challenges 54
2.5.1 Assessment of the actual welding conditions 54
2.5.2 Modelling of the dynamic system response to the welding conditions 56

3 Initial assessment of the system behaviour in default conditions 57
3.1 Analysis of the inertia welders 57
3.1.1 MTI-300T 58
3.1.2 MTI-2000B 62
3.1.3 Conclusions 65
3.2 Machine performance under conventional welding conditions 67
3.2.1 Weld setup 67
3.2.2 Welding trial results 69
3.2.3 Conclusions 76
3.3 Influence of the tooling's elements on the welding surfaces alignment . . 76
3.3.1 Conclusions 83
3.4 Conclusions 83

4 A novel approach for the in-situ monitoring of IFW 85
4.1 Generic concept of the application 86
4.2 Small scale prototype 87
4.2.1 Mechanical setup 87
4.2.2 Instrumentation 90

4.2.3 Assessment of the system geometry . . . 93
4.2.4 Validation of the mechanical setup under process conditions . . 94
4.2.5 Dynamic response of the system to process conditions . . . 98
4.2.6 Validation of the fixturing configuration . . . 103
4.3 Validation system . . . 106
4.3.1 Mechanical setup . . . 106
4.3.2 Instrumentation . . . 109
4.3.3 Assessment of the system geometry . . . 111
4.3.4 Validation of the mechanical setup under process conditions . . 112
4.3.5 Dynamic response of the system to process conditions . . . 115
4.4 Sensors theory of operation . . . 119
4.5 Workpiece design and materials used for this study . . . 127
4.6 Conclusions . . . 130

5 A novel approach for the characterisation of the phenomena in IFW 133
5.1 Methodology . . . 133
5.2 Results and discussion . . . 135
5.2.1 Rundown tests . . . 135
5.2.2 Welding tests . . . 138
5.2.3 Conclusions . . . 154
5.3 Assessment of the observation on a similar machine . . . 155
5.3.1 Methodology . . . 155
5.3.2 Rundown tests . . . 156
5.3.3 Welding tests . . . 160
5.3.4 Conclusions . . . 164
5.4 Conclusions . . . 165

6 Investigation of the dynamic evolution of the alignment of the workpieces **169**

6.1 Methodology . . . 170

6.1.1 Loads induced by non-axisymmetric conditions . . . 172

6.1.2 Dynamic representation of the machine spindle . . . 177

6.1.3 Process parameters . . . 179

6.2 Results and discussion . . . 179

6.2.1 Pressure distribution on the weld interface . . . 180

6.2.2 Equivalent loads and optimisation error analysis . . . 182

6.2.3 Dynamic response of the system to the equivalent loads . . . 186

6.3 Conclusions . . . 187

7 Conclusions **191**

7.1 A novel approach for the characterisation of the system performance in IFW . . . 191

7.2 Conclusions . . . 198

7.2.1 A novel monitoring system for IFW . . . 199

7.2.2 An approach to characterise the process evolution and the system response . . . 200

7.2.3 Analysis of the dynamic response of the system to the process conditions . . . 202

7.3 Future work . . . 204

References **207**

Appendix A Monitoring system - Health and safety considerations **219**

A.1 Assessment of the instrumentation . . . 219

A.2 Handling of the mechanical setup . . . 223

A.2.1 Prototype system 223
A.2.2 Validation system 225

Appendix B Assessment of plastic suitability in withstanding process loads **229**

B.0.1 Setup 230
B.0.2 Results 233
B.0.3 Analysis of the morphology of damaging 236
B.1 Conclusions 239

List of figures

1.1 Trent-1000 turbo-fan engine illustrated cut-out (Credit: Rolls-Royce Plc.) 2

2.1 Classification of friction welding processes [38] 13
2.2 Schematic diagram of a rotary friction welding system [7]. 15
2.3 Schematic of the principal process variables and stages in IFW (Adapted from [7]) 20
2.4 Example of industrial inertia welders for different axial load classes [54] 24
2.5 Examples of inertia welder prototypes patented by Caterpillar Inc. . . . 26
2.6 Examples of inertia welders with tie bars to minimise the deflection under process loads 27
2.7 Schematic of the spindle supported by a radial journal bearing and a hydrostatic thrust bearing (Adapted from [62]) 28
2.8 Schematic diagram of the tooling effect on a tubular workpiece and of the residual stresses induced [31] 30
2.9 Collet with backup used in IFW to clamp workpieces of axisymmetric geometry 33
2.10 Dual collet designed to limit the deformation in thin-walled components (Adapted from [68]) 34
2.11 Collet with elastomeric coating to reduce the damaging on the component external surfaces (Adapted from [69]) 35

2.12 Tooling variation in which serrated round grippers are inserted in the backup to provide additional grip on the workpiece (Adapted from [70]) 36
2.13 Schematic representation of the optimal configuration of the locators for cylindrical components 36
2.14 Alternative machine setup to accommodate long components (Adapted from [73]) 37
2.15 Monitoring system comprising a ring array of condenser microphones that surround the workpiece and capture the airborne audio data from the weld (Adapted from [75]) 40
2.16 Welding setup with the radial fibre-optic vibrometer installed on a tripod outside the machine to monitor the oscillatory behaviour throughout the process (Adapted from [74]) 40
2.17 Monitoring system to measure the process torque throughout the welding (Adapted from [26]) 42
2.18 Schematic representation of an inertia welder in which the key elements of the headstock rotor-bearing system have been highlighted 44
2.19 Lathe spindle-workpiece system [104] 47
2.20 Schematic of a milling machine spindle, including toolholder and cutting tool [109] 49
2.21 Exploded view of the different elements composing the system for the study of the tool holder–spindle and tool–tool holder interfaces, with detail of approximation of the distributed translational and rotational springs (Adapted from [115]) 51

3.1 MTI-300T hybrid rotary friction welder 59
3.2 Default tooling configuration for the MTI-300T machine 60

3.3 Fixturing configuration used by Rolls-Royce for the welding trials with the MTI-300T 61
3.4 MTI-2000B inertia friction welder 62
3.5 Production tooling configuration for the MTI-2000B machine 64
3.6 Backstops for test welds (PDX3) 65
3.7 CAD representation of the workpieces welded and description of the strain gauges configuration 68
3.8 Damaged welded components due to improper fixturing setup 70
3.9 Effect of the serrations on the base metal indented 72
3.10 Comparison between theoretical and actual torque (normalised against the peak theoretical torque) 74
3.11 Details of the FE model developed to validate the output of the strain gauges 75
3.12 Results obtained with the numerical model and comparison with the actual torque 75
3.13 Schematic representation of the axial and radial runout for the spindle workpiece 77
3.14 Schematic representation of backstops for the MTC tooling including the geometrical and dimensional tolerances that affect the axial runout 79
3.15 2D effect of a geometric tolerance in the interaction between a block and a planar surface [135] 80
3.16 Axial runout connected to the rotation angle calculated stacking up the perpendicularity and parallelism errors in the faces of the backstops . . 82
3.17 Comparison between the axial runout obtained stacking up the tolerances calculated with the worst case scenario and a normal distribution . . . 82

4.1 Mechanical setup for the monitoring system prototype including two custom backstop capable to carry the instrumentation and constrain the workpieces . . . 89
4.2 Schematic of the monitoring system with sensors . . . 92
4.3 Schematic representation of the key features inspected . . . 94
4.4 Axisymmetric FE model developed to analyse the stresses in the neck section of tailstock backstop . . . 95
4.5 von Mises stress field in the neck section at the peak loads . . . 96
4.6 Comparison between the analytical and the numerical stress in the backstop neck section . . . 97
4.7 Schematic representation of the FE model used to study the linear perturbation analysis . . . 98
4.8 Eigenmodes for the tailstock backstop . . . 99
4.9 FE dynamic model for the study of the vibrational behaviour of the fixture backstop considering actual process loads . . . 101
4.10 Radial and axial oscillations for the three points used to represent the sensors installed on the bracket . . . 102
4.11 FE model implemented to validate the design of keys and keyways in the backstop . . . 104
4.12 Values of stress and contact pressure in the keys obtained with the FE models . . . 105
4.13 Mechanical setup for the validation system . . . 108
4.14 Instrumentation used for the validation system . . . 110
4.15 Schematic representation of the key features inspected to assess the influence of the geometrical errors on the runout measured with lasers and LVDTs . . . 111

4.16 3D FE model developed to analyse the stresses in the neck section of tailstock backstop 112
4.17 von Mises stress field in the neck section at the peak loads 113
4.18 Comparison between the analytical and numerical stress in the backstop neck section 114
4.19 Schematic representation of the FE model used to study the linear perturbation analysis 115
4.20 Eigenmodes for the tailstock backstop 116
4.21 Schematic representation of the FE model in which it is possible to observe the three points used to model the sensors installed on the bracket and the applied loads 117
4.22 Radial and axial oscillations for the three points used to represent the sensors installed on the bracket 118
4.23 Schematic representation of an LVDT and of the signal conditioning circuit developed to extract an analogue output from the sensor 119
4.24 Kistler 8764B050 accelerometer installed on the backstop 121
4.25 Encoder and custom chassis developed to monitor the headstock angular speed throughout the welding 123
4.26 Encoder and custom chassis developed to monitor the headstock angular sped throughout the weld 124
4.27 Strain gauges configuration to measure torque and axial load 126
4.28 CAD drawings and key dimensions for the workpieces used in the two monitoring systems 129

5.1 Section view of the workpiece with detail of the wall thickness and mean radius of the welding section 134

5.2 Behaviour of the machine in the radial direction (radial runout) during a rundown test 137
5.3 Comparison between the scalograms of laser and LVDT with the angular speed of the spindle 138
5.4 Schematic of the machine for IFW in term of key dynamic elements . . 139
5.5 Comparison among thrust, torque and upset with emphasis on the axial impact at the initial contact of the workpieces 140
5.6 Calculation of the coefficient of restitution (COR) for the welds 141
5.7 Analytical schematic in the axial direction at the initial impact of the two workpieces using a mass-spring-damper approximation. When the piston is activated, the fixture closes the initial gap and collide against the spindle which reacts as a spring-damper system. 142
5.8 Unfiltered torque signal with the two peaks at the conditioning and consolidation phases highlighted. An oscillations spike can be clearly observed at the flywheel stoppage 143
5.9 Model for the torsional oscillations using an inertia-spring-damper approximation and a temperature-dependent stiffness coefficient 144
5.10 Comparison between the values of acceleration for the analytical model of a torsional damper and the experimental data 145
5.11 Radial runout monitored by the lasers during a weld 147
5.12 Spindle centre position calculated from the reading of the two lasers . . 148
5.13 Behaviour of the machine in the axial direction during a weld 149
5.14 Comparison of the axial load measured by the four axial gauges 150
5.15 Analytical model of the fixture side backup in which the influence coefficients have been used to compute the deflection caused by the experimental radial load derived by the axial gauges 151

5.16 Steps of the algorithm to compute an equivalent radial stiffness of the machine . . . 153
5.17 Normalised axial and radial runout of the machine spindle measured with LVDTs and lasers during a rundown test for three different speed ranges . . . 158
5.18 Position of the spindle centre calculated from the readings of the two lasers for three speed ranges . . . 159
5.19 Scalogram (continuous wavelet transform) for the radial and axial runout with superimposed graph of the spindle angular speed . . . 159
5.20 Normalised thrust and torque measured with the monitoring system during a weld in which it is possible to note the impact at part contact and the final flywheel oscillations when the spindle is about to stop rotating . . . 160
5.21 Graph of the radial runout measured by the two lasers in which the duration of a full rotation of the spindle and the three main weld phases are highlighted . . . 161
5.22 Orbit of the spindle centre during the weld obtained combining the readings of the two lasers . . . 162
5.23 Process upset and axial runout monitored during the welding by the LVDTs . . . 163
5.24 Comparison of the normalised thrust measured by the four axial gauges in which the duration of a full rotation of the spindle and the three main weld phases are highlighted . . . 164

6.1 Schematic representation of the approach used for the analysis of the runout evolution during the welding . . . 171

6.2 Graphic representation of the axial and tangential load contributions on the welding surface of the workpiece 173
6.3 Static analytical model for the study of the spindle deflection with details of the bearings adopted for the rear and front supports 176
6.4 Load-displacement curves for the front and rear supports of the spindle 176
6.5 Beam model analysed for the dynamic study 177
6.6 Normalised pressure distribution at the weld interface for five time instances during the welding 180
6.7 Standard deviation of the pressure distribution at the weld interface showing larger variability in the first stages of the welding 181
6.8 Angular position of the pressure peak location around the weld interface during the welding for three welds carried out using the same process parameters, from which it is possible to observe periodicity in the peak location but a different behaviour among the three welds 182
6.9 Normalised equivalent loads and moments in three orthogonal directions obtained from the optimisation algorithm, from which it is possible to observe large non-axisymmetric loads 184
6.10 Comparison between the experimental data and the numerical data computed with the optimisation 185
6.11 Comparison of the radial runout obtained with the static and dynamic models and the experimental data 186

7.1 Schematic representation of the novel approach developed for the characterisation of the system performance in IFW 192

A.1 Lifting setup for the backstops of the prototype system designed to be clamped and lifted with a manipulator arm equipped of claw gripper . 223

A.2 Section view of the model analysed in the FE model in which the key dimensions and constraints are shown 224
A.3 Mises stress in the rod caused by the weight of the backstop 225
A.4 Custom backups lifting and storage details 225
A.5 Eye bolts specs (Adapted from http://www.iandplifting.co.uk) 226
A.6 FE model developed to calculate the stress induced by the weight of the backstop during lifting with a manipulator arm 227
A.7 Mises stress in the neck section of the backstop during lifting with the manipulator arm 227

B.1 Setup used for the characterisation of the plastic testpieces, in which the key elements are the Hermel machining centre, the sensors used to calculate the process loads and temperature (dynamometer and thermocouple), the plastic testpiece and the steel base plate 231
B.2 Schematic representation of the parameter matrix for the characterisation of the plastic testpieces 232
B.3 Cross section of a cylindrical workpiece showing the infinitesimal tangential friction load contribute over the ring of radius and thickness [179] 233
B.4 Test matrix for VICTREX 450CA 234
B.5 Results of the characterisation of Victrex 450CA 234
B.6 Test matrix for Torlon 7130 235
B.7 Results of the characterisation of Torlon 7130 236
B.8 Measured values of friction coefficient and axial load at the instant of failure of the testpiece 237
B.9 Macroscopic damaging for the two types of plastic in which it is possible to observe debris on the metal base plate 237

B.10 Optical micrographs of the damaged surfaces for the two materials analysed and comparison with a study from literature of PEEK analysed with a ball-on-disc tribometer 238

B.11 Analysis of the sub-superficial longitudinal cracks in a Torlon testpiece 239

List of tables

3.1 Values of mass and inertia for the elements of the spindle 58

3.2 Process parameters for the welds accomplished 69

3.3 2D rotational and translational variations associated with the geometrical tolerances applied to various kinematic connections [135] 80

4.1 Sensors and sampling frequency 93

4.2 Values monitored with a CMM with respect to the schematic shown in Fig. 4.3 94

4.3 Sensors and sampling frequency 109

4.4 Diameters for the welding stub of the four types of workpieces used in the prototype and the two used in the production system 130

5.1 Wall thickness and mean radius for the eleven welds 134

5.2 DOE parameters matrix for the eleven welds and the two rundown tests 135

5.3 Parameters for the analytical model which describes the torsional oscillator 145

5.4 Process parameters for the rundown tests discussed 156

5.5 Process parameters for the two welds discussed 156

6.1 Bearing specifications 176

6.2 Geometrical specifications for the beam model studied in the dynamic characterisation of the system 178

6.3 Process parameters and wall thickness for the welds analysed 179

A.1 Health and safety considerations for the power supplies used in the monitoring systems 220

A.2 Health and safety considerations for the controllers used in the monitoring systems 221

A.3 Health and safety considerations for the sensors used in the monitoring systems 222

Nomenclature

$[M]$	Global mass matrix
$[K]$	Global stiffness matrix
$[C]$	Global damping matrix
$[G]$	Global gyroscopic matrix
$\{F\}$	Global vector of the external loads
$\{U\}$	Global vector of the displacement coordinates
α	Angular acceleration
χ	Shear factor
δ	Deflection/runout
ϵ	Strain
η	Process efficiency
γ	Shear strain
μ	Friction coefficient
ω	Rotational velocity
ω_0	Initial angular speed of the spindle
σ, σ_{ii}	Normal stress
τ, τ_{ij}	Shear stress
θ	Angular coordinate
φ	Angle
φ_0	Initial phase

A	Area
c	Damping
c_{cr}	Critical damping
E	Young's modulus
F	Force
F_W	Weight
F_x, F_y, F_z	Load in X, Y and Z direction
F_{A_i}, $F_{A_{tot}}$	Axial load contribution
F_b	Reaction force at the spindle supports
F_{T_x}, F_{T_y}	Tangential load in X and Y direction
G	Shear modulus
I	Rotational inertia
J_p	Torsion constant
k	Stiffness
l, $l_{1,2,...}$	Length
l_g	Position of the centre of mass
M	Moment
m	Mmass per unit of length
M_x, M_y, M_z	Moments in X, Y and Z direction
n_v	Vector normal to a plane
P	Thrust exerted by the ram
P_C	Circumference centre
P_m	Midpoint between two points
$P_{1,2,...}$	Points
r	Radius/Radial coordinate
r_o	Outer radius

r_{mw}	Mean radius of the welding section
T	Torque
t	Time
T_w	Thickness of the welding section
V	Linear speed
$v_{1,2,...}$	Vectors parallel to a plane
W	Section modulus
x, y, z	Linear coordinates
Y_m	Amplitude sinusoidal signal

Chapter 1

Introduction

1.1 Background

The rapid growth the aviation sector has experienced in the last fifty years due to tourism, more affordable airfares, need to maintain communication routes in the current globalised market and the push from emerging economies [1, 2] poses challenges for the manufacturers which aim for improved performances, higher safety standards, reduced downtimes, higher efficiency and smaller environmental footprint [3]. Manufacturers are addressing these issues developing better materials and improved manufacturing methods. In fact, while in the past aluminium was largely used and other materials, such as composites and alloys, were used only in small percentages, nowadays the usage of new materials has exponentially increased, e.g. CFRPs and honeycomb materials for structurally non-critical parts and high strength/high temperature materials (e.g. titanium and nickel-based superalloys) for the engine and critical components. This can be seen in the drastic change in the material ratio used for the 7-series of Boeing jet airlines, where the overall usage of aluminium dropped from the 70% of the Boeing 777, introduced in the 1995, to 20% of the Boeing 787, entered in service in 2011 [4].

Among all the components of modern aircraft, the engine is one of those which presents the biggest challenges for the constant strive to increase temperatures and improve efficiency. Focusing on the hot section of the engine (Fig. 1.1), superalloys are extensively used due to their capability to work at elevated temperatures for extended periods of time while retaining high mechanical strength and good resistance to fatigue, creep and corrosion. Restricting the study to nickel-based superalloys, which can withstand the highest temperatures in the superalloy family, precipitation hardening is the main strengthening mechanism, with the greatest contribution provided by the intermetallic phase γ' due to its characteristics of high temperature stability, ductility and dispersion coherence in the matrix. While early superalloys had a limited volume fraction of γ' phase, companies are pushing for a higher content for higher strength, e.g. Udimet 720 and RR1000. The biggest drawback in high γ' content is the adverse effect on production techniques like welding, which can suffer of two types of defects, hot cracking and strain age cracking. To prevent these defects, bulk material melting must be avoided and solid-state friction-based welding processes become an appealing solution [5, 6].

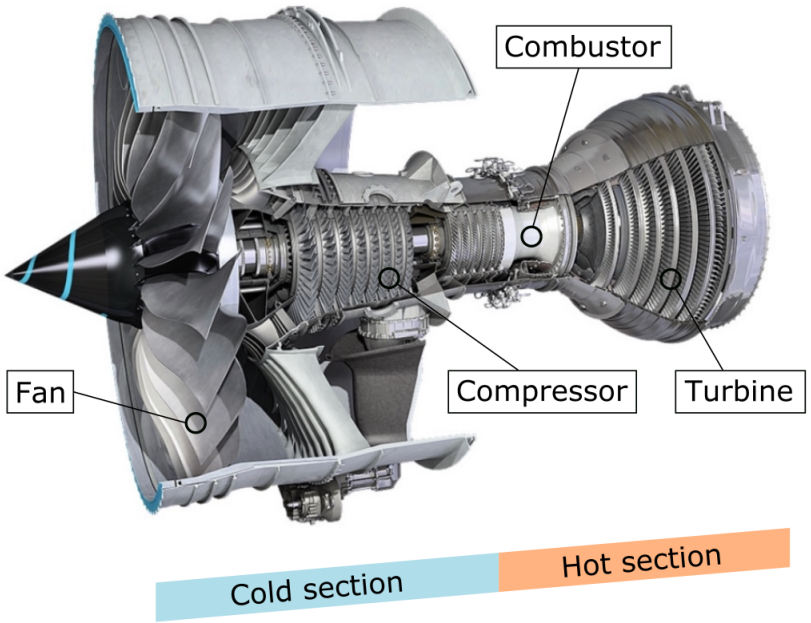


Fig. 1.1 Trent-1000 turbo-fan engine illustrated cut-out (Credit: Rolls-Royce Plc.)

Inertia friction welding (IFW) is a solid-state joining technique that belongs to the rotary friction welding family, in which the kinetic energy stored in a spinning flywheel is converted into thermal energy and plastic deformation through the friction generated at the interface of two components in relative motion, one connected to the flywheel and one clamped in a non-rotating collet or chuck actuated by a hydraulic piston that presses the two parts together. When the process parameters are chosen properly, no bulk material melting is generated and, overall, the process is repeatable and well suited to automation. In addition, IFW is a self-cleaning process and does not require filler material, shielding gas or a vacuum because of the ejection of plasticised material in the form of flash at the interface between the two workpieces. This technique is currently adopted by Rolls-Royce to join high alloy steels (e.g. Super-CMV and AerMet 100) and superalloys (e.g. Inconel 718 and RR1000) [7, 8].

1.2 Research problem overview

IFW has a long history, with the first commercial applications dating back to the late 1960s and early 1970s [7]. Over the years engineers and researchers have focused their attention mostly on the choice of proper input parameters and specific aspects of the process, which can be summarised in four macro-areas:

- **Materials and metallurgical analysis of the weld**

  IFW can be used to join a great number of materials other than superalloys, for this reason, several researchers studied how similar (i.e both workpieces produced with the same material) and dissimilar welds (i.e workpieces of different material) perform in term of joint strength and microstructural integrity. As seen in the previous section, the microstructure of superalloys is of primary importance, therefore, this aspect has attracted significant attention to assess macroscopic

factors, like the width of heat affect zone (HAZ), and microscopic ones, like phases composition, precipitates and grain structure; [9–13]

- **Thermal and thermo-mechanical simulation of the process**

  Even before the adoption of numerical techniques to solve complex thermo-mechanical problems, researchers addressed the solution of the thermal problem in IFW with analytical approaches to try to predict the temperature evolution during a weld, given the set of input parameters [14, 15]. Later, when numerical codes capable of handling the complexities of the coupled thermo-mechanical evolution of a weld were developed, a large number of studies addressed the thermal and mechanical evolution of the process to understand how these affect each other, with particular attention on aspects like the friction coefficient at the weld interface and the flash formation, providing more realistic prediction of the weld evolution; [16–24]

- **Weld efficiency and influence of process parameters**

  Defining efficiency as the ratio between the kinetic energy stored in the flywheel and the actual energy supplied to the weld, IFW is considered a process with relatively high efficiency and in which this is scarcely affected by process parameters. However, when considering the chain of rotating elements that support the spindle, e.g. bearings, it is possible to expect noticeable energy losses and non-linear behaviour. For this reason, researchers characterised the efficiency of the system for different input parameters to find the most convenient working conditions and the efficiency evolution throughout the weld; [25, 26]

- **Analysis of specific elements of the inertia welding machine**

  A few patents and research articles have addressed specific aspects of the system, such as acoustic emission or hydraulic fluctuations in the piston, to monitor the system performance and correlate these to the weld quality. [27–30]

Even if a small number of publications acknowledged the effect of the tooling, inducing deformations and residual stresses in the weld [7, 31–33] due to excessive and uneven clamping forces, along with issues of repeatability because of the cumulative impact of the tolerances in the elements of an inertia welder, all the remaining studies disregarded the effects of tooling and machine, such as the compliance of the supporting structure under the process loads, misalignment of the two workpieces, that can cause the system to be not strictly axisymmetric. In addition, several patents were filed to protect improvements to the inertia welding system against specific phenomena like vibrations [27, 34, 35] and interaction of the workpieces [36], however, while they deal with the specific symptoms, they do not address the problems themselves. When these aspects are analysed from an industrial viewpoint, however, the machine behaviour, the proper configuration of the tooling and the minimisation of misalignment between headstock and tailstock are considered of primary importance to achieve high weld quality and repeatability. Rolls-Royce, industrial partner for this research work, for example, has specialised technicians and engineers that deal exclusively with the maintenance, setup and optimisation of the inertia welder and related systems. Despite their effort and expertise, areas where a more in-depth analysis would be beneficial for the knowledge and understanding of the process can still be found.

It appears clear that studying the aspects of system setup and the non-ideal interaction between the two workpieces would prove beneficial from both an academic point of view, providing tools and techniques to give physical explanations to specific phenomena and quantifying the error intrinsic in the current simplified models, as well as from an industrial one, developing a device and a methodology that can improve the production setup.

1.3 Aims and objectives of the study

The analysis of the state of art presented hereinbefore showed knowledge gaps connected to the inertia welding setup and its effect on the weld. For this reason, the main goal of this research is to understand how the machine and the tooling affect the weld and, in turn, how they react to the process loads by developing a novel monitoring system and a supporting methodology. This information can be used to improve the design of tooling and ancillary systems, develop more realistic numerical modelling of the process and, consequently, obtain more repeatable weld outcomes. The specific objectives of the research can be summarised as follow:

1. **Initial assessment of the system with a pilot study to acquire an understanding of its behaviour under default conditions**

   IFW is usually discussed in the literature using the axisymmetric assumption, resulting in a simplified picture of the real conditions during welding. To gain an understanding of the process evolution in non-idealised conditions, a set of preliminary tests is required. The outcomes of these can provide valuable information to drive the design of a novel monitoring system, the choice of the instrumentation to be installed in it and the selection of most suitable material and geometry for the workpieces to be used to characterise the system;

2. **Development of a novel monitoring system able to analyse the response of the IFW system to the process conditions and act as a powerful diagnosis tool**

   While means of analysing the setup and workpieces before and after welding already exist, being able to study the system throughout the weld is significantly more complex for the relative motion of headstock and tailstock and the confined space near the weld. To overcome these problems a novel system for in-process

monitoring of IFW that can work as an instrumented interface between the machine tooling and the workpiece is required. The system would represent a significant step forward from the existing solutions for its capability to monitor at the same time a large number of parameters (axial and radial runout, vibrational behaviour, angular speed, torque and axial load) and, consequently, provide a holistic view of the phenomena occurring during the process necessary to establish the physical causes behind them;

3. **Investigate the machine response to the process conditions and assess the validity of the axisymmetric assumption with a methodology devised to process the experimental data extracted with the monitoring system**

   Once the monitoring system is developed, its capabilities need to be assessed with a set of welds and free decelerations of the machine spindle. Then, a methodology is required to process the large amount of data generated and provide an approach that can be applied for each test to generate coherent results. Comparing the data from complementary sensors, it is possible to characterise the system response and study the key phenomena related to the interaction between the machine setup and the weld evolution. This can help to shed light upon the physical causes behind the behaviour observed and understand which parameter can be optimised to minimise undesired effects. Finally, applying the approach to different machines and comparing the results, it is possible to extend it to a means of assessing the equivalency of similar systems and understand which phenomena is intrinsic to the process rather than connected to a specific setup;

4. **Analysis of the dynamic response of the system to non-idealised process conditions and development of an inverse approach to obtain the equivalent pressure distribution at the weld interface**

   The inertia welder is a complex rotordynamics system but despite many publications highlighted how the dynamic characteristics of machine tools can affect the quality of the outcomes, no study addressed specifically IFW. To fill this gap, an approach to calculate the equivalent contact pressure and process loads from the data extracted with the monitoring system needs to be developed, then the equivalent loads can be applied to a dynamic representation of the system. From this, the impact of the system compliance to non-idealised process loads and the influence of dynamic effects can be quantified. In addition, studying the correlation between the misalignment of headstock and tailstock and the uneven pressure at the weld interface can help to understand possible implications on the temperature gradients at the weld interface, hotspots, uneven expulsion of flash and, consequently, variation in the joint properties;

5. **Formulate a set of guidelines to extend the monitoring system to a platform for future research and a diagnostic tool for industrial applications**

   The approach developed presents potential as a research platform for future academic study, in which the design of the monitoring system can be adapted to fit the desired combination of sensors. In addition, a simplified version of the system can be used in an industrial environment by technicians and engineers interested in characterising the performance of the machine, conduct periodic inspections and compare different machines. A set of guidelines is formulated, in which the details to be tuned for the different application is highlighted.

1.4 Thesis structure

The research work accomplished during the doctorate in accomplishment to the objectives listed in the previous section was summarised in this thesis; this section will outline its structure.

Chapter 2 presents an in-depth summary of the relevant literature. After the description of the process key features, the conventional setup for IFW is presented, highlighting the progressive evolution and improvements that it has undergone. Then a review of the dynamic analysis of rotating systems for manufacturing applications with similarities to IFW is presented, showing how this can improve the outcomes quality and gain an understanding of the phenomena occurring.

In **chapter 3**, firstly, the characteristics of the two IFW machines used in this study, MTI-300T and MTI-2000B, are described. Then, the results of a set of preliminary tests conducted on the MTI-300T are presented to highlight weaknesses in the system that needed to be addressed and to draw considerations useful in the development of the monitoring system. Finally, the influence on the workpieces alignment of the geometrical errors in the elements of the machine tooling is evaluated.

Chapter 4 introduces the two monitoring systems developed, a prototype system for the MTI-300T machine and a validation system tested on the MTI-2000B. For both systems, aspects like mechanical setup, instrumentation and assessment under the expected process conditions are described. Finally, the details of the geometry and material of the workpieces used for the welding trials are presented.

In **chapter 5** and **chapter 6**, the results and discussion are presented. In **chapter 5**, a methodology for the analysis of experimental data extracted with the monitoring system proposed is described and the results used to characterise the machine behaviour, understand how this is affected by the process conditions, and assess the validity of

the axisymmetric assumption. In **chapter 6**, the dynamic analysis of the system is developed, presenting a novel approach to compute the equivalent contact pressure at the weld interface and the equivalent process loads. Then, these are applied to a rotordynamic model of the machine spindle to quantify the effect of the dynamic components and compliance of the system on the runout behaviour during welding.

Finally, in **chapter 7**, a breakdown of the key steps for applying the novel approach developed to a generic industrial application or for further academic research is presented. Then, the conclusions of the work are drawn to highlight the contributions to the field.

Chapter 2

Literature review

Friction welding is a solid state joining technique used to create high quality welds in a wide variety of materials. The two components to be welded are forced to rub together causing the generation of a high amount of localised frictional heat, inducing the material at the interface of the components to soften and become viscous. In the meanwhile, the relative motion of the two workpieces mixes the softened material that combined with diffusive phenomena creates the bond [37].

Several standards organizations formalised the key aspects of friction welding, for example the ISO 15620:2019 *Welding - Friction welding of metallic materials* [38] defines this as "a method for making welds in the solid phase in which one component is moved relative to and in pressure contact with the mating component to produce heat at the faying surfaces, the weld being completed by the application of a force during or after the cessation of relative motion" and proposes a widely adopted classification based on the different forms of supplying energy and the relative motion between the components. As shown in Fig. 2.1, the first classification considers rotational, linear, angular and orbital relative motion. In addition, the first category, commonly referred as rotary friction welding, includes two subtypes, continuous or direct drive friction welding (CDFW) and inertia friction welding (IFW). These two differ for the way

in which the energy is supplied throughout a weld, in CDFW the energy input is provided directly by an electric or hydraulic motor while in IFW the energy is stored in a flywheel accelerated by a motor. In particular, the large amount of initial energy that the flywheel can store makes IFW particularity suited to join large components. Engineers, wanting to combine the advantages of the two, developed a third type, hybrid rotary friction welding (HRFW), which can run in both configurations and even combine the two in hybrid cycles. [38, 39]

Friction welding has found numerous applications since its introduction, from aerospace components, automotive parts, agricultural machinery, military applications, just to name a few. Rotary friction welding is the oldest and most common variant, followed by orbital friction welding and finally linear friction welding, which proves extremely useful for peculiar applications, such as the fabrication of titanium alloy integrated bladed disks (blisks) for the aerospace industry.

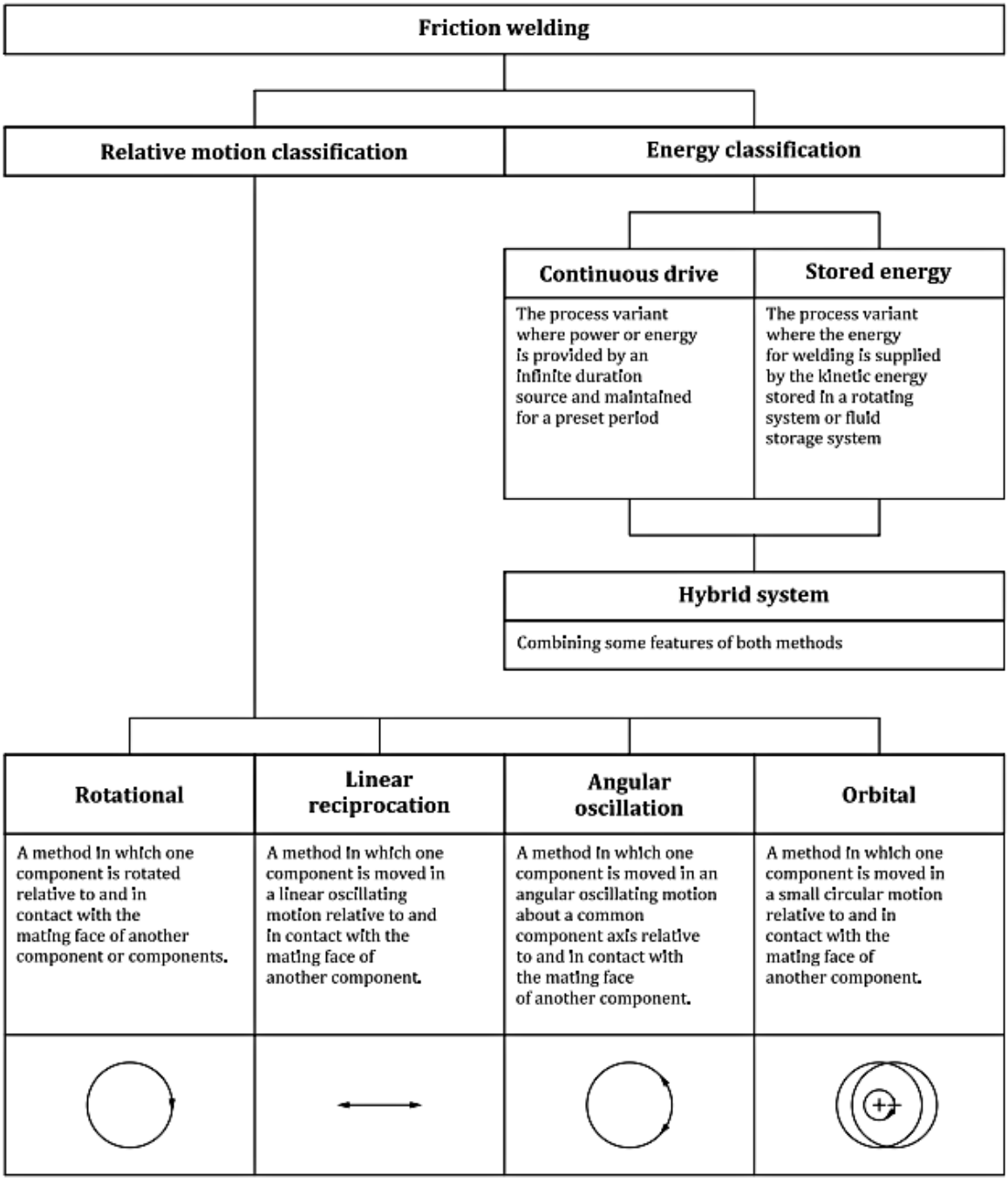


Fig. 2.1 Classification of friction welding processes [38]

2.1 IFW key features

2.1.1 IFW process overview

Fig. 2.2a shows the system schematic for the IFW. An electric or hydraulic motor accelerates the machine spindle that carries a set of flywheels used to store kinematic energy, the majority of which is converted in frictional heat used to create the joint. Two axisymmetric components are clamped by chucks or collets, one connected to the spindle and the other to a non-rotating slide actuated by a hydraulic ram. The process starts when the flywheels are accelerated to the initial angular speed, then the motor is disengaged and the ram used to bring the two parts in contact, starting the welding. While the process proceeds, the spindle angular speed gradually decreases for the friction between the workpieces and energy losses into the system. The friction causes a sudden but localised temperature increase at the interface of the workpieces, which ultimately leads to the formation of a plasticised layer. The axial load exerted by the ram causes an axial shortening of the two parts, termed upset, and the expulsion of the plasticised layer in the form of flash. This allows the expulsion of oxides and other surface contaminants, making the process self-cleaning [7, 40].

Fig. 2.2 compares the schematic diagrams of the setups used respectively in IFW and a CDFW. Between the two, IFW is particularly suited for joining large components. The first reason is the driving system, in fact while in IFW the motor is used only to accelerates the flywheels and then is disengaged, in CDFW the motor drives the spindle for the whole rotational phase, during which the ram applies a limited pressure, then the motor is disengaged and the rotation stopped by a mechanical brake. The second reason is the breaking mechanism, in IFW no mechanical brake is usually adopted during the weld phase and the breaking occurs due to dissipation of the flywheel kinetic energy. Consequently, in IFW it is possible to increase the available energy

by simply increasing the inertia of the flywheels installed or the initial angular speed and a relatively small motor is required only for the flywheels acceleration phase. In CDFW, instead, the power rating of the motor represents the main limiting factor, not allowing to weld parts of large dimensions [7, 40].

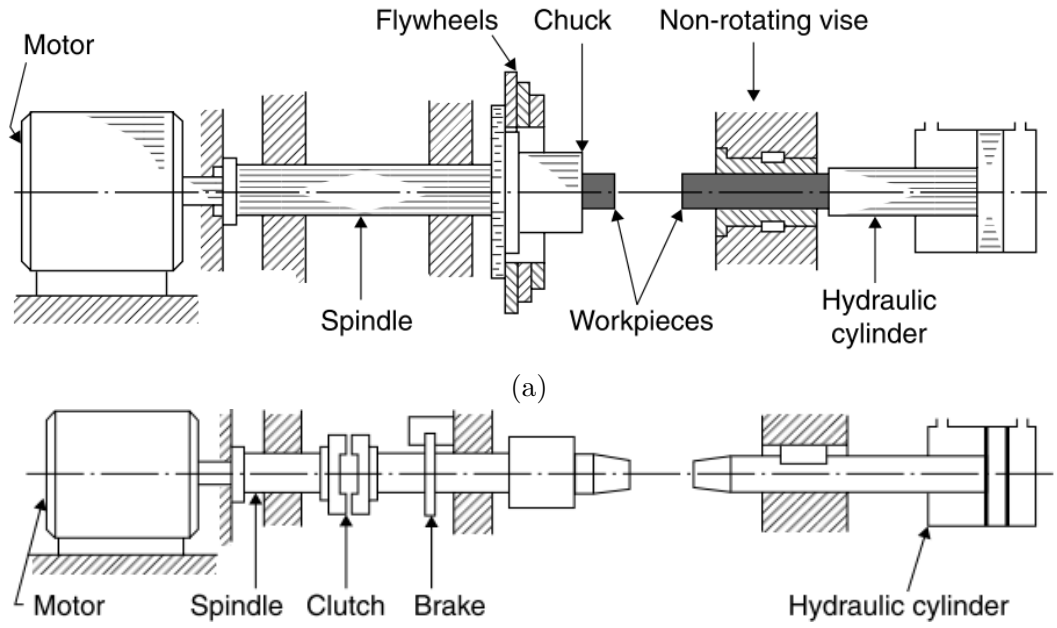


Fig. 2.2 Schematic diagram of a rotary friction welding system [7]: (a) IFW; (b) CDFW.

2.1.2 Process parameters and efficiency

Once the geometry and material properties of the components to be welded are defined, the process can be optimised using three control parameters: initial angular speed of the spindle (ω_0), flywheel inertia (I) and axial load exerted by the ram (P), with the initial speed and inertia determining the available energy for the weld ($E_0 = I \cdot \omega_0^2/2$), while the axial load the rate of energy input. A final aspect worth considering is the power input provided to the weld throughout the process, in fact, defining the power input as the product between the process torque and the instantaneous angular speed, it varies during the welding with a maximum in the conditioning phase when both angular speed and torque are high [7, 13, 40].

Numerous studies correlated the effect of process parameters to the mechanical properties of the junction, e.g. tensile strength, hardness, fatigue resistance and microstructural characteristics (grain size and precipitating phases) [11, 41–45]. Other studies focused on the relation between process parameters and welding efficiency, defined as ratio of the actual energy supplied to the weld (E_S) and the theoretical energy input (E_0):

$$\eta = \frac{E_S}{E_0} \tag{2.1}$$

Conventionally, the efficiency in IFW has been considered constant and not dependent on the process parameters. For example, Wang et al. [23] assumed a fixed friction coefficient of 85% in a coupled thermo-mechanical FE model used to study the thermal history, deformation pattern and final residual stresses of RR1000 nickel-base superalloy tubes inertia welded. Mohammed et al. [46] developed an energy-based approach to assess a realistic value of efficiency and validated the results experimentally in term of upset and temperature. The researchers found good agreement between numeral and experimental data for values of efficiency between 90 and 95%. Bennett [47] developed

a 2D axisymmetric fully coupled thermo-mechanical FE model for the IFW of CrMoV steel tubes, using the process efficiency to tune the heat input. A good match in terms of temperature between the numerical results and experimental data was produced assuming a 70% efficiency. To challenge this simplified view of the process efficiency, Mahaffey et al. [48] expressed the efficiency in the form:

$$\eta = 1 - \frac{E_M}{E_0} \tag{2.2}$$

in which E_M represents the parasitic energy losses inside the welding machine, calculated by the author with the sum of losses in the radial journal bearings and the thrust bearing supporting the spindle shaft. It was found that, for constant values of theoretical energy input, the efficiency increased with the flywheel inertia. Senkov et al. [25] proposed a more advanced methodology to assess the energy losses into the system. First the researchers studied the machine behaviour without the influence of the welding, to do so the spindle shaft was accelerated to the initial speed and then let decelerate freely, approach commonly referred to as rundown test. Then the relation between the instantaneous parasitic frictional torque (T_M) and the angular deceleration of the spindle ($\frac{d\omega}{dt}$) was expressed in the form:

$$-\frac{d\omega}{dt} = \frac{T_M}{I} \tag{2.3}$$

in which I represents the combined inertia of flywheels, spindle shaft and tooling, while the cumulative energy consumed by friction within the machine was calculated as:

$$E_M(t) = \int_0^t T_M \omega dt \tag{2.4}$$

It was again observed that for a constant value of theoretical energy input, the energy consumption occurred at a faster rate for higher initial angular speed and, consequently, smaller flywheel inertia; in addition the major source of energy losses was located in the radial and thrust bearings, as already observed by Mahaffey et al. [48]. Then the efficiency of the system during welding was analysed using a more accurate evaluation of the parasitic energy losses inside the welding machine obtained measuring the torque in close proximity of the non-rotating workpiece with a torque cell and converting it into energy with an integral formulation similar to Eq. 2.4. Finally, using Eq. 2.1, the authors were able to obtain values of efficiency ranging between 29 and 63%, strongly related to the process parameters. In particular, the efficiency was seen to decrease with an increase of initial angular speed (at fixed values of inertia and weld pressure) or weld pressure (at fixed values of inertia and initial angular speed) and with a decrease in inertia (at fixed values of initial angular speed and weld pressure). This approach was expanded by Tung et al. [26] that, using a torque cell to capture the process torque during the weld, was able to calculate the overall and the instantaneous efficiencies, with the latter defined as ratio between the instantaneous weld torque (T_S) and instantaneous theoretical torque input ($T_{tot} = I \mid \frac{d\omega}{dt} \mid$):

$$\eta_I = \frac{T_S}{T_{tot}} \tag{2.5}$$

The results of this study, in agreement with [13], showed that the process parasitic losses were maximum at the beginning of the welding, when the spindle speed is high, and gradually decreased, presenting a minimum in coincidence of the torque peak in the consolidation phase. Finally, Tung et al. [26] proposed two additional approaches to validate the results presented in the article. The first was based on the analytical thermal energy required to heat the volume of material expelled as flash above the

extrusion temperature, while the second made use of a FE thermo-mechanical approach similar to the one proposed by Wang et al. [23].

2.1.3 Weld phases

IFW is traditionally considered a three stage process, as shown in Fig. 2.3, plus an additional one before part contact, required to accelerate the flywheels to the desired initial angular speed: 1) The first phase, called conditioning, starts with the two workpieces coming into contact, an instant conventionally referred to as part contact, causing a spike in frictional torque and a rapid spindle deceleration. This phase, characterised by dry friction between the two workpieces, has the fundamental role to remove imperfections and asperities from the weld interface. The steep and localised increase in temperature causes the plasticisation of a thin layer of material at the weld interface and, consequently, a drop in torque towards the end of the phase when the frictional behaviour is controlled by the shear strength of the material; 2) The second phase, called burnoff, presents a fully plasticised weld interface, with a temporary steady state evolution of the weld, characterised by an approximately constant torque and gradually decreasing spindle angular speed. The thermal energy provided to the weld causes an extension of the plasticised zone, while the thrust exerted by the ram induces the axial shortening of the weld, with a consequent expulsion of plasticised material in form of flash; 3) During the third phase, called consolidation, the decrease in angular speed causes the cooling of the junction and a consequent peak in torque to overcome the material strengthening, while the ram thrust induces additional axial shortening and expulsion of flash. When all the kinetic energy stored in the spindle is consumed causing the shaft rotation to cease, the axial load of the ram is kept until the weld cools and consolidates.

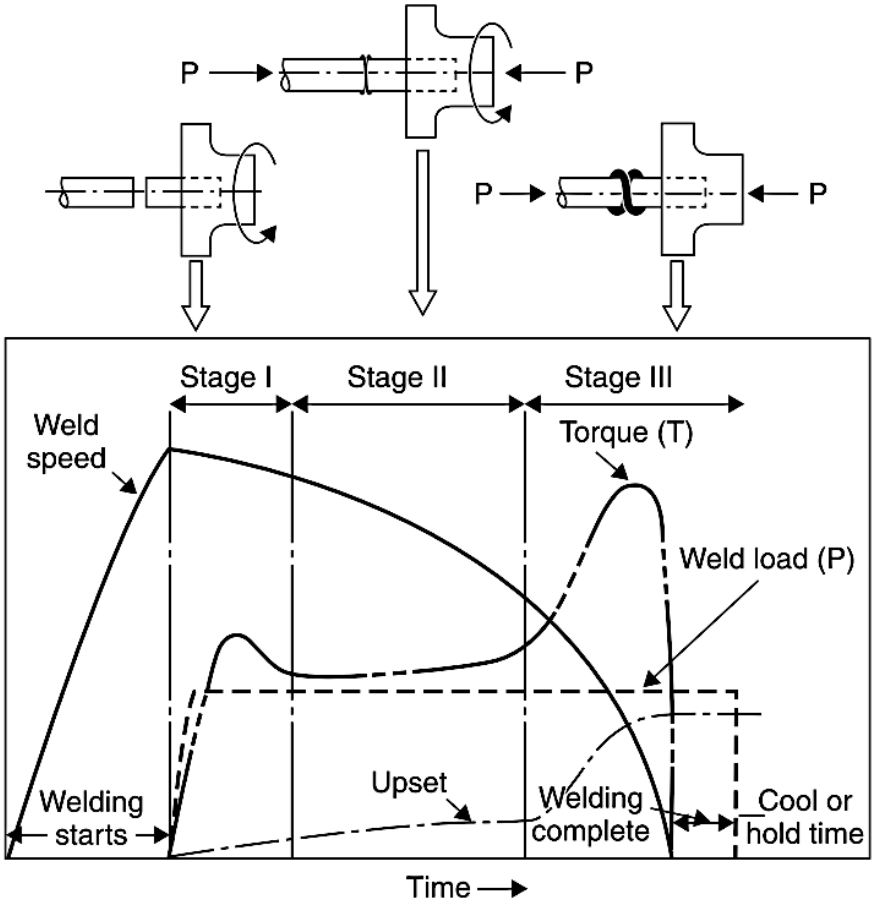


Fig. 2.3 Schematic of the principal process variables and stages in IFW (Adapted from [7])

2.1.4 Frictional behaviour

As previously mentioned, friction plays a key role since it controls the temperature increase at the interface between the workpieces, allowing the conversion of kinetic energy into heat. Despite a significant research effort, the extremely complex friction behaviour of materials interacting in different conditions and the limited knowledge about the weld interface make this one the most complex unresolved problems in friction welding. The first approach developed used Coulomb's model due to its simplicity and proved validity in modelling dry friction. The model relates the friction force (F_f) to the normal force between the contact surfaces (F_n) through a constant, called the

friction coefficient, μ:

$$F_f = \mu \cdot F_n \tag{2.6}$$

and it results independent both from the contact area and the sliding velocity. Wang and Nagappan [17] extended to IFW the approach proposed by Vill' [49] in which the friction coefficient was a function of the angular speed ($\omega(t)$) and radial position (r):

$$\mu(r,t) = \frac{K_W}{(\omega(t) \cdot r)^2} \tag{2.7}$$

in which the constant K_W is determined experimentally. The changing conditions at the weld interface make the assumption of a single friction coefficient for the whole welding not verified. To solve this problem Moal [18] and D'Alvise [19] adopted a Coulomb's friction law for the first phase, in which the shear stress (τ) is proportional to the applied pressure (p):

$$\tau = -\mu p \frac{\Delta V_s}{\mid \Delta V_s \mid} \tag{2.8}$$

and a temperature dependant friction coefficient when the material starts to plasticise, using a formulation based on a thin Norton-Hoff layer subjected to a shear stress:

$$\tau = -\mu K_M(T) \frac{\Delta V_s}{\mid \Delta V_s \mid} \tag{2.9}$$

where ΔV_s is the sliding rotating speed and $K_M(T)$ is the thermo-dependent material consistency.

The difficulty in obtaining an empirical formulation for the friction coefficient are connected to the lack of friction theories of general applicability [37, 50] and the difficulty in assessing the transition from dry friction to viscous behaviour [37, 51]. For this reason, Balasubramanian et al. [52] proposed a methodology that combines the experimental analysis of the temperature in close proximity to the weld zone and

the numerical simulation of the process, introducing the concept of equivalent friction coefficient. This was calculated by trial and error to have an energy input that allowed the numerical results to match the experimental ones. Finally, the authors did a regression analysis to determine the dependence of the equivalent friction coefficient on sliding speed (V), temperature (T), and applied pressure p:

$$\mu = \alpha_0 \cdot T^{\alpha_1} \cdot p^{\alpha_2} \cdot V^{\alpha_3} \tag{2.10}$$

with $\alpha_{0...3}$ the linear regression coefficients. It was observed that the pressure has the highest impact, while the impact of temperature and sliding velocity is lower. In a following work [20] the same authors went a step further and proposed an energy based approach, which completely removed the need for a friction coefficient, instead the energy input was calculated from the experimental values of angular speed and inertia of the spindle. This approach resulted particularly effective and a large number of other researchers have made use of it [8, 21–24, 53]. It is important to underline that also this approach presents drawbacks, in fact the models are no more predictive but rather experimental based, requiring not only the weld's temperature evolution for the final validation but also the experimental angular speed of the spindle. In addition, researchers have to estimate the process efficiency to calculate the actual portion of kinematic energy converted into heat. In this case, the instantaneous equivalent value of friction coefficient at the time step n can be obtained from the instantaneous input kinetic energy (E_I) and the process efficiency (η) [24]:

$$\mu = \frac{\eta \cdot \left(E_I^{n+1} - E_I^n\right)}{-\omega \cdot \Delta t \cdot p \cdot \int_A r dA} \tag{2.11}$$

where ω is the rotational velocity, Δt the timestep, p the weld pressure and $\int_A r dA$ the integral to calculate the welding area.

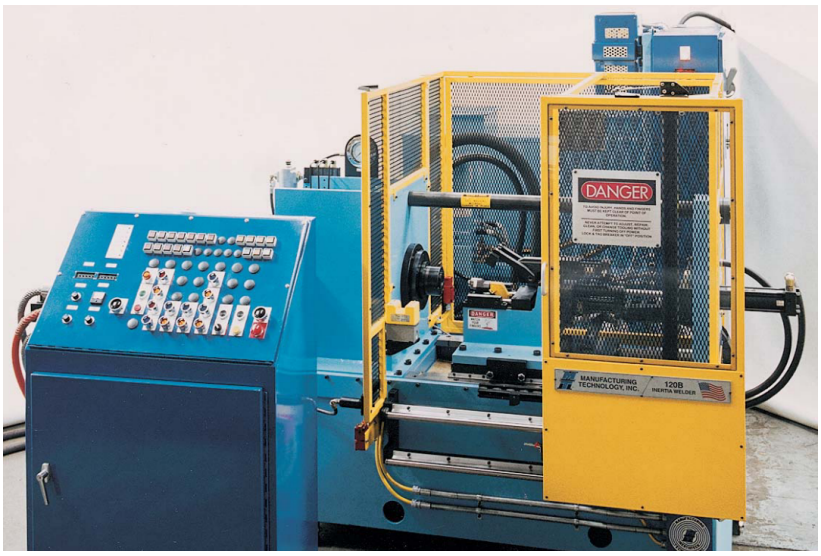
2.2 IFW setup

Inertia welding machines are conventionally classified according to the maximum axial load that the ram can exert. This can range somehow from a few thousands of pounds, for small parts like pistons and pipes, to 4.5 million pounds, for larger components like compressor rotors and drum-drive cones for aerospace applications. Fig. 2.4 shows three examples of industrial inertia welders belonging to different load classes.

2.2.1 Evolution of IFW machines

Understanding the evolution of IFW machines can be of great help in discovering possible weak points that can affect the quality and repeatability of the process outcomes. Even if the machine manufacturers carefully protect their know how, it is still possible to gather useful information analysing the patents filed.

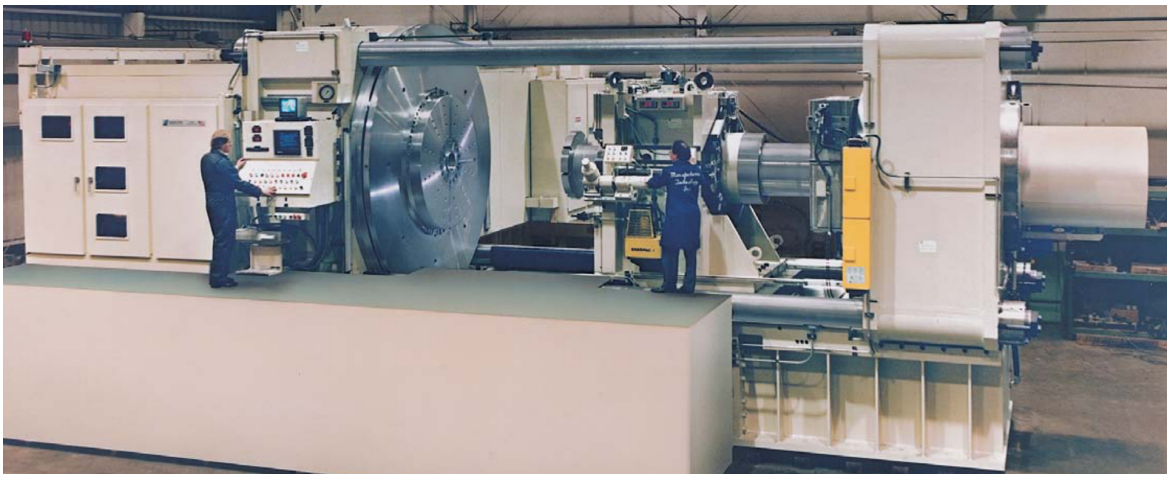
In the first design configurations proposed by Caterpillar and other pioneers of this technology, the friction welders were modified lathes in which flywheels were connected to the headstock and one of the two sides, usually the tailstock, was actuated to slide axially by a ram [55–58]. In the prototype shown in Fig. 2.5a all the key elements are visible; interesting to note is the position of the flywheels between the two ball bearings that support the spindle, completely encased within the headstock body. Comparing this configuration with Fig. 2.5b, it is possible to observe a different flywheel setup, which are installed in a cantilever arrangement with regards to the spindle bearings. On one hand, such a choice is beneficial in simplifying the replacement and accessibility of the flywheels, minimising the production downtime, on the other hand, it can induce sagging of the spindle structure due to the weight of the flywheels and, ultimately, result in alignment errors between the two workpieces. Even if manufacturers tried to limit the sagging of the spindle structure under the weight of the flywheels balancing



(a)



(b)



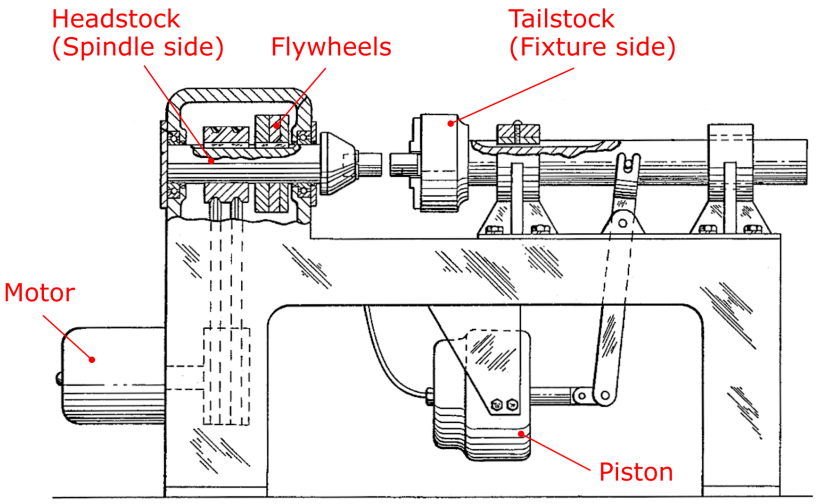
(c)

Fig. 2.4 Example of industrial inertia welders for different axial load classes [54]: (a) MTI 120B (28,000 lb); (b) MTI 250B (200,000 lb); (b) MTI 800B (4,500,000 lb).

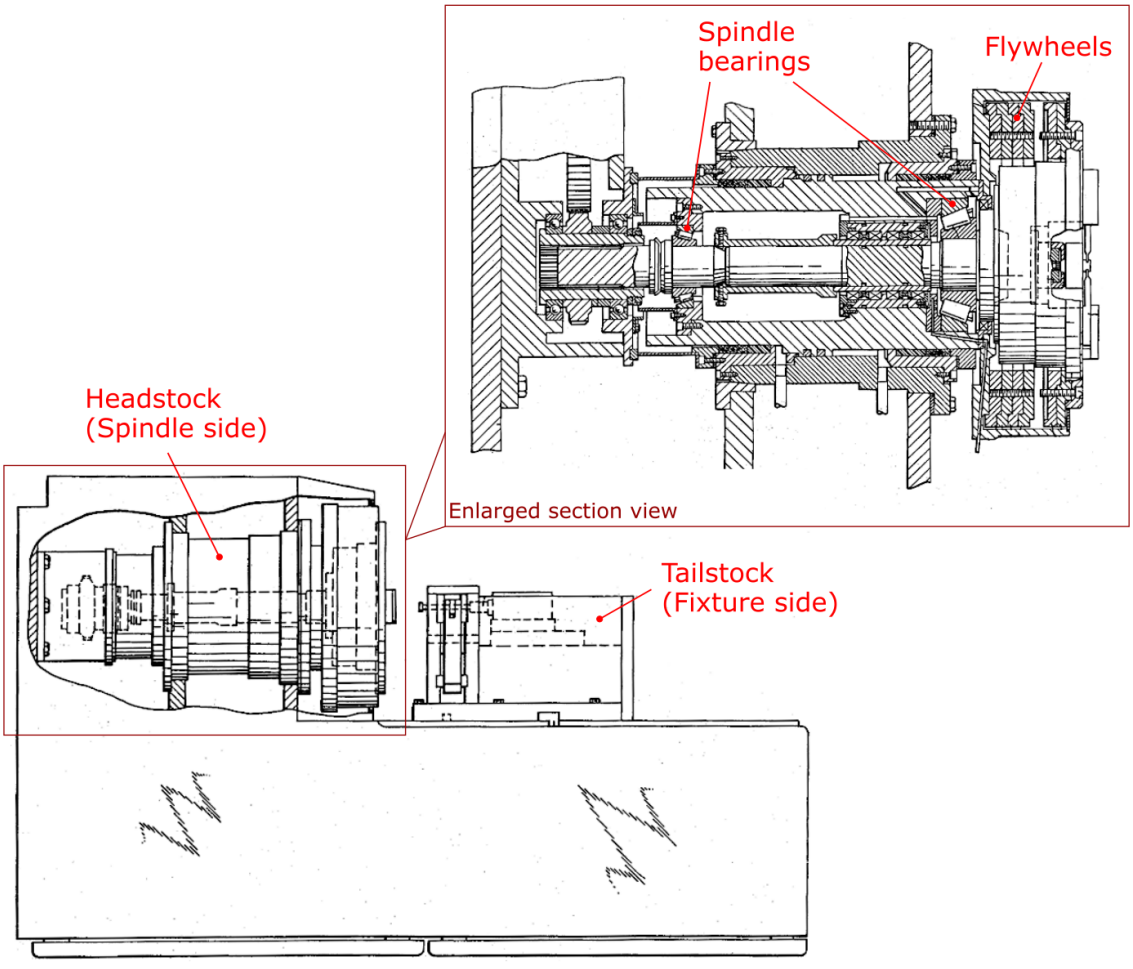
the machine, the problem cannot be completely avoided since the number and mass of flywheels to be used depend on the size and material of the components to be welded, inducing an error that varies from weld to weld. As shown in Fig. 2.4, modern industrial welders, even if much more sophisticated, still present this issue and the choice between the two configurations is guided by a compromise between productivity and accuracy of the process outcomes.

While lathe machines are subjected to very limited axial reactions, the load required to achieve a successful weld is relatively large and it increases with the workpieces size and material strength. For this reason one of the first problems that researchers and engineers had to face was the deflection of the system under process loads [59]. Jones [60] proposed an updated machine design that included tie bars to connect headstock and tailstock, this solution, still currently used in modern inertia welders, is shown in Fig. 2.6 for two popular machine configurations. Tie bars mitigate the problem, even if a certain level of compliance at the peak process loads should still be expected. In addition, having two or more tie bars connected to the tailstock while this slides over the linear guide rails towards the headstock (Fig. 2.6b) can cause over-constraining, adding uncertainty on the final alignment of the two workpieces.

A final aspect of great importance for the machine performance are the bearings that support the spindle shaft. As already discusses in section 2.1.2 they have a key role in the machine efficiency, representing the major source of energy losses, however, they are also of primary importance on the rigidity and dynamic performance of the system under process loads. As shown in Fig. 2.5 the first configurations made use of radial and angular contact bearings because of their compact design, good performance and simple maintenance. However, the requirement of sustain very high loads while rotating at high speed, make them an element particularly difficult to be optimised. In fact, reducing the load capacity of a bearing would normally allow for higher angular



(a)



(b)

Fig. 2.5 Examples of inertia welder prototypes patented by Caterpillar Inc.: (a) Schematic of a machine with sliding tailstock and flywheels installed between the spindle bearings (Adapted from [55]); (b) Schematic of a machine with stationary tailstock, sliding headstock and flywheels cantilever with respect to the spindle supports (Adapted from [56]).

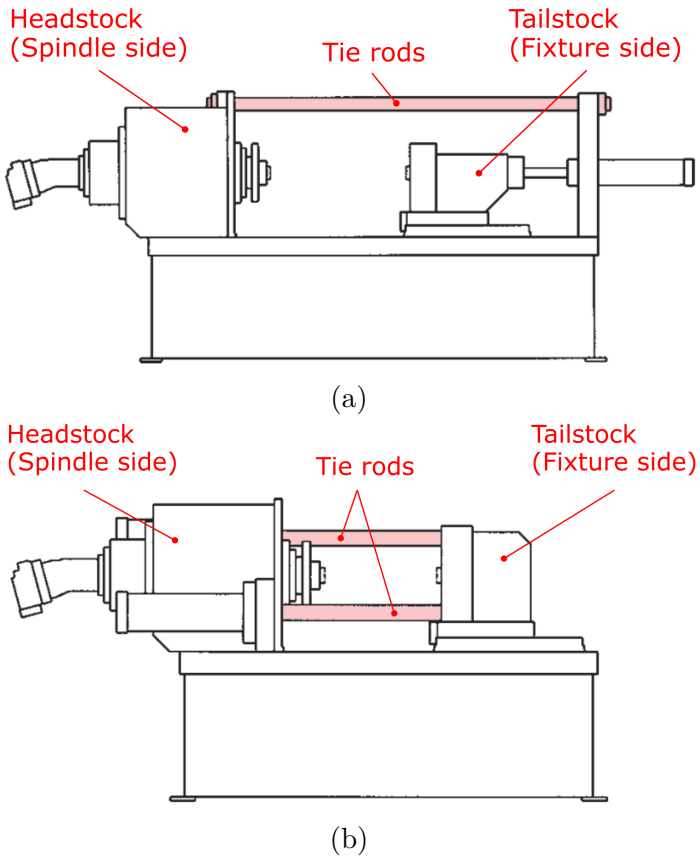


Fig. 2.6 Examples of inertia welders with tie bars to minimise the deflection under process loads: (a) Box style inertia welder (Adapted from [54]); (b) Open top inertia welder (Adapted from [54]).

speed but leads to an unacceptable wear under load, while having bearing with very high load capacity makes them less suitable for high angular velocities and with poor efficiency [61]. For this reason, manufacturers have tested several solutions, for example Kashchenevsky [62] proposed the design in Fig. 2.7, in which the roller element bearings were replaced by a radial journal bearing and a hydrostatic thrust bearing. For current industrial machines, in particular for the ones designed for high forge capacity, the configuration with one hydrostatic thrust bearing together with either rolling element or journal radial bearings is usually adopted. In fact, even if hydrostatic thrust bearings require an external pressurisation system and are more demanding from a maintenance viewpoint, they are characterised by low friction and wear, high stiffness, good damping

and high load carrying capacity [61]. The analysis and periodic maintenance of the machine bearings are of primary importance for a proper behaviour of the machine because alignment errors between the two workpieces, decreased stiffness and overall reduced process repeatability can be experienced when the bearings start to wear.

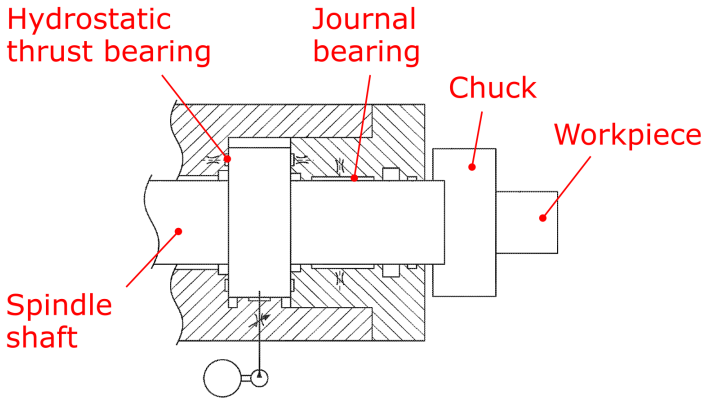


Fig. 2.7 Schematic of the spindle supported by a radial journal bearing and a hydrostatic thrust bearing (Adapted from [62])

2.2.2 Tooling

An aspect of great importance in every manufacturing processes is the capability to accurately locate the workpiece and hold it in place throughout the operation, also known as fixturing. While it is known that a poorly designed fixture can affect the quality of the process outcomes significantly, if not turn them completely into scrap, it does not usually receive the necessary attention. IFW does not make an exception and while it is possible to find evidence in literature of the negative effect of a poorly designed workholding setup, no in-depth analysis on the topic can be found.

Preuss et al. [10] mapped the residual stresses in RR1000 tubular components in the as-welded and after postweld heat-treated (PWHT) conditions using neutron diffraction. The researchers found significant residual stresses in the axial direction that speculated being connected to a bending moment partially induced by the clamping action of

the fixture and partially by uneven heating. These observations were confirmed by Karadge et al. [32] who analysed the residual stresses in U720Li nickel-based superalloy welds. Two different setups have been used, a laboratory inertia welder to weld small tubular workpieces and an industrial machine to weld a full-scale compressor drum assembly. The analysis of the residual stresses in the welds using neutron diffraction showed a marked difference in the axial stresses that the researchers proposed being connected to different clamping conditions in the two machines. In fact, while the laboratory system used a non-optimised tooling setup, generating a strong radial grip behind the weld interface and, consequently, inducing large residual axial stresses when the clamping action was released, the industrial welder was optimised to minimise the gripping force and cause much smaller residual stresses. Pang et al. [31] extended the work of Preuss et al. [10] studying RR1000 tubular components with three different techniques: neutron diffraction, X-ray diffraction and hole drilling methods. Also in this case the researchers detected large axial residual stresses that were attributed to the clamping action of the fixturing. In fact, as shown in Fig. 2.8, the bending moment introduced by an excessive clamping action of the tooling elastically deforms the unwelded parts and then, when the weld is removed from the fixture at the end of the process, the constraining action of the weld just formed opposes to the elastic spring-back, generating residual stresses. In addition, it is pointed out how thermomechanical effects should be excluded from the causes of axial residual stresses due to the low dependence with the axial position along the weld. Finally, the researchers stressed the importance of optimising the fixturing setup to minimise residual stresses and to include the effect of the tooling in the numerical simulation of the process.

Wang et al. [23] developed one of the first FE models that accounted for the tooling, which was modelled as a rigid cylinder embracing portion of the workpiece. The model was able to predict the formation of axial residual stresses that the researchers

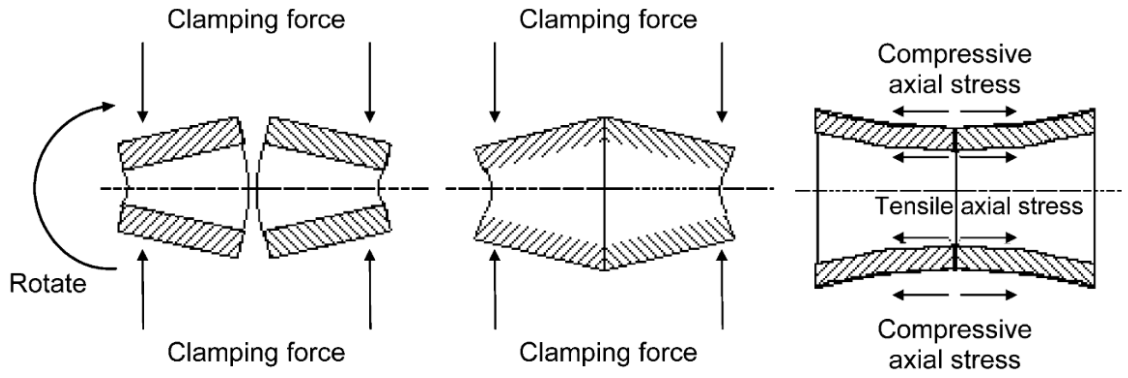


Fig. 2.8 Schematic diagram of the tooling effect on a tubular workpiece and of the residual stresses induced [31]: (a) Deformation of the workpieces due clamping forces before part contact; (b) Deformation of the workpieces during the welding; (c) Elastic spring-back of the welded component when the clamping force is realised with generation of residual stresses due to constraining action of the weld

attributed partially to the effect of the tooling and partially to other thermomechanical effects not detailed. It is important to observe, however, that the representation of the fixture is extremely simplified, with no clamping load included and the constraining action workpiece-fixture most likely enforced with a sticking boundary condition, even if no details were reported. Iracheta, Bennett, and Sun [33] improved the work of Wang et al. [23] testing the effect of several fixturing parameters: clamping conditions, clamping history and the workpiece stick-out length from the fixture, termed component stick-out. Also in this case, a simplified representation of the fixture was used, which was modelled as a rigid die that embraces the workpiece. Different clamping conditions for the workpiece-die contact were tested, sticking condition and frictional contact; the researchers found that no noticeable difference could be observed between the two. For the clamping history, different duration of the cooling period after the end of the weld were analysed but the researchers found no remarkable difference since the majority of the residual stresses were generated in the initial instants of the cooling. Finally, the component stick-out length was analysed and it was observed that a stick-out of half the components length was optimal in term of residual stresses.

The studies presented are of great importance because for the first time they acknowledged in open literature possible issues arising from an improper fixturing setup; however, they appear limited in focus, analysing only the effect on the residual stresses and still heavily relying on simplifications and assumptions. In fact, it is logical to assume that the tooling-workpiece interaction in IFW could be affected by additional issues that can deeply affect the interaction between the two workpieces, such as non-perfect alignment of the workpiece inside the tooling due to improper installation by the operators or geometrical errors in the mating surfaces, and misalignment and runout between headstock and tailstock, which already occurs in other manufacturing processes like turning and milling [63, 64]. These aspects seem not to transpire from the previous studies, which present the problem as perfectly axisymmetric, however, if this assumption on one side greatly helped researchers in simplifying an already extremely complex problem like IFW, on the other could hide additional phenomena. For example, the disagreement regarding the uneven heating as a partial cause for the residual axial stresses, supported by Preuss et al. [10] but refused by Pang et al. [31], could be caused by the study of single sections of the weld rather than analysing the whole circumference. In this case the quote by John A. Wheeler "Never make a calculation until you know the answer" [65] could be playing against the researchers and an analysis that challenges the conventional assumption of axisymmetry would be of great interest. Similar considerations can be applied to the numerical modelling presented in [23, 33], in which the axisymmetry assumption is combined with an extremely simplified representation of the machine tooling that disregards clamping forces, misalignments between the two workpieces and compliance of the machine supports.

2.2.2.1 Tooling configuration

To understand how these problems can arise, it is necessary to analyse the fixture setup conventionally used in IFW. As previously discussed, IFW is used to weld parts of axisymmetric shape, for this reason the first and simplest approach made use of chucks similar to the ones adopted in lathe machines, either mechanically or hydraulically actuated [55–57, 66]. The very high process loads, torque and thrust, typical of IFW, however, make this solution suboptimal, in fact the only way to restrain the workpieces would be to increase the clamping force of the chuck inducing undesired deformation in the workpieces. For this reason, in modern industrial inertia welders a collet usually replaces the chuck and an additional element, termed backstop or backup, is added to the machine tooling.

Fig. 2.9a shows a section view of a collet assembly specifically designed for IFW [67]. This includes a sleeve (3) which is actuated to translate along its axis, when the drawbar pulls internally the wedge surface slides along a corresponding surface in the housing (2) causing the sleeve to tighten on the workpiece, vice versa, when the sleeve is pushed outside the housing, the collet releases the workpiece. A characteristic detail of collets for IFW is the presence of one or more keys (5) that engage the sleeve to avoid its rotation under the torque generated during the weld, as detailed in Fig. 2.9b. Finally, the backstop (1) works as a rear plate against which the workpiece sits and absorbs the thrust exerted by the machine ram, partially helping, in addition, in absorbing the process torque due to the friction generated between the workpiece and the backstop itself. An interesting advantage of this configuration is the capability of exploiting the process axial load to increase the clamping action of the collet. In fact, if not actively repulsed by the collet's actuator, the axial load would carry the collet's sleeve further inside the housing and, consequently, increasing the collet clamping action. The configuration of the collet when allowed to exploit the process thrust is sometimes referred to as thrust augmented.

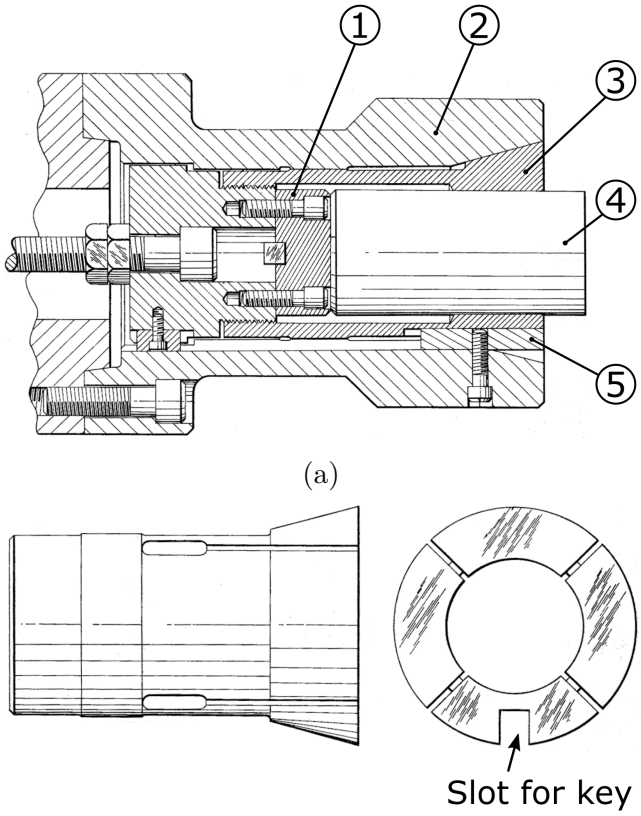


Fig. 2.9 Collet with backup used in IFW to clamp workpieces of axisymmetric geometry (Adapted from [67]): (a) Section view of a collet with backstop: (1) Backstop; (2) Collet housing; (3) Collet sleeve; (4) Workpiece; (5) Key; (b) Detail of the collet sleeve.

Even if the tooling setup with collet and backup has considerable advantage compared to the original jaw chuck, it still presents drawbacks. The first issue is the possible deformation and damaging of the workpiece when clamped tightly by the collet, in fact even if the collet almost completely embraces the workpiece and, therefore, has a better pressure distribution compared to a jaw chuck, it still can induce significant deformations into the workpiece, in particular for thin walled parts, as already pointed out [10, 31, 32]. In the attempt to solve this problem, solutions like the one presented in Fig. 2.10 have been proposed, in which an expanding ring or collet sleeve opposes to the deformation induced by the external collet. While this solution is very effective for thin-walled components, it is worth noting that for workpieces of complex geometry,

e.g. aeroengine compressor drum-drive cone, results in difficult implementation, not considering the added complexity in the system. Furthermore, considering that IFW is considered a near-net-shape process, scratching and indentation of the workpiece's external surface are usually not acceptable. When adding sacrificial material to be removed post-weld is not feasible due to economical or technical problems, solutions like the one in Fig. 2.11 can be adopted. In this configuration an elastomeric coating is applied to the collet jaws to preserve the surface finishing of the workpiece and to conform to its shape, avoiding distortion in the workpiece when the circularity of either workpiece or collet is not perfect. The biggest drawback of this approach is the significant loss in clamping action.

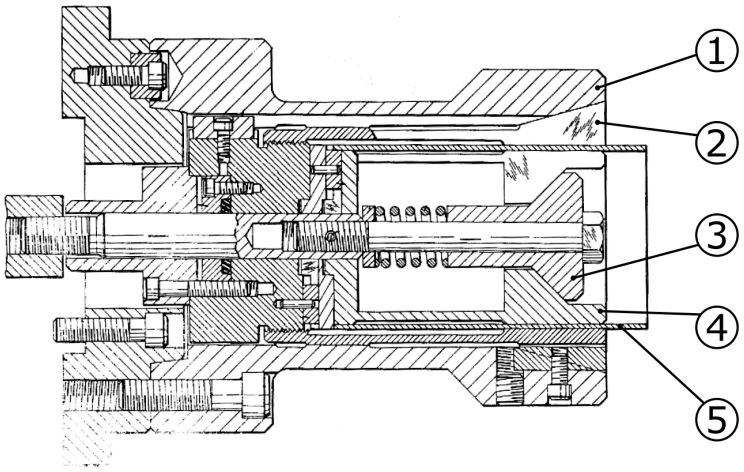


Fig. 2.10 Dual collet designed to limit the deformation in thin-walled components (Adapted from [68]): (1) Collet housing; (2) External collet sleeve; (3) Expander; (4) Inner collet sleeve; (5) Component.

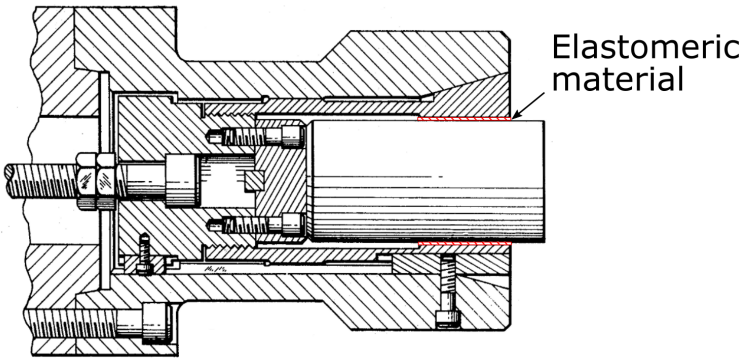


Fig. 2.11 Collet with elastomeric coating to reduce the damaging on the component external surfaces (Adapted from [69])

Another option to reduce the collet clamping force whilst preserving the capability of the system to withstand the process torque is the use of keys or grippers installed into the backstop's surface. Fig. 2.12 shows an approach in which several serrated circular grippers are inserted in the backstops, the teeth of the grippers protrude between 0.1 to 0.5 mm and are built in a material harder compared to the one of the workpiece so that when the axial load is applied they indent the back face of the workpiece. While the use of keys can transmit a high torque, they require workpieces specifically designed with a large shoulder for the key slots, which needs to be removed in the re-machining after the weld. For highly expensive materials like high content γ' nickel-based superalloys is not economically convenient, therefore the solution with gripper is preferred even if a smaller torque is transmissible, depending on the workpieces' material strength, number of grippers and their position. While both configurations are particularly popular in large industrial welders, they can induce problems of overconstraining and misalignment of the workpieces within the tooling. As shown in Fig. 2.13a, the optimal clamping configuration for relatively short cylindrical parts considers to remove two degrees of freedom (DoFs) with a radial locating element, in this case the collet, and three degree of freedom with a planar locating surface, the backstop. Finally, the sixth degree of freedom not shown in the picture, i.e. the rotation of the cylinders around

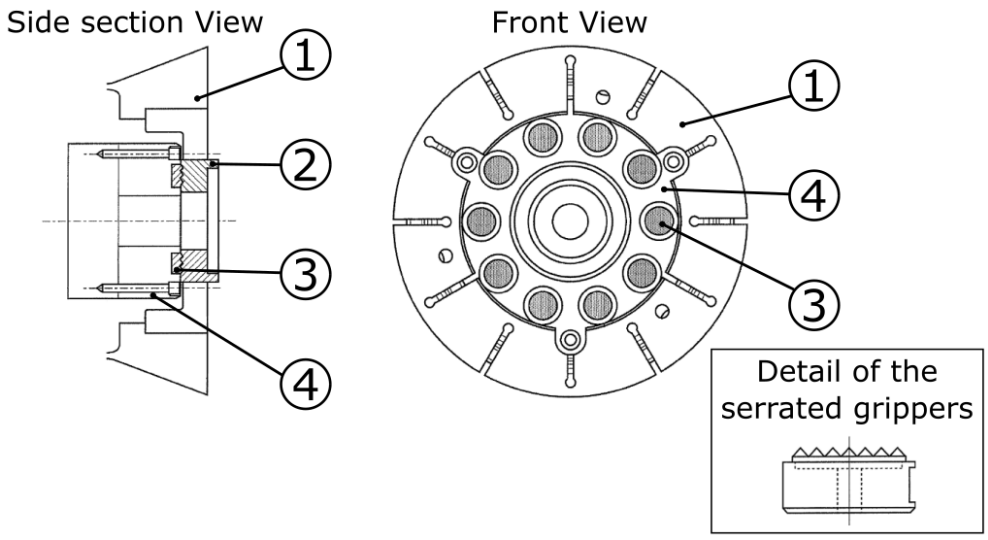


Fig. 2.12 Tooling variation in which serrated round grippers are inserted in the backup to provide additional grip on the workpiece (Adapted from [70])

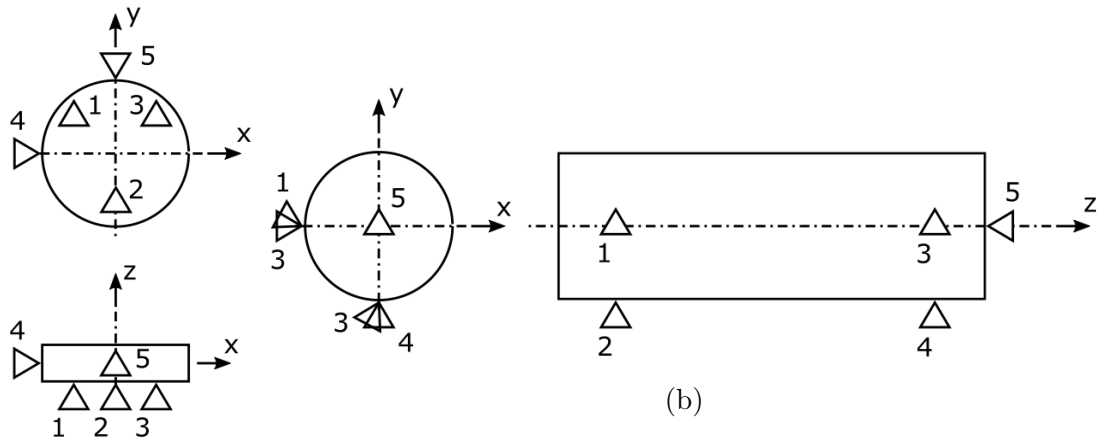


Fig. 2.13 Schematic representation of the optimal configuration of the locators for cylindrical components (Adapted from [71]): (a) Configuration for short cylinders; (b) Configuration for long cylinders.

its axis, is automatically removed by the friction between the collet and workpiece [71, 72]. When keys are added, they add additional constraints that make the system overconstrained, inducing problems of positioning and stresses in the component. When instead grippers are used there is no way to ensure before the weld that the workpiece has been fully indented, with the risk of a misalignment in the case where a partial indentation of some of the grippers occurs.

The misalignment of the workpieces inside the tooling, combined with a possible misalignment between the axis of the headstock and tailstock fixtures, would inevitably result in a runout error on the final weld. This problem becomes even more significant for long workpiece, in fact, as shown in Fig. 2.13b, the location of a long workpiece considers four DoFs removed on the cylindrical surface and only one in the flat base [71, 72]. However, as represented in Fig. 2.14, long components are clamped by an additional second chuck to support the workpiece close to the weld interface. In this case just the presence of the backstop, which as a plane removes multiple DoFs, is sufficient to overconstrain the workpiece.

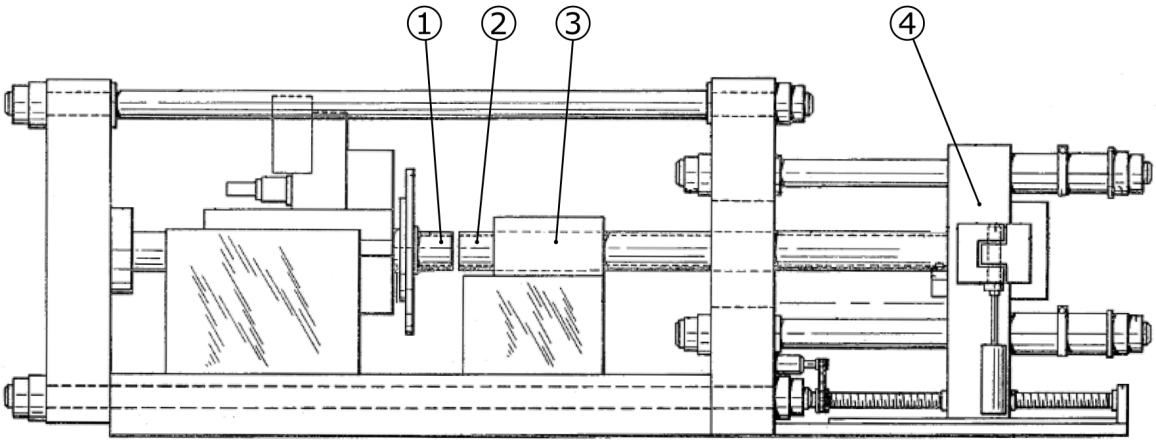


Fig. 2.14 Alternative machine setup to accommodate long components (Adapted from [73]): (1) Headstock component (short); (2) Tailstock component (long); (3) Tailstock chuck; (4) Tailstock backstop.

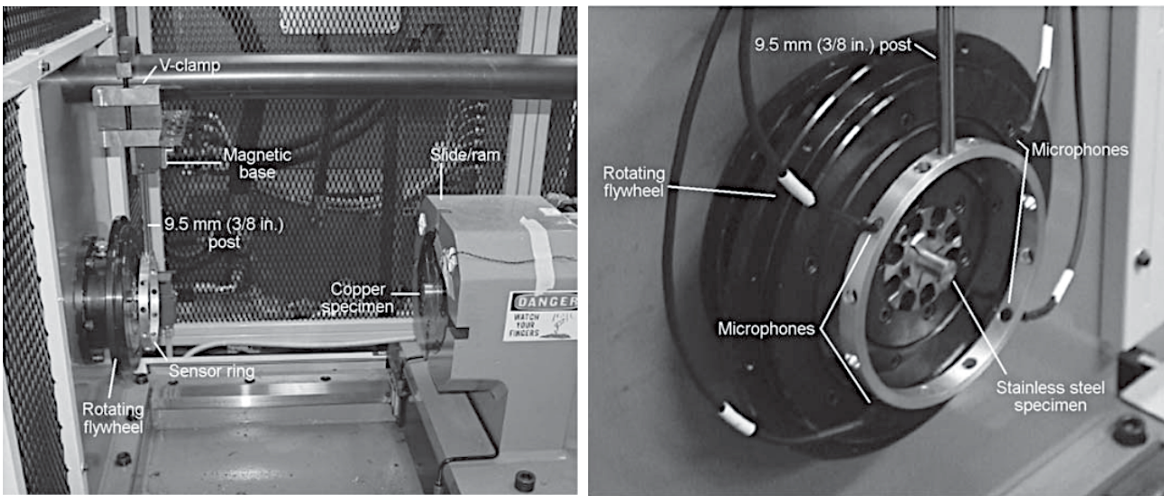
2.2.3 The measurement and monitoring of IFW systems

The study of the system conducted in the previous section showed how several factors could affect the interaction between the two workpieces during the welding and, consequently, affect the quality of the outcomes and their repeatability. While the parameters conventionally monitored by the machine control unit (spindle angular speed of the spindle, upset, thrust exerted by the ram and few other parameters connected to the hydraulic circuits existing in the system, e.g. hydrostatic bearing and collets) are suitable to assess the overall health of the machine, they are not capable of providing information about the weld evolution, due to the size of the machine and the multitude of subsystems embedded. This makes measurements conducted far from the weld zone not representative of the local welding conditions and the data extracted corrupted with noise. To overcome this limitation researchers developed monitoring systems able to investigate specific phenomena.

Wang, Reif, and Oh [28] installed a piezoelectric acoustic emission transducer on the machine fixturing chuck and studied the correlation between the acoustic emissions and the quality of ferrous welds. It was found that for a typical weld two sound bursts can be detected: one during the process and a second one during the post-welding cooling. The author concluded that the first event was caused by the large plastic deformations during the process, while the second one originated from thermal and metallurgical effects, in particular martensitic transformation. In addition, taking the acoustic emission profile of a good weld as a reference, it was possible to assess the quality of successive welds. Having sensors attached to the system, however, is not optimal because the large oscillations generated by the process can cause the sensors to detach [74, 75] and because the sensor, being directly connected to the tooling risk to pick up lots of noise from the machine. Hartman et al. [76] improved the monitoring setup proposed by Wang, Reif, and Oh [28] developing a ring array of

condenser microphones surrounding the two specimens, as shown in Fig. 2.15. The data collected by the monitoring system were used to train a probabilistic neural network (PNN) that was able to classify the welds studied as acceptable, conditional and unacceptable. The validity of the algorithm was verified with visual examination and mechanical/microstructural characterisation of the welds. This work provides an important basis for the non-destructive monitoring of the microstructural quality of the weld, but does not provide any information about the way in which the two components interact during the welding process. In addition, the observations stated by Hartman could be biased by an undersampling in the measurements. In fact, trying to analyse an ultrasonic frequency content with a sampling rate of 40/50kHz [29, 77] is not adequate because, even when the frequency components respect the Nyquist theorem, such a low sampling rate does not allow the spikes in the signal to be captured.

Grooms et al. [27, 78] acknowledged the problem of vibrations during the welding due to the interaction between the two workpieces, detrimental for the weld quality and possible damaging of the tooling. For this reason, they proposed a monitoring system capable of extracting the pressure in the machine ram and use this data to obtain information about vibrations and force fluctuations during the process. Zaeh and Poehler [74] started from the observation that approach of Grooms et al. [27, 78] and similar studies that propose damping systems [34, 35, 79], even if effective in detecting the problem of vibrations and try to reduce it, are not capable of providing explanations regarding their possible causes and proposed a more academically sound approach to investigate the problem. Analysing the experimental data obtained with a radial fibre-optic vibrometer used to monitor the workpieces oscillations in proximity of the weld zone, as depicted in Fig. 2.16, the researchers found two instants in which particularly large oscillations were generated: the impact between the two workpieces at part contact and the final instant of rotation of the flywheel. Simplifying the



(a) (b)

Fig. 2.15 Monitoring system comprising a ring array of condenser microphones that surround the workpiece and capture the airborne audio data from the weld (Adapted from [75]): (a) View of both headstock and tailstock before they are brought in contact to start the welding, in which it is possible to observe the monitoring system connected to the tie bar; (b) Detail of the monitoring system.

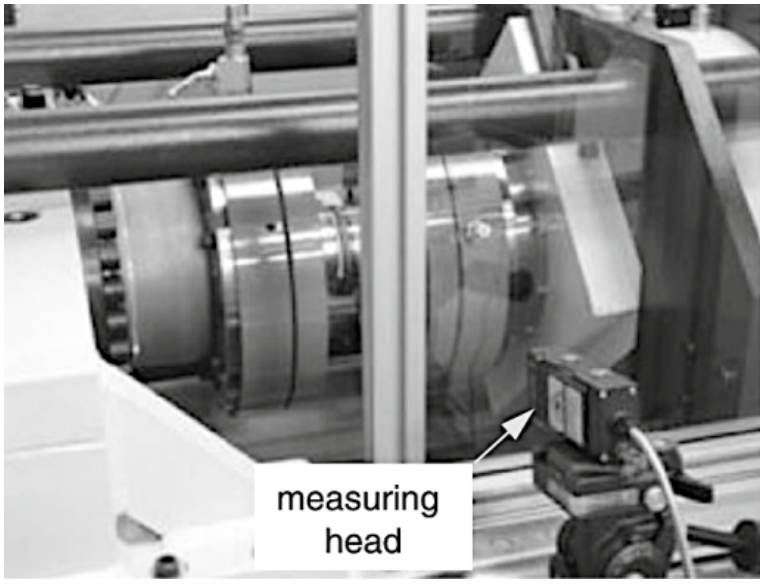
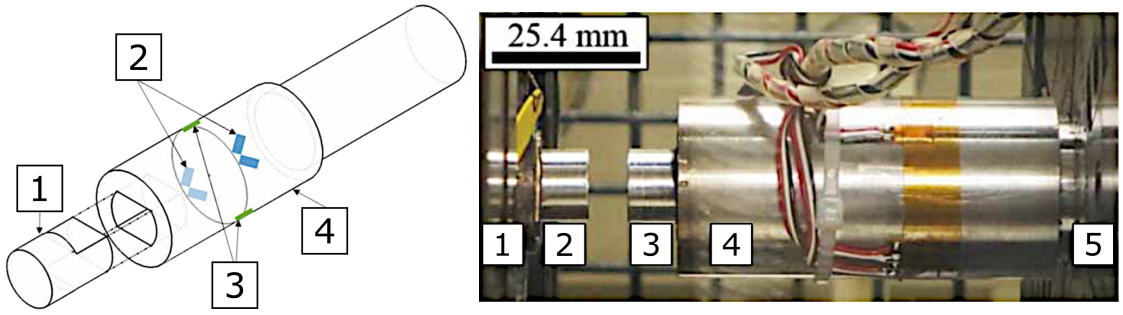


Fig. 2.16 Welding setup with the radial fibre-optic vibrometer installed on a tripod outside the machine to monitor the oscillatory behaviour throughout the process (Adapted from [74])

system with a spring-mass-damper model and studying the behaviour of the system both in the axial and torsional directions, it was found that to reduce the oscillations at the initial impact a more gradual load ramp from the machine ram was be beneficial as well as increasing the damping of the system with an optimised design of the tooling. To address the torsional oscillations at the flywheels stoppage, instead, the researchers suggested a configuration with lower inertia and higher initial angular speed, a solution not always possible due to the sensitivity of certain alloys to high speed and for the efficiency problems motivated in section 2.1.2. A few shortcomings can be found in this study, in fact, the analytical model is based on perfectly constrained cylinders and is not able to take into consideration the real conditions during welding due to the non-ideal characteristics of the workpieces and the machine. In addition, using one single radial vibrometer makes it impossible to correctly decouple the torsional vibrations from the axial ones [80, 81]. Finally, the vibrometer setup used, i.e. a sensor installed on a tripod outside the machine, can provide good results for few experimental welds, but does not seem suitable for a production environment. In fact, the accessibility to the machine by the operators without obstruction to their passage would require the sensor to be moved after each weld, with consequent need for re-alignment, causing unacceptable delays to the production, while the need for the laser to reach the workpieces surface can represent a serious limitation for the machine in which objects or protections can obstruct the direct view of the weld.

Other examples of monitoring systems for IFW have been presented in section 2.1.2, where a few articles [13, 25, 26] proposed the use of a load cell to separate the effective energy converted into heat from the losses into the machine. Fig. 2.17 shows the details of a custom load cell, in which torsional and axial strain gauges are installed on a cylindrical component, and the system works as an interface between the machine tooling and the workpiece. Several drawbacks can be observed in this setup, in fact



(a) (b)

Fig. 2.17 Monitoring system to measure the process torque throughout the welding (Adapted from [26]):
(a) Schematic view of the load cell and the workpiece. The four torsional strain gauges are installed ±45° with respect to the central axis, while the two axial strain gauges are oriented along the central axis: (1) Workpiece; (2) Torsional strain gauges; (3) Axial strain gauges; (4) Load cell body;
(b) Monitoring system installed into an inertia welder: (1) Headstock; (2) Headstock workpiece; (3) Tailstock workpiece; (4) Load cell; (5) Tailstock.

even if the authors recognised the importance of tolerances in the repeatability of the process, the transducer sticking out from the machine collet has a significantly high length-to-diameter ratio. This is clearly undesired as any misalignment inserting the transducer inside the collet would be magnified by the length of the system. The slenderness of the transducer, then, would cause a non-negligible deflection when out of axis loads were applied, producing an uneven stress distribution also in the workpiece. The strain gauges configuration chosen makes this problem even worse, in fact with the axial strain gauges used only for the calibration of the system and not activated during the welding combined with presence of a single full Wheatstone bridge in the torsional direction, no information about possible non uniform loading conditions can be captured, leaving the researchers unaware of possible problems. Finally, the workpiece-load cell interface requires workpieces designed ad-hoc and does not provide any clamping action that can absorb the inevitable play between the mating surfaces, leaving the workpiece inaccurately located.

A few additional patents [82, 83] acknowledged the problem of concentricity and angular alignment between the components and how their detection is on one side fundamental to assess the system performance and on the other extremely time consuming, due to the need to complete the manual measurement, saving the data and forwarding it to the engineering department. For this reason, Yao et al. [82, 83] proposed a system to automate and simplify the collection and remote transfer of the data. Even if the two patents don't go in the details of the invention, it is understood that values of concentricity and angular alignment are supposed to be measured before and after the welding, therefore, even if useful to establish the system performance, are neither able to give an insight in the dynamic alignment of the two workpieces, nor in the physical causes that induce it.

2.3 Dynamics of Rotating Systems

From the analysis conducted in the previous section, the IFW system can be schematically represented according to the diagram in Fig. 2.18. Analysing the headstock, it is possible to observe how this represents a complex rotordynamic system, in which the shaft (5), supported by a combination of radial and axial bearings (2, 4), carries flywheels of large mass and inertia (3), rotates at relatively high and non-constant angular speed and is subjected to high process loads. Starting from late nineteenth century with the work presented by Rankine on the effect of centrifugal forces on rotating shafts [84], researchers started to gain interest in the complex dynamic behaviour of rotating systems, usually referred to as rotordynamics [85]. Since then a significant research effort has addressed the modelling of the two main elements of rotordynamic systems, bearings and spindle.

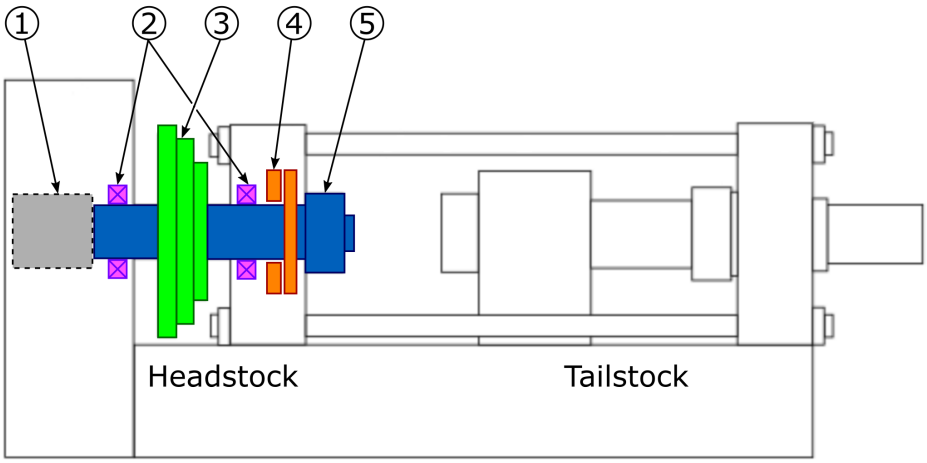


Fig. 2.18 Schematic representation of an inertia welder in which the key elements of the headstock rotor-bearing system have been highlighted: (1) Motor; (2) Radial rolling element bearings; (3) Flywheels; (4) Hydrostatic thrust bearing; (5) Shaft (Based on an MTI's proprietary design)

2.3.1 Modelling of rolling elements bearings

The main objective in modelling bearings is to obtain their stiffness, a factor which has a great impact on the static and dynamic response of spindles systems. Restricting the analysis to rolling elements bearings, which have found large success in many industrial applications, five approaches can be used to describe their behaviour: lumped-parameter, quasi-static, quasi-dynamic, dynamic and FE based. The lumped-parameter approach represents the interaction of rolling elements/races and the effect of the housing with spring-damper elements [86, 87]. The quasi-static approach is more advanced and is based on the force and moment equilibriums for the rolling elements and the bearing races, this method became particularly popular due to its relative simplicity and capability to obtain an explicit formulation of the bearing stiffness. Jones [88] proposed a very popular quasi-static model based on the assumption that the ball elements roll without spinning around one of the two races, called the controlling race, while all spin occurs with respect to the other race. Limitations of the model such as determining which of the two races is the control one, the simplified motion of the balls and the

absence of the cage effect have fostered further research. De Mul et al. [89, 90] proposed a general model based on the load/deflection relationship in matrix form that allows for a straightforward analytical calculation of the bearing stiffness matrix. Although the model is easier to implement compared to that of Jones, it neglects the gyroscopic effects. A significant step forward over Jones' model has been accomplished by Harris [91], in which different load conditions for the bearing are considered. In addition, the model includes differential components in the equilibrium equation to account for the motion of the rotating elements [92], in an approach normally referred as quasi-dynamic. Models that make no use of static constraints but rather employ differential equations to describe the translational and rotational motion are defined dynamic; an interesting example of a dynamic model has been proposed by Gupta [93–96], with six DoFs, which considers the interactions between the rolling elements, cage and races. Finally, in more recent years, FE models become popular to study complex phenomena, such as the contact stresses, fatigue life and bearing behaviour in the presence of defects [85, 97].

2.3.2 Modelling of bearing-rotor system in manufacturing application

The most basic rotordynamic system that can be studied is a Jeffcott rotor, in which a large mass and inertia disk is installed on a massless flexible shaft supported by rigid bearings. Although the simplicity of this model makes it particularly suitable for analytical analysis [98, 99], it also limits its practical application, for this reason more advanced and accurate approaches like rigid shaft, transfer matrix and FE have been developed [85]. In recent years, with high performance computing systems more broadly available, FE models have become increasingly attractive to obtain accurate solutions for complex systems. Among these, beam element approaches have been

widely used due to an excellent trade-off between accuracy and calculation time, while 3D solid element models have been reserved for particularly complex systems or when dealing with asymmetric and anisotropic cases [85, 100].

An important category of rotordynamic systems with a deep industrial impact is represented by machine tools, for which it has been long recognised how the quality measures, e.g. dimensional accuracy and surface finish, are closely related to the dynamic characteristic of the associated spindle-bearing system [101, 102].

One of the first machining processes studied in term of dynamic behaviour was turning, where Bollinger and Geiger [103] presented a predictive finite difference model for the analysis of the static and dynamic response of a machine tool spindle and applied it to a lathe focusing on spindle behaviour, the influence of the bearings and effect of the workpiece. Sharan, Sankar, and Sankar [104] studied the lathe spindle-workpiece system shown in Fig. 2.19 with an Euler-Bernoulli formulation of the motion equation:

$$\frac{\partial^2}{\partial x^2}\left(EI\frac{\partial^2 U(x,t)}{\partial x^2}\right)+m(x)\frac{\partial^2 U(x,t)}{\partial t^2}+k(x)\,U(x,t)+c(x)\frac{\partial U(x,t)}{\partial t}=F(x,t) \quad (2.12)$$

where x and t are the spatial coordinate along the beam and temporal coordinate respectively, U the global displacement, E the Young's modulus, I the moment of inertia, m the mass per unit of length, k the stiffness, c the damping and F the external loads. The vibrational behaviour of the system was analysed using the FE technique and the differential equation of motion converted in the matrix form:

$$[M]\left\{\ddot{U}\right\}+[C]\left\{\dot{U}\right\}+[K]\{U\}=\{F(t)\} \quad (2.13)$$

where $[M]$ the global mass matrix, computed as sum of the mass of the shaft and additional concentrated masses, e.g. disks installed on the shaft; $[K]$ the global stiffness matrix, accounting for both the contribution of the shaft and the bearings; $[C]$ the

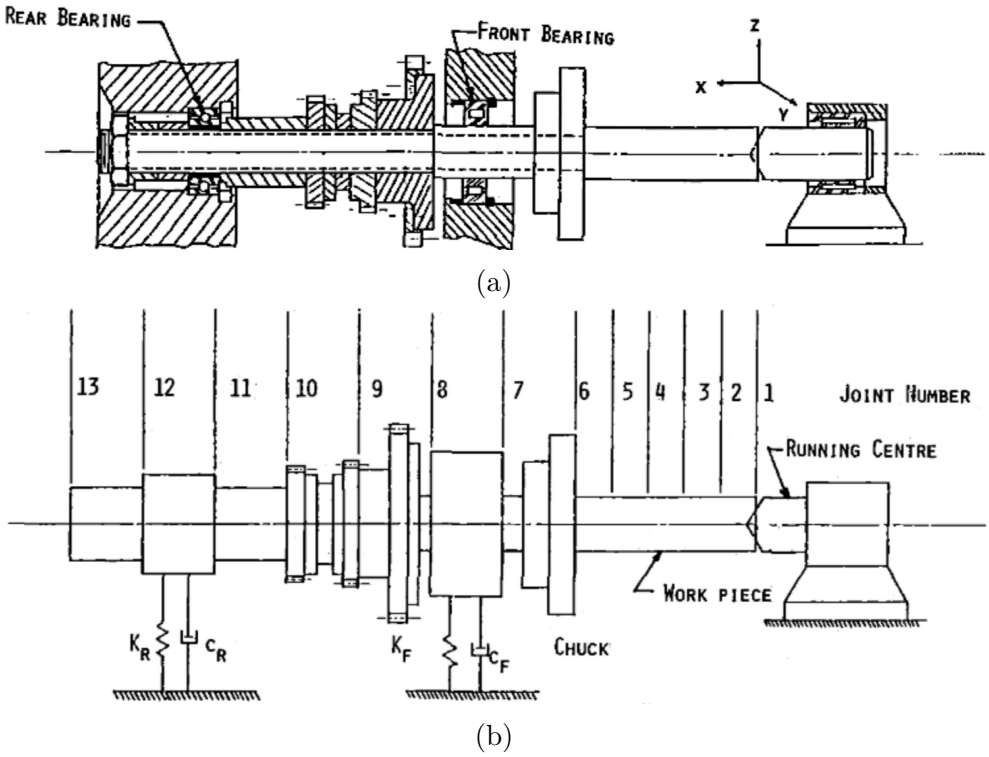


Fig. 2.19 Lathe spindle-workpiece system [104]: (a) CAD model; (b) Schematic used in the FE study of the system.

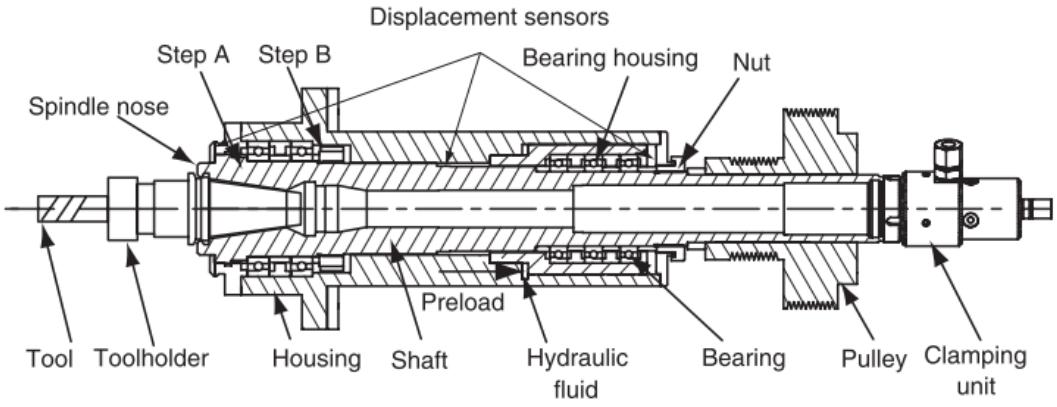
global damping matrix, populated with the only contributions of the bearings; and $\{F\}$ the global vector of the external loads, accounting for the cutting loads. With this approach, the researchers were able to obtain the natural frequencies of the system, analyse the response of the workpiece to the process loads and understand the effect of bearing characteristics and location. Reddy and Sharan [105] later extended the approach of Sharan, Sankar, and Sankar [104] as a tool for the optimization of the lathe design, aiming to minimise workpiece deflection and vibration damping. The two works [104] and [105], even if particularly relevant in displaying the effectiveness of dynamic modelling for manufacturing systems combined with numerical solution techniques, present some major flaws. First a Euler-Bernoulli discretisation of the shaft is not particularly accurate for beam elements not slender as the ones shown in Fig. 2.19b, since they do not allow for transverse shear deformation; in this case

Timoshenko beam elements should be preferred [106]. Then, both papers, even showing the primary importance of the bearings on the system behaviour, adopted a simplified model based on a spring-damper representation that does not account for the non-linear behaviour of the bearings with radial displacement and angular speed [91, 107]. Finally, gyroscopic and centrifugal effects due to the inevitable system unbalance are not taken into account.

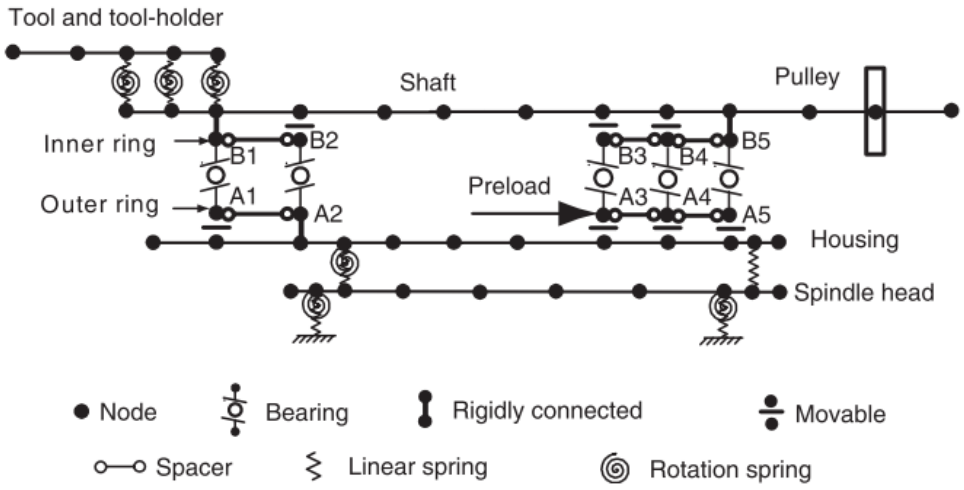
Altintas and Cao [108–110] analysed the natural frequencies, mode shapes and frequency response function of the machine tool shown in Fig. 2.20 under simulated cutting conditions (virtual cutting). Their model used Timoshenko beams for the spindle, including both centrifugal forces and gyroscopic effects, while Jones' approach was used for the bearings, in which different values of constant preloads were considered. To account for these additional contributions, the global equation of motion assumed the form:

$$[M]_S \left\{\ddot{U}\right\} + \left([C]_D - \omega\,[G]_S\right)\left\{\dot{U}\right\} + \left([K]_S + [K(U)]_B - \omega^2\,[M]_C\right)\{U\} = \{F\} \quad (2.14)$$

in which $[M]_S$ represents the global mass matrix for the system spindle/housing, $[C]_D$ the structural damping of the spindle obtained experimentally, ω the spindle angular speed, $[G]_S$ the global gyroscopic matrix for the spindle, $[K]_S$ the global stiffness matrix for the shaft, $[K(U)]_B$ the stiffness matrix for the bearings, $[M]_C$ the mass matrix used for the calculation of the centrifugal force and $\{F\}$ the vector of the external loads, i.e. cutting loads. It is worth noticing that despite the more accurate modelling approach used for the bearings is able to provide a more realistic description of the bearings behaviour, it complicates significantly the solution of the equation of motion. In fact, the stiffness of the bearings becomes function of the displacement, among other factors, but the displacement, in turn, is affected by the bearing stiffness and the external forces, inducing nonlinearities in the model.



(a)



(b)

Fig. 2.20 Schematic of a milling machine spindle, including toolholder and cutting tool [109]: (a) Section view of the system; (b) FE schematic of the system.

Acknowledging the primary importance of bearings in the system behaviour, Cao, Holkup, and Altintas [111] extended this analysis to compare the effect of different types of preload for the bearings, namely rigid and constant, while Zhang et al. [112], adopting a bearing formulation based on the Harris approach, analysed the stability of a rotor–bearing system under three types of excitation: bearing waviness (both in the races and in the rolling elements), the unbalance force due to rotor eccentricity and the finite number of rolling elements. In addition, two recent studies [113, 114] analysed the system response to race waviness, elastohydrodynamic lubrication and clearance for rolling elements bearings. Namazi et al. [115] presented an interesting study that connects the dynamic behaviour of a milling spindle to fixturing issues. In fact, it was observed by the researchers how the interfaces tool holder–spindle and tool–tool holder are the primary source of chatter vibrations in high speed milling due to their flexible connections. Using a FE discretisation of the system based on Timosheko beam elements and modelling the two interfaces with uniformly distributed translational and rotational springs, as depicted in Fig. 2.21, the researchers observed that the drawbar force and the total contact area have a primary effect on the connection stiffness. Finally, the dynamic study of spindle-tool systems has proven particularly important also for high-speed milling, for which several numerical models based on the Timoshenko beam approximation and non-linear stiffness bearings have been implemented to analyse the chatter stability of the system. These studies proved that while negligible at relative low speed, gyroscopic effects and dynamic stiffness drop due to centrifugal force become predominant at high speeds [116, 117].

From this analysis it appears clear how dynamic phenomena and transient process conditions play a primary role for systems the dynamics of which closely resembles the one of an inertia welder. This inevitably will affect the quality and repeatability of the process outcomes. Nevertheless, it is not possible to find in literature any study that addresses this problem for IFW.

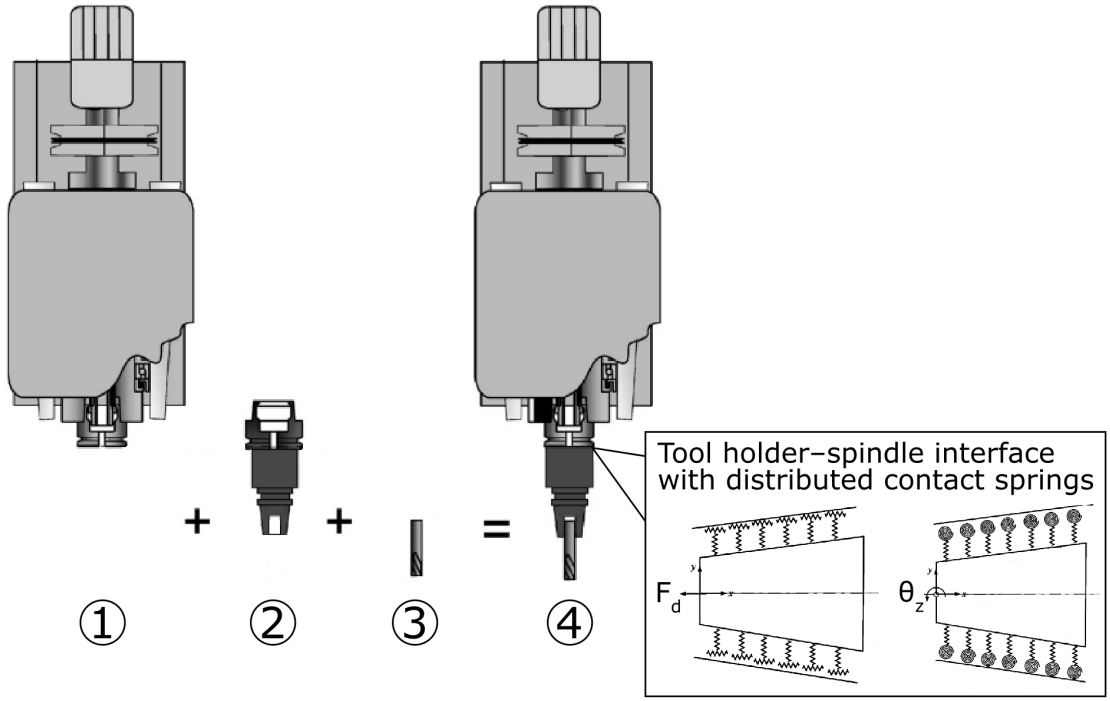


Fig. 2.21 Exploded view of the different elements composing the system for the study of the tool holder–spindle and tool–tool holder interfaces ((1) Spindle; (2) Tool holder; (3) Tool; (4) Assembly), with detail of approximation of the distributed translational and rotational springs (Adapted from [115])

2.4 Summary of the literature

IFW presents a vast literature due its interdisciplinary nature, embracing aspects of materials science, numerical modelling and manufacturing technologies. While the first two aspects have already been comprehensively summarised in excellent review articles [7, 12, 40], the manufacturing aspect received far less attention. This literature review tries to fill this gap providing an in-depth analysis of the manufacturing aspects connected to IFW, which will constitute the fundamental background for the research work presented in the following chapters.

The historical summary showed how the technology development lies mainly in the work of individual inventors and few corporations, aiming at finding solutions to specific industrial needs rather than doing fundamental research. This on one side

helped in keeping the technology relatively straightforward in its development but on the other created a system particularly closed, in which large part of the technical know-how is carefully protected as intellectual property by the owning companies and not available to the public domain.

The system for IFW comprises two parts, the headstock and the tailstock. The headstock includes a shaft carrying flywheels and one of the two workpieces to weld; first the shaft is accelerated to the initial speed by an electric or hydraulic motor, then the motor is disengaged and part of the kinetic energy stored in the flywheels is converted into frictional heat to create the weld. The tailstock carries the second workpiece and is pressed against the headstock by a ram to start the welding. Three main parameters can be controlled to setup the welding: initial angular speed of the spindle, flywheels inertia and axial load exerted by the ram. While it is known that the bearings supporting the spindle are the main source of energy losses, the efficiency for IFW was historically considered constant and relatively high. In recent years, however, studies found that the efficiency can vary from 30 to 70% and that it is deeply affected by the process parameters and the system, due to factors like different assembly tolerances and machine build. IFW is classified as a three stage process, passing from one to another the conditions at the weld interface vary significantly and the Coulomb frictional behaviour typical of the initial phase changes to a shear based approach when the material starts to plasticise. While it is known that the interface conditions deeply affect the process evolution, these still remain an unresolved aspect and the most common approach adopts approximations that try to capture an average condition over the whole interface with an equivalent friction coefficient.

To overcome the lack of information about the setup of the IFW system caused by the intellectual property protection measures taken by the machines manufacturers, an in-depth study of the patents filed has been conducted and the key aspects in the

development of modern inertia welders summarised. Even if this approach could seem excessively practical and of limited academic interest, it provides an insight of the system otherwise not achievable and represents the basis to understand possible research gaps worth investigating. The first inertia welders were modified lathes, problems of deflection under the weight of the flywheels and the high process loads represent some the most critical issues in the alignment headstock/tailstock, therefore several configurations for the flywheels and the addition of strengthening elements have been tested to mitigate the issue. Also the fixturing has undergone several improvements, nevertheless it is still possible to find evidences in literature of tooling-related issues like deformation and residual stresses in the final weld. One of the biggest limitations of modern inertia welders is extracting data from the process, the systems are equipped with sensors but these usually are installed far from the weld zone and not capable to capture reliably local phenomena. In the attempt of solving this issue few monitoring tools have been developed but the number of phenomena they can capture is limited.

The dynamic analysis of manufacturing processes like turning and milling has long attracted the interest of researchers and it is nowadays a topic of great interest. The extremely complex behaviour of spindles rotating at high speed while subjected to the process loads and supported by bearings, which add large nonlinearities to the system, represent a challenge researchers are still tackling with more and more accurate analytical and numerical approaches. However, despite the spindle in an inertia welder is a complex rotordynamic system, rotating at angular speed while affected by the weight and inertia of the flywheels, subjected to high process loads and supported by a combination of rolling elements and fluid bearings, no study available in literature address its dynamic behaviour.

2.5 Research challenges

Based on the extensive review of the current literature, several aspects have been identified as critical research gaps. These can be grouped in two macro-categories: the experimental assessment of the actual welding conditions and the modelling of the dynamic system response to the welding conditions.

2.5.1 Assessment of the actual welding conditions

When manufacturing processes are addressed from an academic viewpoint, the study and the characterisation of the system is of primary importance because it can deeply affect the process outcomes and, therefore, the conclusions of the study. In IFW the research work completely disregards the experimental setup except when laboratory machine are used, which, however, significantly differ from the industrial systems, making the generalisation of the conclusions difficult. For this reason, the development of a methodology to characterise the system results necessary to understand the actual conditions in which the welding occurs, providing a tool to validate and assess the error for the simplified studies so far developed.

- It is possible to find in literature hints that the system can deflect under the weight of its own elements and the process loads, with a behaviour that is different from system to system. Manufacturers tried to improve the inertia welders to minimise these problems but no available study provides a scientifically sound approach to quantify the impact of these on the welding conditions.

- Tooling and fixturing are aspects of primary importance in every manufacturing process governed by rigorous and well defined principles. Nevertheless, it is usually approached by rule of thumb, based on what works. This problem is

present also in IFW, where it is possible find in literature examples of issues connected to non-optimised tooling solutions. Engineers proposed improvements but their analysis shows the need for a rigorous scientific study of the tooling setup.

- The combination of the two effects previously mentioned, compliance of the machine and fixturing issue, is in clear disagreement with the assumption of perfectly axisymmetric welding conditions and lack of impact of the tooling that is the base for the majority of published research. In addition, the majority of the studies about IFW consider an extremely small number of repetitions, causing a possible risk of confusing system induced effects with process features. Therefore, it appears necessary to conduct additional analysis to assess whether these assumptions hold and what magnitude of error they can induce.

- The only tools available to diagnose the system performance are the sensors embedded into the machine, external sensors used to characterise the machine when it is not running and a limited number of monitoring systems proposed in literature. However, the sensors installed on the machine are far from the weld zone and not capable to provide information about local phenomena. In addition, assessing the machine in non-running conditions does not take into account all the dynamic phenomena which, for a complex system like an inertia welder, is logical to assume significant. Finally, the monitoring systems proposed measure a very limited number of parameters, failing to provide a holistic picture of the phenomena occurring during a weld, some of which potentially intercorrelated. For this reason, a novel system capable to fill these gaps represents a pressing need.

2.5.2 Modelling of the dynamic system response to the welding conditions

The spindle of an inertia welder is a complex rotordynamic system, however, even if various manufacturing processes rely extensively on the dynamic analysis of their systems, no available study addresses the dynamic response of the inertia welder to the process conditions. Performing such an analysis would provide new important insights on the process.

- A large number of studies focused on the behaviour of bearings showing how these introduce large non-linearities into the system. For this reason, understanding how these affect the dynamic response of the spindle is of primary importance.
- It has been observed that considering the system as perfectly stiff is not an acceptable assumption and deflections should be expected. From a dynamic point of view this corresponds to create an imbalance which, in turn, can induce gyroscopic moments and centrifugal forces that can alter the dynamic of the system. Quantify their influence is therefore necessary.
- Manufacturing processes with systems that recall the key elements of an inertia welder have been subjected to a large number of studies that proved how significant dynamic effects develop due to the transient conditions of the process and the system layout. These studies allow a better understanding of the physical causes behind the phenomena observed and make possible to propose solutions to limit their effect. Even if problems of oscillations during the welding have been partially addressed, no available study presents an exhaustive dynamic analysis of the inertia welder.

Chapter 3

Initial assessment of the system behaviour in default conditions

This chapter provides a brief introduction of the experimental setup used for this research, analysing its behaviour in default conditions. In particular, two IFW machines were used for the experimental tests, these will be described, paying particular attention to their build, fixturing setup and sensors embedded into the system. Then, the outcomes of a set of welds conducted to analyse the process efficiency and the system behaviour will be presented. Finally, an investigation aiming to get an initial evaluation of the misalignment that should be expected between the workpieces due to the fixturing setup will be detailed. From this analysis, limitations to the default monitoring setup and characterisation approach for IFW machines will appear evident, representing the basis for the work developed in the following chapters.

3.1 Analysis of the inertia welders

Two IFW machines have been used in this research, the MTI-300T located at the MTC (Coventry) and the MTI-2000B at the Rolls-Royce CRF facility (Annesley). In this section the general schematic and tooling configuration for the two machines will be presented.

3.1.1 MTI-300T

The MTI-300T machine, available at the Manufacturing Technology Centre (MTC)[1] has been used by Rolls-Royce to conduct part of their research and development work in IFW. The machine is an advanced hybrid welder capable of exerting 300 tons of axial load and that can be programmed to run in IFW, CDFW or hybrid configurations.

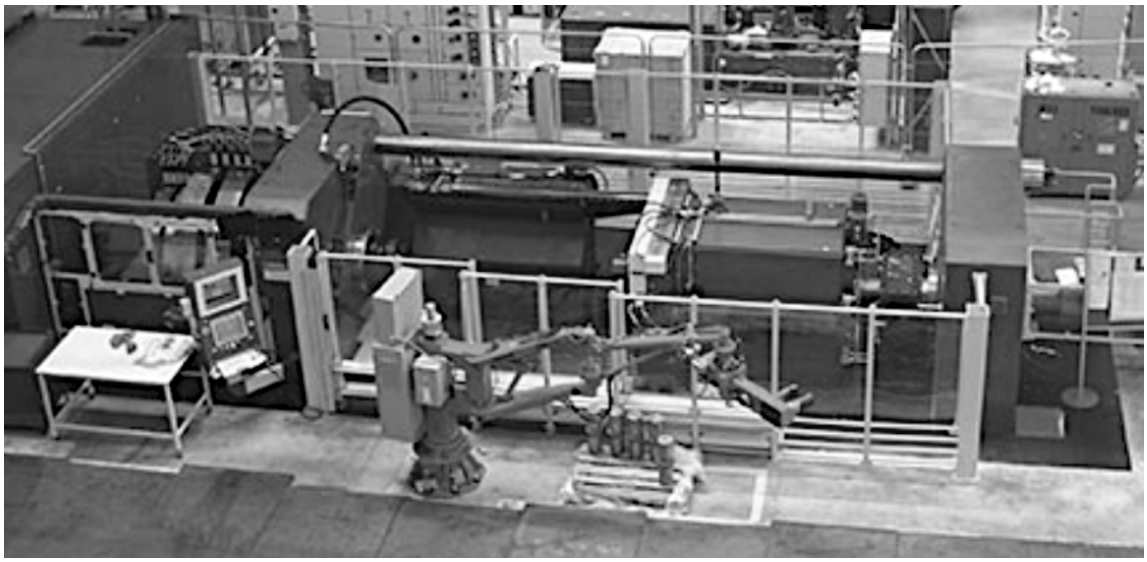
As shown in Fig. 3.1, the machine presents a box-style configuration in which headstock and tailstock are connected by tie bars (6) and the spindle shaft is supported on both ends. The radial supports include a cylindrical roller bearing on the rear side and a combination of a deep groove ball bearing and a cylindrical roller bearing on the front side (11), while a hydrostatic thrust bearing (12), installed immediately after the front radial support, absorbs the thrust exerted by tailstock axial actuators (8). Eight flywheels can be connected to the shaft to change the spindle inertia according to the values reported in Table 3.1; this advanced rotary friction welder has a remotely actuated system to engage and disengage the flywheels and a docking system to keep the flywheels independent from the shaft when not engaged.

Table 3.1 Values of mass and inertia for the elements of the spindle

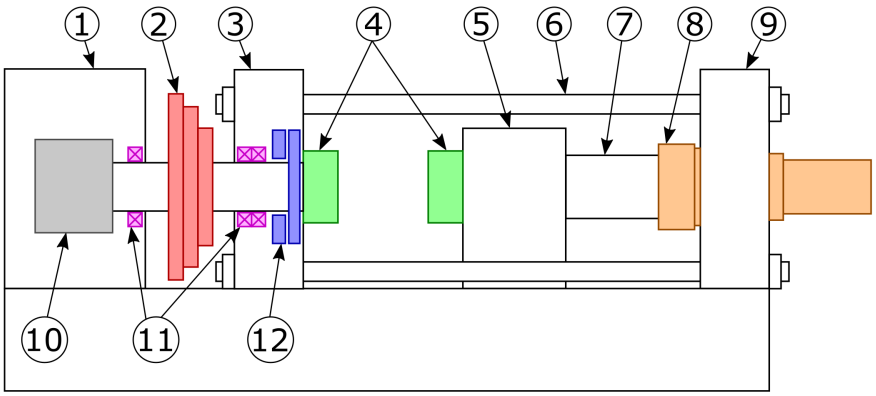
Element	**Mass [kg]**	**Inertia [kg.m^2]**
Spindle shaft	1505	73
Flywheel attachment	801	346
Flywheel small 1	1378	523
Flywheel small 2	1388	522
Flywheel small 3	1393	521
Flywheel small 4	1401	520
Flywheel large 1	3866	2565
Flywheel large 2	3848	2572
Flywheel large 3	3928	2581
Flywheel large 4	3956	2587

[1]The MTI-300T has been purchased by the Advanced Forming Research Centre (AFRC) in 2019 and is currently in their research centre in Glasgow

Finally, the control unit and the sensors installed in the machine can provide few diagnostic parameters useful to characterise the welding and the system behaviour: spindle angular speed, tailstock actuator pressure, upset, pressure in the collets actuators and lubricant flow rate and temperature for the hydrostatic bearing.



(a)

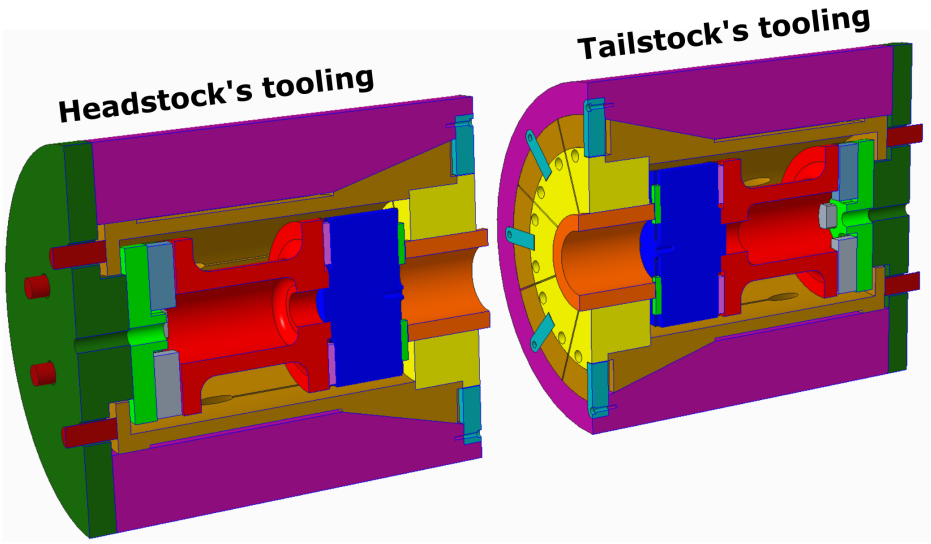


(b)

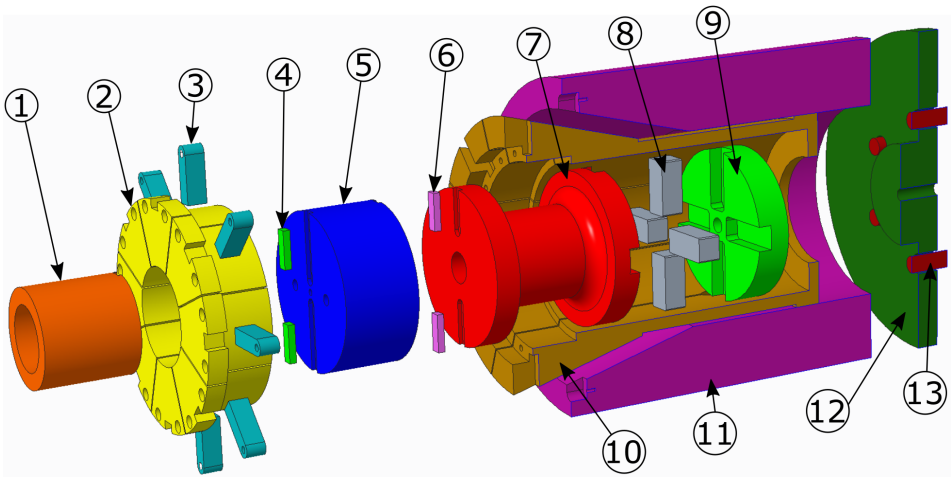
Fig. 3.1 MTI-300T hybrid rotary friction welder: (a) Picture of the machine after being installed at the Manufacturing Technology Centre (Adapted from [118]); (b) Schematic of the machine (1: Motor housing; 2: Flywheels; 3: Hydrostatic bearing housing; 4: Tooling; 5: Tailstock sliding structure; 6: Tie bar; 7: Drawbar; 8: Ram; 9: Tailstock support structure; 10: Hydraulic motor; 11: Radial bearings; 12: Axial thrust bearing) (Based on an MTI's proprietary design).

3.1.1.1 Tooling

The fixturing setup used for the MTI-300T makes use of the conventional collet-backstop configuration for both the headstock and tailstock, as shown in Fig. 3.2a. From the exploded view in Fig. 3.2b, it is possible to observe how the collet sleeve (10) is equipped with replaceable jaws of different inner diameter to clamp workpieces of various size.



(a)



(b)

Fig. 3.2 Default tooling configuration for the MTI-300T machine (Based on an MTI's proprietary design): (a) Section view of the tooling; (b) Exploded view of the fixturing setup (1: Workpiece; 2: Collet jaws; 3: Collet keys; 4: Backup keys; 5: Backup; 6: Backup extension keys; 7: Backup extension; 8: Master backup keys; 9: Master backup; 10: Collet sleeve; 11: Collet housing; 12: Backplate; 13: Drawbars)

In addition, three backstops are stacked on top of the other (5, 7, 9), each connected to the others with bolts and keys (6, 8). While the master backup (9) and backup extension (7) are non-replaceable and always kept installed in the machine, three different thicknesses for the backup (5) are available (30 mm, 75 mm, 120 mm) to accommodate workpieces of different length. Finally, it is possible to observe how the backup is equipped with two keys (4) to support the clamping action of the collet in restraining the workpiece (1) against the process torque.

This machine has been used often by Rolls-Royce as a test system to conduct small scale R&D welds, in these cases, however, a different backup is adopted to replicate the setup used in their production inertia welder. As shown in Fig. 3.3, the backup with keys is replaced by one carrying carbide serrated round grippers (5, 6). The carbide pads indent the workpiece and restrain it from rotating under the process torque but, differently from keys, do not require key slots in the workpiece, saving waste of material and avoiding further post-welding machining operations. The expansion ring (1) installed inside the workpiece is sometimes used to contrast the clamping action of the collet that would tend to distort the workpiece.

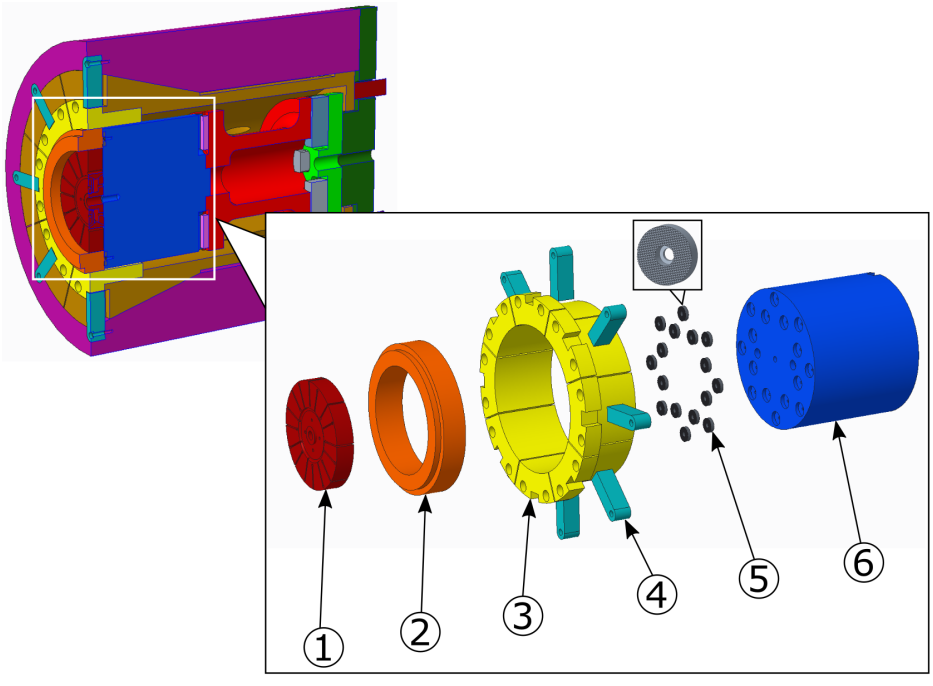
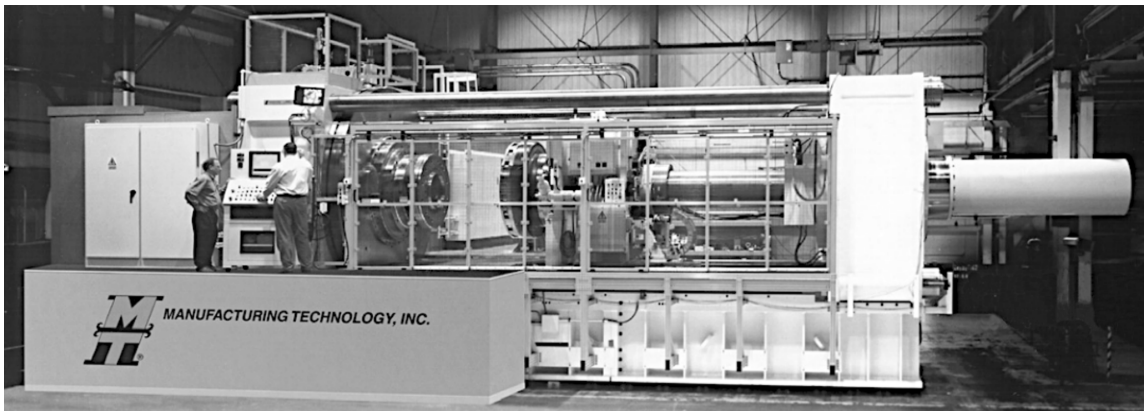


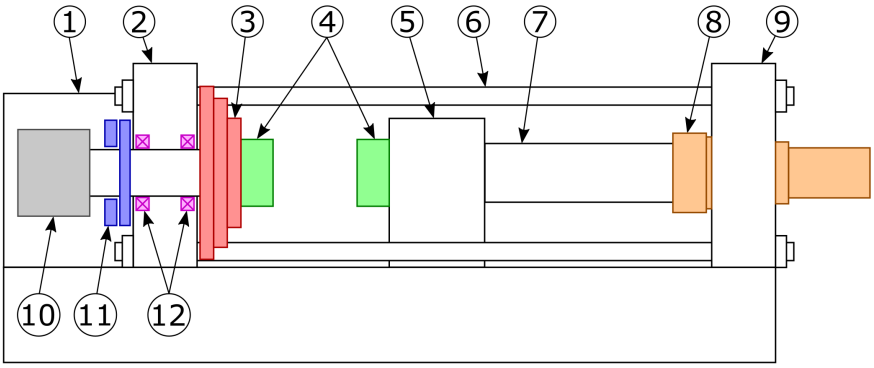
Fig. 3.3 Fixturing configuration used by Rolls-Royce for the welding trials with the MTI-300T (1: Expansion ring; 2: Workpiece; 3: Collet jaws; 4: Collet keys; 5: Serrated round grippers; 6: Backup) (Based on an MTI and Rolls-Royce's proprietary design)

3.1.2 MTI-2000B

The MTI-2000B available at the Rolls-Royce Compressor Rotor Facility (CRF) is used by Rolls-Royce for their production welds. This machine, similarly to the MTI-300T, is characterised by a box-type configuration but it differs in term of size, being able to exert 2000 tons of axial load, and configuration of the spindle. As shown in Fig. 3.4, in fact, the flywheels (3) are installed in a cantilever arrangement with respect to the supports, which include two radial ball bearings (12) and one hydrostatic thrust bearing (11).



(a)



(b)

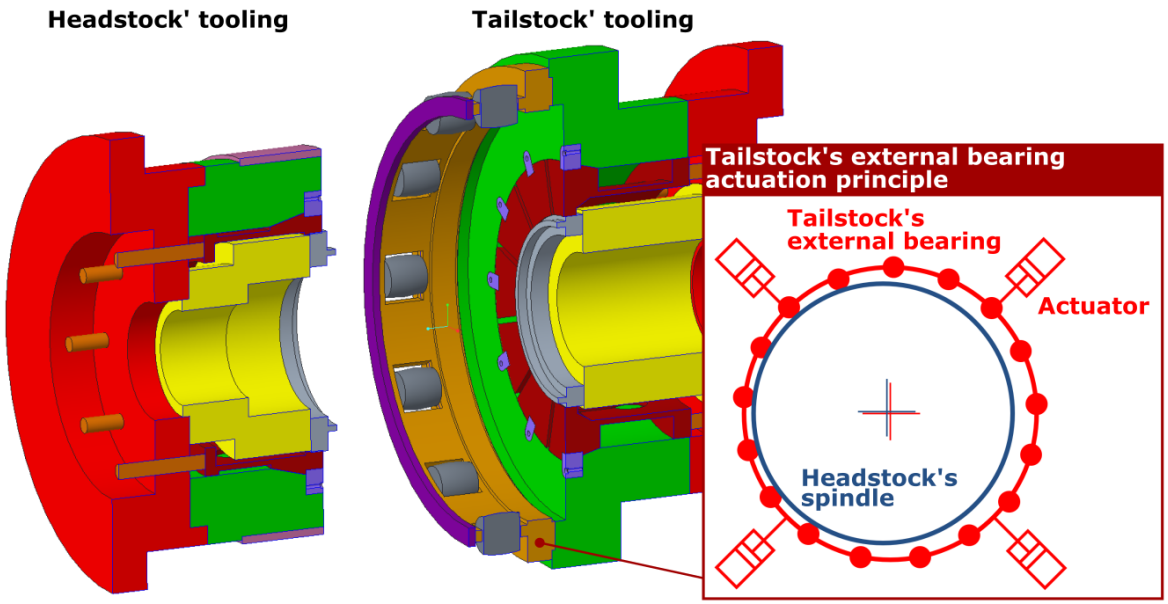
Fig. 3.4 MTI-2000B inertia friction welder: (a) Picture of the machine (Adapted from [7]); (b) Schematic of the machine (1: Motor and hydrostatic bearing housing; 2: Radial bearings housing; 3: Flywheels; 4: Tooling; 5: Tailstock sliding structure; 6: Tie bar; 7: Drawbar; 8: Ram; 9: Tailstock support structure; 10: Hydraulic motor; 11: Axial thrust bearing; 12: Radial bearings) (Based on an MTI's proprietary design).

This configuration, even if more convenient in term of flywheel access, can induce sagging of the spindle structure. To mitigate this, during the machine setup and maintenance, MTI pre-inclines the spindle structure (2) to compensate the weight of the flywheels, however, since different welds require different inertia, this approach is not perfect and a certain misalignment between the workpieces, variable from weld to weld, should be expected.

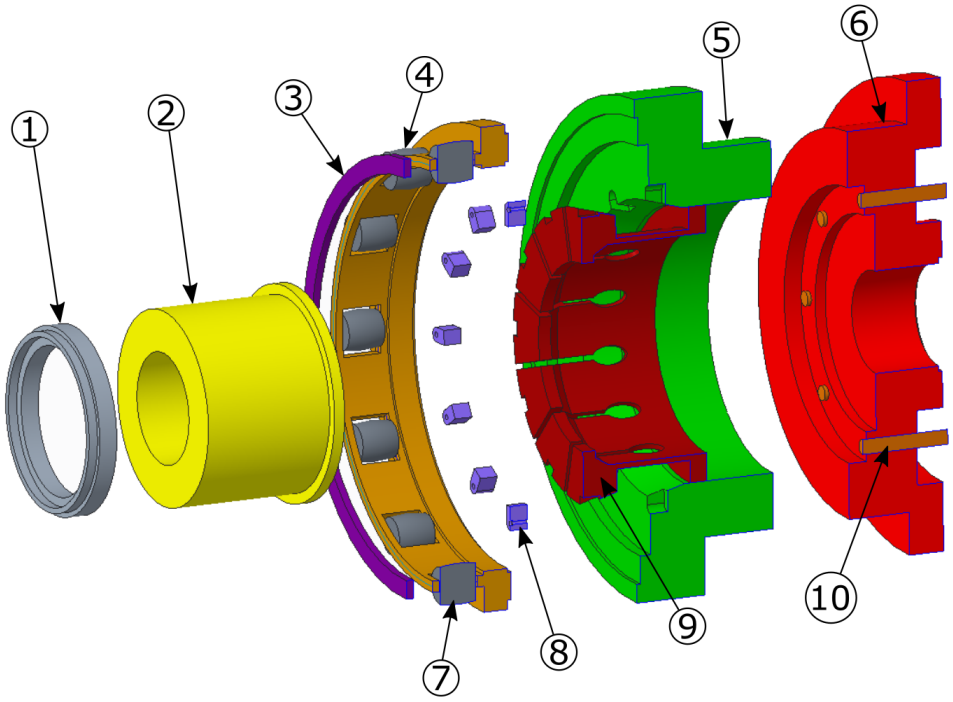
Similarly to the MTI-300T, a control unit and a set of sensors embedded into the machine can log some key performance parameters, such as the spindle angular speed, the thrust exerted by the tailstock actuator, the travel of the fixture side, the pulling force of the collets actuators and the hydrostatic bearing lubricant flow rate and temperature.

3.1.2.1 Tooling

Fig. 3.5 shows the fixturing setup adopted in the MTI-2000B for the production welds, which presents the same key elements of the MTI-300T tooling, a collet (9) to locate the workpiece (1) and prevent it from rotating under the process torque and a backup (2) to absorb the axial load exerted by the tailstock piston. Differently from the MTI-300T tooling, a bearing (4), installed in the tailstock tooling, is used to embrace the headstock during the welding and reduce the runout. The bearing has a slight radial clearance with the spindle mating surface and its alignment can be tuned with four actuators to localise the contact between the bearing rollers and the spindle. This process gives the flexibility for technicians to compensate for runout issues, but is extremely labour-intensive, requiring a trial and error approach. This consists of consecutive iterations of welding, measuring the runout of the joint and moving the bearing cage to compensate for the runout error until the desired alignment is obtained. In addition, the bearing cage can be moved only during the setup of the machine, making it not suitable to compensate for runout errors during welding.



(a)



(b)

Fig. 3.5 Production tooling configuration for the MTI-2000B machine (Based on an MTI and Rolls-Royce's proprietary design): (a) Section view of the headstock and tailstock tooling for the welding of a generic cylindrical component with detail of the actuation principle for the tailstock external bearing; (b) Exploded view of the headstock fixturing setup (1: Workpiece; 2: Backstop; 3: Bearing cage protection; 4: Bearing cage; 5: Collet housing; 6: Backplate; 7: Bearing rollers; 8: Collet's keys; 9: Collet sleeve; 10: Drawbars).

The machine is sometimes also used for R&D welds. In these cases, simpler and less expensive ring components are welded, which still allow the machine behaviour and the weld properties to be assessed without excessive waste of material or complex manufacturing operations. To fit these test components, Rolls-Royce developed a special backstop (PDX3) shown in Fig. 3.6, which extends outside the collet. Differently from the conventional setup, the collet clamps directly the backup while the workpiece is constrained completely by the backup itself.

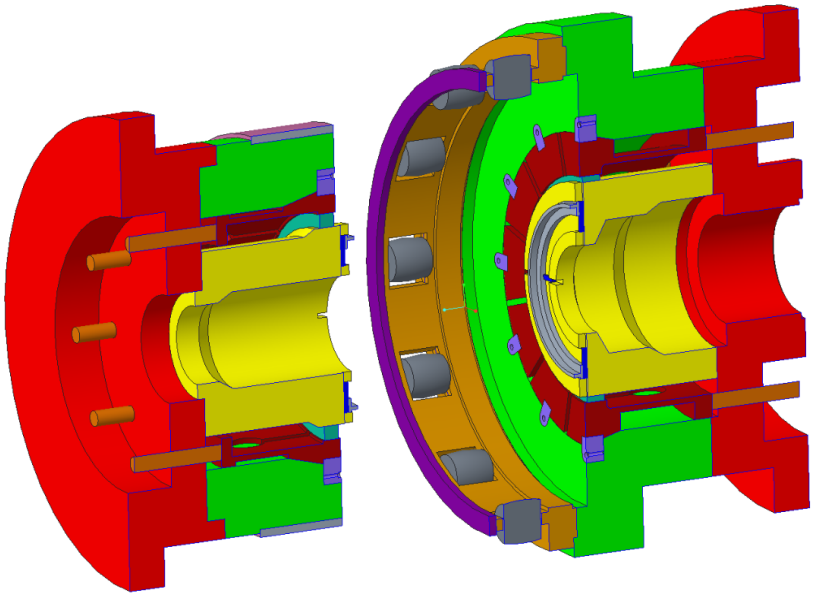


Fig. 3.6 Backstops for test welds (PDX3) (Based on an MTI and Rolls-Royce's proprietary design)

3.1.3 Conclusions

This section presented the details of the two IFW machines used during the PhD: the MTI-300T available at the MTC, which was used to conduct the majority of the experiential tests, and the MTI-2000B installed at the Rolls-Royce CRF, used for the final validation of the research work. While both machines present a box-style

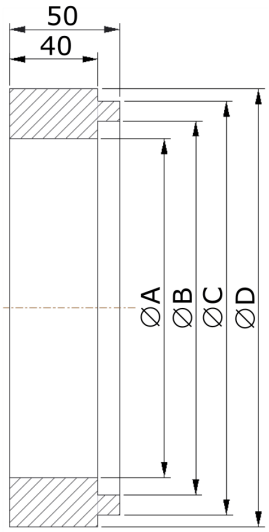
configuration, the position of the flywheels differs. The MTI-300T has the flywheels installed at the centre of the spindle shaft and supported on both ends by bearings, while the MTI-2000B has the flywheels installed in a cantilever configuration. Despite making the access to the flywheels more straightforward, this configuration can cause sagging of the headstock, making the desired alignment of the two workpieces more complex to achieve. The fixturing setup that equips the two machines is similar in principle and includes a collet to locate radially the workpiece and restrain it against the process torque and a series of backstops to absorb the axial load exerted by the tailstock piston. In addition, the backstops are equipped with keys or grippers to absorb part of the torque and allow a lower clamping force of the collet. Even if beneficial in reducing the damaging, deformation and residual stresses induced by the collet to the workpieces, the keys and the grippers could induce issues like overconstraining and misalignment of the workpieces inside the fixture

3.2 Machine performance under conventional welding conditions

Before this PhD, no monitoring system capable to characterise the overall performance of the machine throughout the welding phase has been documented in public domain. In section 3.1 it was observed that industrial inertia welders are usually equipped with sensors; however, these tend to be far from the weld zone and, consequently, not capable to capture local phenomena connected to the welding and affected by noise induced by the multitude of subsystems inside an inertia welder. For this reason, Rolls-Royce adopted an approach similar to what proposed in [25, 26, 48], in which the experimental data were extracted using test components instrumented with strain gauges or thermocouples. The data collected were then compared with the output of the machine sensors, to draw conclusions on the weld efficiency and the machine behaviour. This approach has been put to test with a set of welds in which workpieces instrumented with strain gauges have been welded on the MTI-300T machine equipped with the backstop using serrated grippers (Fig. 3.3).

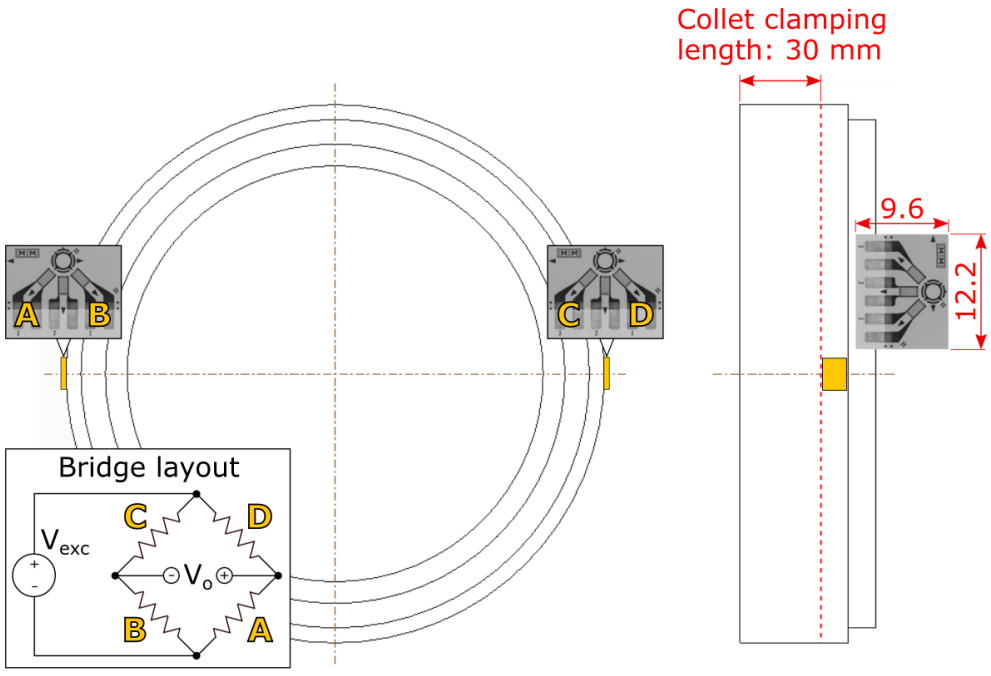
3.2.1 Weld setup

Two geometries of steel rings (EN3B) with the dimensions summarised in Fig. 3.7a were welded. For each set of workpieces, the one to be installed in the tailstock type was instrumented with strain gauges in a configuration suitable to measure torque. Two Vishay CEA-06-062-UM-120 rosettes were installed 180° apart and the 0° and 90° gauges connected in a Type I full bridge, as shown in Fig. 3.7b. Finally, a NI SCXI-1520 strain-gauge input module, installed in a NI-SCXI 1000 chassis equipped with a SCXI-1600 USB digitizer, was used for the data sampling.



	Geom. 1 [mm]	Geom. 2 [mm]
A	97	153
B	119.5	169
C	137.5	187
D	145	198

(a)



(b)

Fig. 3.7 CAD representation of the workpieces welded and description of the strain gauges configuration: (a) Section view of the workpiece with summary in tabular form of the dimensions for the two geometries adopted; (b) Strain gauges configuration.

Overall, four welds were studied, two of geometry 1 and two of geometry 2, Table 3.2 summarises the process parameters used.

Table 3.2 Process parameters for the welds accomplished

	Geom. 1	Geom. 2
Initial angular speed [RPM]	416	354
Inertia [kg·m^2]	500	500
Weld pressure [MPa]	70	70

3.2.2 Welding trial results

The results of these welding trials provided an invaluable insight into the system performance in non-optimised conditions. In fact, to develop the instrumentation and methodology presented in the following chapters, it was first necessary to analyse the weak points of the system in the default configuration. Issues connected to the fixturing system and the external monitoring setup appeared evident, confirming the need for the research developed as part of this PhD.

3.2.2.1 Fixturing considerations

Three welds showed severe problems of slippage, with the combined action of the collet and serrated grippers not capable of restraining the workpieces. The marks shown in Fig. 3.8 suggest that, despite both collet and grippers were indenting the workpiece, the non-optimised tooling conditions used in this development machine along with the limited shear resistance of EN3B steel compared to Ni-based superalloys, conventionally welded with this setup, were the causes of the unsuccessful welds. For the remaining weld, a larger indentation depth of the grippers into the workpiece (0.3 mm) was selected, allowing the weld to be successfully completed without slippage.



(a) (b)

Fig. 3.8 Damaged welded components due to improper fixturing setup: (a) Marks produced by the collet; (b) Marks caused by the serrated grippers.

Despite the workpiece slippage, it is clear that a clamping force of the collet high enough to induce indentation in the workpiece is unacceptable in terms of surface damage for a near-net-shape process like IFW and the deformation and residual stress induced. For the serrated grippers, the situation was different, in fact, despite being described as "high friction elements" in the patent that first proposed them for IFW applications [70], it appears clear their restraining action relies on indentation depth and material shear strength. When analysing the formula proposed in the patent [70] for the calculation of the required friction coefficient that the grippers should be able to provide (μ):

$$\mu = \frac{T}{P \cdot r} \tag{3.1}$$

where T is the process torque, P the forge load and r the radius at which the grippers are installed with respect to the spindle central axis, therefore, μ should be considered an apparent friction coefficient, i.e. a coefficient that allows the complex interaction between the grippers and workpiece to be reduced to an ideal dry friction behaviour.

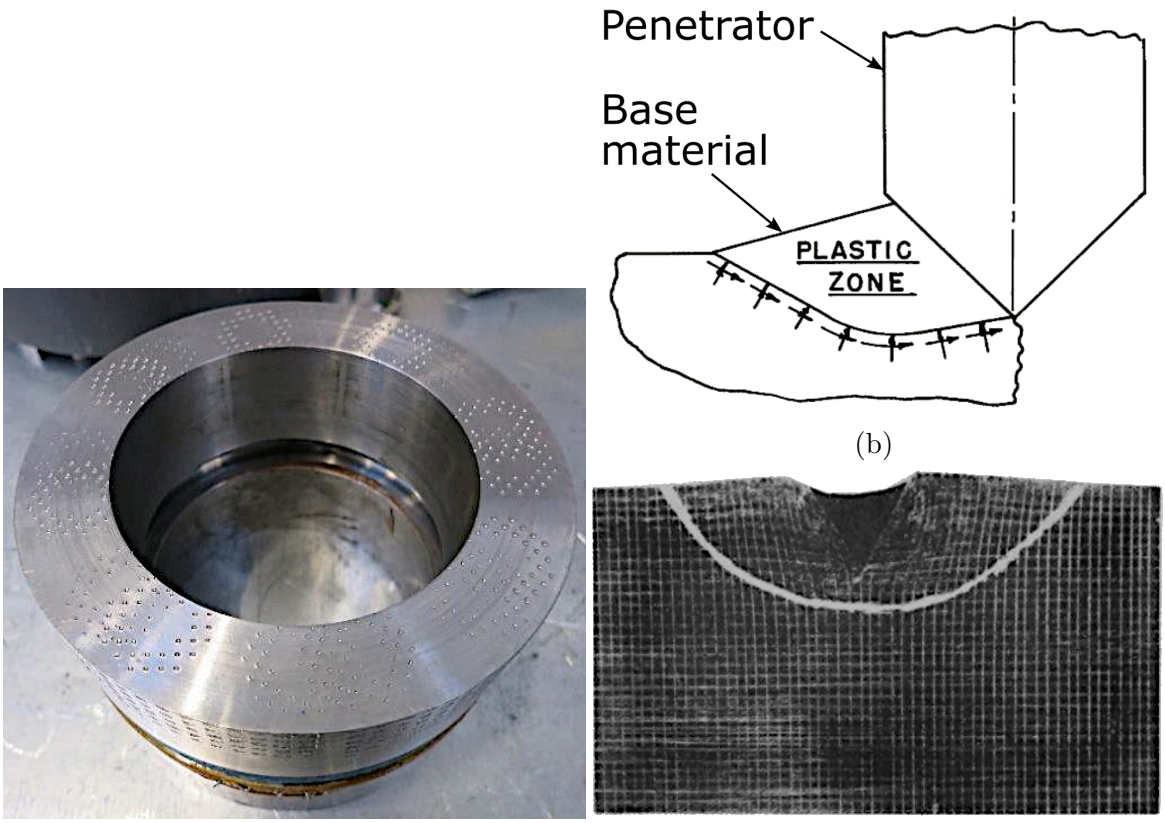
The ploughing and adhesion for sliding metals have attracted the interest of researchers since the beginning of the twentieth century, when indentation tests to characterise material properties became popular [119–122]. After the success of Merchant [123] and Merchant [124] in analysing the mechanics of metal cutting, studies like Moser [125] started applying the theory of ploughing and adhesion to fixturing, with the assumption that the results obtained for a single penetrator can be extended to an array of penetrators, as in a serrated clamping element. Using the approach introduced by Bowden, Moore, and Tabor [119], the apparent friction coefficient (μ) that affects the interaction between a base material and a wedge-like penetrating element can be written in the form:

$$\mu = \frac{F_T}{F_V} = \mu_{adh} + \mu_{plo} \tag{3.2}$$

in which F_T is the transverse load, F_V is the vertical load, μ_{adh} the adhesive friction coefficient and μ_{plo} the ploughing friction coefficient. From this formulation, it appears clear that both the force required to shear the metallic junctions between the penetrators and the base metal and the force required to displace the softer metal from the path of the slider should be taken into account. The two contributes are usually determined with simplified theories that, however, do not account for phenomena like the interaction among neighbour penetrators [120, 125], with numerical models [126, 127] or experimentally [121, 122], for which great importance is put on the material properties and the serrated grippers geometry.

A final aspect to take into account is the effect of the serrations when the fixturing manages to constrain the workpiece successfully. In fact, even when no slippage of the workpiece inside the tooling occurs, the simple indentation of the grippers serrations causes part of the metal to flow on the side of the serrations causing a force that would tend to push the workpiece away from the backup, causing possible detriment to its alignment inside the fixture. This can be shown in Fig. 3.9a that represents the only

weld accomplished without slippage, in which it is possible to observe indentation marks similar in morphology to other examples known in the literature [120, 121, 125] and summarised in Fig. 3.9b and Fig. 3.9c.



(a) (b) (c)

Fig. 3.9 Effect of serrations on the base metal indented: (a) Marks produced by the grippers when no slippage between workpiece and tooling occurred; (b) Schematic of the effect of a penetrator in the base metal in which the raise of plasticised material on the side of the tool is predicted (Adapted from [125]); (c) Section view of the indentation left by a cone in ductile steel in which the raise of plasticised material on the side of the crater can be observed (Adapted from [120]).

3.2.2.2 Analysis of the monitoring apparatus

Applying strain gauges directly on the workpiece is a simple and inexpensive technique to obtain information about the process. A similar approach in which thermocouples are installed in the workpiece to measure the temperature at different locations in the

workpiece during the weld is well documented in the literature [24, 52, 128]. Ideally, the measurements would be conducted near the weld interface, however, the harsh conditions of the interface, such as extremely high temperature, metal plasticisation, large deformations and upset, do not make this possible. For thermocouples, two approaches are possible, sacrificial thermocouples, which are installed close to the weld interface and capture the temperature evolution only for a short while before being destroyed, or thermocouples installed far from the weld interface, which can monitor the temperature for the whole duration of the process but, for which a large temperature drop from the weld interface should be expected. For strain gauges, a few differences should be noted, in fact, while the closeness to the weld interface is not so critical as for thermocouples, the geometrical shape of the workpiece is instead of primary importance. In fact, while it is sufficient to keep the thermocouples in contact with the base material, strain gauges are greatly influenced by geometrical features.

In the case analysed, for example, constraints in term of workpiece geometry and the need to preserve the strain gauges throughout the welding, required the installation of the sensors in the position shown in Fig. 3.7b. When the actual torque obtained with the strain gauges was analysed and compared to the theoretical torque, product of the angular deceleration and spindle inertia, it appeared clear that considerations on the sensors location and signal processing techniques were of primary importance to develop a monitoring system able to provide data easily understandable. In fact, analysing Fig. 3.10 that compares theoretical and actual torque (values normalised against the peak theoretical torque), it is possible to observe a large difference, resulting in unrealistically low process efficiency. To understand the causes of this difference, an FE model which simulate the tailstock workpiece subjected to the process torque and a constant efficiency of 0.8 was developed. As shown in Fig. 3.11, the model, which makes use of the axisymmetric assumption, replicated the fixturing conditions

with a sticking boundary condition to a perfectly rigid die. Solving the model, the results in Fig. 3.12a were obtained, in which a good match between numerical and experimental data can be observed. To understand why the experimental data matches the numerical torque but not the theoretical one, it is necessary to study Fig. 3.12b. From this it is clear that the location in which the strain gauges were installed is affected by geometry effects caused by the change in diameter, which affect the strain field and, consequently, the torque derived.

This analysis showed that the location of the strain gauges is of primary importance, this should be neither too close to the change in diameter, to avoid geometry effects, nor too close to the collet, to avoid the clamping force to alter the strain field.

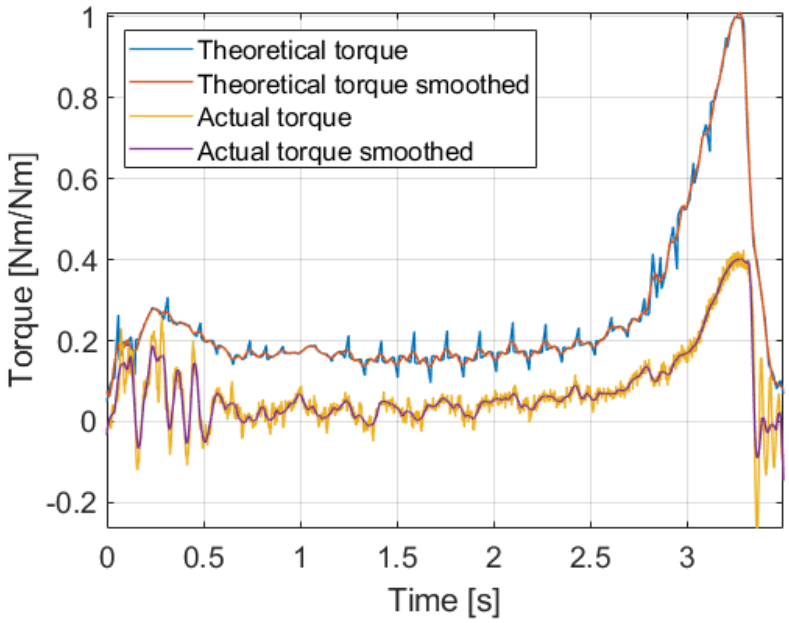


Fig. 3.10 Comparison between theoretical and actual torque (normalised against the peak theoretical torque)

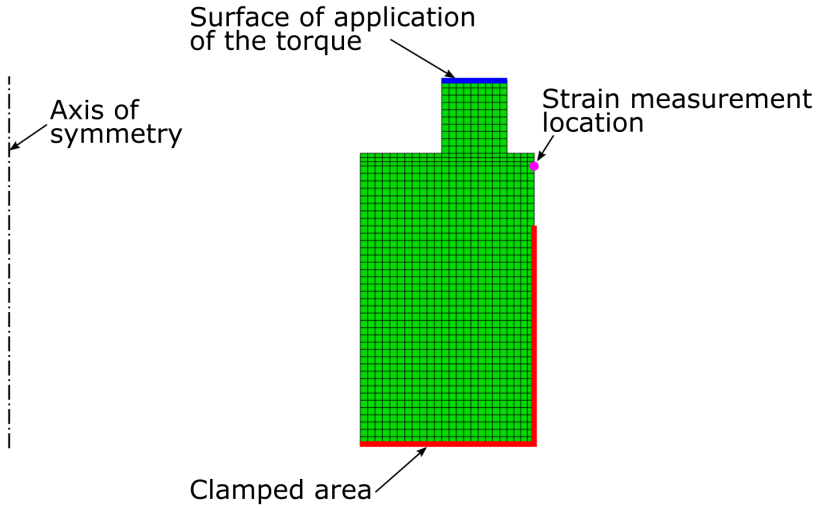
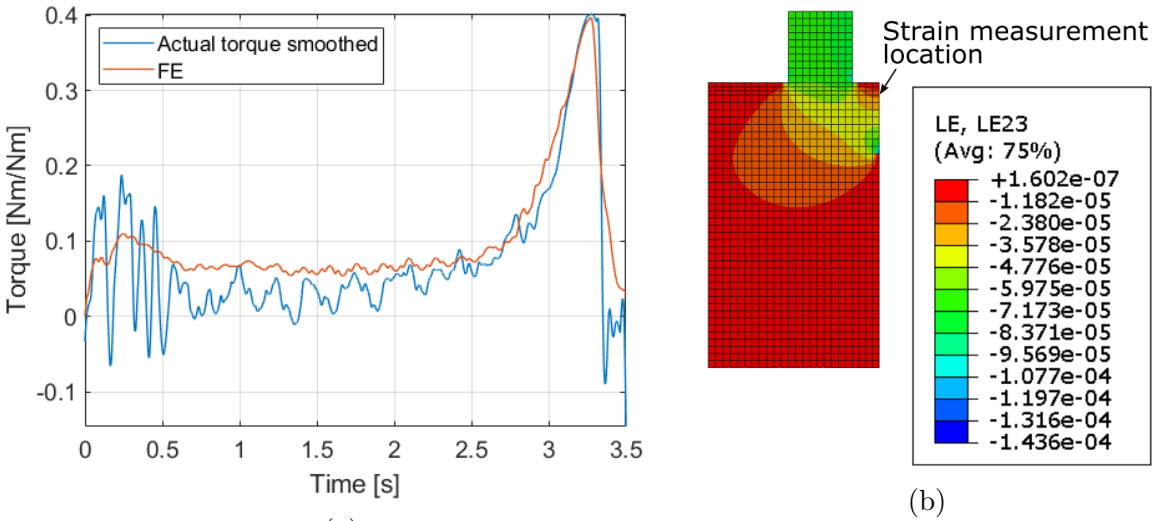


Fig. 3.11 Details of the FE model developed to validate the output of the strain gauges



(a) (b)

Fig. 3.12 Results obtained with the numerical model and comparison with the actual torque: (a) Comparison between normalised actual torque and the one obtained from the FE model; (b) Strain field obtained from the FE model in which it is possible to observe the local effect induced by workpiece geometry and clamping action.

3.2.3 Conclusions

This section summarised the outcomes of a series of welds conducted on the MTI-300T development machine using the default setup to evaluate the system efficiency and study the process behaviour. This makes use of a set of simplified steel workpieces instrumented with strain gauges, the outputs of which are compared with the data collected with the machine sensors. Issues connected to the capability of a non-optimised tooling to constrain properly the workpieces were observed, while considerations on the grippers and their clamping mechanics were proposed. The approach of installing the sensors directly on the workpiece, despite being economical and simple, appears suitable only when a very limited number of welds has to be accomplished, due to the setup time and the risk of inconsistent results. In addition, strain gauges installed directly on the workpiece can be greatly affected by the workpiece geometry, making this approach not desirable. Finally, it was observed that the output of both machine and external sensors are affected by large noise due to the transient conditions of the welding and the multiplicity of elements coexisting in the friction welder, this requires the definition of a standard procedure able to filter the signals and make them comparable even when extracted from different systems.

3.3 Influence of the tooling's elements on the welding surfaces alignment

In chapter 2 it was highlighted how the alignment between the two workpieces is of primary importance in IFW, this aspect can be expressed in terms of relative runout. In particular, using the ISO-1101:2017 [38] as the reference standard, the runout is differentiated according to the oscillation direction, following the schematic in Fig. 3.13.

The radial runout is defined as the difference in radii of two coplanar concentric circles which contains the profile of any cross-section with respect to the reference axis. The axial runout, instead, is described as the axial distance between two circles, with axis coincident to the selected datum, that contains the extrema of the cylindrical section on which the tolerance is applied. Similarly to milling machines and lathes, the runout of the spindle is affected by the coaxiality between casing and shaft, in which the bearings play a fundamental role [102, 129, 130], and the stack-up of manufacturing and assembly errors in the elements of the system [26]. While the effect of the first contribution will be evaluated in the following chapters using a novel monitoring system and methodology developed to characterise the machine behaviour, considerations about the second contribution can be made knowing the key elements of the system and, in particular, the tooling. Such analysis can be valuable in discerning the different contributions to the alignment of the workpieces.

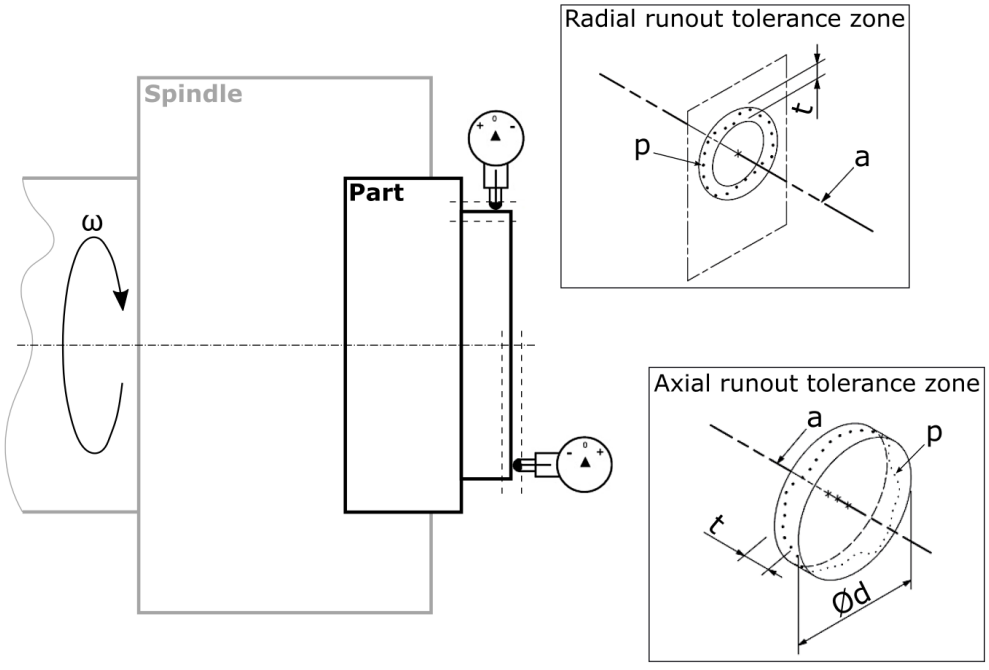


Fig. 3.13 Schematic representation of the axial and radial runout for the spindle workpiece (a: Datum axis, t: Tolerance, p: Points measured) (Adapted from [38])

Section 3.1 showed that both machines adopt a similar fixturing setup with a collet to locate the workpiece in the radial direction and a series of backstops to locate it axially. Collets are well established fixturing elements used in a multitude of manufacturing systems and the concentricity accuracy they offer depends on the precision of the wedge profiles on both the housing and sleeve. Specialised literature reports values of concentricity ranging from few microns to 10-20 microns [131, 132]. The impact of the backstops on the axial runout, fundamental to guarantee a flat-to-flat contact between the two workpieces and, consequently, constant pressure around the weld surface, is more complex to evaluate, since custom backstops are often manufactured to accommodate the specific workpieces to weld.

Fig. 3.14 shows a schematic of the backstops for the MTI-300T machine tooling in which it is possible to observe the three backstops (2, 3, 4) a reference surface (1) with normal aligned in the X direction, which represents the backplate of the collet. As represented in the figure, backstops are normally dimensioned paying particular attention to the parallelism between its flat faces and their perpendicularity to the central axis, in an attempt to have a good contact between the two workpieces. The dimensional tolerances on the backstops length (Δl), on the other hand, are of secondary importance since small deviations from the nominal value can be compensated by the machine control system that adjusts the axial position of the tailstock to guarantee contact between the two parts before each weld.

While the effect of dimensional tolerances is easy to understand and several approaches to stack-up their contributes exist [133], the situation is different for geometrical tolerances. It was observed [134–136] that geometrical tolerances affect how the elements in an assembly interact, in fact, as shown in Table 3.3, depending on the kinematic connection between two interacting bodies, geometrical tolerances can induce a combination of rotational and translational variations in their contact. It is

possible to recognise that the mating conditions among the backplate, the backstops and the workpiece can be approximated with a planar contact so that perpendicularity and parallelism tolerances induce a pure rotation. Fig. 3.15 gives a schematic representation of this concept for a flatness tolerance that, similarly to perpendicularity and parallelism, induces rotation for a planar contact. Even if it is debatable whether rotational variations should also include a translational component, the approach assumes that this is automatically accounted for by the dimensional tolerance applied to the element length (Δl). The rotation angle ($\pm\varphi$) can be calculated as the ratio between the tolerance value (tol) and the characteristic length of contact (l_c) [135]:

$$\varphi = \arctan\left(\frac{tol}{l_c}\right) \tag{3.3}$$

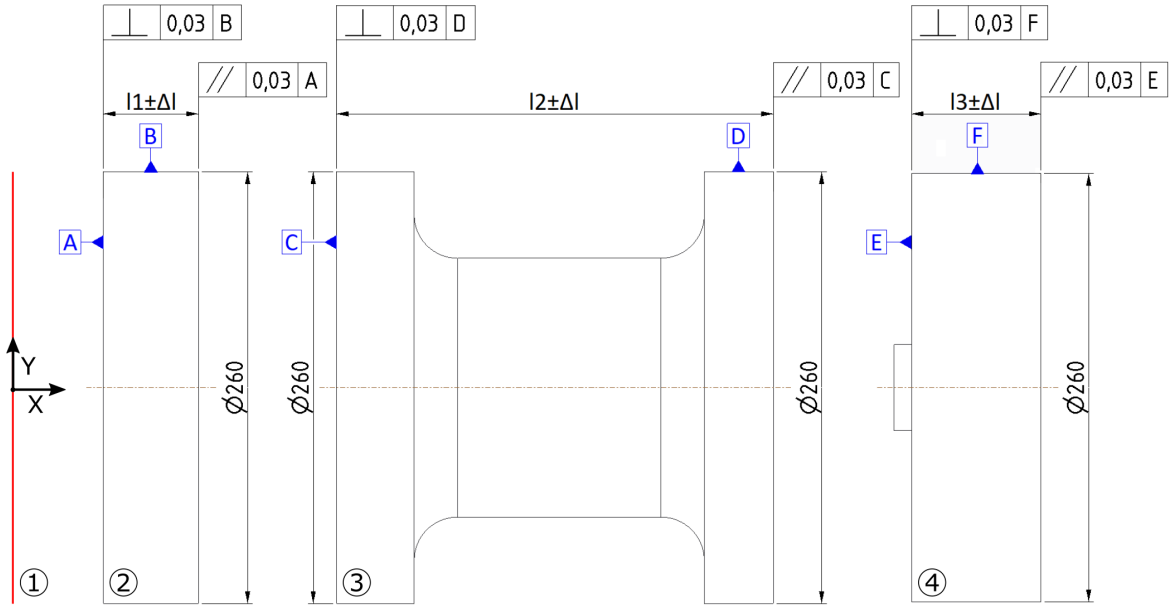


Fig. 3.14 Schematic representation of backstops for the MTC tooling including the geometrical and dimensional tolerances that affect the axial runout (1: Reference plane (backplate); 2: Master backup; 3: Backup extension; 4: Backup) (Based on an MTI's proprietary design)

Table 3.3 2D rotational and translational variations associated with the geometrical tolerances applied to various kinematic connections [135]

Joints \ Geom Tol	▱	—	○	⌭	⌓	//	⊥	∠	⌰	◎	⌖
Planar	R	R			R	R	R	R	RT	RT	
Cyl Slider	T	T	T	T	T	T	T	T	T		
Edge Slider	T	T	T	T	T	T	T	T	T	T	T
Revolute										T	T
Par Cylind		T	T	T	T				T		

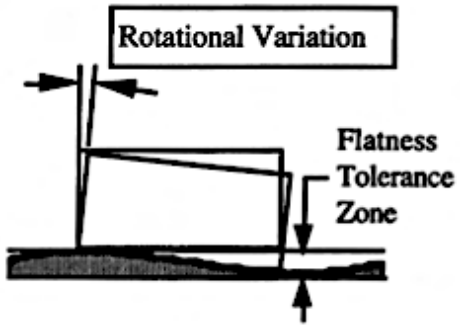


Fig. 3.15 2D effect of a geometric tolerance in the interaction between a block and a planar surface [135]

Applying this methodology to the assembly in Fig. 3.14, in which the characteristic length is assumed equal to the backstops diameter ($l_c = 260$ mm), it is possible to obtain an estimation of the axial runout magnitude. As a first approach, a worst case scenario in which all the tolerances are their highest admissible value (0.03 mm) is considered. Summing the rotation contributes for the three backups, calculated using equation 3.3, an overall angular rotation of 0.020° is obtained. If this rotation is applied to two workpieces introduced in section 3.2.1 of nominal dimensions listed in Table 3.7a, using the simplified planar approach summarised in Fig. 3.16, an axial runout of 0.095 mm for the workpiece of geometry 1 and 0.117 mm are for the one of geometry 2 are obtained. A worst case approach is useful to obtain the upper boundaries, however more realistic values of runout can be obtained using the Monte Carlo approach and statistically distributed values of tolerances. It is commonly

assumed that manufacturing tolerances follow a normal distribution with mean zero and standard deviation equal to one third of the tolerance zone, which corresponds to a 99.73% rate of acceptance usually accepted for the manufacturing of mechanical components [135, 137, 138]. Fig. 3.17a and Fig. 3.17b show the axial runout for the two workpieces obtained over one million iterations of the Monte Carlo approach and compares it against the worst case scenario. The comparison shows that for normally distributed tolerances mean values of 0.010 mm and 0.013 mm are obtained for the two workpieces, which is significantly smaller than the values calculated with the worst case approach and closer to the values reported by Rolls-Royce for their industrial machine. Nevertheless, it is important to observe that even this second approach represents a worst case scenario because, in reality, the problem is not planar and therefore the angular rotation induced by the tolerances can have any orientation around the circumference, which overall is expected to reduce the angular rotation of the workpiece. In addition, as observed in Chase et al. [135], reducing perpendicularity and parallelism to pure rotations is a simplified approach because in reality the waviness of the surface can occur in such a way to cause just a partial tilt in the interaction with the mating surface.

Analysing the tooling of the MTI-2000B shown in Fig. 3.5 and Fig. 3.6 to the one of the MTI-300T, it is possible to observe that only one backup is used, for which, in addition, tighter tolerances of perpendicularity and parallelism are used. Therefore, despite the larger diameter of the backstops and of the workpieces welded, an axial runout from a few microns up to a few tenths of microns should still be expected.

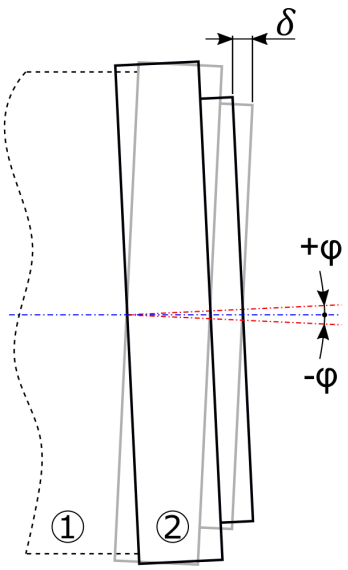


Fig. 3.16 Axial runout (δ) connected to the rotation angle ($\pm\varphi$) calculated stacking up the perpendicularity and parallelism errors in the faces of the backstops (1: Backstop; 2: Workpiece)

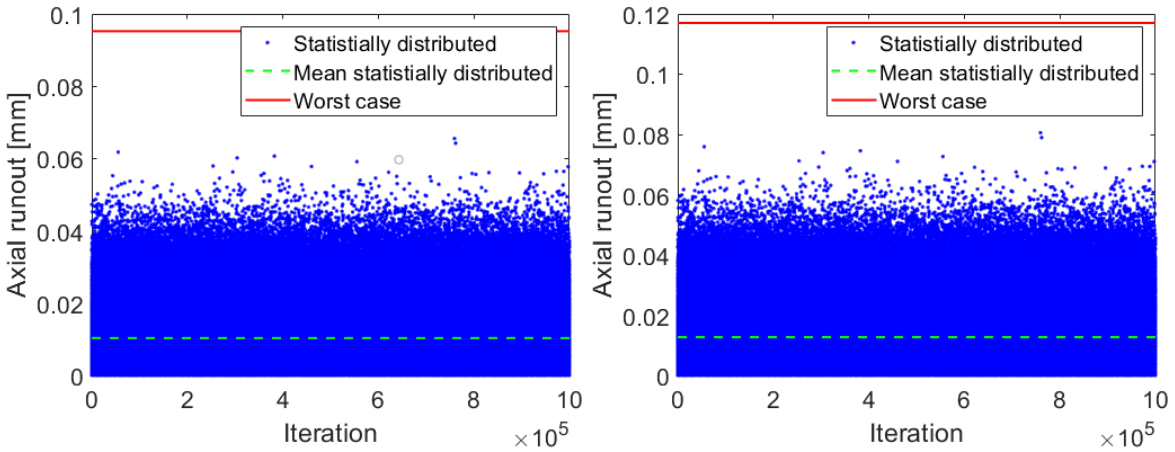


Fig. 3.17 Comparison between the axial runout obtained stacking up the tolerances calculated according to the worst case scenario and a normal distribution: (a) Workpiece geometry 1; (b) Workpiece geometry 2.

3.3.1 Conclusions

This section presented an analysis of the runout in radial and axial directions that it is possible to expect due to the tooling setup. It was observed that in the radial direction, the concentricity between the workpiece and the spindle is mainly guided by the collet and values from a few microns to a few tenths of microns should be expected. In the axial direction, the evaluation of the runout is more complex, but using an approach based on the stack-up of the geometrical tolerances in the backstops, values of runout similar to the ones in radial direction were obtained.

3.4 Conclusions

This chapter provided a description and analysis of the systems used during the research activities in default conditions. Section 3.1 summarised the key details in term of general build and tooling configuration for the two machines used during the PhD, the MTI-300T available at the MTC and the MTI-2000B installed at the Rolls-Royce CRF. Section 3.2 presented the results of a series of welds completed with the default monitoring configuration used by Rolls-Royce to characterise the machine behaviour during the welding. Finally, section 3.3 analysed possible issues of axial and radial runout that can arise due to the tooling setup. This analysis allowed to draw some key observations:

- Industrial inertia welders can present different configurations and each of these has characteristics strengths and weaknesses. In addition, tooling related issues, such as over-constraining and imperfect location of the workpiece, can affect the quality and repeatability of the process. A means of comparison for different systems would be useful to analyse the outcomes and explaining the variability in the results;

- Inertia welders are usually equipped with sensors embedded into the machine. These, however, are positioned far from the weld zone and consequently are not able to capture local phenomena occurring during the welding. In addition, the data monitored by the sensors is affected by noise induced by the transient conditions of the welding and the multitude of additional systems embedded into the machine.

- The default approach to characterise the system using instrumented workpieces, despite being inexpensive and easy to setup for a limited number of tests, is not ideal for large studies because of the setup time and possible inconsistencies in results. Moreover, the installation of the sensors directly on the workpieces can induce inaccurate readings because the measurements are deeply affected by the position of the sensors and the shape of the workpieces.

These observations suggested that problems of non-idealised contact between the workpieces and repeatability in the process outcomes can occur due to the setup used in IFW. In addition, neither the sensors installed into the machine nor other approaches that make use of additional instrumentation mounted directly on the workpieces can effectively characterise the system and be used to compare different setups. These problems will be addressed with a novel monitoring system and methodology presented in the following chapters.

Chapter 4

A novel approach for the in-situ monitoring of IFW

Chapter 3 presented a detailed analysis of the key features and possible weaknesses of the IFW system in default conditions. From this analysis, the need to develop a system capable of characterising an IFW machine, with the flexibility to be used on similar systems to compare their performance, emerged. However, only a limited number of commercially available transducers can withstand the very high loads typical of IFW and the few that can are either extremely specialised and only capable of measuring very few aspects at the same time, or with form factors not suitable to be installed in an IFW machine. Moreover, section 2.2.3 showed that the few examples of monitoring systems for RFW described in literature present drawbacks and are extremely specialised and not suitable to give a holistic picture of the phenomena occurring during the welding. To fill this gap, a novel monitoring system was introduced, first the concept was validated with a prototype tested on a MTI-300T machine, then a second system was developed to validate the observations from the prototype on a larger MTI-2000B machine. This ensured that the phenomena analysed were characteristic of the process rather than artefacts caused by a specific system. In addition, cross comparing the data

from the two systems it was possible to extend the approach developed to a method to analyse the equivalency of similar systems to provide comparable outputs. This chapter will present a detailed description of the mechanical setup, the instrumentation installed and the workpieces welded for the two systems.

4.1 Generic concept of the application

The first step was the choice of the aspects to monitor. The efficiency is a useful parameter that allows the machine performance to be characterised, the state of the bearings to be determined and the performance of different machines to be compared. Considering the formulation in Eq. 2.5, which expresses the efficiency as ratio between the theoretical and the actual torque, two quantities were required: the angular speed of the spindle for the theoretical torque, and the torsional strain in proximity of the weld interface for the actual torque. Another aspect of interest was the interaction between the two workpieces. It was observed in chapter 2 that IFW is conventionally studied using the axisymmetry hypothesis, to understand the validity of this approximation, the axial and radial runout (defined in accordance with the ISO-1101:2017 standard [38]) were also included. In addition, to understand the effect of the interaction of the workpieces in non-ideal conditions, the axial strain at multiple locations around the circumference were monitored. Finally, the response of the system to the process loads was characterised by studying the vibrational behaviour in the axial, radial and tangential directions (assuming the axial direction is aligned with the spindle axis).

The second step was analysing potential constraints in the design arising from the IFW setup. The rotation of the headstock made the installation of the sensors difficult because no wired connection could be used and self-contained or wireless solutions were difficult to install due to the limited space available. In addition, having sensors and other equipment connected to the spindle represented a hazard for the personnel in the

proximity of the machine that could get severely injured if any element detached and got expelled at high speed. For this reason, instrument the tailstock was preferable, even if some aspect still needed to be considered.

Firstly, the axial translation of the tailstock combined with additional moving elements inside the machine made it necessary to have all the sensors installed directly on the backstop and suitable cable management. Secondly, the limited clearance between the tailstock and headstock required consideration of the form factor of the sensors and on the fixturing setup for the workpieces.

4.2 Small scale prototype

Starting from the considerations in section 4.1 a prototype to fit the MTI-300T machine was developed. The system was designed as an interface between the tooling of the inertia welder and the workpieces, serving at the same time as the physical support for the instrumentation and fixturing for the workpieces.

4.2.1 Mechanical setup

The need to bring the instrumentation close to the weld area made it necessary to rethink the conventional fixturing approach and the two custom backstops showed in Fig. 4.1 were developed to fit inside the machine tooling according to the schematic in Fig. 4.1e. With this design, the machine collet clamped the backstop while the workpieces were fully constrained by the backstops themselves. The front faces of the backstops were used to axially locate the workpiece and absorb the thrust exerted by the ram, while four keys (2 in Fig. 4.1a and 6 in Fig. 4.1c) constrained the workpiece against the process torque and located it radially. Then, serrated fixed edge clamps (3 in Fig. 4.1a) on the headstock side and spring plungers (5 in Fig. 4.1c) on the tailstock

side prevented the workpieces from moving before the part contact and allowed the self-release of the weld at the end of the process. This last point, summarised in Fig. 4.1e, was particularly critical because, at the end of the welding, the two sides of the machine are so close together that the technicians are not able to get close to the weld to release it. In the conventional setup, this problem is circumvented with hydraulic collets that can be actuated remotely; in this configuration, instead, the weld was automatically released by the spring plungers in the tailstock backstop, while the serrated fixed edge clamps in the headstock backstop refrained the workpiece from falling when the sides of the machine were moved apart.

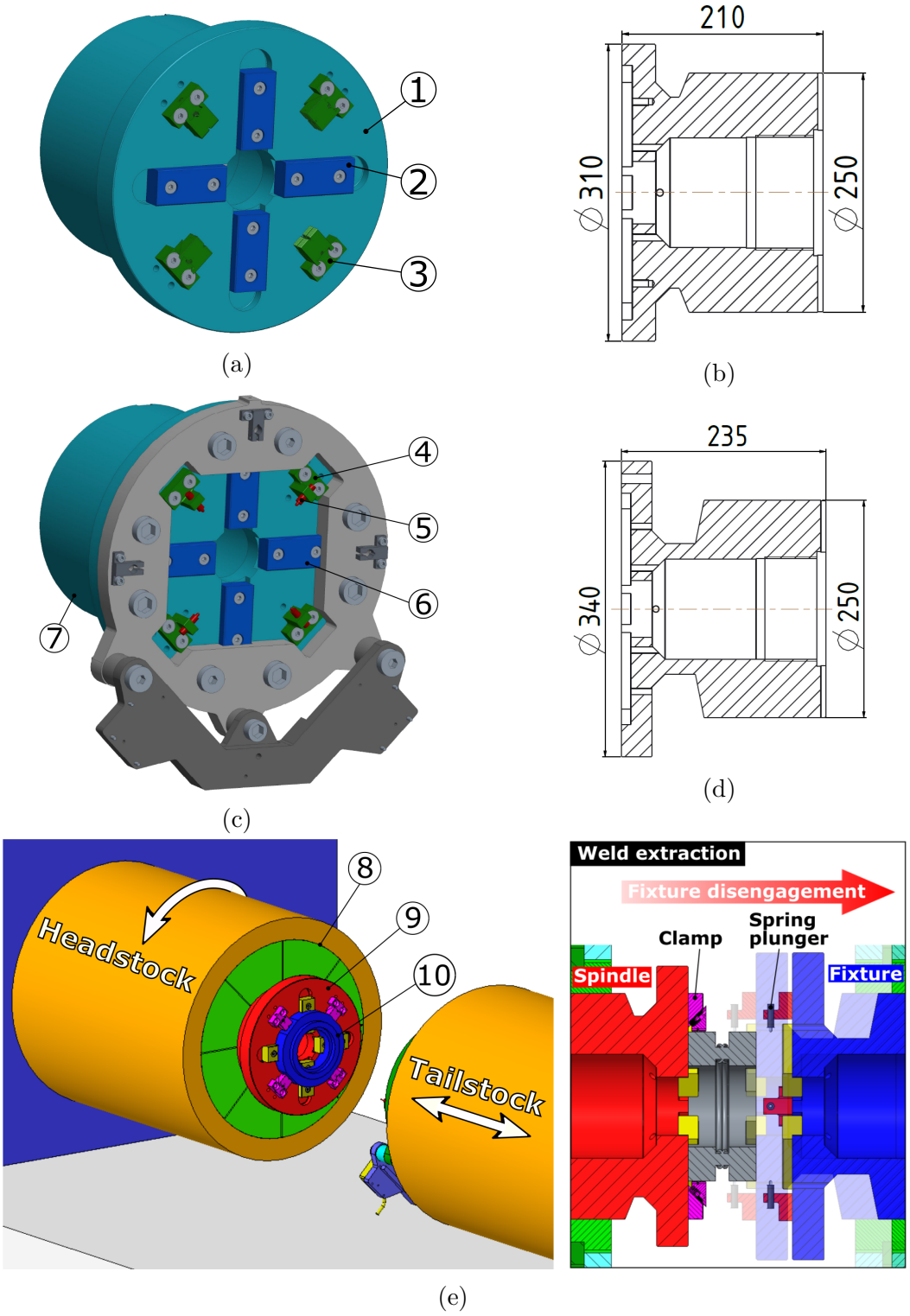


Fig. 4.1 Mechanical setup for the monitoring system prototype including two custom backstop capable to carry the instrumentation and constrain the workpieces: (a) Headstock backstop (1: Backstop; 2: Keys; 3: Serrated fixed edge clamps); (b) 2D section view of the headstock backstop with key dimensions; (c) Tailstock backstop (4: Plunger brackets; 5: Spring plungers; 6: Keys; 7: Backstop); (d) 2D section view of the tailstock backstop with key dimensions; (e) Monitoring system inserted into the MTI-300T tooling with a detailed view of the fixturing setup for the workpieces and self-releasing mechanism (8: Machine collet; 9: Headstock backstop; 10: Workpiece).

4.2.2 Instrumentation

As shown in Fig. 4.2, all the instrumentation was designed to fit into the tailstock backstop. Four stacked 0°/45°/90° 3-element rectangular rosettes (5) were installed equispaced around the circumference of a thinner neck section designed to provide sufficient strain sensitivity while withstanding the process loads. The 0° and 90° gauges for each pair of opposing rosettes (SG 1-SG 3 and SG 2-SG 4) were connected in a full bridge configuration to capture the torque, while the 45° gauge from each rosette connected in a quarter bridge configuration to measure the axial load. Vibrations were measured with a triaxial accelerometer (2), while a bracket was designed to carry and precisely locate two lasers displacement sensors (4) and a rotary encoder (3). The laser sensors were installed with a relative angle of 90° to characterise the relative runout between the headstock and tailstock. In fact, using this configuration it was possible to get a direct measurement of the spindle displacement in two orthogonal directions, while approximating the circumference of the backstop with a perfect circle, an approximation that holds due to the negligible circularity tabulated in section 4.2.3, it was possible to obtain the displacement of the centre of the headstock backstop using the formulation for the centre of a circumference ($P_c = (x_c, y_c)$) given two points ($P_1 = (x_1, y_1)$, $P_2 = (x_2, y_2)$) and the radius (r):

$$q = \sqrt{(x_2 - x_1)^2 + (y_2 - y_1)^2} \tag{4.1}$$

$$x_c = \frac{x_1 + x_2}{2} \pm \frac{y_1 - y_2}{q} \cdot \sqrt{r^2 - \left(\frac{q}{2}\right)^2} \tag{4.2}$$

$$y_c = \frac{y_1 + y_2}{2} \pm \frac{x_2 - x_1}{q} \cdot \sqrt{r^2 - \left(\frac{q}{2}\right)^2} \tag{4.3}$$

Limiting the analysis of the behaviour to the radial direction, however, was not sufficient because the lack of parallelism between the two workpieces could cause problems such

as vibrations at the initial contact and localised heat input (hot spots) [36]. To address this, the relative axial runout was measured with three LVDTs (1) installed 90° apart. Knowing three points (P_1, P_2, P_3) on the front face of the headstock backstop, allowed not only the axial runout at different locations to be calculated, but also to acquire information on the angular alignment of the two sides of the machine by fitting a plane through the points. In fact, a normal to the plane (n_v) can be calculated with the cross product between two vectors parallel to the plane (v_1, v_2):

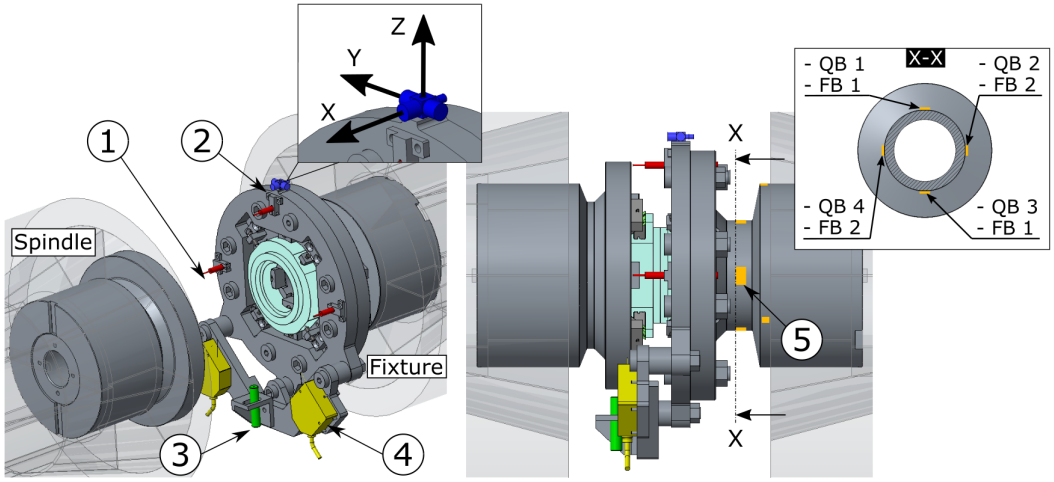
$$v_1 = P_2 - P1 \tag{4.4}$$

$$v_2 = P_3 - P1 \tag{4.5}$$

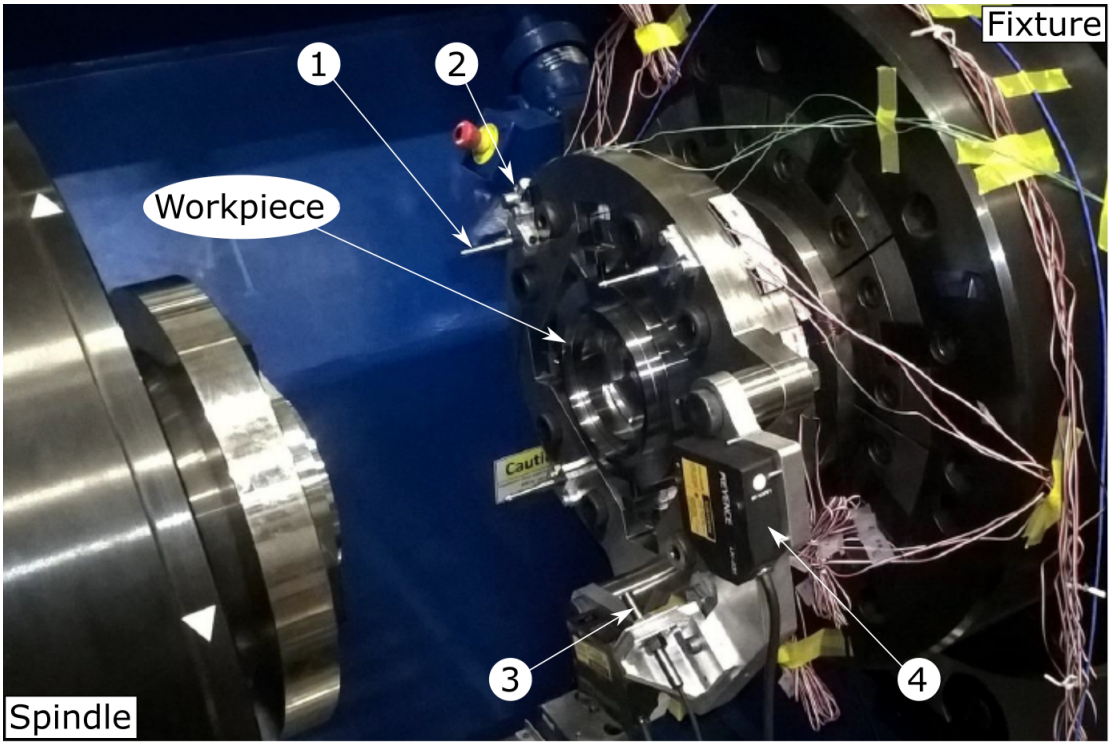
$$n_v = v_1 \times v_2 \tag{4.6}$$

It is worth noting that in contrast to strain gauges and accelerometers, sensors like lasers, LVDTS and encoder require a reference surface against which to conduct the measurements; for this reason, the headstock backup served the additional role of reference surface for these sensors. Finally, the temperature in the proximity of the sensors closest to the weld interface (LVDTs, accelerometer and strain gauges) was monitored with thermocouples to make sure it did not exceed the temperature limit for the sensors and ensure the consistency among different welds.

The instrumentation was connected to two DAQ systems: NI SCXI-1600 (modules: SCXI-1540, SCXI-1520, SCXI-1102) and NI CompaqRio-9066 (modules: NI 9223, NI 9234 and NI 9403) synchronised via software. Table 4.1 summarises the details for the monitoring setup.



(a)



(b)

Fig. 4.2 Schematic of the monitoring system with sensors (1: LVDTs, 2: Triaxial accelerometer, 3: Encoder, 4: Laser disp. sensors, 5: Strain gauges): (a) CAD schematic of the rig with details of the sensors installed; (b) Image of the rig installed on the machine.

Table 4.1 Sensors and sampling frequency

No.	Sensor type	Sensor model	DAQ module	Sampling freq.
1	LVDTs	RDP D5/400AG	NI SCXI-1540	1kHz
2	Accelerometer	Kistler 8792A100	NI 9234	50kHz
3	Encoder	LCZ260-30	NI 9401	50kHz
4	Laser sensors	Head: Keyence LK-G32 Controller: Keyence LK-G3001P	NI 9223	50kHz
5	Rectangular rosette (0°/45°/90°)	MM 062WW (4 @ 90°)	NI SCXI-1520	1kHz
6	Tee rosette (0°/90°)	MM 125LT (3 @ 120°)	NI SCXI-1520	1kHz
7	Thermocouples	5TC-TT-KI-30-2M	NI SCXI-1102	1kHz

4.2.3 Assessment of the system geometry

In the previous section, it was shown that the sensors responsible to assess the alignment tailstock-headstock were the laser displacement sensors, used to measure the radial runout of the headstock custom backstop with respect to the tailstock, and the LVDTs, used to monitor the axial runout between the two. According to the definition stated in the ISO-1101:2017 standard [38], the runout is a composite measurement that includes both geometrical errors in the monitored surfaces and the overall dynamic behaviour of the component. In the radial direction, the runout accounts for both concentricity and circularity, while in the axial direction for flatness and parallelism. Therefore, it was necessary to distinguish which portion of runout was ascribable to dimensional errors in the monitoring system from the dynamic behaviour of the machine spindle, which represents the aspect to be investigated. For this reason, the actual geometry of the headstock backstop was particularly critical. Fig. 4.3 and Table 4.2 summarise the geometrical errors measured with a Mitutoyo Euro-C-A121210 CMM. For the radial runout, it was necessary to evaluate the concentricity between the section of the backstop clamped with the collet (1) and the surface monitored by the laser displacement sensors (2), for which a value of 22 μm was obtained, and the circularity

of surface 2 itself, 2 μm. The combined value of concentricity and circularity errors needed to be subtracted from the reading of the lasers during the welding to obtain the actual runout of the machine spindle. For the axial runout, instead, the effect of the flatness of the front surface of the backstop (A) and its parallelism with the back face (B) were measured and values of 4 μm and 16 μm respectively were obtained. In this case, however, the actual axial runout of the spindle could not be simply calculated subtracting the planarity and parallelism errors from the output of the LVDTs but the process upset needed to be subtracted as well.

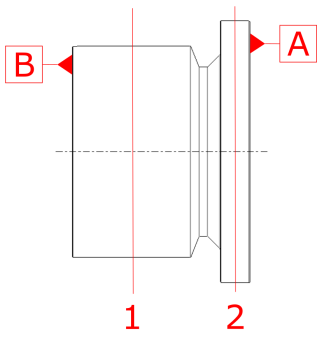


Fig. 4.3 Schematic representation of the key features inspected

Tolerance	Measured value
Circularity section 2	2 μm
Concentricity 1-2	22 μm
Flatness A	4 μm
Parallelism A-B	16 μm

Table 4.2 Values monitored with a CMM with respect to the schematic shown in Fig. 4.3

4.2.4 Validation of the mechanical setup under process conditions

Analysing the geometry of the custom backstops it is possible to observe that the weakest point is the neck section in the tailstock backstop. This was designed with an optimised wall thickness to withstand the process loads and to provide enough sensitivity for the strain gauges. To achieve this, an axisymmetric static FE representation of the system was developed according to the schematic in Fig. 4.4. The two elements included in the model, the backstop and the workpiece, interact with a sticking boundary condition, while the clamping effect of the machine fixture is simulated by constraining all the

DoFs on the external cylindrical surface of the backstop (boundary condition A) and constraining the translation in Y direction on the back face of the backstop (boundary condition B). Considering the low variability of Young's modulus and Poisson's ratio for steel, values of 207 GPa and 0.3 respectively were assumed for both the backstop (EN24T) and the workpiece (EN9) [139], while triangular quadratic elements were used to mesh the two components. Finally, the response of the system to the process conditions was simulated applying two loads to the weld surface[1], a torque to simulate the frictional torque and an axial load to represent the thrust from the ram. For both loads, the magnitude was ramped from zero to the maximum value, 20 kNm for the torque and 896 kN for the thrust.

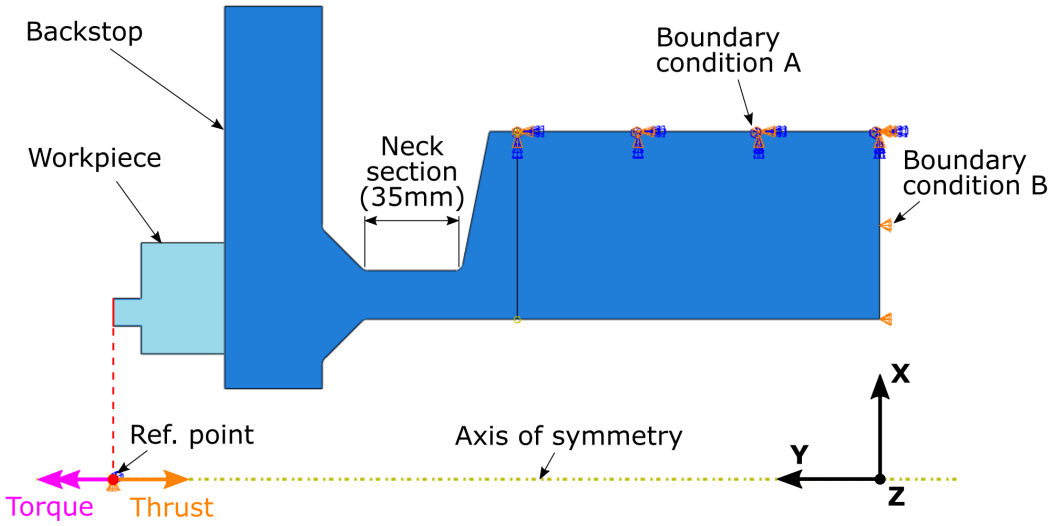


Fig. 4.4 Axisymmetric FE model developed to analyse the stresses in the neck section of tailstock backstop

Fig. 4.5 shows the von Mises stress in the neck section at the peak loads, revealing how the peak stresses are localised at the rounds. Since the two backstops were

[1] Abaqus, the FE software used in this analysis, does not allow moments and concentrated loads to be applied to surfaces. To achieve a similar effect, it is possible to create a reference point, connected by a kinematic coupling to the surface to which the loads needs to be applied

manufactured in EN24T, rated with a yield strength of approximately 650 MPa [140], the design showed a safety factor larger than 1.5, confirming its suitability from a mechanical standpoint. Chapter 3, however, showed that when strain gauges are involved it is also important to make sure that the strain field where the strain gauges are installed is not affected by stress concentration features or border effects. Fig. 4.6a and Fig. 4.6c show the normal (σ_{yy}) and shear (τ_{yz}) stress fields, while Fig. 4.6b and Fig. 4.6d compares the numerical stresses evaluated at the centre of the neck section with the analytical values calculated using the formulation from classical mechanics:

$$\sigma_{yy} = \frac{P}{A} \tag{4.7}$$

$$\tau_{yz} = \frac{T \cdot r_o}{J_p} \tag{4.8}$$

where P is the thrust, A is the area at the evaluation point, T the torque, r_o the outer radius of the neck section and J_p the torsion constant. The comparison between analytical and numerical data shows an almost perfect match confirming the suitability of analysing the output of the strain gauges with Eq. 4.7 and Eq. 4.8.

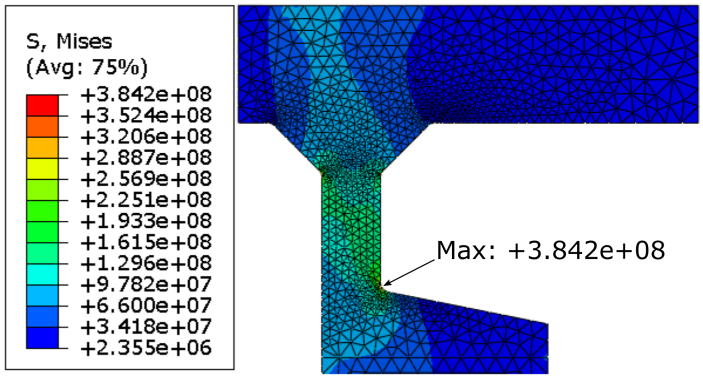


Fig. 4.5 von Mises stress field in the neck section at the peak loads

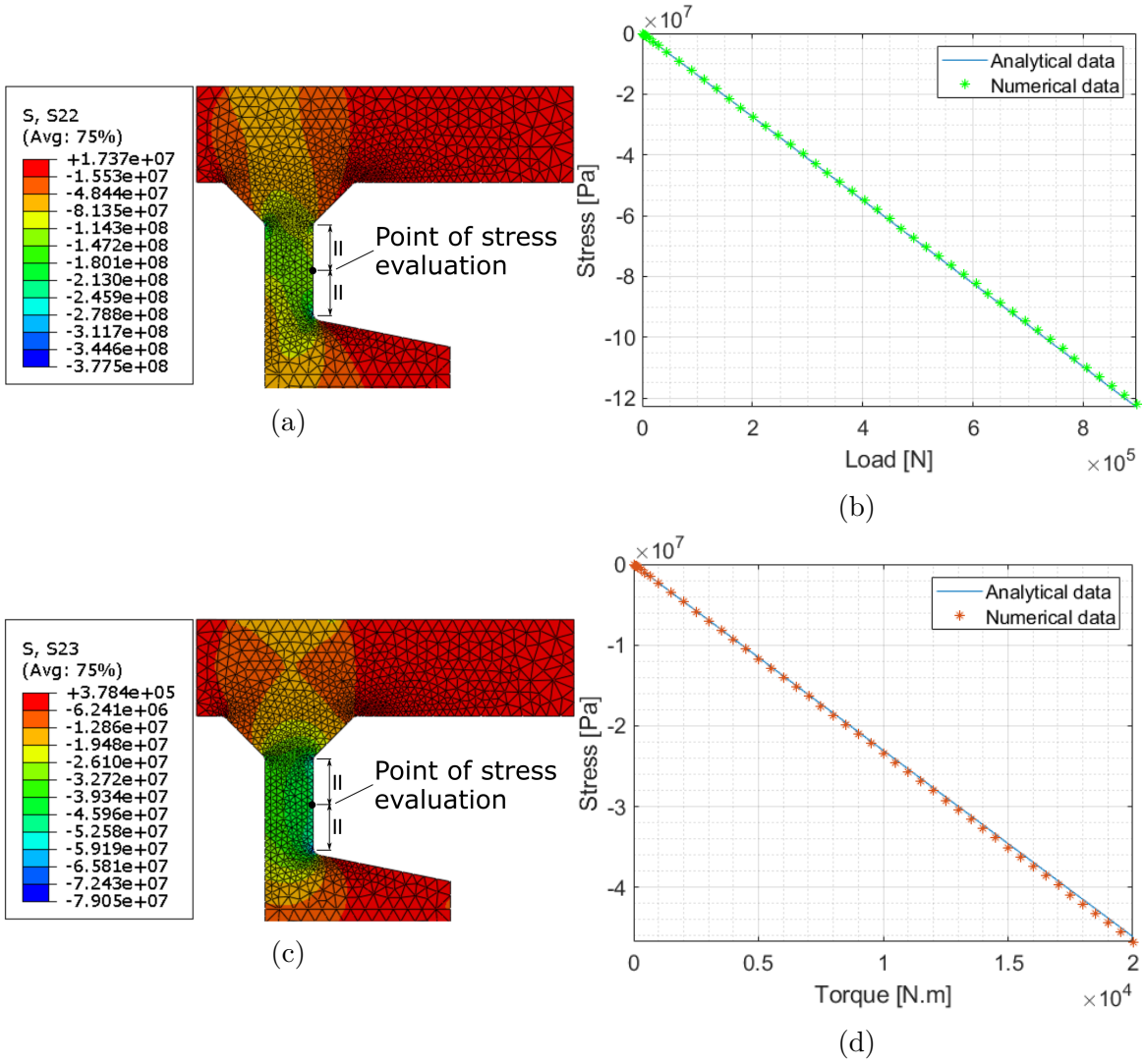


Fig. 4.6 Comparison between the analytical and the numerical stress in the backstop neck section: (a) Normal stress field (σ_{yy}); (b) Comparison between the analytical and numerical normal stresses at the centre of the backstop neck for various level of thrust; (c) Shear stress field (τ_{yz}); (d) Comparison between the analytical and numerical shear stresses at the centre of the backstop neck for various level of torque.

4.2.5 Dynamic response of the system to process conditions

IFW is a transient process characterised by decreasing speed of the machine spindle, non-constant process loads and evolving conditions at the interface of the two workpieces. Therefore, it was necessary to estimate the response of the custom backstops to the transient welding conditions to guarantee the safety of the system and to validate the readings of the sensors that rely on the stability of the support structure.

The first step was the analysis of the eigenfrequencies to ensure that even the lowest of these were higher than the angular rotation of the spindle to avoid resonance. Restricting the analysis to the portion of backstop sticking out from the machine collet, the FE model in Fig. 4.7 was studied with a linear perturbation analysis (eigenvalue extraction). Also in this study, for the backstop (1), the adaptor plate (2) and the spacers (3), the typical values of Young's modulus, Poisson's ratio and density common for steel were used (207 GPa , 0.3 and 7850 kg/m^3 respectively [139]), while for the bracket (4), machined in aluminium, 70 GPa , 0.32 and 2700 kg/m^3 [139]. Finally, the components were meshed with 3D linear hexahedral elements and an encastre applied to the back face of the model to remove the six DOFs.

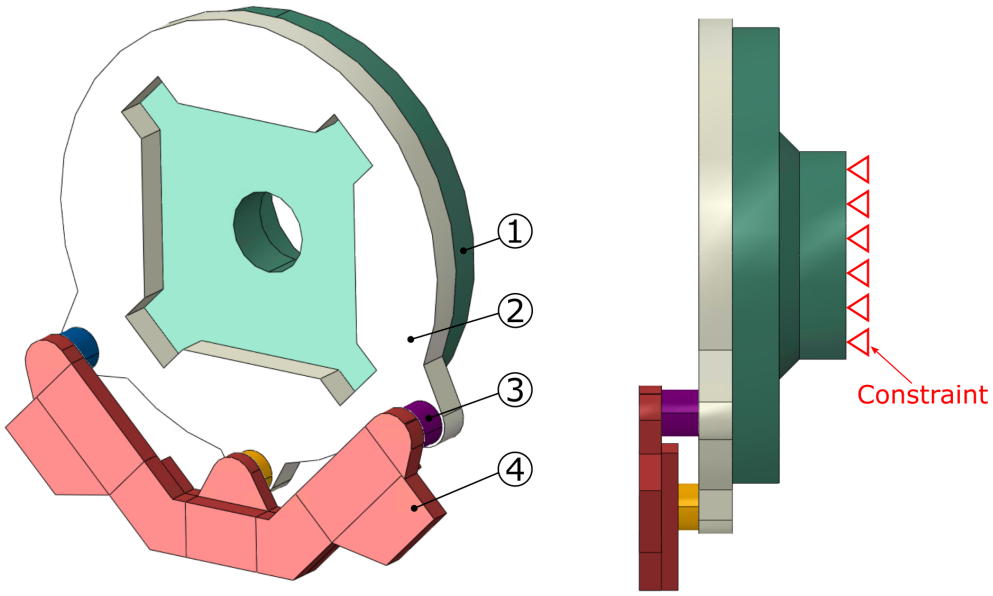


Fig. 4.7 Schematic representation of the FE model used to study the linear perturbation analysis (1: Backstop, 2: Adaptor plate, 3: Spacers, 4: Bracket)

Fig. 4.8 shows five eigenmodes corresponding to the lowest eigenfrequencies. The lowest eigenfrequency obtained was 1180.3 Hz, a value noticeably larger than the peak angular speed used for the tests (275 RPM $\approx$ 4.6 Hz).

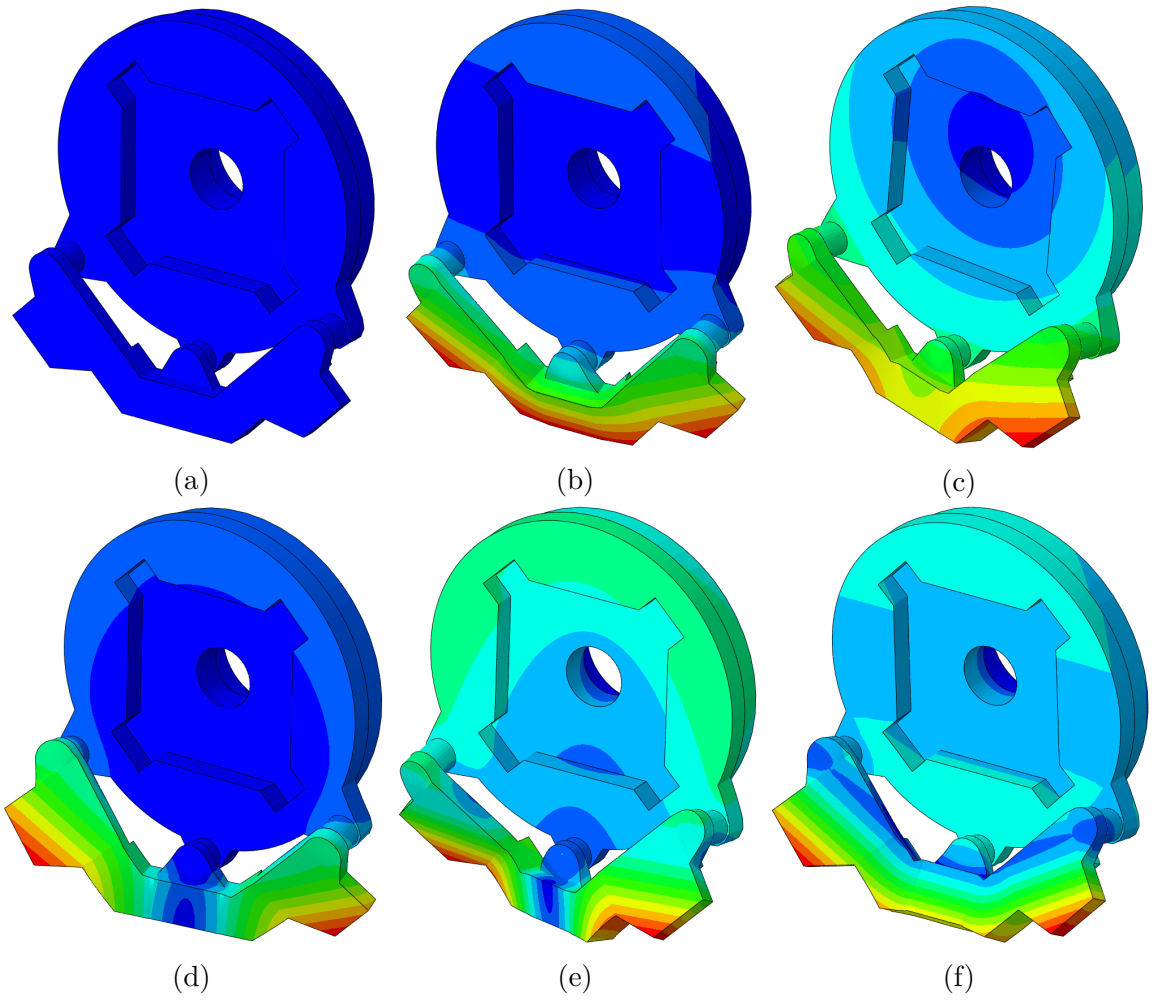
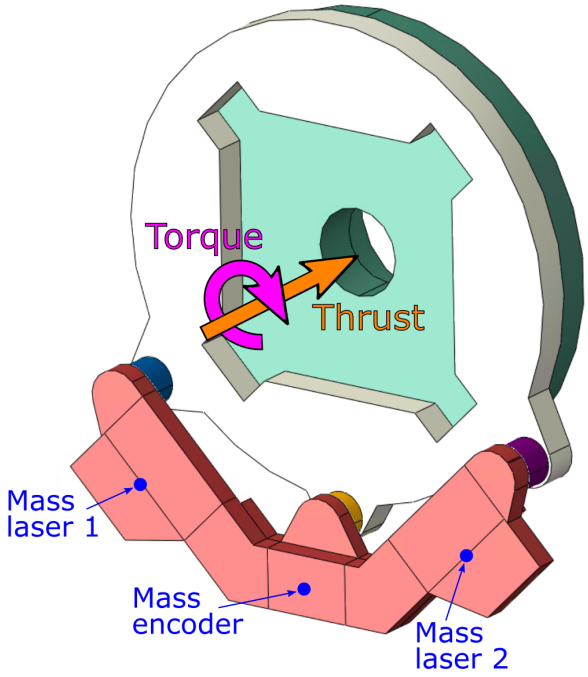


Fig. 4.8 Eigenmodes for the tailstock backstop: (a) Undeformed system; (b) Eigenmode 1: 1180.3 Hz; (c) Eigenmode 1: 1195.4 Hz; (d) Eigenmode 1: 1297.2 Hz; (e) Eigenmode 1: 1729.1 Hz; (f) Eigenmode 1: 1861.5 Hz.

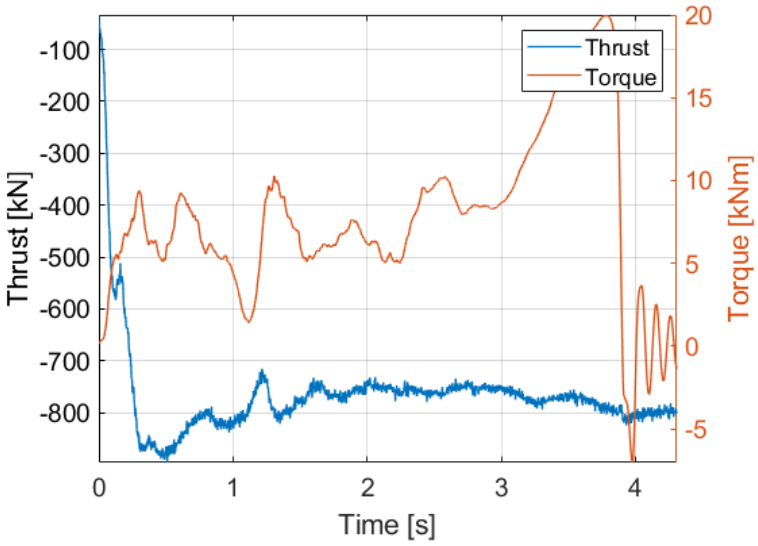
The second aspect to analyse was the effect of impulses induced by phenomena like parts contact or the final flywheel deceleration. These effects, despite not being dangerous in term of resonance of the system, could have induced vibration peaks detrimental for the stability and repeatability of the sensors readings. To predict

the behaviour in process conditions, the loads monitored in a sample steel weld run on the MTI-300T machine were used as input loads for a dynamic study of the FE models previously used in the eigenvalue extraction, as shown in Fig. 4.9a. To study a worst-case scenario, the load characteristics were scaled so that the peak values of torque and thrust were matching the ones used for the backstop validation (torque: 20 kNm, thrust: 896 kN), as shown in Fig. 4.9b. The study of the natural frequencies showed that the largest oscillations should be expected in the bracket that supports lasers and encoder, for this reason, reference points with associated the mass of the respective sensors (laser heads: 0.28 kg, encoder: 0.3 kg) where connected to the bracket in the designated locations of these sensors.

Solving the dynamic model, the radial and axial displacement for the three reference points are shown in Fig. 4.10. The graphs show similar behaviour, with both the axial and radial displacement that gradually increase with the load. In particular, it appears that the deflection of the system induced by the thrust has the dominant effect, while the impulse at part contact and at the final instant of rotation of the flywheel do not induce significant vibrations. The magnitude of oscillation is negligible considering the values of runout expected or any oscillation that could negatively affect the contact between the encoder and the spindle, in particular, considering that the case simulated represents the worst-case scenario since, in reality, the contact with the headstock workpiece would provide an additional constraint. Comparing the results for the three points, it is possible to note a larger difference between the axial and radial behaviour for the location in which the encoder is installed; this can be explained considering the stiffness and constraining conditions of the bracket.

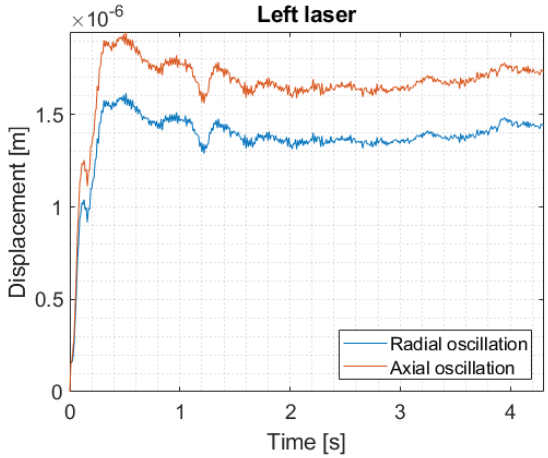


(a)

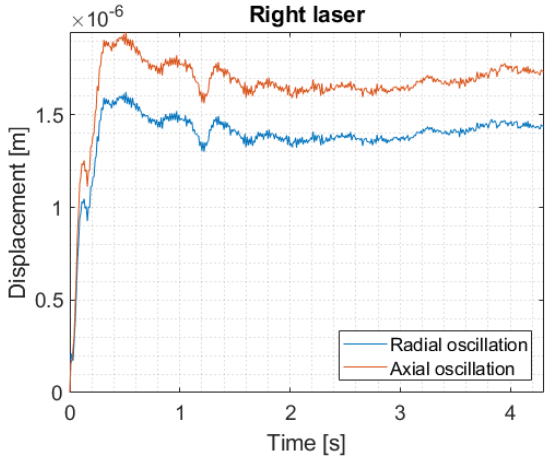


(b)

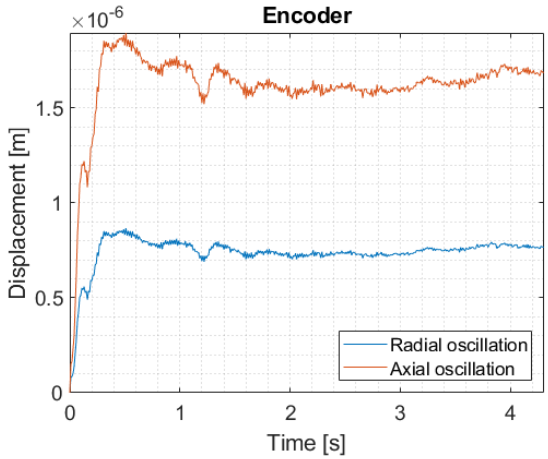
Fig. 4.9 FE dynamic model for the study of the vibrational behaviour of the fixture backstop considering actual process loads: (a) Schematic representation of the FE model in which it is possible to observe the three reference points used to model the sensors installed on the bracket and the applied loads; (b) Input loads for the FE model calculated scaling values of thrust and torque monitored in a sample weld to the peak admissible values used to dimension the system.



(a)



(b)



(c)

Fig. 4.10 Radial and axial oscillations for the three points used to represent the sensors installed on the bracket: (a) Oscillation of the left laser; (b) Oscillation of the right laser; (b) Oscillation of the encoder.

4.2.6 Validation of the fixturing configuration

As detailed in section 4.2.1, the application required a new fixturing setup for the workpiece and a solution that made use of keys to locate and constrain the workpiece was proposed. Keys are conventionally dimensioned with two approaches: shear strength resistance and maximum allowable surface pressure [139]. The first ensures that the shear strength of the keys is sufficient to withstand the shear load while the second one verifies that the contact pressure at the interface key/keyway is lower than the allowable contact pressure of the materials used.

For this application, four keys in EN9 steel with a cross section 36 mm x 22 mm (width x height) and a length of 78 mm were selected; the suitability of this design was validated with the FE model shown in Fig. 4.11. The system includes the front face of the backstop (in this case the tailstock backstop is shown but since the key configuration is analogous for both sides of the machine, the results can be extended to the headstock as well), the four keys and the workpiece. Since all the components were manufactured in steel, Young's modulus and Poisson's ratio were selected equal to 207 GPa and 0.3 respectively [139], while 3D linear hexahedral elements were used for the mesh. All six DoFs of the backstop were constrained to simulate the clamping action of the machine collet, while a sticking boundary condition was applied between the keys and the backstop; the contacts among the remaining surfaces were handled considering a 0.3 constant friction coefficient [141]. Finally, similar to what already done in section 4.2.4, the process loads were simulated by imposing a toque and a thrust on the welding surface with an amplitude equal to the maximum rating for the system (20 kNm for the torque and 896 kN for the thrust).

Solving the FE model and analysing the peak loads (worst-case scenario), the results in Fig. 4.12 were obtained. For EN9 in the R heat treatment condition, a minimum yield strength of 480 MPa was used [140] and analysing the von Mises stress shown

in Fig. 4.12a it is possible to observe how this does not exceed the yield strength of the material at any point of the keys. For the analysis of the contact pressure, Fig. 4.12b shows peak values below 400 MPa. The heat treatment condition R achieves a surface hardness between 223 and 277 HB with a limiting ruling section of 64 mm [142], which gives values of equivalent yield strength even higher compared to the core value previously reported [143], confirming the suitability of the design also against surface damage.

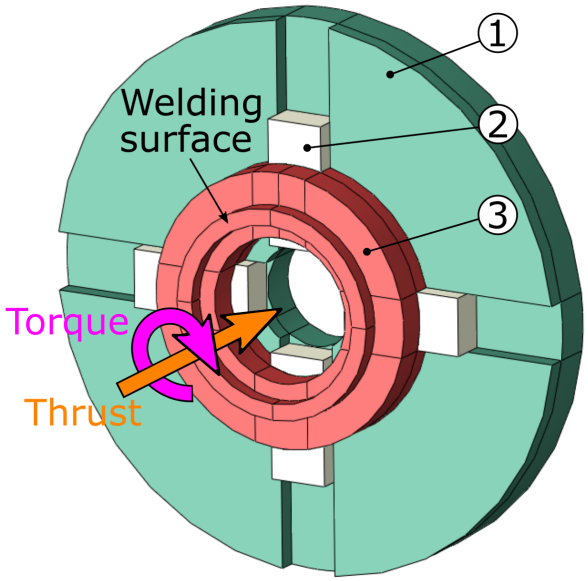
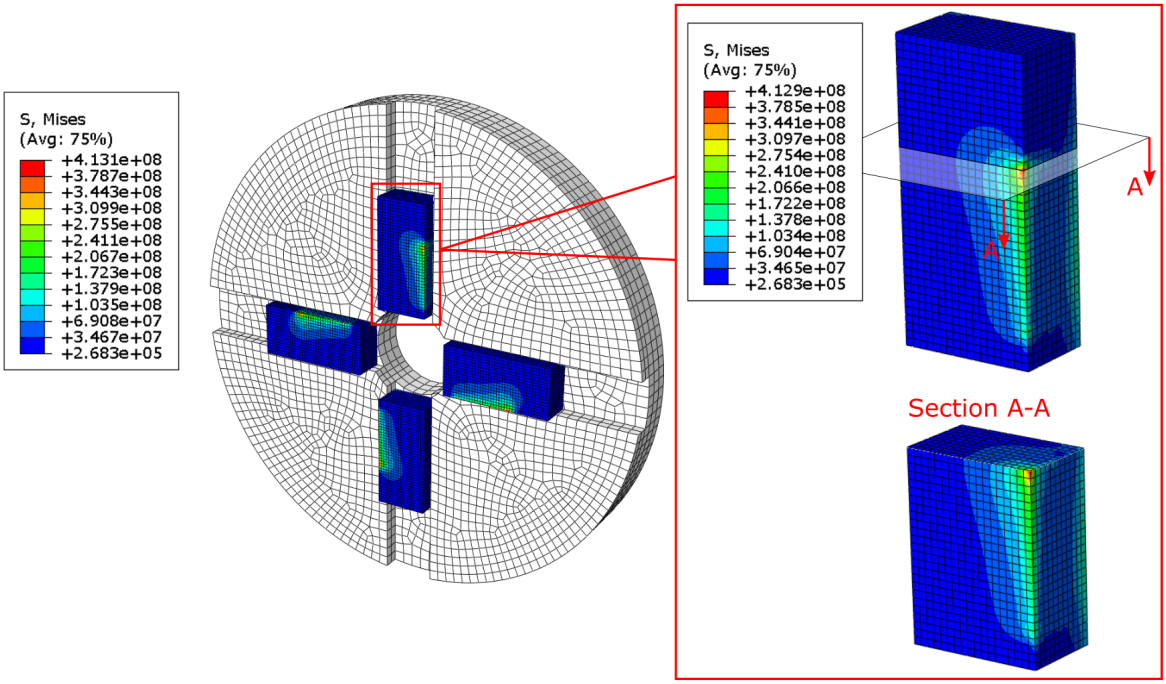
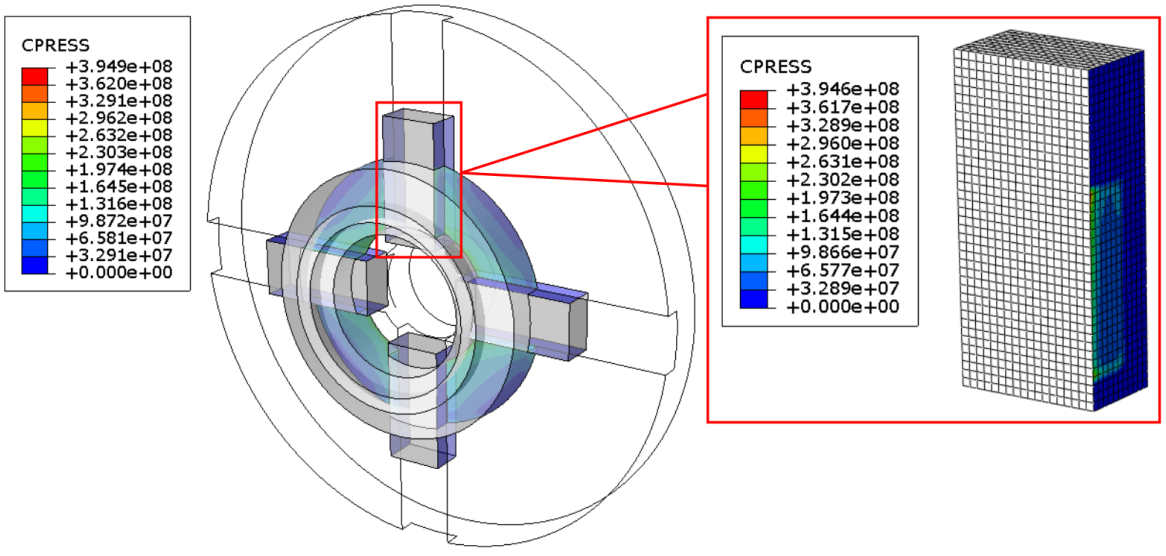


Fig. 4.11 FE model implemented to validate the design of keys and keyways in the backstop (1: Backstop; 2: Keys; 3: Workpiece)



(a)



(b)

Fig. 4.12 Values of stress and contact pressure in the keys obtained with the FE models: (a) von Mises stress for the keys; (b) Contact pressure between the workpiece and the lateral faces of the keys.

4.3 Validation system

Using a design similar to the prototype, a second system was developed as an instrumented interface between an MTI-2000B machine and the workpieces, capable of carrying the required instrumentation and serving as fixturing for the workpieces. This section will detail the mechanical setup and the instrumentation installed.

4.3.1 Mechanical setup

The mechanical setup designed to fit the MTI-2000B started from the PDX3 configuration described in section 3.1.2.1, to create a system that could comply with the severe checks required by Rolls-Royce for their production machines. Also for this system, all the instrumentation was installed on the tailstock side, leaving the headstock backstop to hold one of the workpieces and only act as the reference surface for lasers and LVDTs. Starting from this assumption, it was possible to modify and reuse the existing PDX3 headstock backstop to accommodate the precisely machined ring shown in Fig. 4.13c and Fig. 4.13d, serving as a reference surface for the sensors. The custom tailstock backstop was designed as a hybrid between the PDX3 backstop and the prototype previously described. In fact, as shown in Fig. 4.13a and Fig. 4.13b, a neck section was added to the design of the PDX3 to accommodate the strain gauges, while the front face was customised to fit all the required instrumentation. Having already assessed the capability of an alternative fixturing configuration with the prototype, in which the collet clamps the backstop while the workpiece is constrained by a feature in the backstop itself, the original configuration used for the PDX3 was preserved. This setup is displayed in Fig. 4.13e and included four small keys to locate the workpiece (4), carbide serrated grippers (3) to constrain the workpiece against the process torque and radial elements to prevent the workpiece moving before part contact. These should

ensure the self-release of one of the two workpieces at the end of the weld, for this reason, set screws were adopted in the headstock backstop (1) while spring plungers in the tailstock (2). Finally, the backstops were connected to the machine tooling using a combination of screws (6) and keys (5).

This configuration has the advantage of being highly interchangeable with the PDX3 system, allowing a straightforward switch from one system to the other; aspect of primary importance for a production machine in which long downtimes are not acceptable.

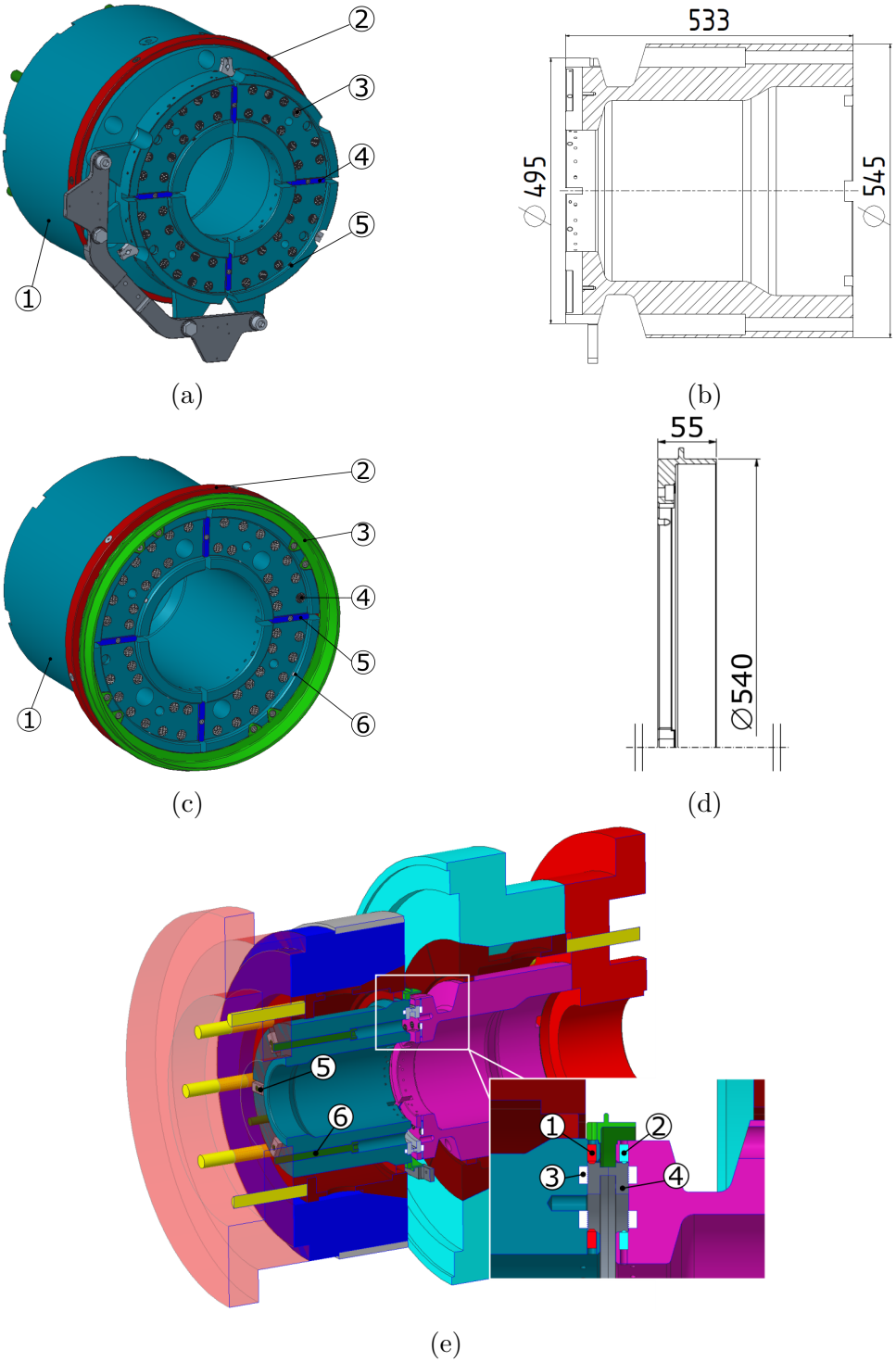


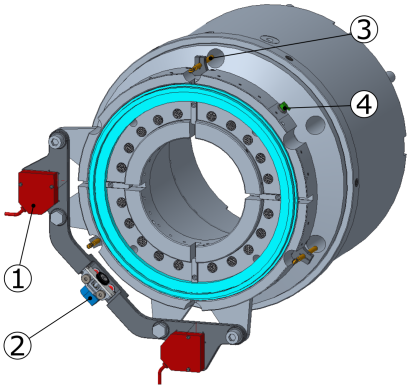
Fig. 4.13 Mechanical setup for the validation system: (a) Tailstock backstop (1: Backstop; 2: Collet ring; 3: Serrated grippers; 4: Keys; 5: Spring plungers); (b) 2D section view of the tailstock backstop; (c) Headstock backstop (1: Backstop; 2: Collet ring; 3: Reference ring; 4: Serrated grippers; 5: Keys; 6: Set screws); (d) 2D section view of the reference ring; (e) Monitoring system inserted into the MTI-2000B tooling with detail of the fixturing setup for the workpieces (1: Set screws; 2: Spring plungers; 3: Serrated grippers; 4: Workpieces; 5: Keys backstop/machine tooling; 6: Screws backstop/machine tooling);

4.3.2 Instrumentation

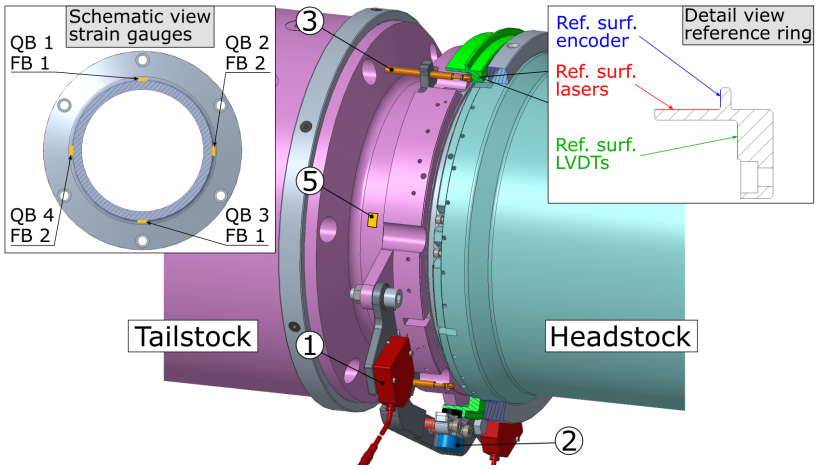
Given the good results obtained with the prototype, the same sensor configuration was adopted, which is schematically represented in Fig. 4.14a and Fig. 4.14b and summarised in Table 4.3. Three LVDTs installed 120° apart were used to monitor the axial runout and a three axial accelerometer was attached radially to the front face of the backstop. Four 0°/45°/90° rectangular rosettes were installed in the backstop neck section, with the 0° and 90° strain gauges of opposing rosettes connected in two full bridges (FB 1 and FB 2) to monitor the process torque and the 45° strain gauges connected in a quarter bridge configuration (QB 1, QB 2, QB 3, QB 4) to capture the thrust at four different locations. Finally, two laser heads (1) 90° apart, used to measure the radial runout, and an encoder were installed on a bracket connected to the front face of the backstop. The magnetic encoder used in the prototype was replaced with an optical encoder encapsulated in a custom chassis (described in detail in section 4.4) to obtain a better resolution on the headstock angular speed.

Table 4.3 Sensors and sampling frequency

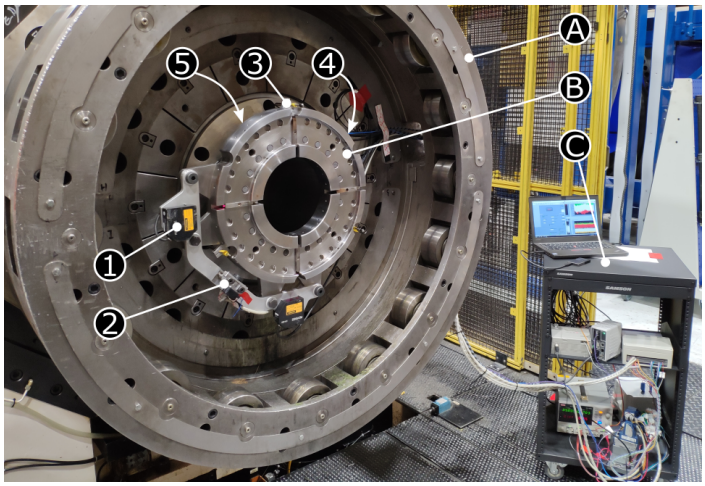
Sensor type	**Sensor model**	**DAQ module**	**Sampling freq.**
LVDTs	RDP D5/400AG	AD598 / NI 9239	2kHz
Accelerometer	Kistler 8764B050BB	NI 9234	51.2kHz
Encoder	Broadcom HETL-5540	NI 9401	1kHz
Laser sensors	Head: Keyence LK-G32 Controller: Keyence LK-G3001P	NI 9223	2kHz
Rectangular rosette (0°/45°/90°)	L2A-06-062WW-350 (4 @ 90°) C2A-06-125LT-350 (1 @ 45°)	NI 9237	2kHz



(a)



(b)



(c)

Fig. 4.14 Instrumentation used for the validation system (1: Lasers; 2: Encoder; 3: LVDTs; 4: Accelerometer; 5: Strain gauges): (a) CAD model of the tailstock custom backstop highlighting the instrumentation installed; (b) CAD model of headstock and tailstock backstops with detail of the strain gauge configuration and description of the key features in the headstock reference ring; (c) Picture of the custom tailstock backstop installed on the MTI-2000B with the instrumentation connected to the respective power supplies and control boards (A: Machine tooling; B: Instrumented custom backstop; C: Power supplies and control boards).

The custom ring was designed to fit the PDX3 headstock backstop and act as a reference surface for the encoder, the lasers and the LVDTs is shown in Fig. 4.14b. It was designed so that, after part contact, a portion of the tailstock backstop is embraced providing an additional layer of safety, acting as a cage and preventing any item detaching from the system during the welding from being expelled at high speed towards the operators standing close to the machine.

Finally, a rack cabinet (C in Fig. 4.14c) was used to store all the power supplies and control boards required by the sensors, improving the safety of the operators accessing the machine and protecting the integrity of the instrumentation.

4.3.3 Assessment of the system geometry

Similarly to the prototype, it was necessary to assess the dimensional precision of the spindle custom ring to evaluate its influence on the radial and axial runout monitored with the lasers and the LVDTs respectively. Fig. 4.15 summarises the key geometrical features inspected using a DEA Global Silver Advantage slant bridge CMM. A total runout of 22 μm was obtained for section 1 with reference to spindle backstop axis (A), while the parallelism between face 2 and the reference plane B was 19 μm.

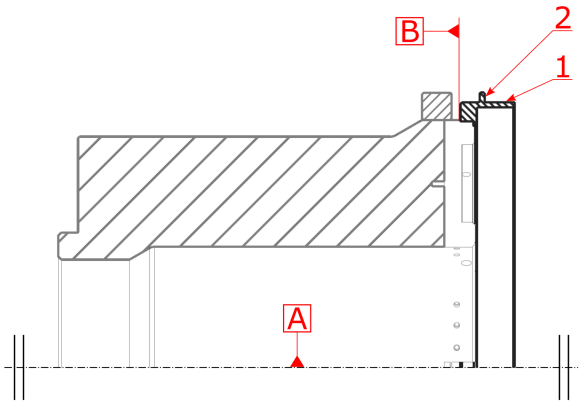


Fig. 4.15 Schematic representation of the key features inspected to assess the influence of the geometrical errors on the runout measured with lasers and LVDTs

4.3.4 Validation of the mechanical setup under process conditions

The design of the backstop was optimised to ensure a sufficient safety margin against the expected peak loads and geometry suitable for strain gauges. Differently from the prototype backstops, in this case, a large number of features made its design not axisymmetric, for this reason, a 3D model was developed. As shown in Fig. 4.16, only the portion of backup sticking out from the collet was considered and the constraining action of the collet was accounted for removing all six DoFs from the back face of the model. Since the backstop was manufactured in EN36 steel, Young's modulus and Poisson's ratio equal to 207 GPa and 0.3 were selected [139], while 3D quadratic tetrahedral elements were used to mesh the part. Finally, the process conditions were simulated by applying an axial load of 3600 kN and a torque of 200 kNm to the front face.

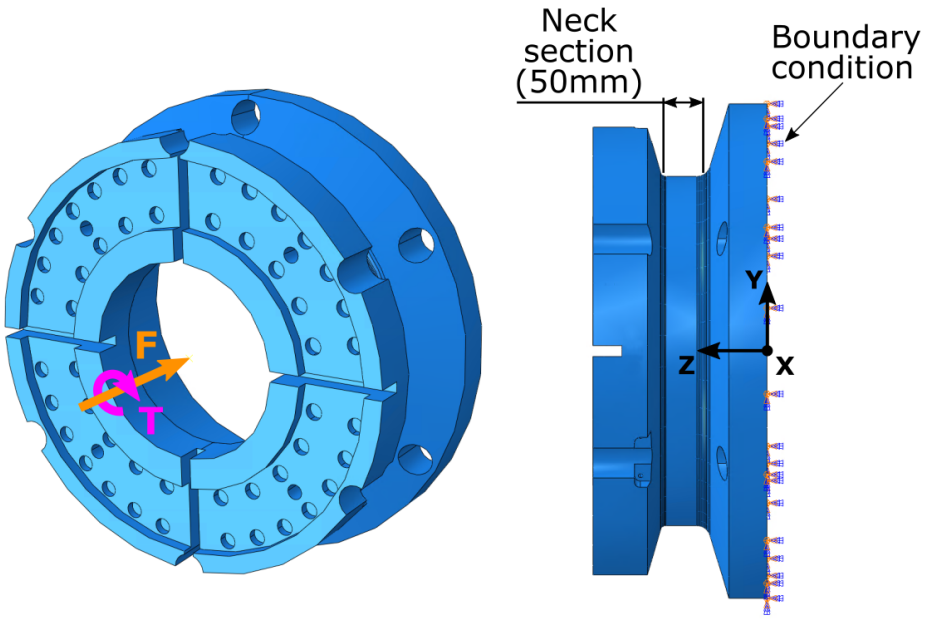


Fig. 4.16 3D FE model developed to analyse the stresses in the neck section of tailstock backstop

Fig. 4.17 shows the von Mises stress in the neck section at the peak loads, where it is possible to observe peak stress of 250 MPa close to the rounds. Considering for EN36 a minimum yield strength of 540 MPa [140], a safety factor larger than two was ensured. As in the prototype, the strain gauges were installed midway along the neck, to ensure that the strain field in that location was not altered by stress concentration features or border effects the stresses in axial (σ_{zz}) and torsional (τ_{zx}) directions were compared to the analytical values obtained from Eq. 4.7 and Eq. 4.8. Fig. 4.18 shows an excellent match, confirming the design of the neck section.

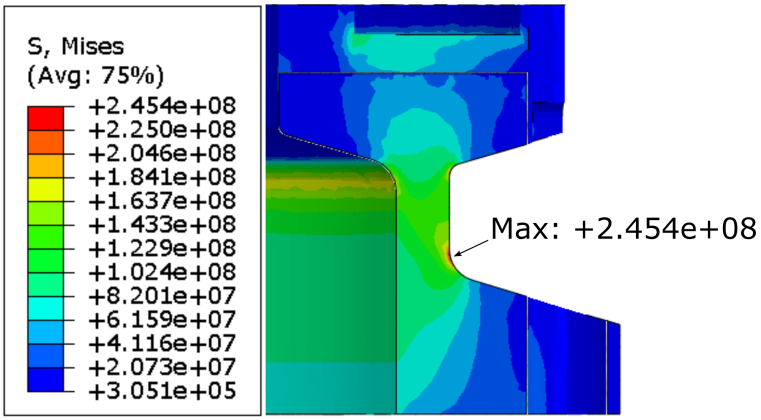


Fig. 4.17 von Mises stress field in the neck section at the peak loads

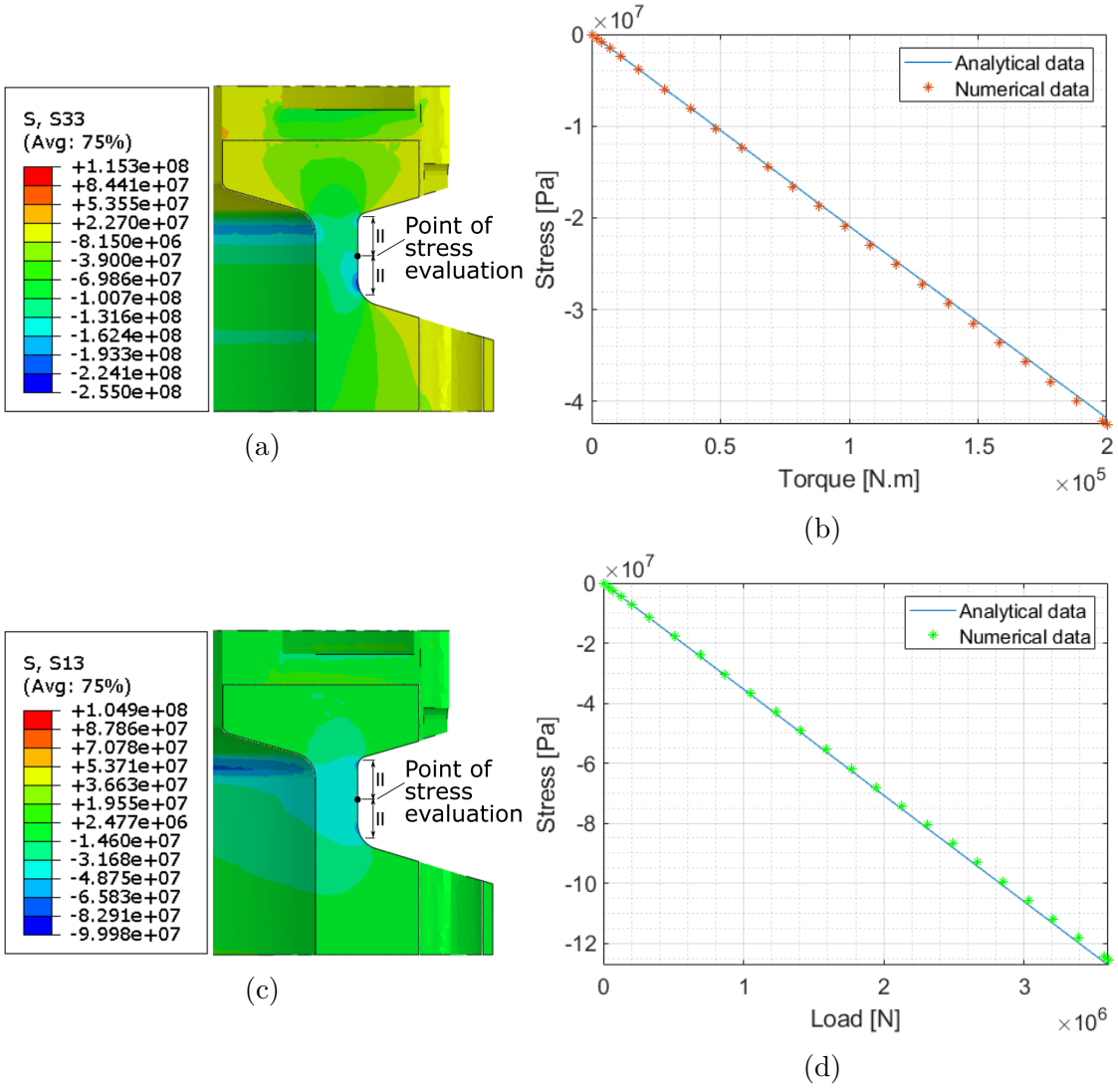


Fig. 4.18 Comparison between the analytical and numerical stress in the backstop neck section: (a) Normal stress field (σ_{zz}); (b) Comparison between the analytical and numerical normal stresses at the centre of the backstop neck for various level of thrust; (c) Shear stress field (τ_{zx}); (d) Comparison between the analytical and numerical shear stresses at the centre of the backstop neck for various level of torque.

4.3.5 Dynamic response of the system to process conditions

To extract the eigenfrequencies and associated eigenmodes for the tailstock backstop, the portion of system sticking out from the machine collet was analysed. As shown in Fig. 4.19, the system is composed of a portion of the backstop (1) and the bracket (2), in which the small features were removed, having a negligible effect on the system response but a profound impact on the mesh size and, consequently, the computation time. The values of Young's modulus, Poisson's ratio and density conventionally adopted for steel were used for the backstop: 207 GPa, 0.3, and 7850 kg/m^3, while for bracket made in aluminium: 207 GPa, 0.32 and 2700 kg/m^3. Finally, the components were meshed with 3D linear hexahedral elements and the back surface of the backstop was fully constrained removing all six DoFs.

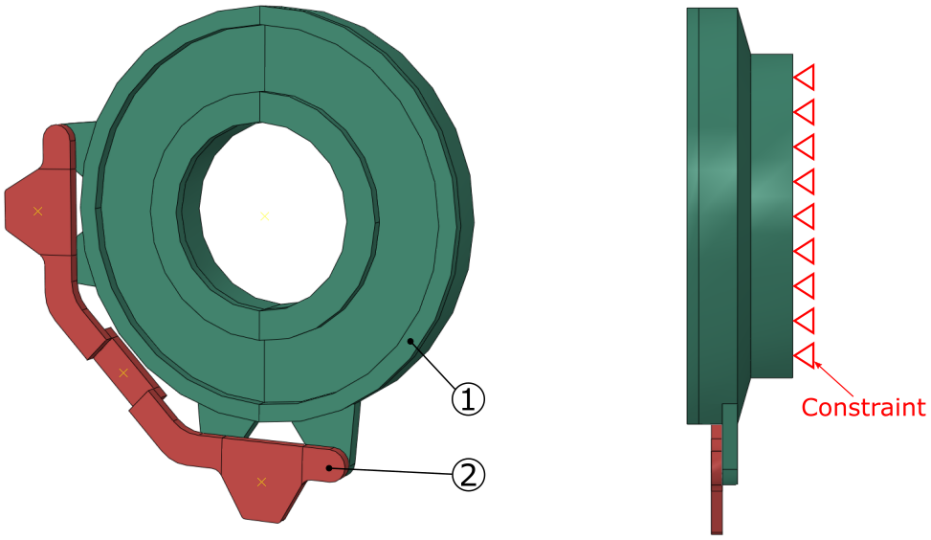


Fig. 4.19 Schematic representation of the FE model used to study the linear perturbation analysis (1: Backstop, 2: Bracket)

Fig. 4.20 shows the first five eigenmodes. The lowest eigenfrequency is 696.88 Hz, a value significantly larger than the maximum angular speed to which the MTI-2000B machine is run, excluding the risk of resonance in the system.

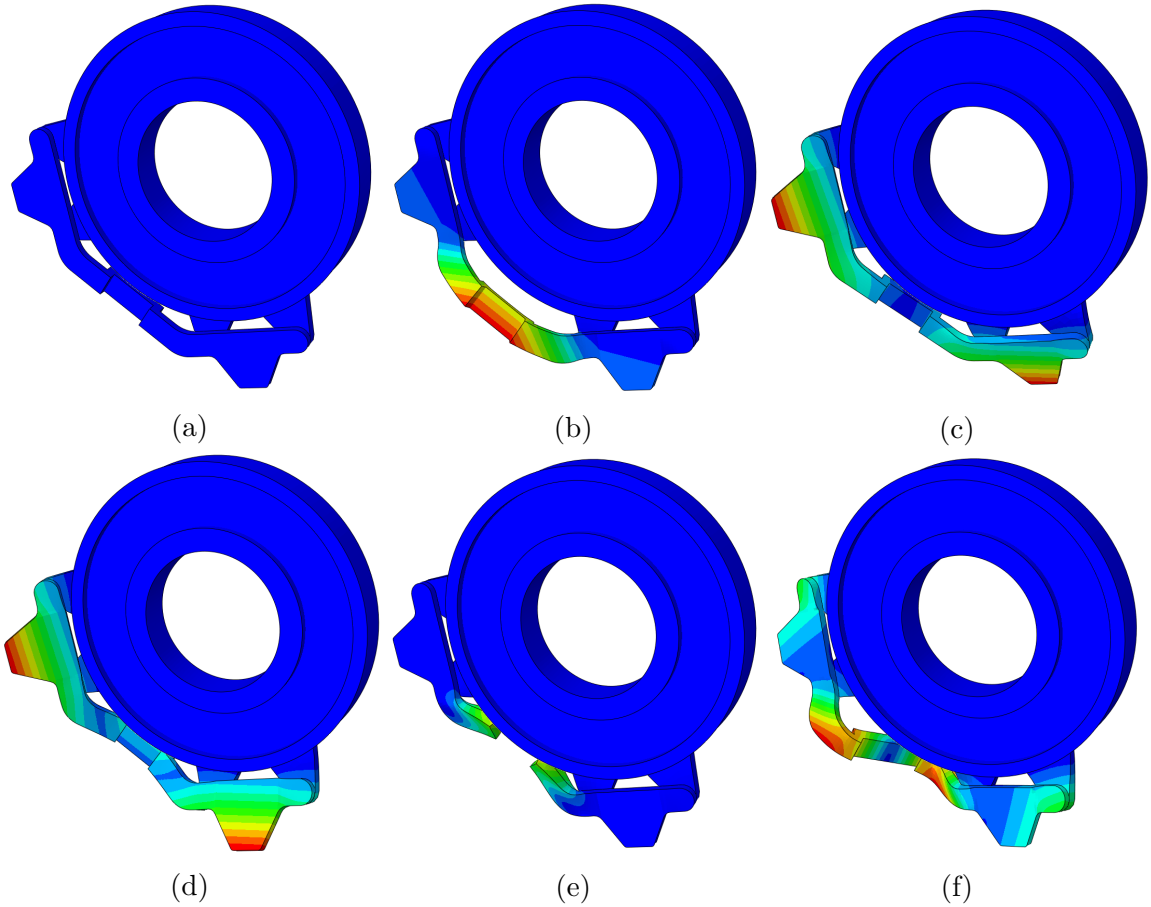


Fig. 4.20 Eigenmodes for the tailstock backstop: (a) Undeformed system; (b) Eigenmode 1: 696.88 Hz; (c) Eigenmode 2: 1135.2 Hz; (d) Eigenmode 3: 1179.9 Hz; (e) Eigenmode 4: 1534.2 Hz; (f) Eigenmode 5: 2207.7 Hz.

To assess the vibrational behaviour of the backstop under process conditions, a model similar to the one used for the eigenvalue extraction was adopted, as shown in Fig. 4.21. In this case, the loads already used in the prototype system (Fig. 4.9b) were applied to the front face of the backstop and scaled up to have peak thrust of 3600 kN and peak torque of 200 kNm. Finally, reference points with associated the mass of the

laser heads (0.28 kg) and the encoder (0.38 kg) were connected to the bracket where the sensors would be installed.

The axial and radial oscillations of the three reference points are shown in Fig. 4.22; results analogous to the prototype were obtained, in which the axial and radial displacement follow the deformation in the system caused by the thrust.

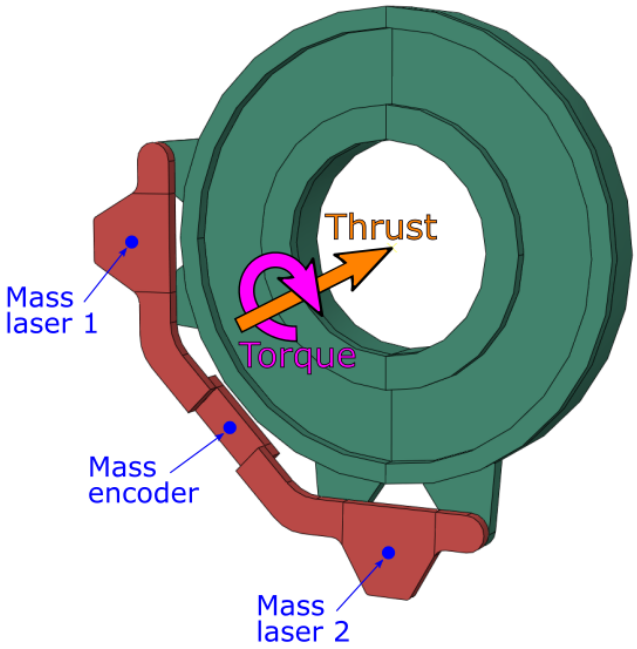
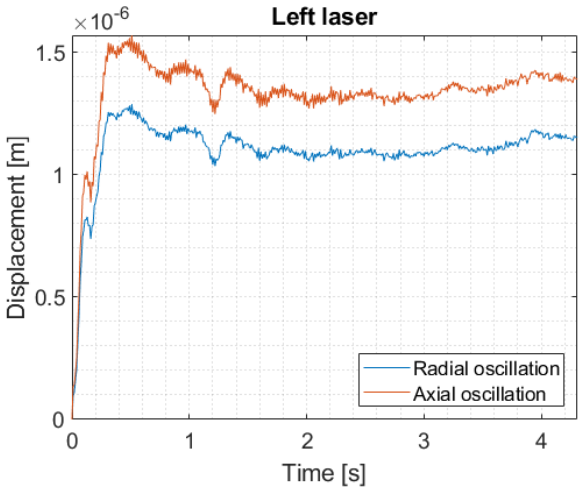
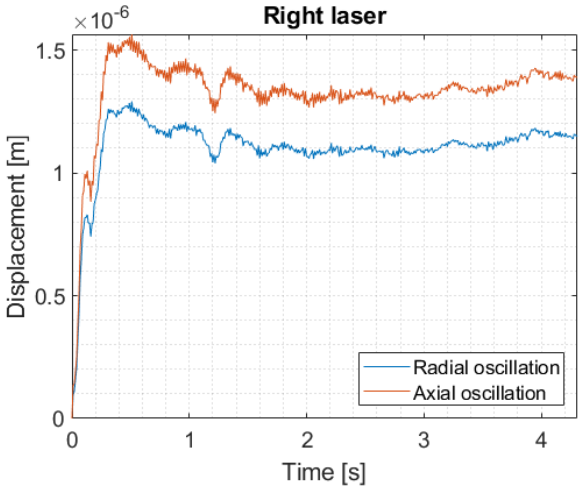


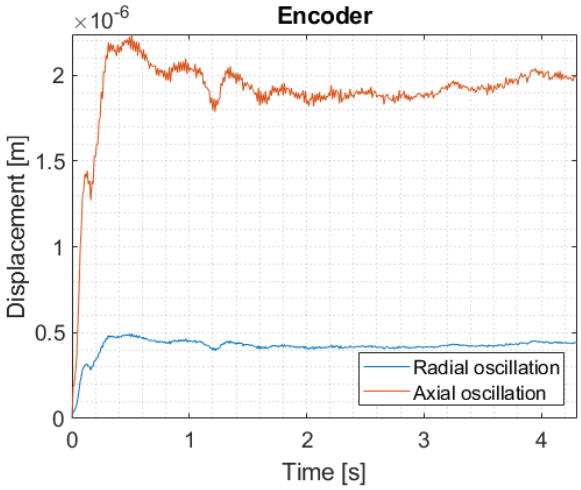
Fig. 4.21 Schematic representation of the FE model in which it is possible to observe the three points used to model the sensors installed on the bracket and the applied loads



(a)



(b)



(c)

Fig. 4.22 Radial and axial oscillations for the three points used to represent the sensors installed on the bracket: (a) Oscillation of the left laser; (b) Oscillation of the right laser; (c) Oscillation of the encoder.

4.4 Sensors theory of operation

LVDTs

LVDTs (Linear Variable Differential Transformer) are transducers that convert linear motion into an electrical signal, making use of three solenoidal coils and one cylindrical ferromagnetic core that slides inside the coils. The central coil, called primary, is powered with alternating current and causes a voltage in the two secondaries proportional to the position of the core. [144]

LVDTs require a signal conditioner to provide an analogue output signal proportional to the displacement of the central core. For this reason, starting from an Analog Devices AD598 chip, the signal conditioning circuit shown schematically in Fig. 4.23 was developed. The circuit required a power input of 30 V DC and a maximum current draw of 20 mA, which was provided with an external power supply, while the analogue output was captured with a NI939 module sampling at 2 kHz. Finally, RDP D5/400AG LVDTs were upgraded with high-accuracy roller tips characterised by lower friction coefficient and lower wear impact on the mating surface compared to the standard tungsten carbide tips.

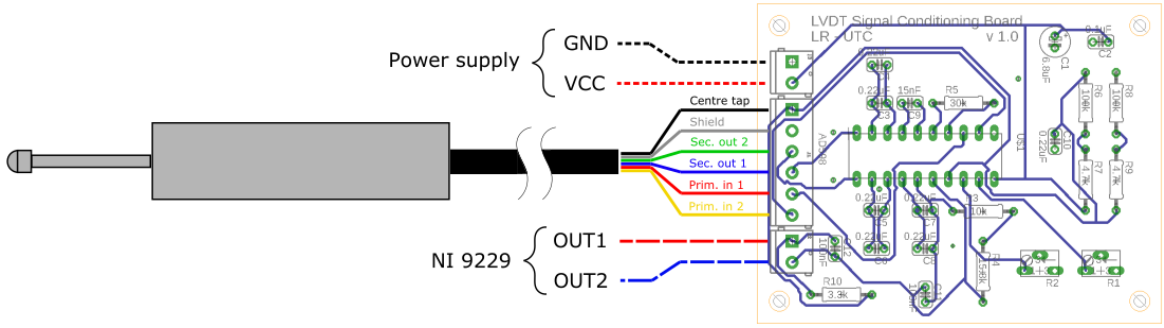


Fig. 4.23 Schematic representation of an LVDT and of the signal conditioning circuit developed to extract an analogue output from the sensor

The LVDTs were added to the system to capture the macroscopic oscillations in the spindle rather than high frequency effects, which, instead, were studied with an accelerometer. For this reason, the output signals of the sensors were post-processed in MATLAB to remove the high frequency-low amplitude noise using a Savitzky-Golay FIR smoothing filter of polynomial order three, a technique that found numerous applications because distortionless and more effective at preserving the shape of the signal compared to other algorithms, such as moving average [145].

Accelerometer

Piezoelectric accelerometers convert a mechanical impulse in an electric signal exploiting the piezoelectric effect, i.e. the capability of certain materials to generate an electrical charge in response to mechanical stress applied. A popular variant of this technology called IEPE (Integrated Electronics Piezo-Electric) presents a preamplifier used to convert the conventional high impedance output into a low impedance signal, which can be transmitted at relatively long distances and without the need of special low noise cable. [146]

For this application, the triaxial Kistler 8764B050 IEPE accelerometer shown in Fig. 4.24 was used. This is characterised by a ±50 g acceleration range and 0.5…10000 Hz ±5% frequency response (0.3…15000 Hz ±10% frequency response). To guarantee a non-invasive but stable installation, the sensor was installed with M2.5 screw to a support base attached in a semi-permanent way to the backstop using high strength epoxy glue. Finally, the sensor was connected to a NI 9234 input module using an M4.5 4 pin to 3 x BNC fluoropolymer jacketed breakout cable (Kistler 1784B3K03).

The accelerometer was sampled at high frequency (50 kHz) to avoid aliasing and the output of the sensor was post-processes with a band-pass filter to retain only the frequency content within the ±5% response range of the sensor. The conversion from time to frequency domain is a powerful technique to characterise the vibrational

behaviour of mechanical systems. The most common approach makes use of the Fourier transform, which, however, requires the system to be linear and the data to be strictly periodic or stationary [147]. In IFW these conditions are clearly not respected due to the decreasing angular speed of the spindle and transient phenomena, such as the impact at part contact and the stick-slip at the weld interface. The simplest solution to the problem is provided by the Short Time Fourier Transform (STFT) that splits the signal into several "windows" and relying on the assumption of piecewise stationary data applies a Fourier transform to each window. Despite its simplicity and low computational cost, several drawbacks can be identified. Firstly not always the signal when partitioned presents a stationary behaviour, secondly, even if the data are piecewise stationary it is often difficult to found a window size that matches the stationary time scales [147, 148]. For this reason, more advanced techniques have been developed, such as the popular wavelet transform that can be seen as an adjustable window STFT [147, 149]. In this research, the continuous formulation of the wavelet transform (CWT) implemented in MATLAB was adopted.

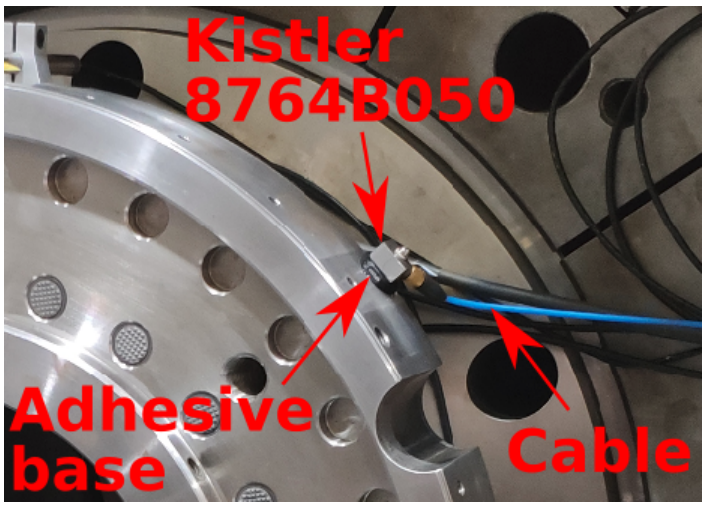


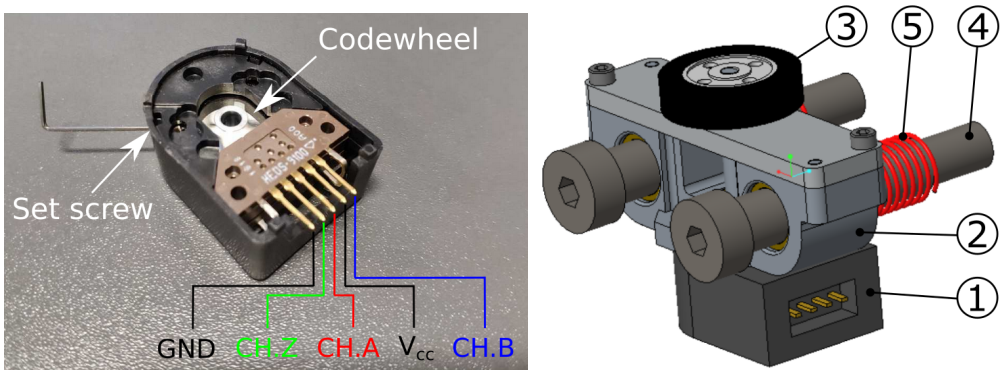
Fig. 4.24 Kistler 8764B050 accelerometer installed on the backstop

Encoder

Optical encoders are electromechanical devices that convert the position or motion of a shaft into an electrical signal. A typical configuration includes a LED source that shines through the gaps of a code wheel and a photodetector that reads the optical pattern. The sequence of light and dark are then used to calculate the rotary position and by successive differentiation the speed and acceleration. [150]

An Avago HEDS-9140, shown in Fig. 4.25a, was selected for this application due to its good resolution, low noise and small packaging. The biggest challenge to be faced using an encoder in IFW is the relative axial displacement (upset) of headstock and tailstock. In fact, if the sensor was installed rigidly to the headstock it would be either not in contact with the spindle or crashed when the two sides of the machine approach. For this reason, the encoder (1) was installed on the custom chassis (2) presented in Fig. 4.25b. An aluminium and rubber wheel (3) attached to a shaft driving to the encoder stays in contact with the spindle and rotates alongside with it. The shaft is supported by two bushings that protect the encoder against side loads induced by the interaction wheel/spindle. The chassis slides axially on two shoulder bolts (4) preloaded with compression springs (5), allowing to keep the wheel in contact with the spindle while the tailstock progressively approaches the headstock.

The encoder was powered using a 5V power supply and the TTL digital output captured with a NI9401 module. To reduce the undesired noise generated during the differentiation of the encoder signal, the data of speed and angular acceleration were processed with a Savitzky-Golay FIR smoothing filter of polynomial order three.



(a) (b)

Fig. 4.25 Encoder and custom chassis developed to monitor the headstock angular speed throughout the welding: (a) Detail of the Avago HEDS 9140 encoder; (b) Custom chassis that allows keeping the encoder in contact with the spindle throughout the weld (1: Encoder; 2: Chassis; 3: Wheel; 4: Shoulder bolts; 5: Compression springs).

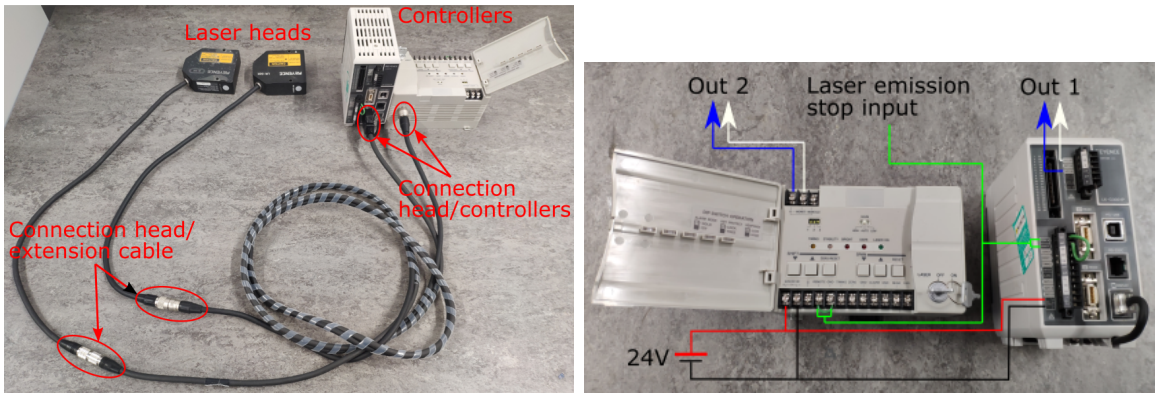
Laser displacement sensors

Laser triangulation sensors are a type of laser displacement sensors in which a laser beam is emitted by a light source, hits the target surface and part of it gets reflected and collected back by a light-receiving element. When the distance from the target changes, the laser beam moves on the detector, which then sends a signal used to measure the relative distance from the target. [144]

The position of the spindle during the process was monitored using the two Keyence laser heads (LK-G32 and LK-031) shown in Fig. 4.26a. The high resolution, repeatability ($0.05\mu m$) and sampling frequency (up to 50kHz), in fact, make these sensors an ideal candidate to capture a dynamic variable like the spindle runout. The two laser heads were connected to the LK-G3001P and the LK-3100 controller respectively shown in Fig. 4.26b, to convert the output from the lasers into analogue signals which were then captured with a NI9223 voltage input module.

Despite having the potential to measure relatively high frequency phenomena, the laser displacement sensors served a role similar to the one of LVDTs, capturing the macroscopic behaviour of the system. Therefore, to produce a comparable output,

the signals from the lasers were pre-processed with the same filter (Savitzky-Golay) adopted for the LVDTs.



(a) (b)

Fig. 4.26 Encoder and custom chassis developed to monitor the headstock angular sped throughout the weld: (a) Detail of the Avago HEDS 9140 encoder; (b) Mechanical setup develop to hold the encoder and allow to monitor the angular speed of the headstock throughout the weld.

Strain gauges

Strain gauges are sensors in which the electrical resistance changes proportionally to the strain in the component which they are connected to. Strain gauges are characterised by the gage factor (GF), which express quantitatively its sensitivity to strain and for metallic strain gauges is approximately 2:

$$GF = \frac{\Delta R/R}{\epsilon} \tag{4.9}$$

where R is the electrical resistance of the gauge, ΔR its variation and ϵ the strain. The values of strain are usually very small and consequently so are the changes in resistance. To capture such minute variations a Wheatstone bridge is used. This consists of an electrical circuit with four resistive arms and powered by a voltage, usually referred to as excitation voltage (V_{EX}), when the resistance in the four arms is equal, the output voltage of the bridge (V_{CH}) is zero and the bridge is said to be balanced; any change

in resistance in one of the arms, on the other hand, causes a nonzero output voltage. Therefore, if a strain gauge is connected to one of the arms of the bridge, any change in the resistance of the strain gauge would induce an imbalance in the bridge and consequently a non-zero output voltage proportional to the strain.

Depending on the number of active elements, i.e. strain gauges, it is possible to determine three different Wheatstone bridge configurations: quarter bridge (one active element), half bridge (two active elements) and full bridge (four active elements). As detailed in the previous sections, the monitoring system developed includes full bridges to capture the torsional strain in the system and quarter bridges for the axial strain. Considering a component of cylindrical shape and installing the strain gauges according to the schematic in Fig. 4.27a, it is possible to capture the output voltage from the Wheatstone bridge with a bridge module like the NI9237, the connections of which are shown in Fig. 4.27b. The torque (T) applied to the component can be then obtained as:

$$\epsilon = \frac{-V_r}{\mathrm{GF}} \tag{4.10}$$

$$\gamma = 2 \times \epsilon = \frac{\tau}{G} \tag{4.11}$$

$$T = \frac{\tau \cdot J}{r_o} \tag{4.12}$$

where $V_r = \frac{V_{CH}(strained) - V_{CH}(unstrained)}{V_{EX}}$ is the voltage ratio, γ the shear strain, τ the shear stress, J second moment of area, G shear modulus and r_o the outer radius. The axial load (F), on the other hand, can be measured installing a stain gauge as shown in Fig. 4.27c and using once again a module like the NI9237 with the connections

showed in Fig. 4.27d. The calculation in this case is as follows:

$$\epsilon = \frac{-4 \cdot V_r}{\mathrm{GF}\,(1+2V_r)} \tag{4.13}$$

$$\sigma = \epsilon \cdot E \tag{4.14}$$

$$F = \sigma \cdot A \tag{4.15}$$

where E is the Young's modulus and A the area of the section. [151]

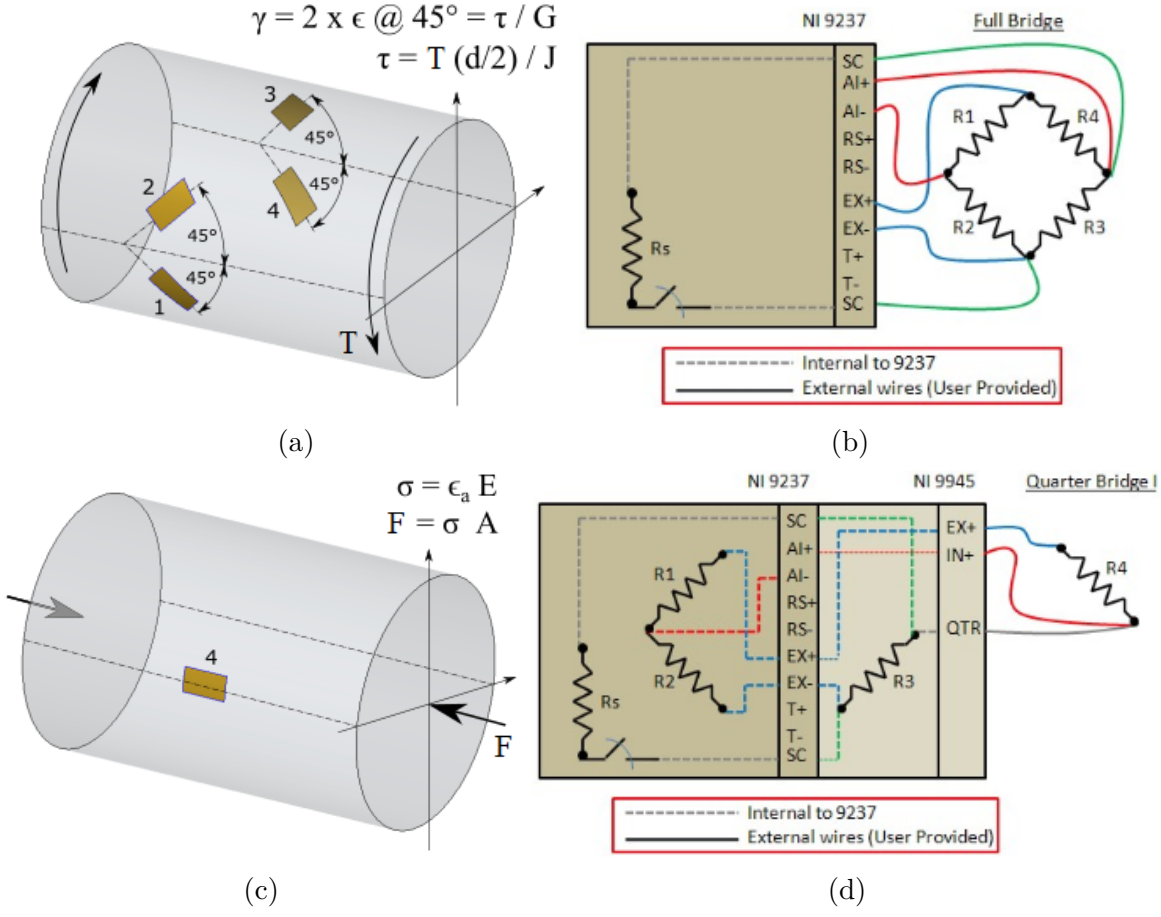


Fig. 4.27 Strain gauges configuration to measure torque and axial load: (a) Connection of the strain gauges to a cylindrical component to measure torque; (b) Connection of four strain gauges to a Wheatstone bridge in a full bridge configuration (Adapted from [152]); (c) Connection of a strain gauge to a cylindrical component to measure axial load; (d) Connection of one strain gauge to a Wheatstone bridge in a quarter bridge configuration (Adapted from [152]).

Finally, the output signal of the strain gauges was pre-processed with the same Savitzky-Golay filter already employed for lasers and LVTDs to have comparable output. This approach allowed to remove the baseline electrical noise from the signal, while preserving the process related features.

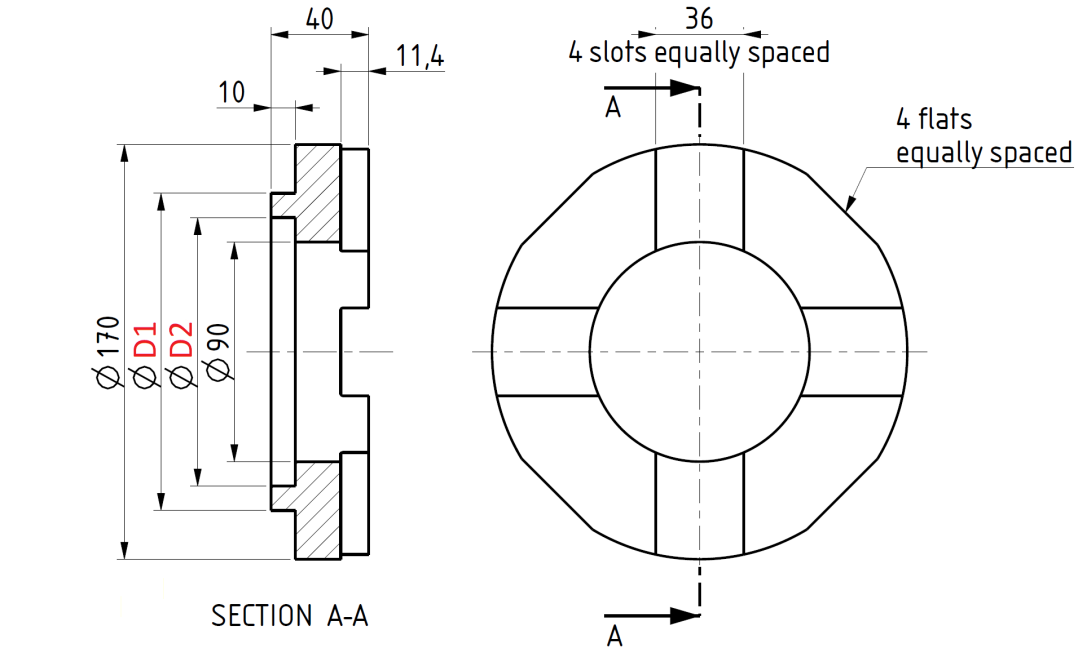
4.5 Workpiece design and materials used for this study

The geometry and the material of the workpieces to be welded with the monitoring system represented another aspect of primary importance in the approach developed. In fact, differently from a conventional weld where all the focus is put on the quality of the junction, this research aimed to characterise the system response to certain process conditions. For this reason, the optimal workpiece for the application would have been inexpensive and with a geometry flexible enough to allow the machine to run in a wide range of working conditions.

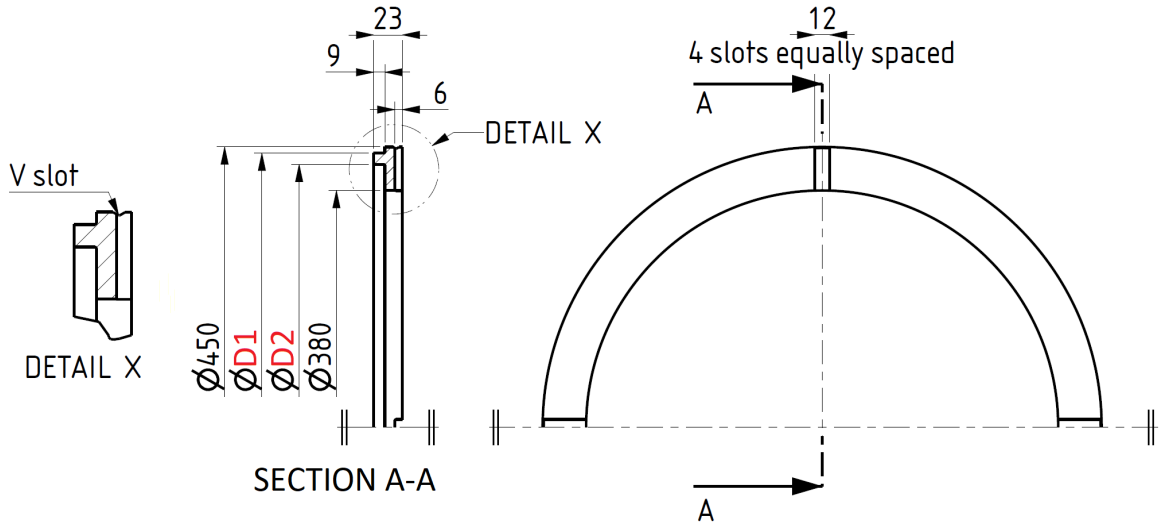
The first aspect analysed was the material. While nowadays IFW is commonly used to weld high strength-high temperature materials like Nickel-based superalloys, these are extremely expensive and complex to machine. For this reason, alternative materials, cheaper and easier to manufacture, were analysed. Initially, plastics were considered to have the machine run under the desired process conditions but without having an actual weld, however, the few types capable to withstand the high pressure-tangential speed combinations expected during a test were extremely expensive, with little availability and limited wear resistance, making them withstand the process conditions just for few seconds (Appendix B). Finally, EN9 (070m55) carbon steel was selected because of its relative low cost, wide availability, ease of machining and known behaviour, a

factor particularly useful to determine easily the process parameters and the workpiece geometry.

The second consideration regarded the geometry of the workpieces. Fig. 4.28 shows the CAD models of the workpieces used in the two monitoring systems. A parametric design for the inner and outer diameters (D1 and D2) of the welding stubs was implemented to have workpieces welding under the desired range of process conditions. In particular, four combinations for the prototype and two for the production system were developed, using the values of diameter in Table 4.4. While both designs present four keyways to engage the keys in the backstops, additional clamping features were added specifically to match the fixturing configuration of the two systems: four flats equally space for the prototype and a V slot around the whole circumference of the workpiece for the production system.



(a)



(b)

Fig. 4.28 CAD drawings and key dimensions for the workpieces used in the two monitoring systems: (a) Workpiece used in the prototype system tested using the MTI-300T machine; (a) Workpiece used in the production system tested using the MTI-2000B machine.

Table 4.4 Diameters (see Fig. 4.28) for the welding stub of the four types of workpieces used in the prototype and the two used in the production system

		D1 [mm]	**D2 [mm]**
Prototype workpiece	Type 1	130	104
	Type 2	130	110
	Type 3	130	118
	Type 4	130	90
Production workpiece	Type 1	328	310
	Type 2	440	422

4.6 Conclusions

This section presented a detailed description of the design and validation of the monitoring systems developed, along with the details of the workpiece design to fit each system. The two systems present a similar setup with custom backstops that fit inside the machine tooling and have the double role of physical support for the instrumentation and fixturing for the workpiece. The instrumentation includes laser displacement sensors and LVDTs to monitor the radial and axial runout, a triaxial accelerometer to study the vibrational behaviour of the system, an encoder to measure the angular speed and acceleration of the headstock and strain gauges to capture the process torque and thrust.

Differently from any existing monitoring system, the solution presented in this chapter allows getting a holistic picture of the phenomena occurring during a weld, providing several complementary measurements that can help in distinguishing effects related to the welding, the machine and the actual interaction between the workpieces in non-idealised conditions. In addition, the design and the instrumentation chosen were optimised to be self-contained and suitable to be employed in an industrial environment without posing a hazard for the operators or the machine. Such a system

combines academic and industrial objectives, being able to analyse the process and the system from a viewpoint never studied before and helping researcher to understand the physical causes behind some phenomena difficult to explain when monitored from the perspective of a single sensor, while providing a tool that can be easily used in industrial environments to periodically characterise IFW systems with minimal downtime of the machine.

Two monitoring systems were developed to fit two inertia welders, a prototype used with the MTI-300T machine and a validation system for the MTI-2000B machine. The second system was required to validate the concepts proposed with the prototype and to expand the approach to a means of assessing the equivalency of similar systems. On one hand, this has academic importance because allows assessing if the phenomena monitored were connected only to a specific setup, rather than characteristic of the process, on the other hand, it is a technique that can be used in an industrial environment to assess if different machines behave sufficiently similarly to be considered interchangeable.

Chapter 5

A novel approach for the characterisation of the phenomena in IFW

In this chapter, the results of a series of rundown tests and welds completed on the MTI-300T and the MTI-2000B machines equipped with the two monitoring systems will be presented. On one side, these will prove the suitability of the approach developed in characterising the system, which, exploiting the multitude of complementary parameters monitored simultaneously, can help obtain a holistic picture of the phenomena occurring during the weld and giving them a physical interpretation. On the other, comparing the results of the two systems, it is possible to assess which phenomenon is connected to the process rather than to a specific setup.

5.1 Methodology

The set of welds was designed using a 2^k factorial DOE with three factors: initial angular velocity, flywheel inertia and axial force. Table 5.2 summarises the configuration

for each test, where the high values are indicated by "+1", the low ones by "-1" and the central points by "0"; the three central points were added to study the linearity and the repeatability of the system response. The thickness (T_w) and mean radius (r_{mw}) of the welding section, shown in Fig. 5.1, was selected to have sufficient total upset for the process parameters chosen, Table 5.1 summarises the numerical values for the different welds. The length of the welding stub was chosen as short as possible to minimise the misalignment between the two workpieces, while ensuring a safety margin on the predicted upset. The input parameters for the rundown tests were chosen to guarantee approximately the same initial energy between them, with the small difference (approximately 0.4%) caused by the discrete values of inertia for the flywheels and use of integer values for the initial angular speed.

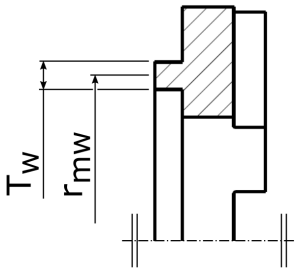


Fig. 5.1 Section view of the workpiece with detail of the wall thickness (T_w) and mean radius (r_{mw}) of the welding section

Table 5.1 Wall thickness (T_w) and mean radius (r_{mw}) for the eleven welds

Test No.	W1	W2	W3	W4	W5	W6	W7	W8	W9	W10	W11
T_w [mm]	20	13	13	10	6	13	20	10	13	13	6
r_{mw} [mm]	55	58.5	58.5	60	62	58.5	55	60	58.5	58.5	62

Table 5.2 DOE parameters matrix for the eleven welds and the two rundown tests

	Steel welds											**Rundown**	
Test No.	W1	W2	W3	W4	W5	W6	W7	W8	W9	W10	W11	RD1	RD2
ω_0	+1	0	-1	+1	0	+1	+1	-1	0	0	0	0	+1
I	+1	0	+1	-1	-1	-1	+1	+1	0	0	-1	+1	-1
P	-1	0	+1	-1	-1	+1	+1	-1	0	0	+1	-	-

Where the values high (+1) and low (-1) and the central points (0) are as follow:

- ω_0: +1=275RPM; -1=125RPM; 0=165RPM
- I: +1=97,63lb-ft2; -1=24,306lb-ft2; 0=60,957lb-ft2
- P: +1=700psi; -1=250psi; 0=500psi

5.2 Results and discussion

The rundown tests and the welds completed successfully, confirming the suitability of the fixturing setup for constraining the workpieces and extracting the experimental data. For this reason, only the results of a few cases will be presented to explain the phenomena common among tests without adding redundant information. All the data were normalised to unity except for the runout values which were normalised against the shape error of the backstops, sum of circularity and concentricity errors, to make the magnitude of effective oscillation easier to quantify. The normalisation of the output variables is particularly important to obtain results that are generic and not related to the input parameters used for a specific test.

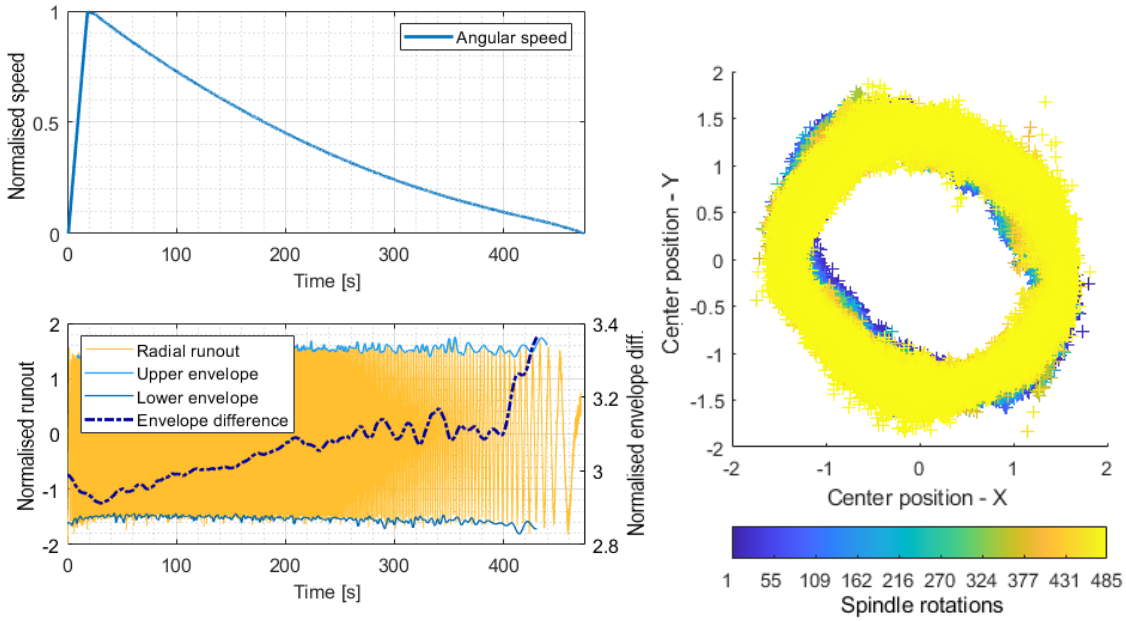
5.2.1 Rundown tests

During a rundown test, the two workpieces do not interact, which proves particularly important to characterise the behaviour of the spindle when no external loads are applied. Bringing the fixture side close to the spindle but without an actual contact of

the two, it was possible to measure the spindle radial and axial runout with lasers and LVDTs respectively.

Fig. 5.2a compares the radial runout with the angular speed of the spindle. It can be seen that the two lasers measured a sinusoidal signal with an amplitude almost double the geometrical error in the rig. Constructing the upper and lower envelope for the laser output as a spline that connects the peaks and minima of each oscillation and computing their difference, i.e. the oscillation amplitude, it is possible to observe how this presents a minimum at the highest speed while it increases for decreasing speed. Simplifying the spindle to a Jeffcott rotor [153], it is known that the radial oscillation of the system should increase for increasing speed, having a maximum at the critical speed [100]. Since the machine is showing the opposite behaviour, it is possible to exclude major rotordynamics influences. The oscillation amplitude, without the geometrical error of the rig, can be associated to the orbiting of the spindle that tends to spin off-axis, while the small differences at different speed can be attributed to the dynamic support conditions of the radial bearings.

Considering that the circularity error of the spindle backup was one order of magnitude smaller than the runout measured with the lasers, it was possible to simplify a section of the backup with a circle of known radius and use the readings of the two lasers to compute the position of the circle centre at each time step. This approach recalls the concept of Poicaré maps used in the study of dynamic systems. Fig. 5.2b shows the evolution of the spindle centre throughout the rundown where each rotation of the spindle corresponds to a different colour in the plot, dark blue the first rotation and yellow the last one. The results show how the spindle tends to follow a circular path without diverging towards any preferential directions, reinforcing the assumption that the runout should be attributed to the orbiting of the shaft.



(a) (b)

Fig. 5.2 Behaviour of the machine in the radial direction (radial runout) during a rundown test: (a) Angular speed and radial runout; (b) Spindle centre position throughout the rundown test calculated from the reading of the two lasers

The behaviour of the system in the axial direction was analogous to the one in the radial direction, with the three LVDTs that measured a sinusoidal signal 3.75 times in magnitude than the shape error of the rig. Fig. 5.3 shows the frequency spectrum for the output of one of the lasers and one of the LVDTs. The frequency domain is commonly studied with Fourier spectral analysis, this approach, however, requires the system to be linear and the data strictly periodic or stationary [154, 155], making it not suitable for IFW, where the speed of the process changes throughout the weld and the system is non-linear. For this reason, an implementation of the generalized Morse wavelets was used. This family of wavelets are suitable for studying signals with amplitude and frequency varying in time and have parameters, such as the symmetry and the time-bandwidth that can be optimised for the specific application [156, 157]; in this study a symmetry parameter equal to 3 (symmetric wavelet) and a time-bandwidth

equal to 60 were found to provide a good compromise between time and frequency resolution. Comparing both signals to the angular speed of the spindle, it is possible to observe a good match, which suggests how both components can be attributed to the rigid motion of the spindle with coupled motion in the axial and radial directions.

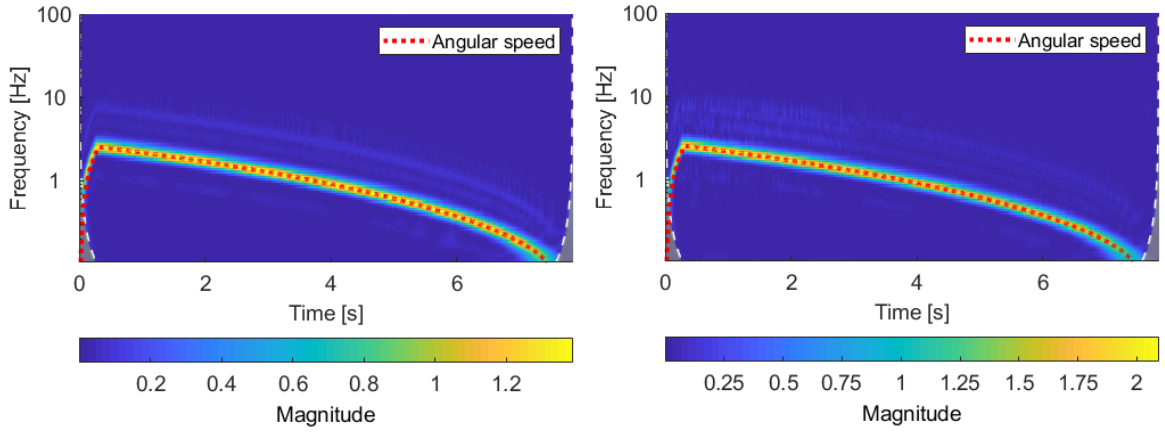


Fig. 5.3 Comparison between the scalograms of laser (a) and LVDT (b) with the angular speed of the spindle (dashed line)

5.2.2 Welding tests

Zaeh and Poehler [74] observed that two impulses should be expected during a weld, one at the initial impact and a second one at the final flywheel deceleration, and used the dynamic equations for oscillators to describe the system. This approach was extended to develop a model that took into consideration the key elements of the inertia welder, Fig. 5.4, including the change in stiffness of the weld due to temperature evolution, the effect of dry friction, the contribution of damping and stiffness related to the IFW machine. The proposed model was experimentally validated against the output of LVDTs, strain gauges and encoder. This approach, in which several complementary sensors monitor at the same time a common aspect of the weld, has the key advantage of highlighting more clearly the underlying physical phenomena.

Before a weld, the fixture side is brought close to the spindle side. When the flywheel has reached the desired initial speed, the pressure in the ram is raised and the two parts collide to start the welding. Although oscillations due to the initial axial impact were previously reported [74], significant effects can arise in the IFW process depending on how this first contact occurs. Based on the system conditions, the impact can be classified as inelastic (i.e. the workpieces stick together after the collision) or elastic (i.e. the impacting workpiece bounce back). The desired interaction is characterised by an inelastic impact and a small impulse to reduce the vibrations and have repeatable contact conditions between the two parts. Fig. 5.5 depicts the upset, measured with the LVDTs, against the axial load and torque, measured by the strain gauges. It is possible to note a spike at the initial contact between the two parts that can be traced to a bounce of the two parts before they acquire a stable contact and start the welding process.

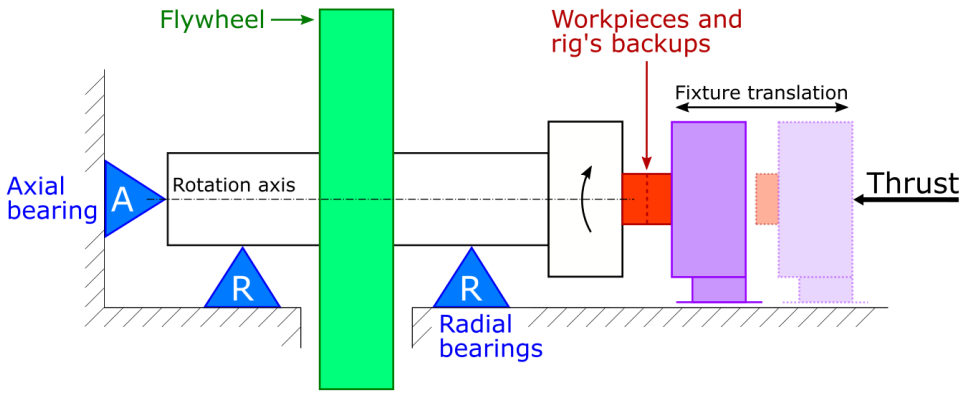


Fig. 5.4 Schematic of the machine for IFW in term of key dynamic elements

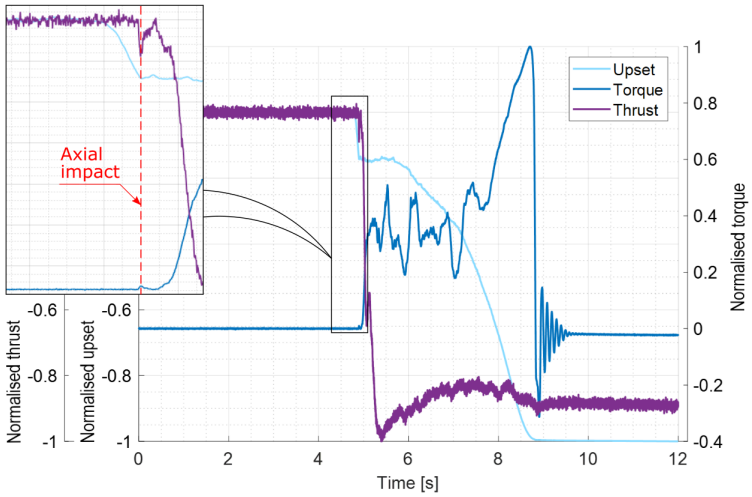


Fig. 5.5 Comparison among thrust, torque and upset with emphasis on the axial impact at the initial contact of the workpieces

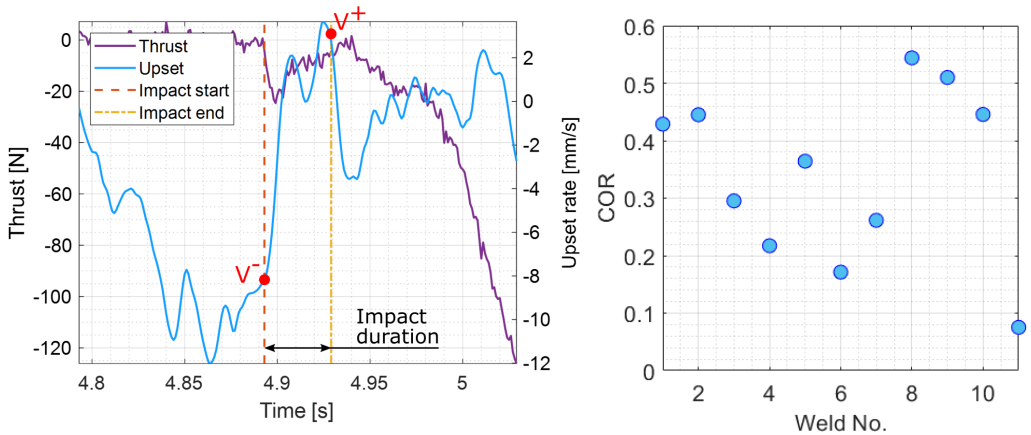
The usual approaches to model colliding bodies can be classified based on the duration of impact as either instantaneous or with a finite duration. In the first case, the analysis is divided into two phases, before and after the impact, related by the coefficient of restitution (COR) which takes into account the energy dissipated in the collision [158, 159]. In its most popular formulation, it is defined as the ratio between the approach speed immediately after (V^+) and before (V^-) the impact ($\text{COR} = V^+/V^-$); assuming COR=1 for a perfectly elastic collision and COR=0 for a perfectly inelastic one [158]. When the duration of the impact cannot be considered as instantaneous, the collision contact forces must be included in the analysis.

Wanting to exploit the simplicity of the COR concept and assuming that the local deformations at the point of contact were negligible, the impact was modelled as instantaneous. The approach speed was calculated by differentiating the fixture displacement measured with the LVDTs over the impact period (upset rate) determined from the axial gauges, as represented in Fig. 5.6a. Fig. 5.6b shows the COR for the eleven welds, it can be seen that all the cases have a COR greater than zero even if to a different degree. In addition, the three central points (welds 2, 9 and 10) show a similar

value of the COR. Recalling that the COR is a measure of energy dissipation during the impact and considering that welds with similar geometry and input parameters have similar values of COR, it is possible to characterise the system and act to minimise the bounce. Simplifying the system as in Fig. 5.7 and disregarding the sliding friction force of the fixture, it is possible to express the equation of motion for the collision interval in the form:

$$m \cdot \ddot{x} + c \cdot \dot{x} + k \cdot x = F + P \tag{5.1}$$

where m is the mass of the system, c is the viscous damping, k the stiffness, P the thrust exerted by the ram and F the reaction load caused by the impact. Several formulations exist for F, from simple ones which make use of a Kelvin-Voigt viscoelastic approach to more complex models based on the Hertzian contact theory [158, 159]. Modulating the piston thrust and tuning the stiffness and the damping of the machine backup, it is possible to optimise the system to avoid the bouncing at the initial impact.



(a) (b)

Fig. 5.6 Calculation of the coefficient of restitution (COR) for the welds: (a) Comparison between thrust and upset rate from which it is possible to compute the impact duration and the COR (ratio between the upset the rate at "impacts end" and "impact start"); (b) Comparison of the values of COR for the eleven welds.

The acceleration peak at the end of the weld can be attributed to the flywheel deceleration and described as a torsional oscillator [74]. While oscillations during the sudden deceleration of the flywheel in the consolidation phase can be expected, the

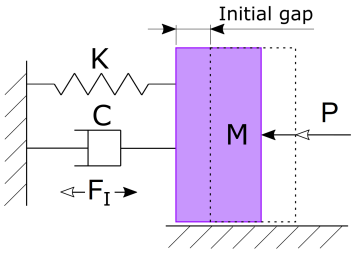


Fig. 5.7 Analytical schematic in the axial direction at the initial impact of the two workpieces using a mass-spring-damper approximation. When the piston is activated, the fixture closes the initial gap and collide against the spindle which reacts as a spring-damper system.

unfiltered output of the torsional gauges showed in Fig. 5.8 displays an oscillatory behaviour also at the end of the second torque peak, when the flywheel approaches 0 RPM. This can be explained with a spring back reaction to the flywheel rotation which ends up oscillating back and forth before the energy is completely dissipated through viscous damping or friction. The system was described with the differential equation of a torsional oscillator:

$$I \cdot \ddot{\theta} + c \cdot \dot{\theta} + k \cdot \theta = T \cdot sgn(\dot{\theta}) \tag{5.2}$$

where I is the inertia, mainly localised in the flywheel and the spindle tooling, c is the viscous damping, the sum of the internal damping in the system elements and the bearings, k is the system stiffness, with the weld and the rig backup representing the most compliant elements and T the effect of dry friction which can occur if elements in relative motion slide in presence of inadequate lubrication. The dry friction, however, makes the equation non-continuous due to the presence of the sign function and an iterative approach is required to make the friction force always acting in opposite direction to the speed [160, 161].

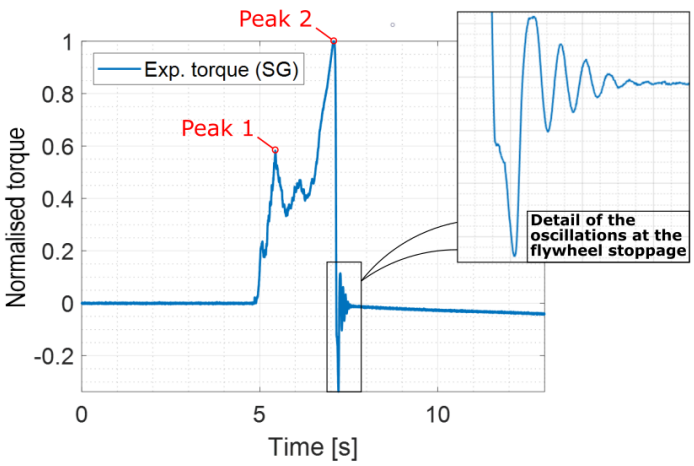


Fig. 5.8 Unfiltered torque signal (strain gauges) with the two peaks at the conditioning (peak 1) and consolidation phases (peak 2) highlighted. An oscillations spike can be clearly observed at the flywheel stoppage.

While the inertia was known with certainty, the damping, stiffness and friction force presented a level of uncertainty, therefore, they were computed numerically minimising the error between the experimental flywheel acceleration, calculated as the ratio of the torque and moment of inertia, and the one from the torsional oscillator. When dealing with optimisation algorithms, the choice of the initial parameters is always particularly important, while for the damping coefficient and the friction force the critical damping for the system ($c_{cr} = 2\sqrt{I \cdot k}$ [162]) and 0 Nm were assumed respectively, select a value for the stiffness was more complex. Zaeh and Poehler [74] considered a constant stiffness with room temperature material properties, which represents a strong simplification due to the rapid thermal evolution at the weld interface typical of IFW. To get a more realistic initial guess for the stiffness, the cooling of the weld was studied with the commercial FE package Abaqus assuming temperature-dependent material properties [163] and using the model schematically shown in Fig. 5.9. The simulation was split into two intervals, an initial heating stage to simulate the welding, for which the heat input was computed from the angular deceleration of the flywheel, disregarding the energy losses [52], and a second one in which the welded assembly was cooled with

a known torque (T_k) applied. The stiffness of the welded assembly (k_w) was then calculated from the angular displacement (θ) obtained from the model ($k_w = T_k/\theta$). The sum of the stiffness of the backup and weld, considered as elements in series, was used as the initial guess. If the proposed model describes correctly the system, only inertia, damping and stiffness should affect its response, so the comparison of two cases with similar initial speed, inertia and wall thickness but different thrust is presented.

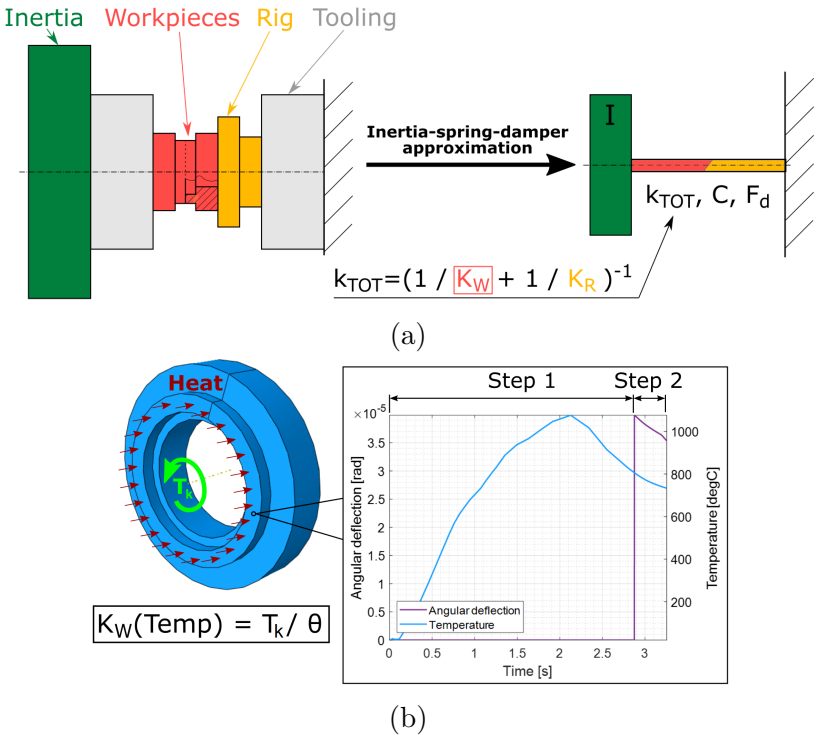


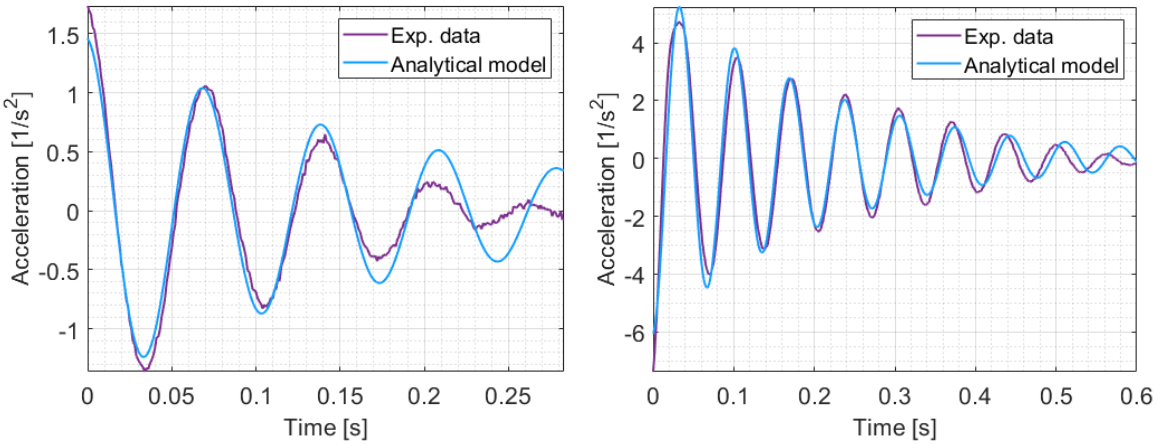
Fig. 5.9 Model for the torsional oscillations using an inertia-spring-damper approximation and a temperature-dependent stiffness coefficient: (a) Analytical model using an inertia-spring-damper approximation. The stiffness coefficient is given by the sum of the contribution from the weld, temperature-dependent, and the backup, constant; (b) Detail of the FE model developed to obtain a temperature-dependent stiffness coefficient for the workpiece.

Table 5.3 summarises the results of the optimisation for the two cases used as an example. When these values are substituted into the equation of the torsional oscillator, the results shown in Fig. 5.10 are obtained, from which it is possible to

observe a good match with the experimental data. It is worth noting that the different number of cycles for the two cases (weld 5 and weld 11) is caused by the different weld evolution and, consequently, the different initial conditions for the oscillatory stage. The similarity in the values of stiffness, damping and friction force gives an additional confirmation that the system behaved as a torsional oscillator and that the axial load did not have any effect on it. The values of dry friction close to zero suggest that no metal-to-metal occurred and that the bearings were properly lubricated even at very low angular speed.

Table 5.3 Parameters for the analytical model which describes the torsional oscillator

Weld	**Thrust**	**Type**	**k** $\left[\frac{N \cdot m}{rad}\right]$	$\zeta = \frac{\mathbf{c}}{\mathbf{c_{cr}}}$	**T** $[Nm]$
5	Low	Initial guess	$11.2e6$	1	0
		Results	$10.4e6$	$5.6e{-}2$	$1.6e{-}3$
11	High	Initial guess	$10.9e6$	1	0
		Results	$11.4e6$	$5e{-}2$	$0.3e{-}3$



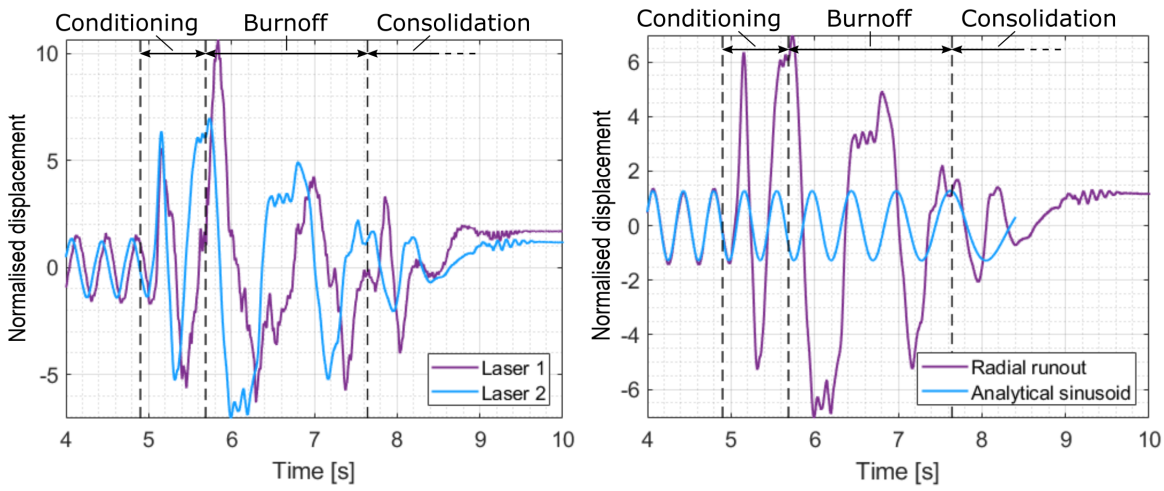
(a) (b)

Fig. 5.10 Comparison between the values of acceleration for the analytical model of a torsional damper and the experimental data: (a) Low thrust case (weld No. 5); (b) High thrust case (weld No. 11).

5.2.2.1 Behaviour of the system during welding

If the choice of a wide range of weld input parameters was necessary to characterise the system response over a large operating range, it caused welds with different total duration and relative duration of the three key phases, conditioning, burn-off and consolidation. For this reason, the central points of the tests matrix were chosen to analyse the behaviour of the system during welding since they present medium total duration, allowing the transition between the three phases and, consequently, the phenomena occurring to be seen clearly.

Repeating the analysis described for the rundown tests during a weld, it was possible to observe how the process loads affect the system. Fig. 5.11a shows the runout measured by the two lasers in two mutually orthogonal directions, X and Y. Before the contact of the two workpieces, the magnitude of oscillation is analogous to the one registered during the rundown tests, between three and four times the geometrical error in the spindle backup, while when the two parts are brought into contact, the runout spikes due to the compliance of the system under the process loads. Finally, when the rotation of the spindle ceases, the signal shows a steady horizontal behaviour caused by the constraining action of the joint that, when cooling down, acquires strength and locks the relative position of spindle and fixture, not allowing the signal to return to zero. During the welding, the upset caused a relative motion between the fixture and the spindle backups and, consequently, an axial translation of the laser; this effect, however, was neglected causing an error several orders of magnitude smaller than the runout measured.

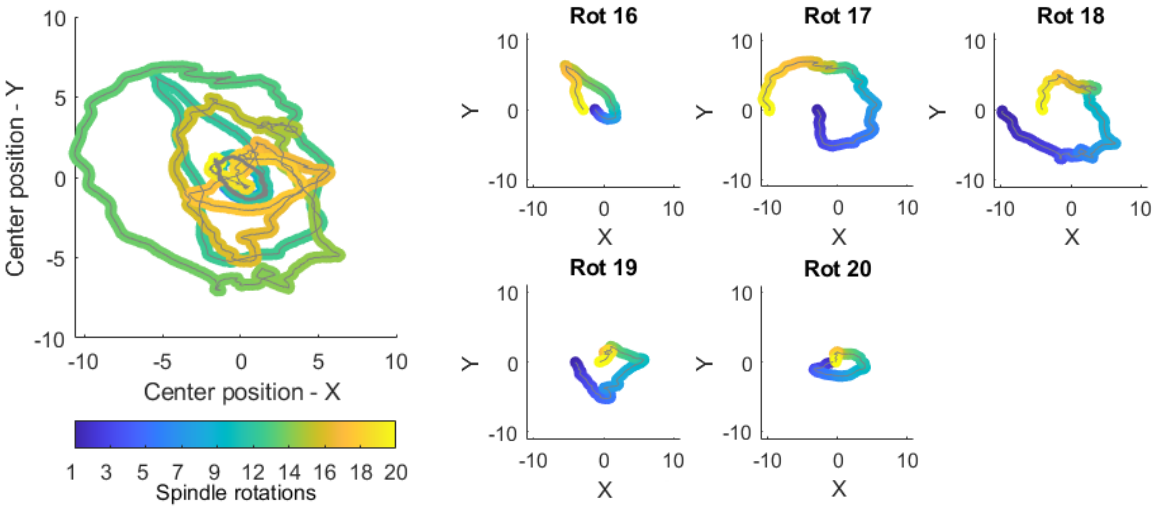


(a) (b)

Fig. 5.11 Radial runout monitored by the lasers during a weld: (a) Comparison between the readings of the two lasers; (b) Comparison between the output of laser 2 and an analytical sinusoid signal generated in phase with the angular speed to study the influence of the weld on the frequency and magnitude of the radial runout.

In Section 5.2.1 it was shown how the runout was in phase with the angular speed and constant in magnitude, to study this condition during welding, the output of one of the lasers was compared with an analytical sinusoidal signal ($y(t) = Y_m \cdot sin(2\pi \int \omega(t)dt + \varphi_0)$) generated in phase with the angular speed of the spindle ($\omega(t)$), magnitude (Y_m) and initial phase (φ_0) computed fitting the runout before part contact. Comparing the analytical and experimental signal shown in Fig. 5.11b, it is possible to observe how, during the weld, not only the magnitude of oscillation changes but also the phase. Fig. 5.12a and Fig. 5.12b show the spindle centre position obtained by combining the signals from the two lasers; in these plots the same convention introduced in Fig. 5.2b is adopted, in which the time progression is represented by different colours, with dark blue which corresponds to the beginning of the interval considered and yellow the end. The comparison of these graphs with the ones in Fig. 5.2b allows a physical interpretation of the runout behaviour, where oscillation spikes correspond to larger and distorted orbits of the spindle while the shift in frequency causes a complex

revolution motion of the spindle with runout orbits out of phase with the angular speed of the spindle. Analysing the evolution of the spindle centre trajectory for the three central point welds, it is possible to assert that this is mainly stochastic, not showing a common pattern. This can be explained considering the multitude of complex different factors that interact during a weld and can affect the runout. Apart from the input parameters and the machine itself, the thermo-mechanical conditions at the interface of the two workpieces affect how they interact and the constraining action that the weld exerts on the radial displacement.



(a) (b)

Fig. 5.12 Spindle centre position calculated from the reading of the two laser sensors: (a) Overall plot including both the initial spindle acceleration without part interaction and the weld; (b) Plots of every single rotation of the spindle during the weld; from these, it is possible to observe orbits of distorted shape and larger magnitude compared to the one during the rundown tests

In contrast to the rundown tests, the output of the LVDTs does not provide a direct measurement of the axial runout, but the superposition of this with the weld upset, as shown in Fig. 5.13a. If a plane is fitted through the three LVDTs, this will have a motion that is a combination of a pure translation, induced by the upset, and a pure rotation, caused by the axial runout. Isolating the translation component of the fitted

plane and subtracting it from the output of the LVDTs, it is possible to obtain a good estimate of the axial runout. Similarly to the analysis performed on the laser signals, the runout was compared to an analytical sinusoidal signal generated in phase with the spindle angular speed to study the influence of the weld on the phase and magnitude of oscillation. As shown in Fig. 5.13, the oscillation magnitude is distorted during the weld, although the signal stays in phase with the spindle. This can be explained considering that the presence of the second workpiece acts as a physical obstacle to additional movements in the axial direction.

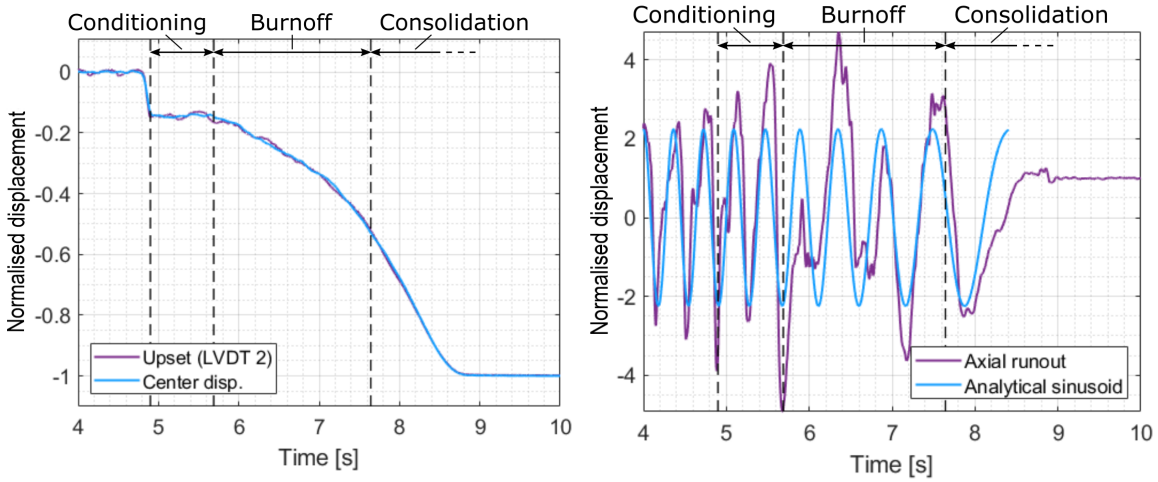


Fig. 5.13 Behaviour of the machine in the axial direction during a weld: (a) Comparison between the output of one of the LVDTs, combination of both upset and axial runout, and the process upset obtained by isolating the translation component from the motion of the fit plane through the three LVDTs; (b) Axial runout during the process compared with an analytical sinusoid signal generated in phase with the angular speed to study the influence of the weld on the frequency and magnitude of the axial runout.

Having observed a runout during the weld, it is reasonable to expect to be able to capture the resultant effects with the strain gauges. The average of the four axial gauges provides a useful indication on the total axial load applied to the weld and can be compared with the theoretical thrust to characterise the piston of the machine; however, when they are considered individually they can give interesting information

on the axisymmetry of the load. Analysing Fig. 5.14, it is possible to observe not only a great variability in the strain monitored by each gauge, but how opposing gauges (SG1-SG3 and SG2-SG4) show values similar in magnitude but opposed in sign. This behaviour is typical of bending stresses and, since thrust and torque are the only loads theoretically occurring in IFW, likely to be associated with the runout. Using the stress obtained from the strain gauges to calculate an equivalent radial load that would induce the same radial deflection and dividing it by the deflection itself, it was possible to obtain an equivalent radial stiffness of the machine, useful not only to characterise the system but also to speculate about which elements had the greatest contributions.

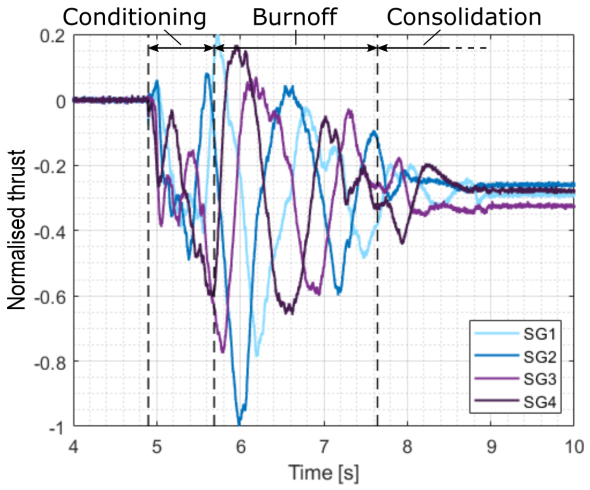


Fig. 5.14 Comparison of the axial load measured by the four axial gauges

To achieve this, the system was simplified with the portion of the rig sticking out from the machine collet and the workpiece, as shown in Fig. 5.15. Disregarding the deformation in the welding stub, the neck of the rig is the major source of compliance in the system, for this reason, an analytical model was developed in which a cantilever beam composed of two parts, one deformable of length l_1 and one rigid of length l_2, with an external vertical load at the tip. For simplicity only the strain gauges in position 1-3 were considered. Computing the equivalent bending stress (σ) from the

stresses in position 1 (σ_{P1}) and 3 (σ_{P3}) it was possible to compute the equivalent load (F):

$$\sigma = \frac{\sigma_{P1} - \sigma_{P3}}{2} \tag{5.3}$$

$$F = \frac{\sigma \cdot W}{l_1 + l_2} \tag{5.4}$$

where W is the section modulus.

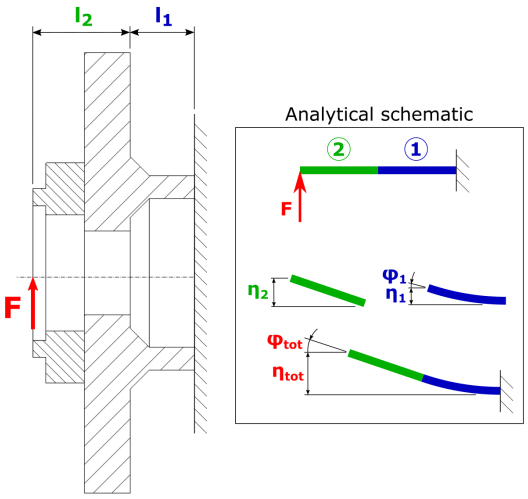


Fig. 5.15 Analytical model of the fixture side backup in which the influence coefficients have been used to compute the deflection caused by the experimental radial load derived by the axial gauges

If radial loads were generated during the process, it is possible to expect also deflection in the sticking out portion of the backups. This factor and the orbiting of the spindle needed to be removed from the laser runout measurements to obtain the effective deflection of the spindle caused by the interaction of the spindle and fixture during the weld.

The deflection of the sticking out portion of the backups was approximated just with the deflection in the neck of the fixture side backup which represents the element with the lowest stiffness. For this reason, the same model described in Fig. 5.15 was adopted and the radial displacement obtained using the influence coefficients calculated

with the force method [164] adding the effect of translation (δ) and the rotation (φ) in each of the two portions of beam:

$$\delta_1 = \frac{(F \cdot l_2) \cdot l_1^2}{2E \cdot J} + \frac{F \cdot l_1^3}{3E \cdot J} + \chi \frac{F \cdot l_1}{A \cdot G} \tag{5.5}$$

$$\varphi_1 = \frac{(F \cdot l_2) \cdot l_1}{E \cdot J} + \frac{F \cdot l_1^2}{2E \cdot J} \tag{5.6}$$

$$\delta_{tot} = \delta_1 + \delta_2 = \delta_1 + \varphi_1 \cdot l_2 \tag{5.7}$$

where E is the Young's modulus, J the second moment of area, G the shear modulus and χ a shear factor depending on the beam shape (10/9 for circular shape). It is important to note that the component connected to shear ($\chi \frac{F \cdot l_1}{A \cdot G}$) became dominant due to the shortness of the neck when compared to its diameter. The analytical values were compared with the numerical results (FE) of the same model showing a root mean square error of 0.75%. The effective deflection of the spindle connected to the interaction of the spindle and fixture during the weld was calculated subtracting the deflection in the fixture side backup just described and the orbiting of the spindle shaft approximated with the analytical sinusoidal model previously introduced (Fig. 5.11b) to the experimental runout in the vertical direction, obtained by interpolating the reading of the two lasers, as shown in Fig. 5.16a. Considering the oscillating behaviour of the actual spindle deflection and the equivalent radial load plotted in Fig. 5.16b, the amplitude of the two was estimated as difference of upper and lower envelope, dashed line and dotted respectively. The ratio between the amplitude of the actual spindle deflection and the equivalent radial load gives the equivalent radial stiffness of the system shown in Fig. 5.16c, from which values in the order of 10^8 N/m can be observed. This stiffness matches that normally reported for radial bearings [165, 166] which, consequently, can be assumed as the key element in the system compliance.

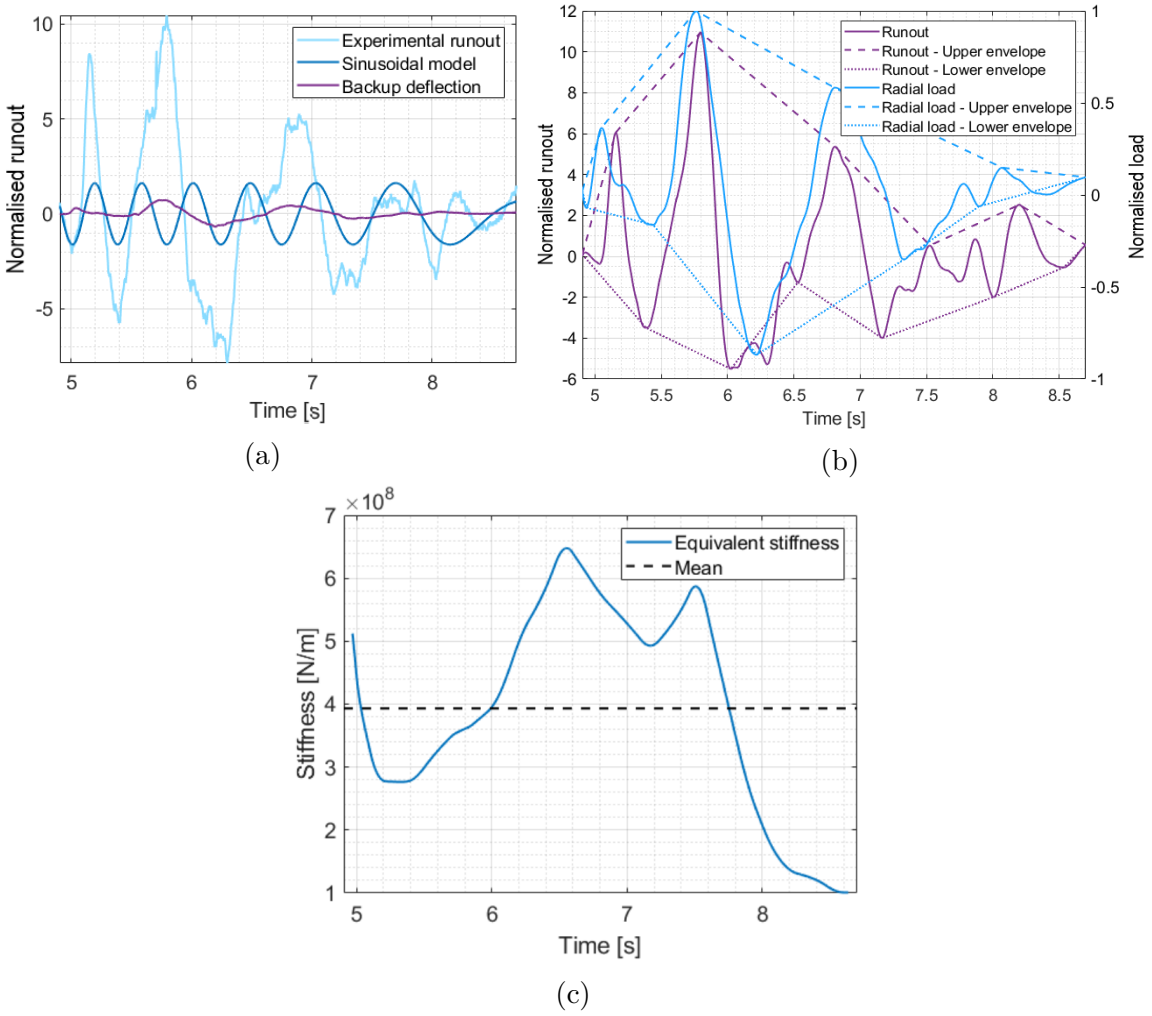


Fig. 5.16 Steps of the algorithm to compute an equivalent radial stiffness of the machine: (a) Step 1: Removing backup's deflection and spindle orbiting (sinusoid model) from the exp. runout; (b) Step 2: Computing the amplitude of effective runout and equivalent radial load. Given the oscillatory nature of the two signals, the respective envelopes have been calculated to give an estimate of the amplitude; (c) Step 3: Computing the equivalent spindle's stiffness from the amplitude (envelope) of the effective runout and equivalent radial load. The mean of the equivalent stiffness, plotted in dashed line, has been used as a representative parameter to be compared with the typical values of stiffness for bearings.

5.2.3 Conclusions

Considering the outcomes of the study on the MTI-300T machine equipped with the prototype monitoring system, the following conclusions can be drawn:

- The vibrational analysis of the system showed that the impact at part contact and the torsional oscillations when the spindle approaches zero rpm are problematic events that can reduce the control of the welding process and cause additional stress on the weld. Two dynamic models were developed to describe these phenomena, showing how modulating the piston pressure and tuning the stiffness and damping of the tooling it is possible to reduce the initial axial rebound; while the flywheel inertia, torsional stiffness of the weld at the flywheel stopping, viscous damping in the bearings and process duration control the final torsional oscillations;

- Due to the fabrication and assembly tolerances and the compliance of the supporting elements, the spindle of the machine is likely to spin with a certain runout. The monitoring system confirmed this and showed a constant runout 3.75 times bigger in magnitude than the shape error in the backstops during the rundown tests. During the welds, the amplitude of the runout shows spikes in magnitude up to 15 times the shape error in the backstops and phase alterations, corresponding to irregular orbits of the spindle. This can be explained with the interaction of the two workpieces under the thrust considering the compliance of the supports;

- The increase in runout when the two parts come into contact can be explained considering compliant supports in the spindle structure. Using a novel algorithm developed to estimate the radial stiffness of the machine, a value in the order of $10^8 N/m$ was obtained, according to which the bearings that support the spindle can be considered the critical elements for the compliance into the system;

- Comparing the behaviour of the thrust measured with the axial gauges and the runout, it is possible to notice larger oscillations during the conditioning and burnoff phases. This can be explained by the constraining effect provided by the weld cooling down and gaining strength during the consolidation phase.

5.3 Assessment of the observation on a similar machine

5.3.1 Methodology

To confirm the observations from the prototype, the validation monitoring system was used to study a set of rundown tests and welds on the MTI-2000B machine. Despite a large number of tests being accomplished with this system, all showed similar behaviour, for this reason only the results of a limited number of them will be presented. Table 5.4 and Table 5.5 summarise the process parameters for the rundown tests and the welds respectively. As it can be observed in Table 5.4, the rundown tests present three different speed ranges ($\omega_0 \rightarrow \omega_{\text{end}}$), this is a common approach for large machines equipped with high inertia flywheels, in which a single rundown test from a high initial angular speed would require a long time due to the high initial kinetic energy of the spindle; splitting the test over multiple steps at different speed range allows the characterisation over a large range of speed while reducing the test time.

Table 5.4 Process parameters for the rundown tests discussed (ω_0: Initial angular speed; ω_{end}: Final angular speed; I: Inertia)

Test No.	R1	R2	R3
ω_0 [RPM]	295	180	85
ω_{end} [RPM]	200	120	23.5
I [lb-ft2]	79783	79783	79783

Table 5.5 Process parameters for the two welds discussed (ω_0: Initial angular speed; I: Inertia; P: Ram pressure; T_w: Welding section thickness)

Test No.	W1	W2
ω_0 [RPM]	82	117.2
I [lb-ft2]	579783	329783
P [psi]	550	600
T_w [mm]	10	10

5.3.2 Rundown tests

The results from this second system confirmed the periodic oscillations associated with the rotation of the spindle observed with the prototype. Fig. 5.17 shows the angular and radial runout measured with the lasers and the LVDTs respectively against the angular speed of the spindle, in which the values of runout were normalised against the geometrical errors in the monitoring system detailed in chapter 4 and the resulting values were scaled to compensate for the difference in size between the prototype and validation system, to have comparable values. The MTI-2000B showed values of runout in both radial and axial directions smaller compared to the MTI-300T, result expected considering the extremely tight tolerances required on a production system that manufactures aerospace components. Combining the reading of the two lasers, then, it was possible to obtain the position of the spindle centre. As shown in Fig. 5.18, this described approximately circular orbits, a result that confirms what observed with

the prototype and that can be connected to the combination of geometrical errors in the elements of the headstock and the plays inside components such as bearings. This observation is confirmed by the scalograms in Fig. 5.19 obtained with the same implementation of the continuous wavelet transform described in section 5.2.1, which compare the frequency content of the runout over time against the angular speed of the spindle. In fact, observing that the majority of the frequency content for the radial and axial oscillations is in phase with the headstock angular speed (red dotted line), the oscillations are likely to be connected to the orbiting of the spindle rather than to additional effects.

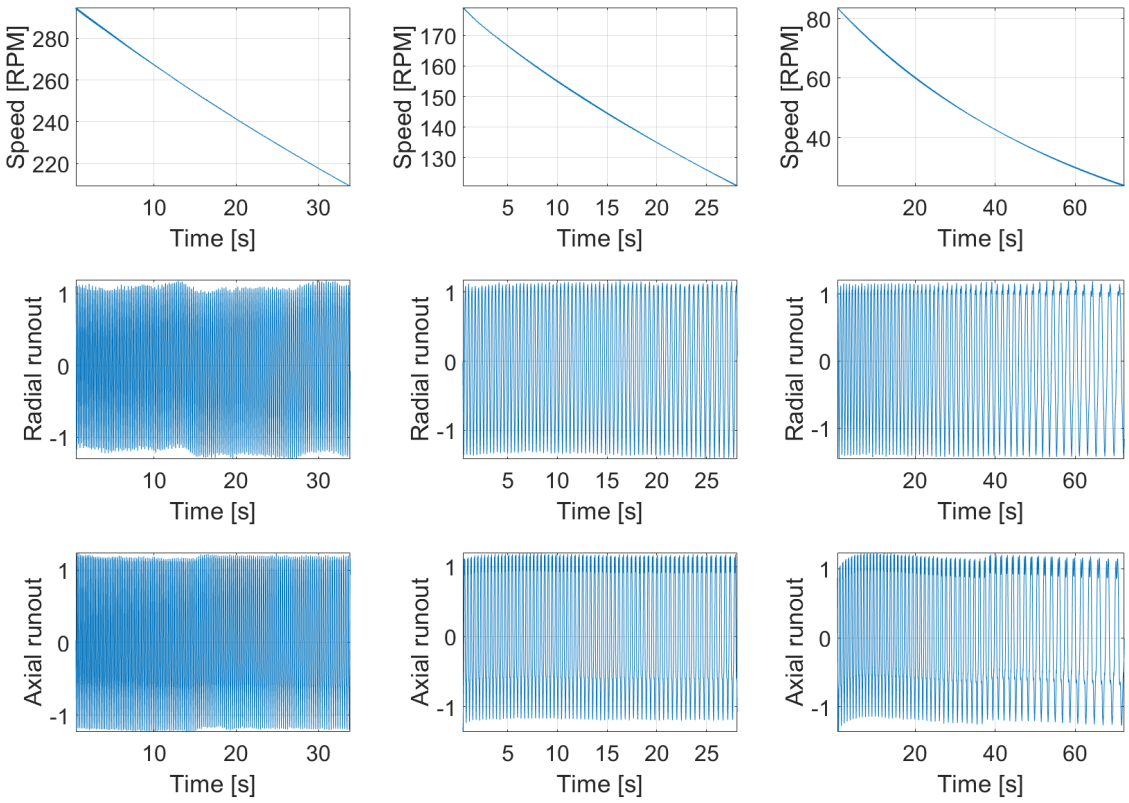


Fig. 5.17 Normalised axial and radial runout of the machine spindle measured with LVDTs and lasers during a rundown test for three different speed ranges: (a) Runout for angular speed between 295 and 200 RPM; (b) Runout for angular speed between 179 and 120 RPM; (c) Runout for angular speed between 84 and 23.5 RPM.

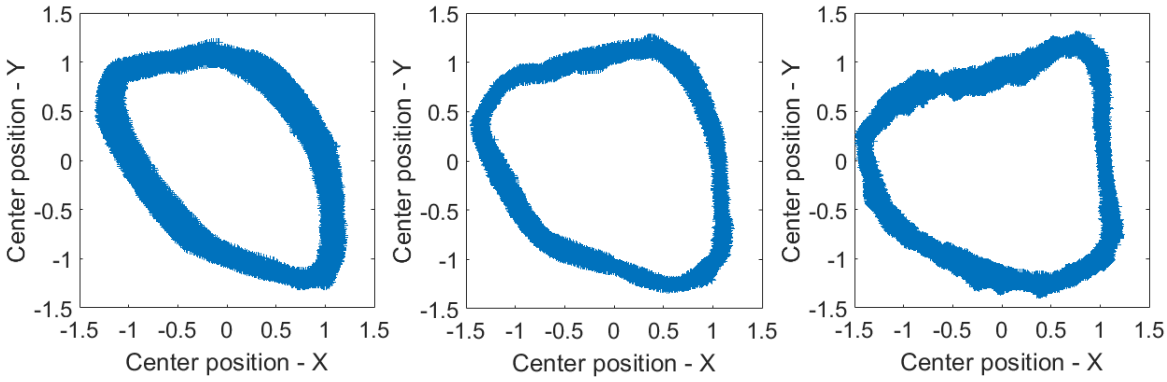


Fig. 5.18 Position of the spindle centre calculated from the readings of the two lasers for the three speed ranges in Fig. 5.17: (a) Angular speed between 295 and 200 RPM; (b) Angular speed between 179 and 120 RPM; (c) Angular speed between 84 and 23.5 RPM.

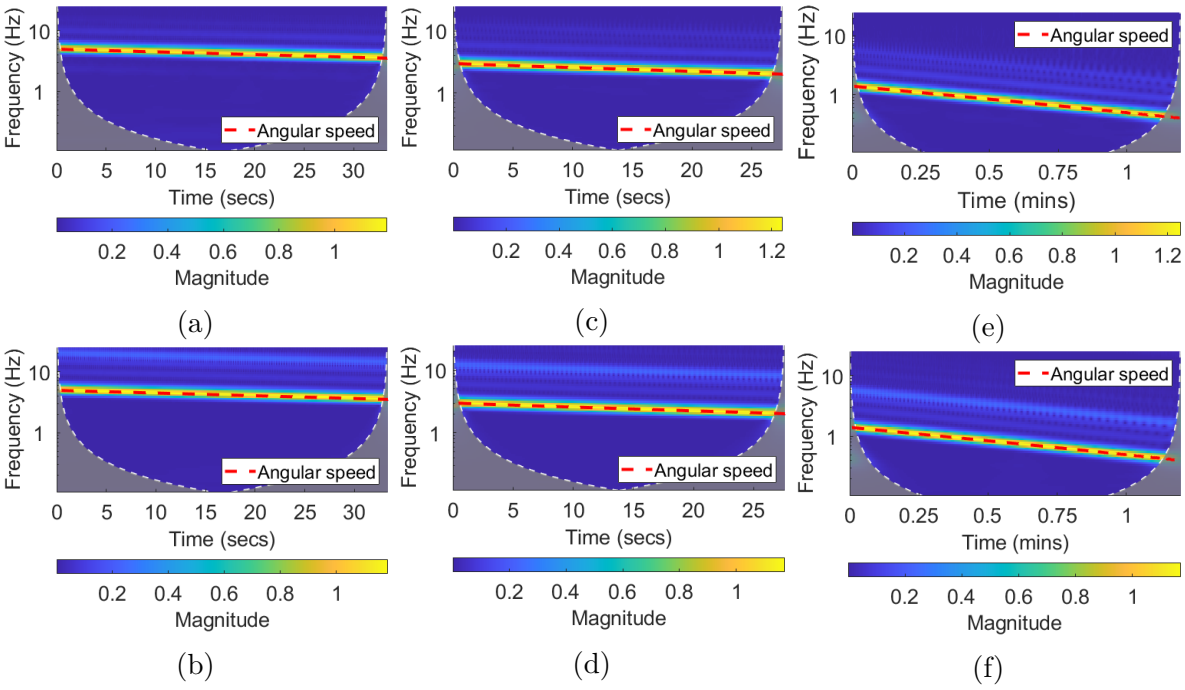


Fig. 5.19 Scalogram (continuous wavelet transform) for the radial and axial runout showed in Fig. 5.17 with superimposed graph of the spindle angular speed: (a) Radial runout (angular speed between 295 and 200 RPM); (b) Axial runout (angular speed between 295 and 200 RPM); (c) Radial runout (angular speed between 179 and 120 RPM); (d) Axial runout (angular speed between 179 and 120 RPM); (e) Radial runout (angular speed between 84 and 23.5 RPM); (f) Axial runout (angular speed between 84 and 23.5 RPM).

5.3.3 Welding tests

Fig. 5.20 shows the thrust obtained averaging the values measured with the four axial gauges (average thrust) and the torque from one of the two full bridges, with the values of thrust and torque normalised against the peak thrust and the peak torque respectively. The familiar behaviour for IFW can be observed with two torque peaks in the conditioning and consolidation phases, while the thrust rapidly ramped up from zero to the welding thrust. Despite reaching a stationary behaviour during the consolidation phase, the thrust showed an initial transitory that culminated with a large fluctuation when the spindle was about to stop rotating. Also for this system, it was possible to observe the effect of the impact at part contact, which induced an initial spike in the thrust and torque signals (A), and the torsional oscillations at the final spindle stoppage, clear from the torque signal (B).

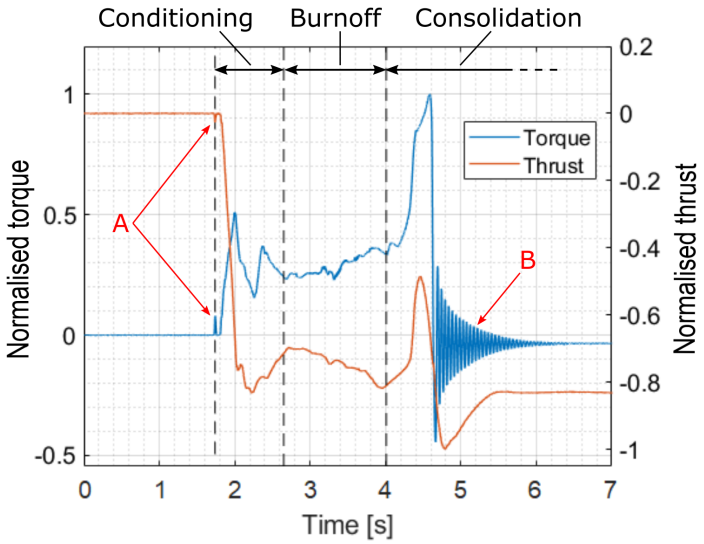


Fig. 5.20 Normalised thrust and torque measured with the monitoring system during a weld in which it is possible to note the impact at part contact (A) and the final flywheel oscillations (B) when the spindle is about to stop rotating

Another aspect of primary importance is the spindle dynamics. It was observed during the rundown tests that the spindle was characterised by a periodic runout in axial and radial directions. Fig. 5.21 shows the radial runout monitored with the two lasers immediately before part contact and during the weld, from which the transition from a periodic behaviour to transient one is clear. Using the same normalisation factor used for the rundown tests, it is possible to observe how not only the magnitude of oscillation is lower compared to that measured on the MTI-300T, but also the distortion of the signal during the welding is less evident, with the oscillations that remain sufficiently in phase with the rotation of the spindle. These results are confirmed by analysing the orbit plots for the spindle centre, obtained combining the readings of the two lasers. In fact, from Fig. 5.22 it is possible to observe orbits of smaller diameter and more regular shape. This difference between MTI-300T and MTI-2000B can be explained with the different setup for the two machines, larger size and, consequently, higher stiffness of the MTI-2000B.

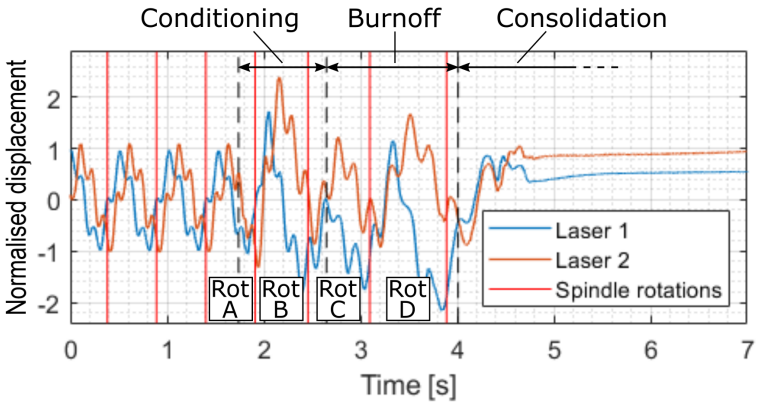
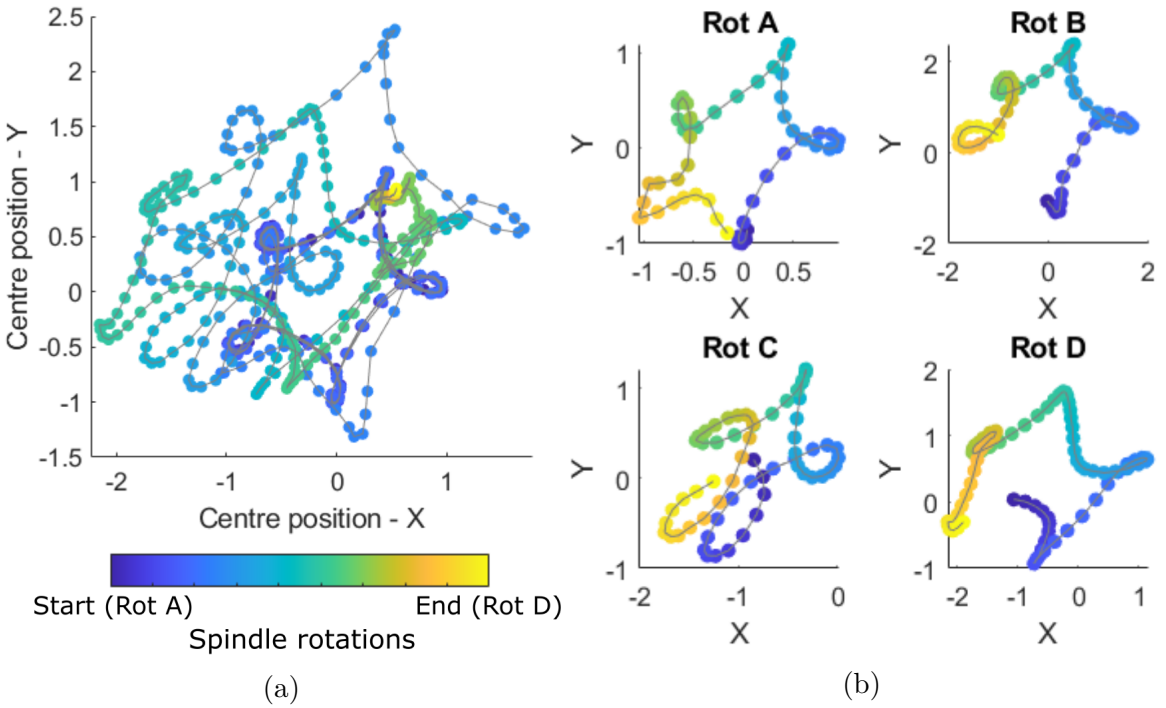


Fig. 5.21 Graph of the radial runout measured by the two lasers in which the duration of a full rotation of the spindle and the three main weld phases are highlighted

The behaviour in the axial direction is shown in Fig. 5.23. Fig. 5.23a compares the output of one LVDT against the overall axial displacement of the tailstock, calculated combining the readings of the three LVDTs, and shows the oscillations at part contact connected to the partially inelastic collision when the two sides of the machine first



(a) (b)

Fig. 5.22 Orbit of the spindle centre during the weld obtained combining the readings of the two lasers shown in Fig. 5.21: (a) Overall plot thought the weld; (b) Orbit plots for each of the last four revolutions shown in Fig. 5.21.

collide. To isolate the axial runout, the overall axial displacement of the tailstock (upset) needed to be removed from the LVDTs output and behaviour in Fig. 5.23b was obtained. Similarly to the radial runout, the periodic oscillations before part contact become more irregular during the weld but less noticeable compared to that observed for the MTI-300T machine.

Finally, Fig. 5.24 shows the thrust measured by each of the four axial gauges. Despite the load oscillations in the conditioning phase, the strain gauges show a more regular behaviour compared to that observed in Fig. 5.14 for the MTI-300T. This difference can be justified by considering the smaller and more regular runout measured during the weld and, consequently, much smaller bending effects in the tailstock backstop where the sensors are installed. However, it is interesting to note how the largest variation between the reading of the four gauges is localised in the

conditioning phase. This factor can be justified with the imperfect contact between the two workpieces in the first stage of welding when asperities can induce a partial contact and, therefore, a pressure gradient in the circumferential direction, which, however, tends to disappear when the surface imperfections are abraded and plastic deformation occurs.

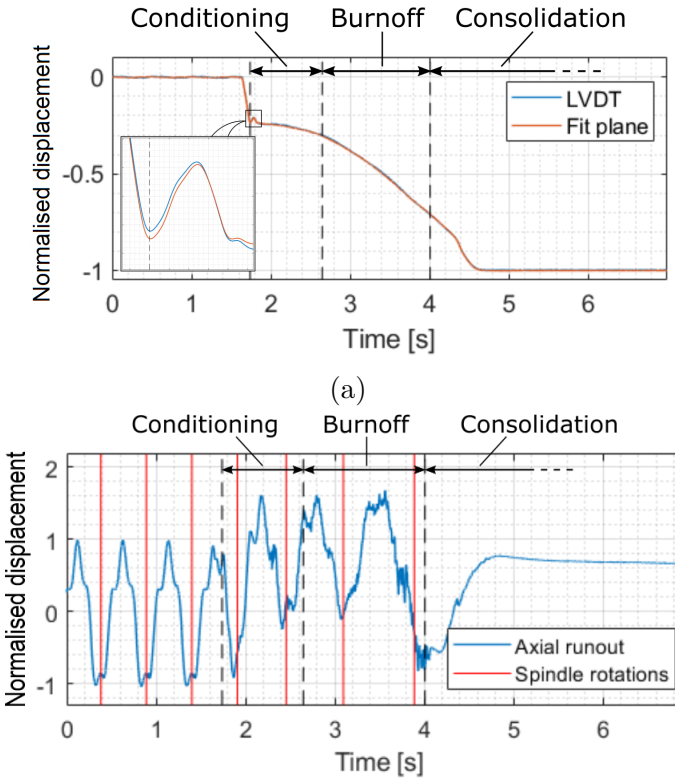


Fig. 5.23 Process upset and axial runout monitored during the welding by the LVDTs: (a) Comparison between the reading of one LVDT and the overall axial displacement of the tailstock calculated combining the readings of the three LVDTs; (b) Axial runout obtained subtracting the output of the LVDT to the overall axial displacement of the tailstock, in which the duration of a full rotation of the spindle and the three main weld phases are highlighted.

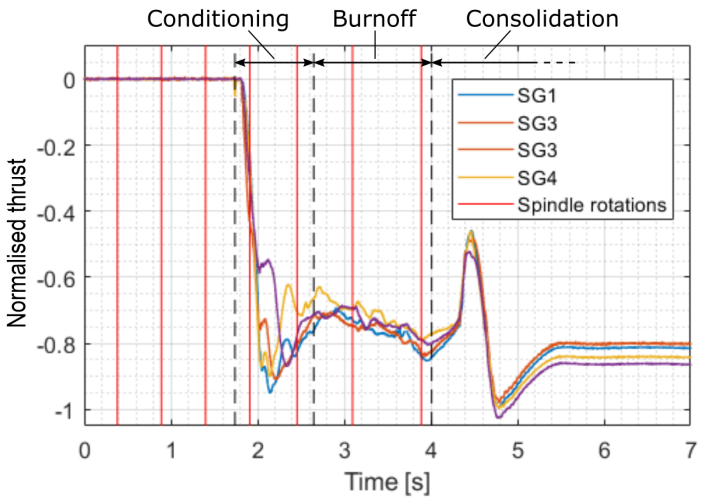


Fig. 5.24 Comparison of the normalised thrust measured by the four axial gauges in which the duration of a full rotation of the spindle and the three main weld phases are highlighted

5.3.4 Conclusions

A set of rundown tests and welds were completed on the MTI-2000B machine equipped with the validation monitoring system, from these the following observations can be drawn:

- Despite the larger size and different build of the MTI-2000B compared to the MTI-300T, the two machines behaved similarly, confirming how the phenomena observed with the prototype system were not system-related but rather connected to the process;
- The impact at part contact and the torsional oscillations at the spindle stoppage are a characteristic problem of the system for IFW, which can be attenuated with a careful choice of the system parameters, e.g. gradual increase of the piston thrust, but not completely eliminated;
- The headstock of an IFW machine is a complex rotordynamic system for which a certain runout should be expected for misalignments induced by geometrical

errors in the elements of the system and clearance for components like bearings. The runout causes the workpieces to interact in non-ideal conditions, inducing non-axisymmetric load contributions that contribute to the process loads and contribute distorting the regular runout that characterises the spindle before part contact;

- The stiffness and conditions of different machines can affect their dynamic response to the process conditions; the monitoring system proposed proved effective in comparing the behaviour of the two machines analysed.

5.4 Conclusions

In this chapter, the outcomes of a series of tests conducted with the monitoring systems developed on two different IFW machines, an MTI-300T and an MTI-2000B, were analysed. On one side this allowed validating the concepts introduced with the monitoring system proposed, while on the other they were used to draw interesting observations on the real conditions during a weld and how the machine plays an important role in the welding evolution. The conclusions of this study can be summarised as follow:

- The use of the monitoring system during the free spinning of the machine and rundown tests can be useful to assess the headstock behaviour in absence of process loads. In particular, a periodic runout in axial and radial directions in phase with the angular speed was observed. The lack of a noticeable dependence between the amplitude of oscillation and the spindle angular speed suggests a static source of runout, such as the presence of geometrical errors in the elements of the headstock and clearance in some key component, e.g. bearings, that cause the spindle to rotate out of axis;

- A change in behaviour of the runout was observed during the welding, with larger and less regular oscillations. This was attributed to the compliance of the machine headstock which deflects elastically to the process loads. Machines of different size and build present different stiffness and react to the process conditions differently. In particular, it was observed that the larger MTI-2000B was less affected by the welding conditions, showing a smaller and more regular runout compared to the MTI-300T;

- For the MTI-300T a model was developed to calculate an equivalent spindle stiffness suitable to justify the change in runout during the welding. A value of radial stiffness in the order of 10^8 N/m was obtained, which suggested the bearings supporting the spindle should be regarded as the critical element for the system compliance;

- The impact at part contact and the torsional oscillations when the spindle is about to stop spinning are two critical aspects for the vibrational behaviour of the system. Two dynamic models were developed to describe these phenomena. They showed the ram thrust characteristic, the stiffness and damping of the machine in the axial direction can be optimised to reduce the oscillations at part contact, while the flywheel inertia, the torsional stiffness of the joint and the viscous damping in the bearings control the oscillations in torsional direction;

- The runout of the machine spindle causes a non-ideal interaction between the two workpieces and, consequently, a non-constant pressure distribution around the weld interface. This was confirmed by the irregular axial strain measured with the strain gauges around the circumference of the tailstock backstop. Comparing the axial strain output for the two machines, it was possible to observe that larger values of runout were related to a larger variability in strain. For the MTI-2000B

machine this variability was particularly clear in the conditioning phase while for the MTI-300T it extended also in the burnoff phase, but in both cases it ceased in the consolidation phase. This result can be explained with the conditions at the weld interface, in fact, while during the conditioning phase the two workpieces have not reached a complete contact, contributing to the pressure gradient, and in the burnoff phase the plasticised material provides limited constraint to the relative motion of the two workpieces, in the consolidation phase the cooling of the junction induces the material to regain strength and, therefore, act as a constraint for the relative motion between the two workpieces;

- The similar results obtained with the monitoring systems installed on machines of different size and build suggest that the phenomena monitored are characteristic of the welding process rather than connected to a specific setup and it confirmed the suitability of the approach developed in comparing the behaviour of similar machines.

Chapter 6

Investigation of the dynamic evolution of the alignment of the workpieces

The results presented in chapter 5 showed how, in reality, several factors cause the welding conditions to differ from the assumption of perfect axisymmetricity conventionally adopted to study IFW. Among these factors, the headstock-tailstock runout is particularly important because it affects how the two workpieces interact and is connected with their final alignment. While it was observed in chapter 5 that the constant runout before part contact could be explained with the misalignment in the elements that constitute the headstock, it was observed that during the welding the runout tends to become larger in magnitude and lose periodicity with the rotation of the spindle. This aspect was explained with the non-axisymmetric loads induced by the interaction of the two workpieces in non-ideal conditions and the compliance of the headstock that deflects under these loads. In addition, considering the deep impact that rotordynamic effects have on manufacturing processes that use machines with similarities to the inertia welder, it is necessary to understand if these have an

impact also in IFW. To study these factors, a novel approach was developed in which, firstly a new technique was implemented to compute the equivalent loads generated during the welding when the two workpieces interact, then a dynamic representation of the spindle system was developed. Applying the equivalent loads computed to the dynamic model and comparing the outputs with the experimental data from a set of steel welds, it was possible to assess the contribution of the different phenomena on the runout evolution during the process.

This study was restricted to tests conducted on the MTI-300T machine equipped with the prototype monitoring system, however, its general approach makes it suitable also for other IFW machines.

6.1 Methodology

To obtain an understanding of the physical causes for the runout during the process, a novel methodology to compute the non-axisymmetric loads that originate when the two workpieces interact in non-ideal conditions was developed. The loads were used as input for a 3D dynamic beam representation of the machine spindle, the outcomes of which were validated against the experimental data of strain and radial runout extracted with the prototype monitoring system. Fig. 6.1 provides an overview of the algorithm developed and outlines the two main steps of the approach:

Step 1 - Calculation of the equivalent loads originated by the interaction of the workpieces during the welding: Values of pressure distribution at the weld interface (1.2) were first obtained from the experimental data measured with a monitoring system (1.1). These were converted into equivalent process loads and used as input for an optimisation which adjusted the values of pressure to minimise the error in two objective functions: an FE model of the monitoring system (1.3), in which

the strain induced by the equivalent loads were compared to the experimental strain and an analytical static representation of the spindle (1.4), in which the deflection induced by the equivalent loads were compared to the experimental data of runout.

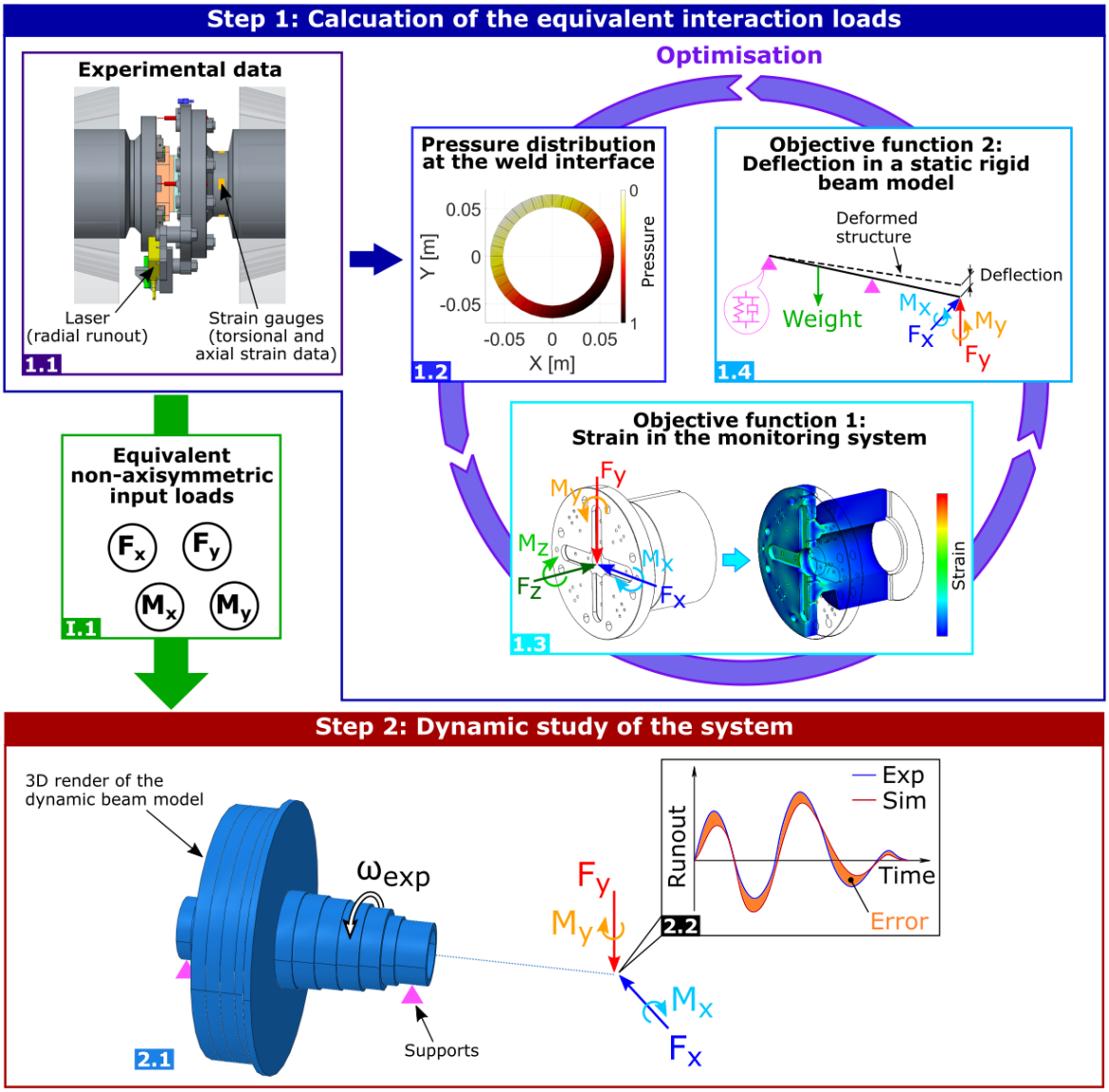


Fig. 6.1 Schematic representation of the approach used for the analysis of the runout evolution during the welding

Step 2 - Dynamic evolution of the runout during the process: First a 3D dynamic representation of the machine spindle was developed using Timoshenko beam elements and Harris' theory to model the radial supports, then the equivalent loads computed in step 1 (I.1) and the experimental angular speed were applied to the model. Finally, the model's outcomes were compared against the experimental data of runout and the static representation developed in step 1 (1.4).

6.1.1 Loads induced by non-axisymmetric conditions

The process loads, in terms of torque and axial load, are conventionally obtained with the sensors embedded in the inertia welder. These values, however, are intrinsically smoothed by the remote location of the sensors relative to the weld zone, which induces a sensitivity loss to the local phenomena induced by the interaction of the workpieces. To address this limitation, a novel approach to compute equivalent process loads, starting from the experimental strain conditions near the weld zone, was developed. Ultimately, the approach aims to provide a more accurate representation of the loads generated during a weld when the two workpieces interact under non-idealised conditions.

The approach is based on the observation that the process loads, along with the weld evolution, are guided by the conditions at the interface of the two workpieces. For this reason, the values of axial load at specific circumferential positions (F_{A_i}) were interpolated over the welding surface, discretised with a structured mesh and finally used to compute the equivalent loads ($F_{A_{tot}}$, F_{T_x} and F_{T_y}) and moments (M_x, M_y), as shown in Fig. 6.2 and detailed in Eq. 6.1-6.5.

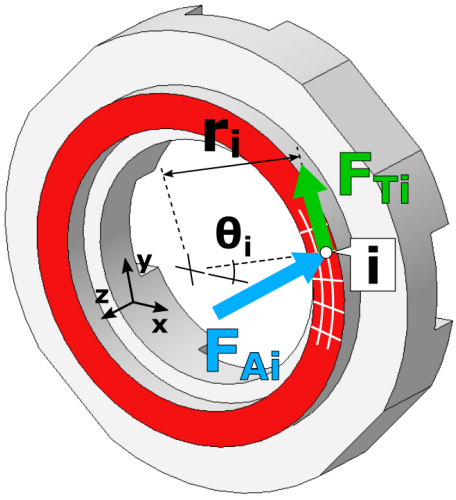


Fig. 6.2 Graphic representation of the axial and tangential load contributions on the welding surface of the workpiece

Normal direction

$$F_{A_{tot}}(t) = \sum F_{A_i}(t) \tag{6.1}$$

$$M_x(t) = \sum F_{A_i}(t) \cdot r_i \cdot \sin\theta_i \tag{6.2}$$

$$M_y(t) = \sum F_{A_i}(t) \cdot r_i \cdot \cos\theta_i \tag{6.3}$$

Tangential direction

$$F_{T_x} = \sum \mu(t) F_{A_i} \cos\left(\theta_i + \frac{\pi}{2}\right) \tag{6.4}$$

$$F_{T_y} = \sum \mu(t) F_{A_i} \sin\left(\theta_i + \frac{\pi}{2}\right) \tag{6.5}$$

The tangential loads expressed by equation (6.5) make use of the concept of an equivalent friction coefficient [40] and were calculated from the contributions of the axial loads and the experimental torque (T) as:

$$\mu(t) = \frac{\sum F_{A_i}(t) \cdot r_i}{T(t)} \tag{6.6}$$

It is important to note two aspects, firstly the experimental measurements used as the input to compute the axial contribution over the welding interface provide just a coarse approximation of the actual pressure field, due to the limited number of sensors which can be installed in the monitoring system. Secondly, the measurements of axial load with strain gauges aligned with the axis of the spindle are not sufficient to fully decouple the contribution of radial loads and moments, therefore multiple combinations of loads can result in to the same value of strain measured experimentally. For this reason, the load components cannot be obtained directly from the experimental measurements, but rather the equivalence between the model and the actual system is ensured with an optimisation algorithm that iteratively updates the load components to minimise the difference in strain and radial runout.

To reduce the computational cost of the optimisation, rather than optimise the value of each axial contribution, a third order Fourier series was used to describe the axial load variation around the weld interface. The choice of a Fourier series over other fit functions is justified by the expected fixture/spindle misalignment to be in phase with the angular rotation of the spindle and, consequently, the pressure over the weld surface to vary periodically. The parameters of the Fourier series were updated by the optimisation algorithm so that the value of the two objective functions were minimised. The first objective function compares the experimental strain at different points in the monitoring system with the solution from a 3D FE model of the backup when the equivalent loads are applied (1.4 in Fig. 6.1) while the second compares the experimental runout of the spindle with the displacement induced in a static beam that represents the spindle (1.3 in Fig. 6.1). Neglecting the axial contribution and analysing separately the two orthogonal directions X and Y, the problem becomes planar and can be studied with the model in Fig. 6.3 for which the load and moment equilibrium equations can be respectively written as:

$$F_{b_A}(\delta_A) - F_W + F_{b_B}(\delta_B) = F \tag{6.7}$$

$$-F_W \cdot l_g + F_{b_B}(\delta_B) \cdot l_1 = F \cdot l_{tot} + M \tag{6.8}$$

where F_{b_A} and F_{b_B} are the reaction forces of the rear and front supports respectively, δ_A and δ_B the displacements of the shaft at the support locations, F_W the weight of the spindle, F the equivalent radial process load, l_g the position of the centre of mass of the spindle shaft, l_1 the distance between the supports and l_{tot} the overall length of the spindle shaft, including the tooling and workpiece. All the dynamic effects, such as spindle rotation and the damping of the supports, were neglected in this model, however, their quantitative influence on the system response was investigated by analysing the rotordynamics of the spindle, as it will be shown in section 6.1.2. IFW

machines conventionally have a combination of bearings to support the spindle [13, 25] and for this study a single cylindrical roller bearing was assumed for the rear support and a combination of a deep groove ball bearing and a cylindrical roller bearing for the front support. Using the approach presented by Harris [91], the relationship between the radial load acting on the bearing (F_b) and the radial displacement of the bearing (δ_r) can be obtained summing the components acting on each rotating element as:

$$F_b = ZK_n \left(\delta_r - \frac{1}{2}P_d\right)^n J_r\left(\epsilon_{df}\right) \tag{6.9}$$

where Z is the number of rolling elements, K_n the deflection constant that takes into account the deformation of a rolling element, assuming Hertzian contact with the bearing races, P_d the diametral clearance, n a constant that depends from the type of rolling element (3/2 for ball bearings and 10/9 for roller bearings), J_r the radial load integral and ϵ_{df} the load distribution factor, which can be expressed as:

$$\epsilon_{df} = \frac{1}{2}\left(1 - \frac{P_d}{2\delta_r}\right) \tag{6.10}$$

Since the radial integral is a function of ϵ_{df}, which includes δ_r, a direct solution of equation Eq. 6.9 is not possible. Therefore, when the value of external load F_r is known, the deformation of the bearing, δ_r, can be obtained by iteratively solving the equation; first a guess value of δ_r is assumed and used to compute the radial load integral, following this the value of δ_r was updated until the two sides of Eq. 6.9 were equal. Using the representative dimensions reported in Table 6.1, the radial load-displacement characteristic for the two types of bearings were computed. From these, the load-displacement characteristics for the rear and front supports were determined as shown in Fig. 6.4, where the front support was obtained considering a single roller bearing while the rear a combination of ball and roller bearings.

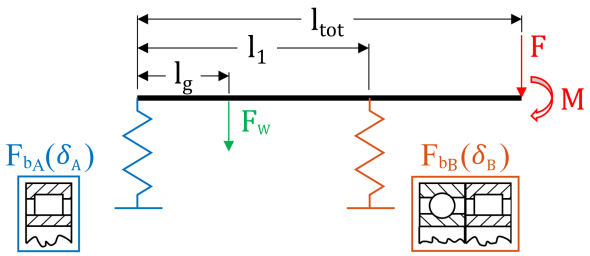


Fig. 6.3 Static analytical model for the study of the spindle deflection with details of the bearings adopted for the rear and front supports

Table 6.1 Bearing specifications

		Ball bearing	**Roller bearing**
Bore diameter	d	400 mm	400 mm
Outer diameter	D	600 mm	600 mm
Bearing width	w	90 mm	90 mm
Diametral clearance	P_d	100 μm	100 μm
Number of rolling elements	z	15	26
Width roller	w_r	-	50 mm
Ball diameter	d_b	60 mm	-

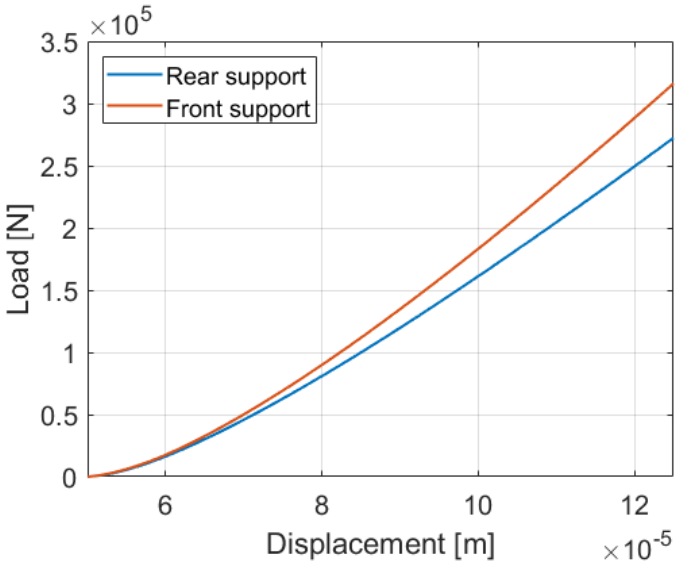


Fig. 6.4 Load-displacement curves for the front and rear supports of the spindle

6.1.2 Dynamic representation of the machine spindle

To assess the influence of dynamic phenomena on the runout of the spindle, a study using the beam model presented in Fig. 6.5 was carried out. The system comprises: a variable section Timoshenko beam partitioned into 14 segments; the radial supports, using the same bearing configuration considered for the static model in section 6.1.1; and a rigid connection beam which represents the elements between the front radial support and the workpiece (thrust bearing, tooling and the flywheels). The choice of a rigid connector rather than a flexible beam is motivated by the significantly larger stiffness of the thrust bearing and tooling compared to the shaft that supports the flywheels, which makes the deflection of these elements negligible. Table 6.2 summarises the geometrical details of the beam model.

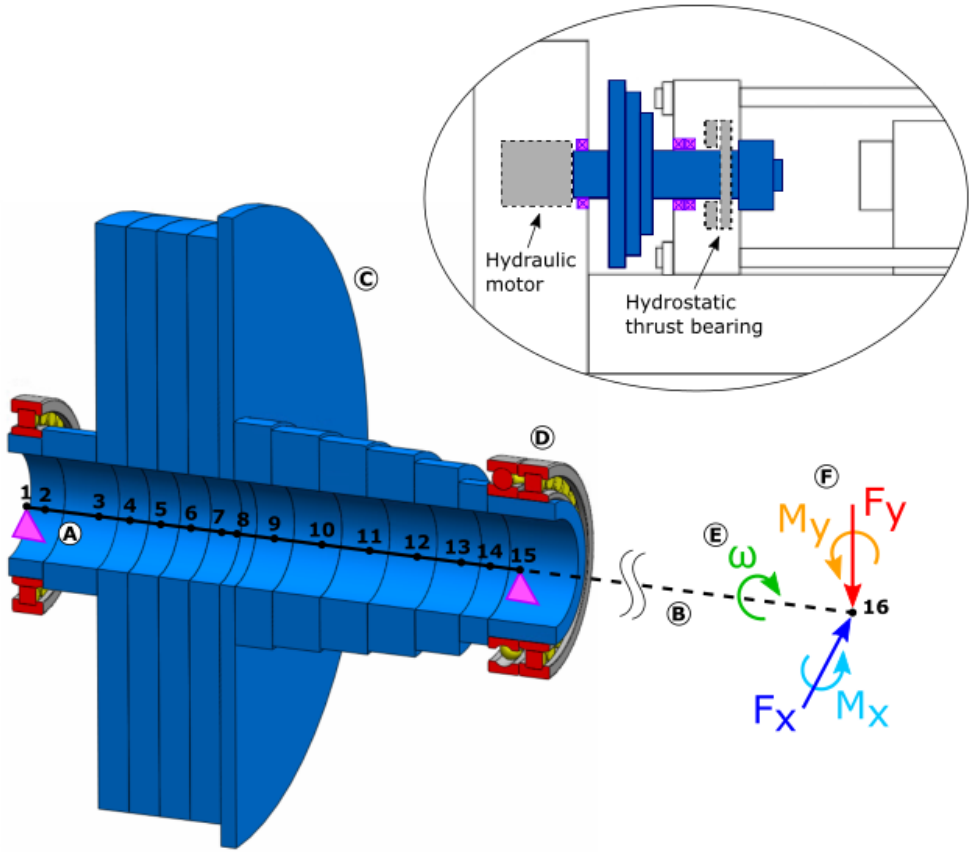


Fig. 6.5 Beam model analysed for the dynamic study (A: Beam model with details of the supports and nodes; B: Rigid connector beam; C: Beam profile render; D: CAD representation of the radial supports; E: Experimental angular speed; F: Equivalent process loads) (Based on an MTI's proprietary design)

Table 6.2 Geometrical specifications for the beam model studied in the dynamic characterisation of the system

Segment	Nodes ID	Inner diameter	Outer diameter	Length
1	1-2	300 mm	400 mm	100 mm
2	2-3	300 mm	450 mm	160 mm
3	3-4	300 mm	1660 mm	90 mm
4	4-5	300 mm	1660 mm	90 mm
5	5-6	300 mm	1660 mm	90 mm
6	6-7	300 mm	1660 mm	90 mm
7	7-8	300 mm	1780 mm	45 mm
8	8-9	300 mm	630 mm	110 mm
9	9-10	300 mm	610 mm	140 mm
10	10-11	300 mm	590 mm	140 mm
11	11-12	300 mm	570 mm	140 mm
12	12-13	300 mm	530 mm	130 mm
13	13-14	300 mm	450 mm	90 mm
14	14-15	300 mm	400 mm	200 mm
15	15-16	- (Rigid connector)	- (Rigid connector)	2000mm

The equation of motion for this model can be written in the form [100, 167]:

$$[M]\left\{\ddot{U}\right\}+([C]-\omega[G])\left\{\dot{U}\right\}+[K]\{U\}=\{F\} \tag{6.11}$$

where $[M]$ is the mass matrix, $[C]$ the damping matrix, $[G]$ the gyroscopic matrix, ω the angular rotation of the shaft, and $\{U\}$ and $\{F\}$ the coordinates and loads vectors. Neglecting the effect of material damping, the terms in the stiffness matrix were obtained from the load/displacement characteristic curves presented in section 6.1.1 while a constant damping coefficient of 1000 Ns/m was considered to populate damping matrix [168, 169]. The experimental time-dependent value of angular speed was adopted to have realistic rotordynamic loads and, finally, the equivalent process loads computed in section 6.1.1 were used to populate the load vector. The resulting system of equations was solved using the commercial finite element software Abaqus.

6.1.3 Process parameters

A set of steel welds (EN19) were carried out on the MTI-300T hybrid welder equipped with the prototype system monitoring. The welds shared the same values of initial speed (ω_0), ram pressure (P), flywheel inertia (I), and wall thickness of the welding section (T_w) to ensure the repeatability of the results; Tab. 6.3 summarises the numerical values.

Table 6.3 Process parameters and wall thickness for the welds analysed

ω_0 [RPM]	165
I [lb-ft2]	60,957
P [psi]	500
T_w [mm]	13

6.2 Results and discussion

The results obtained by applying the methodology developed to the set of steel welds will be presented in this section. First, the outputs of the algorithm to compute the equivalent process loads are presented, then the process loads are applied to the dynamic representation of the machine, finally, the comparison of the machine behaviour in static and dynamic conditions will allow conclusions to be drawn on the main causes behind the runout evolution during welding. While considering through the results, it is important to remember that the proposed approach aims to gain an insight into the physical phenomena connected to the runout evolution in IFW and that it should not be interpreted as a predictive model. For this reason, the results of only a few of the welds carried out will be presented as a representative case study, with the conclusions maintaining a general perspective rather than being specific to the machine setup or welding parameters.

6.2.1 Pressure distribution on the weld interface

Using the approach described in section 6.1.1 the pressure distribution over the weld interface was computed. Fig. 6.6 shows the interpolated pressure fields for one of the welds at five different time instances: initial contact between the workpieces (P1), halfway through conditioning (P2), end of conditioning (P3), end of burnoff (P4), and flywheel stoppage (P5), normalised against the nominal interface pressure caused by the axial load exerted by the ram.

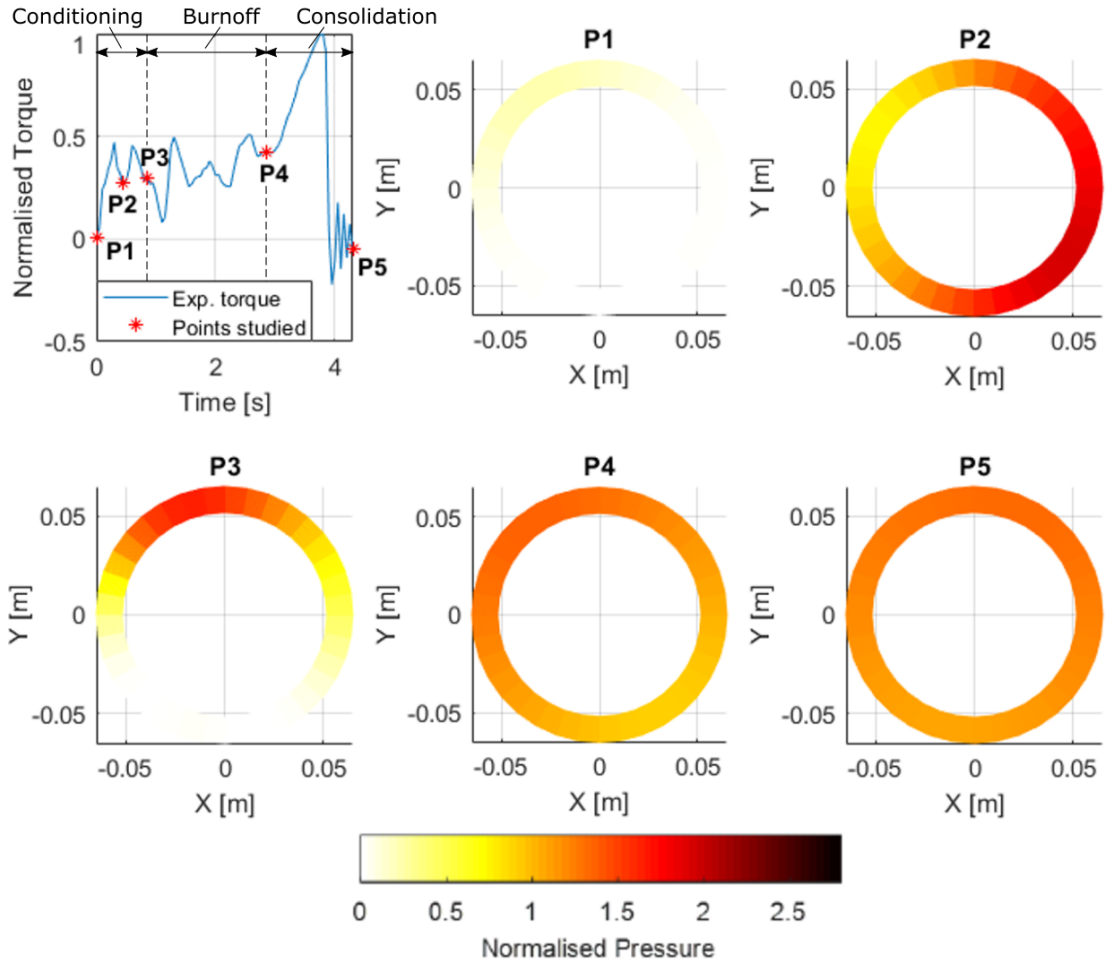


Fig. 6.6 Normalised pressure distribution at the weld interface for five time instances (P1, P2, P3, P4 and P5) during the welding

As initially assumed, the results show that the pressure distribution around the weld surface is not axisymmetric, with the variation more severe in the initial phases (P1-P3) compared to the end of burnoff and consolidation (P4, P5). This result can be explained considering how the inevitable geometrical imperfections and misalignments in the workpieces, which cause an uneven pressure distribution, get smoothed out during the conditioning and the beginning of burnoff due to the abrasion of the asperities at the weld interface and the plastic deformation. This aspect becomes particularly clear when calculating the standard deviation of the normalised pressure around the circumference, as shown in Fig. 6.7. In fact, the standard variation is much larger during conditioning and burnoff, while it drops in the consolidation phase, confirming a larger dispersion from the average pressure values.

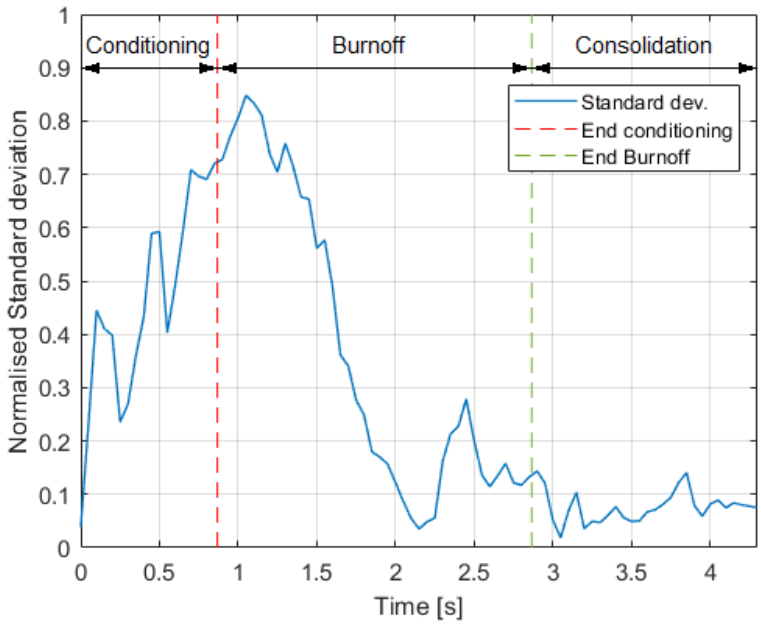


Fig. 6.7 Standard deviation of the pressure distribution at the weld interface showing larger variability in the first stages of the welding

A final aspect of interest in the analysis of the pressure distribution is the position over time of the peak pressure around the circumference, shown in Fig. 6.8 for three different welds run with the same process parameters. When comparing the position of

the peaks against the spindle rotations, it is possible to observe that even if a periodic behaviour is present, the peak pressure location is out of phase with the angular rotation of the spindle. Combining this with the different shape of the curves and, consequently, location of the pressure peaks over time for the three cases, it is possible to conclude how this behaviour must be affected mainly by the variable conditions at the interface of the workpieces rather than the system or its set-up.

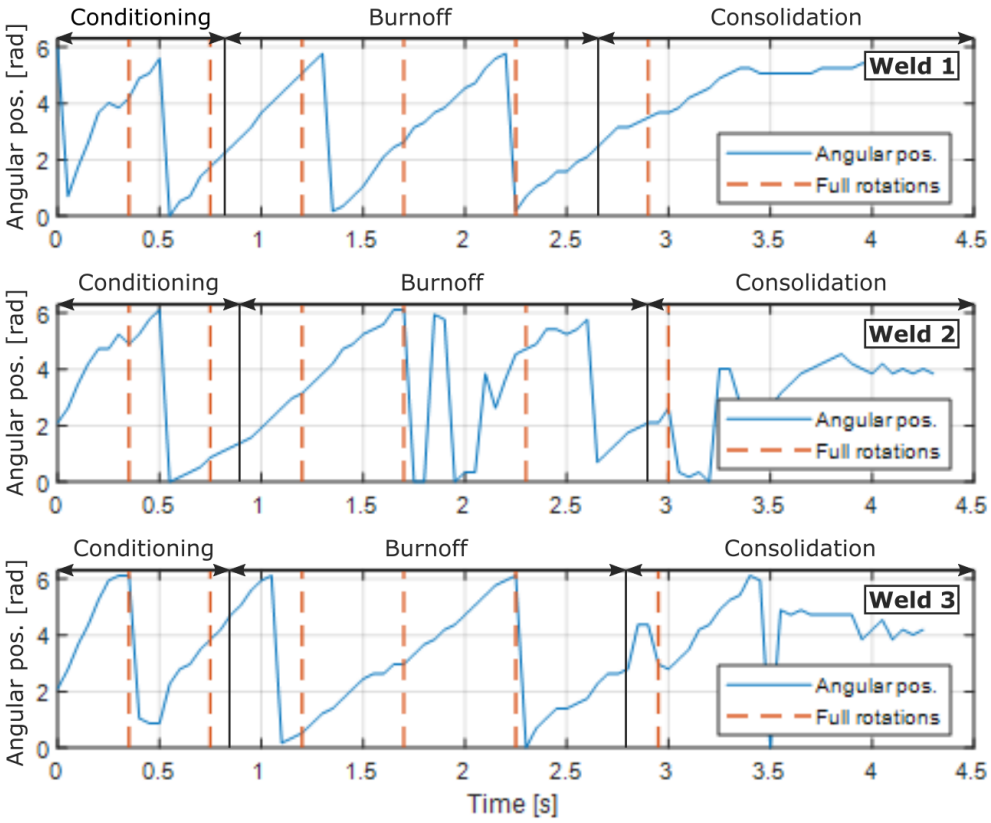


Fig. 6.8 Angular position of the pressure peak location around the weld interface during the welding for three welds carried out using the same process parameters, from which it is possible to observe periodicity in the peak location but a different behaviour among the three welds

6.2.2 Equivalent loads and optimisation error analysis

Starting from the values of pressure distribution at the workpiece interface, the equivalent process loads were determined. Fig. 6.9 shows the values of force, normalised to the peak load in the axial direction (F_z), and the moments, normalised to the peak

torque (M_z), for one of the welds. Large non-axisymmetric loads can be observed, with the radial forces (F_x and F_y) and moments (M_x and M_y) that show peak values 40% larger than the peak axial force (F_z) and torque (M_z) respectively. In addition, these loads follow a trend similar to that of the spindle runout (Fig. 6.10b), with larger oscillations during the conditioning and burnoff phases rather than in the consolidation. This phenomenon can be explained by a combination of the perfect contact between the two workpieces at the end of the process and the constraining action of the weld that opposes the motion of the spindle when it acquires strength at the end of the process. Analysing the force and moment in the axial direction of the spindle, F_z and M_z, it is possible to see the characteristic behaviour typical of IFW. F_z presents first a steep increase at the beginning of the process from zero to the peak load when the ram is activated and the two workpieces are brought into contact. Then, after a transitory period characterised by load fluctuations at the beginning of the burnoff phase, the load tends to stabilize. M_z shows a steep rise at the beginning of the conditioning phase, followed by a semi-stable value during the burnoff phase and a final peak when the joint starts to cool down in the consolidation phase. The oscillations observed during the burnoff phase can be connected once again to the intrinsically unstable nature of the interface conditions.

The output of the two objective functions is shown against the experimental data in Fig. 6.10. The first objective function shows a good agreement in term of strain for the four axial gauges, with a similar mean absolute error of 0.17 (normalised strain) for the four strain gauges, while the comparison for the torsional strain is not included because the error is two orders of magnitude smaller than the one in the axial direction and therefore negligible. This is a consequence of the approach for calculating the friction coefficient, in which the experimental torque is used to obtain an equivalent friction coefficient (Eq. (6.6)). Fig. 6.10b compares the displacement obtained from the

second objective function with the experimental radial runout, in which it is possible to observe again a good match between numerical and experimental data with a mean absolute error of 0.09 (normalised runout) for both X and Y directions.

These results show that the proposed technique is capable of calculating equivalent process loads able to verify with a good approximation the equivalence in strain and displacement conditions between the numerical and the experimental data, using an inverse approach that makes use of experimental parameters easier to measure. In addition, the good match in displacement shown in Fig. 6.10b is of primary importance for the current investigation because the static analytical model used in the optimisation algorithm disregards the rotation of the spindle along with all possible rotordynamic phenomena. This result gives a first hint that the root cause in the runout behaviour during the welding could be related to the reaction loads caused by the interaction of the two workpieces rather than connected to the dynamics of the spindle.

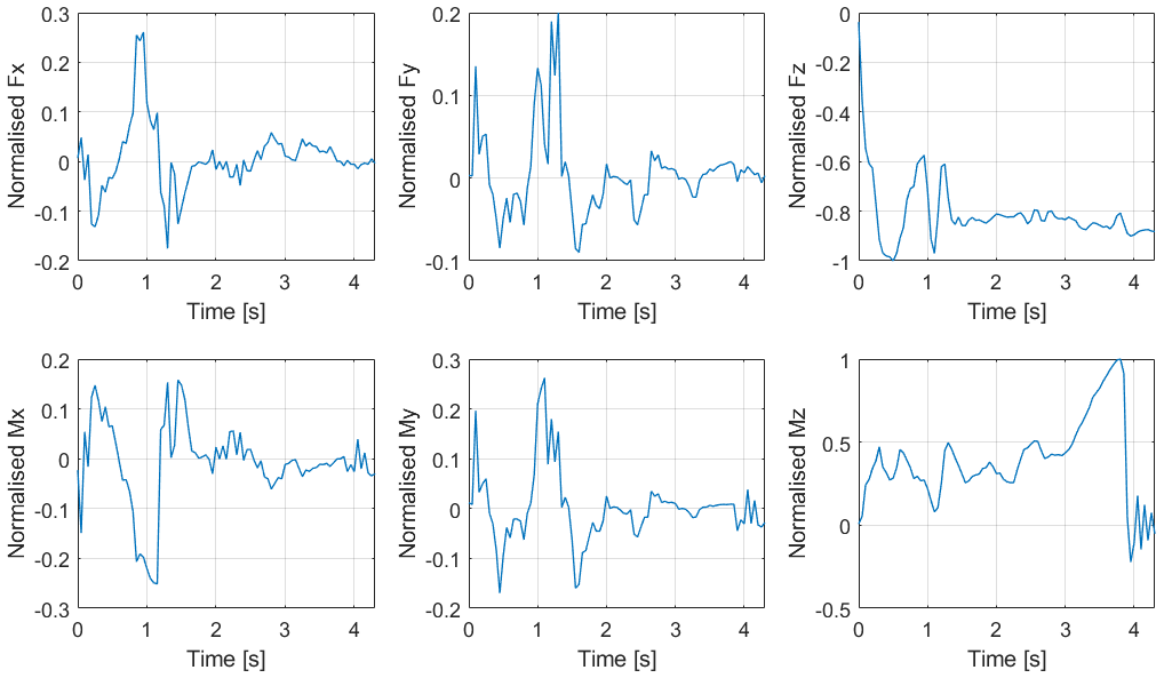
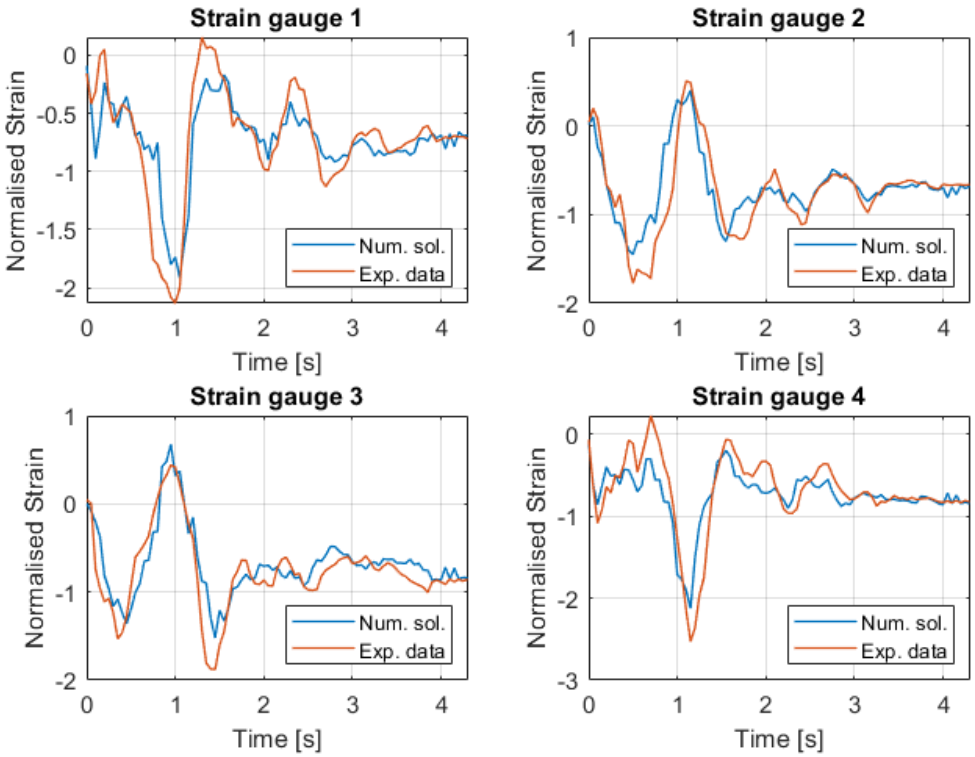
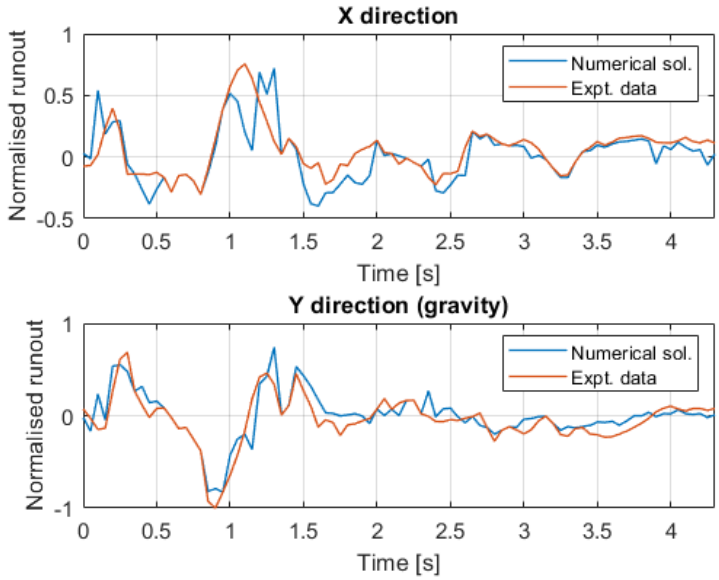


Fig. 6.9 Normalised equivalent loads and moments in three orthogonal directions obtained from the optimisation algorithm, from which it is possible to observe large non-axisymmetric loads (F_x, F_y, M_x and M_y)



(a)



(b)

Fig. 6.10 Comparison between the experimental data and the numerical data computed with the optimisation: (a) Strain comparison at four locations 90° apart around the backup's neck; (b) Spindle runout comparison for the two orthogonal directions, X and Y.

6.2.3 Dynamic response of the system to the equivalent loads

To further investigate the influence of the loads generated by the interactions of the workpieces on the runout, the dynamic representation of the machine spindle presented in section 6.1.2 was used. Fig. 6.11 shows the response of the dynamic model in terms of radial displacement when the experimental angular speed and the equivalent loads calculated in the previous section are taken into account and compares it with both the static solution (second objective function of the optimisation) and the experimental radial runout. A very good agreement between the static and dynamic solutions can be observed, with small differences (mean absolute error (normalised runout) of 0.029 in X direction and 0.048 in Y direction) ascribable to the flexibility accounted in the Timoshenko beam elements used for the dynamic model but neglected in the rigid beam of the static one.

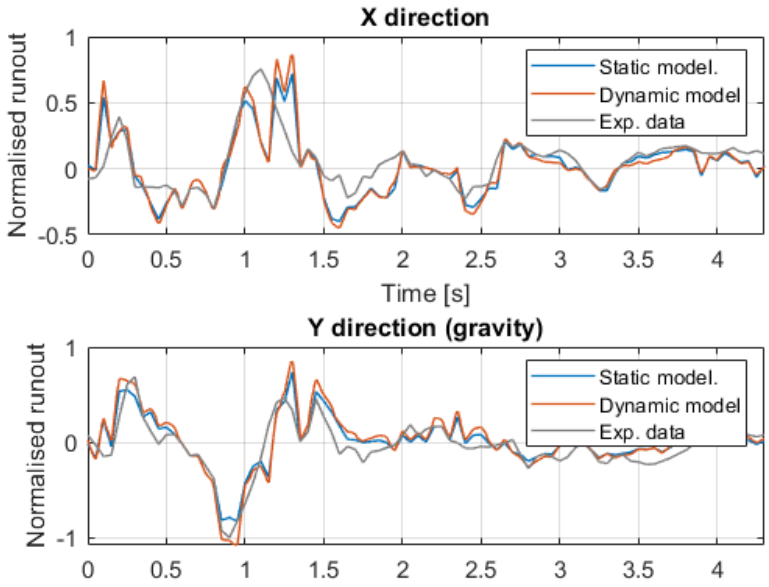


Fig. 6.11 Comparison of the radial runout obtained with the static and dynamic models and the experimental data

The good agreement between the experimental data and numerical solutions supports the hypothesis presented in the previous section that the loads generated by the non-ideal interaction of the two workpieces represents the major influence on the runout evolution. This imperfect contact can be attributed to misalignment between the fixture and spindle sides as well as geometrical imperfections in the workpieces.

6.3 Conclusions

This analysis challenged the popular assumption of treating IFW as a perfectly axisymmetric process, showing instead how the two workpieces tend to interact during the welding in non-ideal conditions due to the presence of small misalignments, which induce considerable non-axisymmetric process loads. In fact, the analysis of a set of steels welds completed on the MTI-300T industrial inertia welder equipped with the prototype monitoring system showed significant non-axisymmetric loads and a non-negligible runout. These phenomena can have a significant impact on the repeatability and quality of welds, considering the strict geometrical tolerances on inertia welded components for aerospace applications. For this reason, a novel approach was developed to compute equivalent process loads from the measured strain data and it was possible to observe how large radial loads and moments are induced by the interaction of the workpieces when the system is analysed in non-idealised conditions. Then the loads obtained were applied to two models, a static and a dynamic representation of the inertia welder spindle, to analyse the system response and draw conclusions on the physical causes of the runout observed. It is finally important to note that the approach presented, even if developed specifically for IFW, is versatile enough to be applied to rotary friction welders of different configurations.

The outcomes of the study presented can be summarised as follows:

- The novel approach developed to calculate the equivalent loads generated by the interaction of the two workpieces during the welding achieved a good agreement with the experimental data, confirming its suitability as an inverse technique to calculate the actual process loads from auxiliary parameters easier to monitor during the welding (strain and runout). More specifically, the optimisation algorithm converged to solutions able to satisfy two objective functions: an FE representation of the monitoring system used to extract the experimental data, which ensured a load equivalency between the numerical solution and experiential data, and a static representation of the machine spindle, which compared the deflections induced by the equivalent process loads in a non-rotating rigid model of the spindle with the experimental data. The second objective function, required to avoid local minima in the solution, indicated how static effects could be sufficient to explain the runout observed in the machine spindle;

- The pressure distribution at the weld interface of the two workpieces calculated with the optimisation algorithm showed large variations, suggesting how the constant pressure distribution conventionally assumed could be not representative of the actual conditions during the welding but just a simplified assumption based on averaged conditions. This was particularly noticeable during the conditioning and burnoff phases, while it tended to flatten in the consolidation phase. The pressure variation can be connected to the imperfect contact of the workpieces during the conditioning phase and the unstable nature of the process in the burnoff phase and it could be particularly significant due to the risk of generating hot spots in the first phases of the welds at the localised pressure peaks;

- The equivalent process loads calculated from the pressure distribution at the weld interface showed how significant radial loads and bending moments should

be expected when non-idealised contact conditions between the two workpieces are considered. In fact, along with the axial load and torque conventionally considered in IFW, radial loads and bending moments showing peaks up to 40% greater in magnitude than the experimental axial load and torque respectively were obtained;

- The non-axisymmetric interaction loads between the two workpieces combined with the flexibility of the spindle supports should be regarded as the major factor in the runout evolution during the weld. First, a dynamic representation of the machine spindle was developed using 3D Timoshenko beam elements, Harris theory for the radial supports, the experimental data of angular speed and the equivalent process loads calculated with the optimisation algorithm. Then the results of this model were compared against the outcomes of the static model used in the optimisation and it was possible to conclude that no noticeable rotordynamic effects influenced the response of the system.

Chapter 7

Conclusions

This chapter will present a summary of the key aspects analysed in this research, highlighting the contribution of this research to the scientific knowledge of the field, while providing an approach that can also prove useful in an industrial environment. Firstly, section 7.1 will present a brief summary of the capability of the approach developed and how it can be applied to a generic inertia welder, then section 7.2 will discuss the conclusions of this research from an academic viewpoint. Finally, section 7.3 will present new opportunities that this work has opened for further research.

7.1 A novel approach for the characterisation of the system performance in IFW

The novel approach developed can be summarised with the schematic in Fig. 7.1, in which three main steps can be observed.

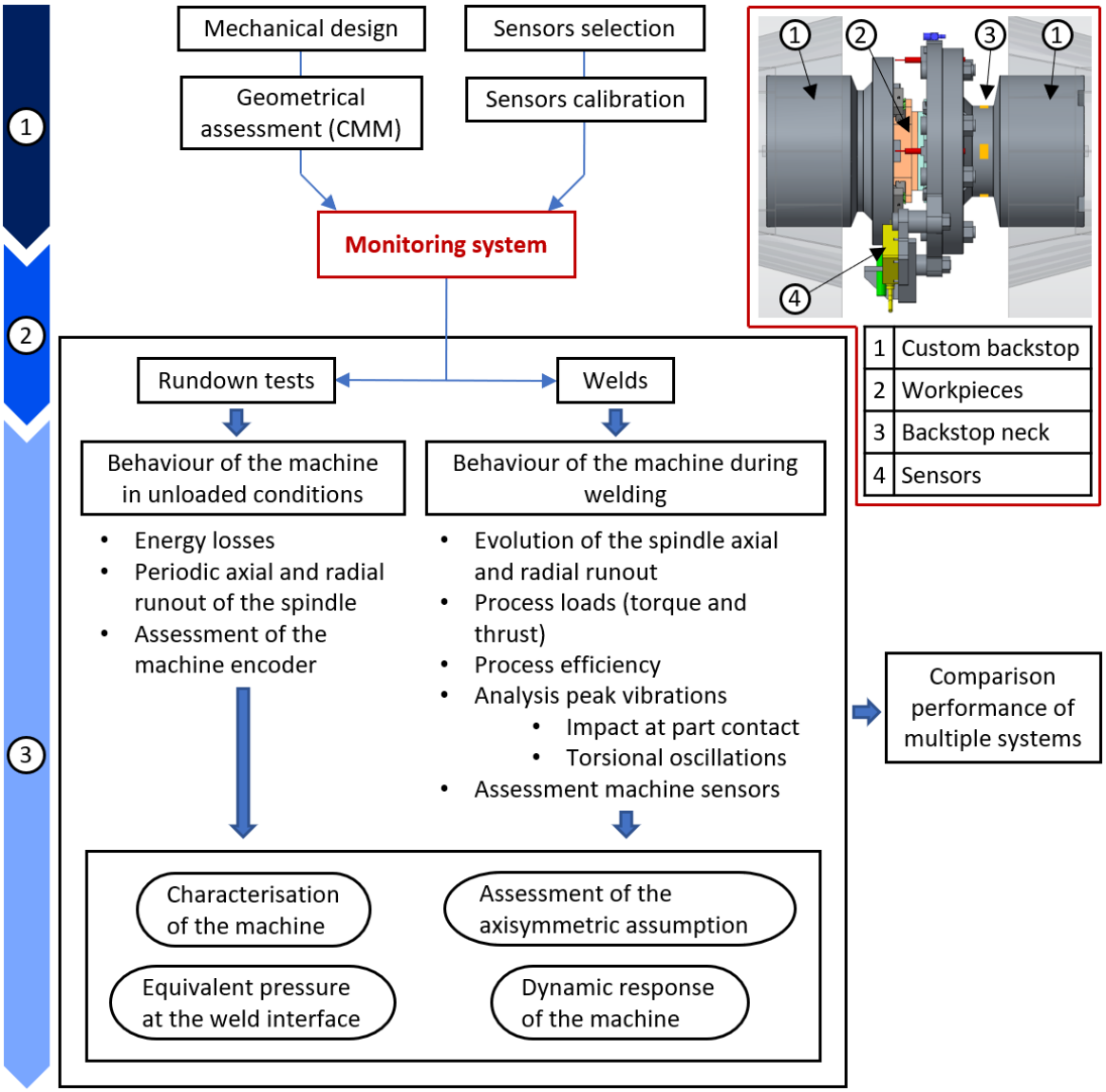


Fig. 7.1 Schematic representation of the novel approach developed for the characterisation of the system performance in IFW (1: Design and manufacturing stage; 2: Experimental assessment; 3: Methodology for the analysis of the experimental data)

Step 1 - Design and manufacturing: The key aspect of the novel approach proposed is a monitoring system designed as an interface between the workpieces and the machine, serving at the same time as fixturing for the workpieces (2) and physical support for the instrumentation (4).

Dimensioning the custom backstops (1) accordingly to the specific tooling of the inertia welder to be analysed, the system can fit machines of almost any dimension. In addition, the modular design of the fixturing system for the workpieces can accommodate workpieces of various geometry, simply changing the number and dimensions of the keys and the type of radial grippers. The diameter and length of the backstop neck (3) can be optimised to study the desired working conditions of the machine. This element should be strong enough to withstand the peak loads but sufficiently compliant to allow a strain measurable with the strain gauges, while the length should be selected to avoid geometry effects where the strain gauges are installed and minimise the stick out of the backstop from the machine tooling. A final aspect of great importance is the assessment of the geometrical accuracy of the backstops after manufacturing. In fact, when the sensors measure the relative runout between headstock and tailstock, it is necessary to remove the geometrical error intrinsic in the backstops from the actual dynamic behaviour of the spindle. The key dimensions to analyse are the flatness between the front and back face of the backstops and the concentricity between the section clamped by the machine collet and the front face. In addition, for the tailstock backstop, it is necessary to assess the position of sensors like lasers and LVDTs, the output of which is deeply affected by position errors.

The monitoring system was designed to carry strain gauges, laser displacement sensors, LVDTs, an encoder and a triaxial accelerometer. The strain gauges were used to measure the frictional torque and the thrust exerted by the piston. Four stacked $0°/45°/90°$ 3-element rectangular rosettes were installed $90°$ apart around the neck section of the tailstock backstop. With this configuration, the four $45°$ gauges, aligned with the backstop axis, were connected in quarter bridge configuration and used to have four independent measurements of the thrust exerted by the ram; the average of the four gauges can be used to assess the behaviour of the piston, i.e. ensure that

the theoretical and experimental thrust coincide, while comparing the reading of each gauge it is possible to make considerations on the axisymmetricity of the thrust. The 0° and 90° gauges of opposing rosettes can be connected in full bridge configuration and used to measure the frictional torque. While one full bridge is sufficient to obtain the torque and additional bridges are beneficial just in term of redundancy, numerous axial gauges are advantageous to have a better resolution studying the thrust variation in the circumferential direction. The lasers and LVDTs can be used to measure the radial and axial runout respectively. In the design proposed, two lasers 90° apart and three LVDTs distributed around the backstop circumference were adopted. Having two lasers in orthogonal directions instead of a single one allows a 2D description of the spindle centre location throughout the process to be obtained, while three LVDTs are necessary to characterise the angular misalignment between headstock and tailstock. In fact, the LVDTs positioned between the two backstops capture the superposition of the process upset and the angular misalignment, fitting a plane through the three points measured by the LVDTs, the upset (the overall translation of the plane) can be separated from its orientation (direction of the normal to the plane). The choice of different sensors to measure the runout in axial and radial directions was dictated mostly by the favourable form factor and the capability to accommodate for the relative motion of headstock and tailstock, rather than by considerations of accuracy and sampling rate. In fact, since the runout is a macroscopic effect with a frequency related to the angular speed of the machine (in the order of few Hz) both sensors are suitable for the application. The triaxial accelerometer was selected to capture high frequency signals and it needs to be installed as close as possible to the weld interface to minimise the noise coming from the machine. In IFW the speed of the spindle gradually decreases down to zero RPM, therefore, a large frequency response range should be considered, with the peak oscillations both in magnitude and in frequency that should be expected at impact at

part contact and in the final instants of rotation of the flywheel. The magnitude and frequency of the peaks depend on the process parameters chosen, the weld geometry, and the machine setup. A final aspect to consider regarding the accelerometer is the connection to the backstop, due to the large vibrations and the relatively large mass of a triaxial accelerometer, semi-permanent mounting making use of epoxy glue or a screw connection should be preferred to mounting wax or other forms of light connection. The encoder can be useful to assess the performance of the machine encoder, however, some aspect has to be considered in its development. Firstly, the encoder should be able to account for the relative motion between headstock and tailstock, therefore non-contact sensors, e.g. magnetic encoders, should be preferred when designing a custom sensor is not possible. Secondly, it should provide enough resolution (i.e. the number of pulse per revolution) to characterise the spindle deceleration.

Final considerations regard the safety against thermal damaging of the sensors and their calibration. In the initial assessment of the system conducted with the prototype, it was observed that having installed the sensors on the backstop rather than on the workpiece proved successful in avoiding thermal damage, with peak temperatures just a few degrees above room temperature. Finally, considering the limited access to IFW machines for research analysis, it is convenient to calibrate the sensors before installing them on the backstop and the periodic re-assessment of their performance is suggested to ensure that no damage or loss of calibration occurs.

Despite the sensors selected proved effective in characterising the process evolution and the machine response for the case study presented, the modularity of the monitoring system allows to easily remove, replace or add additional sensors with only minor modifications.

Step 2 - Experimental assessment: Once the monitoring system has been manufactured, assembled and calibrated, the following step is the extraction of the experimental

data necessary for the methodology developed. This can be obtained from a set of rundown tests and welds.

The rundown tests give information on the machine behaviour in unloaded conditions and, when possible, the machine should be tested over the full range of angular speeds and flywheel inertia conventionally used to weld. It is worth noting that for large machines equipped with high inertia flywheels, a full rundown test from the initial speed down to zero RPM can result in an extremely long test duration. When this is not acceptable, the test can be split over several speed ranges, exchanging a continuous characterisation over the speed interval for a shorter overall duration.

To analyse the response of the system to the welding conditions, a set of welds can be devised with process parameters that span over the range of interest; to minimise the number of tests without restricting the range of the parameters, techniques like Design of Experiments (DOE) can be used. In the approach developed, the focus was on the machine behaviour rather than on the weld characteristics, therefore the workpiece design was optimised to be simple and economically convenient, with the only constraints of being compatible with the tooling of the custom backstops and a welding section suitable to achieve the desired upset for the process parameters selected. Despite this, the geometry and the material of the workpieces can be changed according to the needs.

Step 3 - Methodology: The range of sensors installed in the monitoring system and the relatively high sampling frequency required to monitor a transient process like IFW produce a large volume of data during the tests. These need to be processed with a methodology able to filter out the undesired noise induced by the multitude of sub-systems embedded in the inertia welder and extract information useful to characterise the weld evolution and the machine performance. In addition, having a

well-defined methodology to apply systematically to all the tests is fundamental to avoid inconsistencies and have comparable results.

In the case of rundown tests, the analysis of the spindle deceleration can be used to calculate the energy losses in the bearings that support the spindle. In addition, using the readings of the LVDTs and the lasers, it is possible to assess the periodic and constant runout of the spindle. When instead the data from the welds is studied, the response of the system to the welding conditions can be evaluated. Also in this case the lasers and LVDTs provide an insight in the spindle runout, which, however, can differ to that observed during rundown tests due to the reaction of the machine to the process loads. Comparing the theoretical torque calculated from the spindle inertia and the angular deceleration with the torque obtained from the strain gauges, it is possible to get the process efficiency, while the comparison of the experimental thrust with the theoretical one defined as process parameter can be used to diagnose the behaviour of the ram. Then, comparing the complementary information provided by the different sensors (e.g. strain gauges, LVDTs and accelerometer), it is possible to analyse the vibrational behaviour of the machine, focusing in particular on part contact and the last instants of rotation of the spindle, which were shown presenting the peak oscillations in the axial and torsional directions respectively. Finally, the sensors in the monitoring system, which can easily be removed from the system, calibrated and installed before a test on the machine, can be used to assess the performance of the machine sensors, which often cannot be accessed directly. In addition, parameters like the runout and the process efficiency can be used to evaluate the state of key elements in the system, e.g. bearings, carry out periodic maintenance inspections of the machine and understand their contribution to process drift.

The experimental data provided by the monitoring system, therefore, allows obtaining a full spectrum characterisation of the process evolution and machine behaviour.

When this data is used as input for the methodology presented in chapter 6 it possible to gain a more deep understanding of the physical implications of the phenomena monitored, e.g. how a certain runout not only can affect the final alignment of the workpiece but also the consequences on the interface pressure or the way a specific build configuration and setup of the machine can affect the spindle dynamics.

As shown in the previous chapters the monitoring system is self-contained and easily scalable to fit machines of different size, these characteristics make it suitable to compare different machines. In fact, after having run a set of tests to characterise the first machine over the range of parameters of interest, the monitoring system can be disassembled, installed on a second machine and used to run analogous tests. The comparison of the data extracted allows determining whether the two machines behave similarly, with a more deep insight compared to the simple comparison of the welds.

7.2 Conclusions

In chapter 2, a review of the available literature about IFW was presented, from which several research gaps were observed. Among these, two in particular were investigated: the assessment of weld evolution in non-idealised conditions and the dynamic response of the system to the process conditions. On one hand, it was clear that despite problems with the traditional fixturing used in IFW and deflection of the machine to the large process loads were documented, oversimplified modelling techniques that assume the process as perfectly axysimmetric with the workpieces clamped by infinitely rigid fixtures are conventionally adopted. On the other hand, despite the analysis of the machine reveals how the spindle represents a complex rotordynamic system and manufacturing processes with similarities to IFW showed that dynamic effects can have a great impact on the process evolution, no study addressed the dynamic analysis of IFW. To fill these research gaps, firstly, a novel monitoring system suitable

to characterise the machine behaviour with the in-process measurement of key aspects was developed, then a supporting methodology was devised to analyse the experimental data and extract evidence to question the axisymmetric assumption usually adopted to analyse IFW. Finally, the dynamics of the system was studied to gain an understanding of the physical causes behind the phenomena observed and how they can impact on the interaction between the workpieces. The following section will provide a summary of the main academic contributions.

7.2.1 A novel monitoring system for IFW

Section 7.1 summarised the technical aspects of the monitoring system developed, from which it is already possible to observe how this system represents a step forward compared to the other solutions presented in the literature. The key aspects introduced with the monitoring system can be summarised as follows:

- The monitoring systems available in the literature were devised to study a specific feature of the process. This approach fails in providing a holistic view of the system behaviour that, however, is necessary to address fundamental aspects of IFW, such as the non-idealised interaction of the workpieces. The approach proposed allowed to identify unexpected phenomena, while, comparing the output of different sensors measuring complementary factors at the same time, it helped in understating the physical causes behind the behaviour observed;

- Despite being developed to accommodate a certain set of sensors, the design of the monitoring system is suitable as a research platform for additional analysis. In fact, one of the biggest limitations in studying IFW is to bring the instrumentation close to the weld interface due to the limited space available and the relative motion between headstock and tailstock, which often prevents phenomena connected to the welding to be isolated from the noise of the machine. Using the backstop

rather than the machine tooling to hold the workpiece allowed the stick out of the backstops from the machine collet to be optimised to fit the desired sensors, while minimising the negative effects on the alignment of the workpieces;

- One of the main objectives while designing the monitoring system was to create a system easily scalable to compare the performance of different machines. This aspect, in fact, is not only useful from an industrial viewpoint, allowing to assess if two machines can be considered interchangeable but, most importantly, it is necessary to assess the generality of the phenomena observed. This represents a significant step forward from the works available in the literature, which always consider data from a single machine, disregarding the influence that the dynamics of the headstock or the effect of the multitude of subsystems inside the inertia welder can have on the system behaviour and the process outcomes.

7.2.2 An approach to characterise the process evolution and the system response

During the research work, two monitoring systems were developed, a first one to fit an MTI-300T machine and a second one for an MTI-2000B. The two machines differ in terms of size, build configuration, and year of construction, with the smaller and more recent MTI-300T that presents flywheels located in between the bearings that support the spindle while the MTI-2000B has flywheels installed in a cantilever configuration. Despite the geometrical differences, however, the two monitoring systems were designed to provide comparable data. For both systems, a set of rundown tests and steel welds were carried out to extract experimental data. One of the biggest challenges was to devise a methodology capable of dealing with a large amount of data, filter out undesired components and highlight the physical causes behind the system behaviour, with an approach that could be applied sequentially to all the tests to ensure that the

outcomes were not affected by inconsistencies in the methodology. From this analysis the following observations can be drawn:

- The analysis of the evolution of the alignment between headstock and tailstock showed that, during the rundown tests, the spindle was characterised by a runout in phase with the angular speed and a magnitude approximately constant, which was explained with the spindle rotating out of axis due to geometrical errors and clearance in the key elements of the headstock, such as bearings. During welding, oscillations up to five times the values in the rundown tests and no longer in phase with the spindle speed were measured. This change could be attributed mainly to the compliance of the machine to the loads induced by the interaction of the two workpieces. Comparing the data from the MTI-300T and the MTI-2000B machines, the MTI-2000B showed a smaller and more regular runout compared to the MTI-300T, which can be explained considering the larger size of this machine and, consequently, higher stiffness. In addition, the comparison of the runout magnitude showed how this can vary from machine to machine depending on how well the spindle is centred and the headstock stiffness;

- The axial strain showed large variations in the circumferential direction for both machines even if with different behaviour. For the MTI-300T, large strain oscillations were observed during the conditioning and the burnoff phases, while the MTI-2000B, showed smaller strain oscillations and mainly localised in the conditioning phase. This behaviour, similar to what observed for the runout, suggests a correlation between the runout and non-axisymmetric loads, with the workpieces that, when not perfectly aligned, generate non-axisymmetric loads, which cause deflections in the system and, consequently, larger misalignments. In addition, the drop in variability at the beginning of the consolidation phase can be justified considering that when the weld cools down and gains strength,

its constraining action prevents large relative displacements between headstock and tailstock and strain variability;

- Despite being a parameter of primary importance on the response of the machine, the radial stiffness of the headstock is typically not known. In fact, while the machine manufacturers can provide information on the stiffness of the bearings that support the spindle, this can vary significantly depending on the bearing clearance, lubrication and wear. For this reason, an inverse approach to calculate an equivalent radial stiffness of the headstock starting from the data of runout and strain was devised. Applying the technique to the MTI-300T, a radial stiffness of 10^8 N/m was obtained, a value that suggests the bearings that support the spindle are the critical element in the system compliance. This technique can prove particularly useful for periodic inspection of the system health.

7.2.3 Analysis of the dynamic response of the system to the process conditions

The machine for IFW is characterised by a spindle carrying flywheels of large inertia supported by a combination of radial and axial bearings, which rotates at relatively high and non-constant angular speed and is subject to significantly high process loads induced by the interaction of the two workpieces pressed together by a ram. Considering, in addition, the rapidly evolving conditions at the weld interface, it is clear the machine for IFW is a complex dynamic system. Despite a large number of articles published in the literature have highlighted that for machine tools properties like the dimensional accuracy and surface finish of the process outcomes are directly connected to the dynamic properties of the system, no study carried a rigorous analysis on the dynamics of IFW. To fill this research gap, firstly, the impact between the two workpieces at part contact and the torsional oscillations when the spindle is about to stop were analysed,

describing the dynamics of the system with the theory of oscillators. Then the runout evolution and its relationship with the pressure distribution at the weld interface were analysed. After having devised an approach to convert the equivalent pressure distribution calculated from the output of lasers and strain gauges into equivalent process loads, the rotordynamics of the spindle was studied to analyse the contribution of the dynamic components and the process loads on the runout evolution during welding. The main conclusions of this analysis can be summarised as follows:

- The study of the vibrational behaviour suggested that the impact at part contact and the torsional oscillations in the last instants of rotation of the spindle are particularly important, showing the peak vibrations in the axial and torsional directions respectively. The dynamic analysis of the two phenomena showed that modulating the load exerted by the ram, tuning the stiffness and damping of the machine, the axial vibrations at part contact can be minimised. To reduce the torsional oscillations, detrimental to the newly formed joint because resulting in a high frequency impulse while it has not yet acquired full strength, it is possible to optimise the flywheel inertia, the torsional stiffness of the joint and the viscous damping in the bearings. However, considering the inertia welder, differently from a CFDW machine, is not equipped with an external brake, makes it impossible to completely remove the torsional oscillations;

- To investigate the correlation between the non-ideal alignment of the workpieces and the conditions at the weld interface, a novel approach to compute the equivalent weld pressure was devised. A large pressure variability in circumferential direction during the conditioning and the burnoff phases was observed, while more constant values were obtained for the consolidation phase. Converting the pressure field into equivalent process loads, large radial components and bending moments were obtained, with peak values for the MTI-300T almost 40%

of the experimental peak axial load and torque respectively. Therefore, while the axisymmetric assumption can hold in an average sense, when local effects at the weld interface or the precise evaluation of the loading conditions need to be studied, the 3D modelling of the system with workpieces interacting in non-ideal conditions can be necessary. In addition, the correlation between misalignment and pressure gradient at the weld interface stresses the importance of having a rigid and well-balanced headstock to minimise temperature gradients, hotspots, uneven expulsion of flash and, consequently, variation in the joint properties in the circumferential direction;

- A 3D dynamic representation of the machine spindle was developed to gain an understanding of the physical causes behind the dynamic response of the system to the process conditions and shed light on the runout evolution. The results showed that rotordynamic phenomena, such as gyroscopic moments and centrifugal forces, were negligible on the behaviour of the spindle, confirming how the machine stiffness and the process loads had the greatest influence on runout evolution. The versatility of the approach makes it suitable to compare the dynamic behaviour of different IFW systems and improve their dynamic response.

7.3 Future work

The research work allowed to develop a novel monitoring system and a support methodology that challenged the traditional approach of treating IFW as a perfectly axisymmetric process, observing how the interaction between the machine and the process conditions produces non-negligible effects. The good contributions to the field

have opened opportunities to further research, some areas with particular potential are here summarised:

Using the monitoring system as a platform for further analysis

- In this study, the workpieces used were of simplified geometry and produced in steel. An aspect worth investigating is the effect that other materials and specific workpiece geometries can have on the process evolution, an aspect particularly important for the new generation superalloys, whose extremely high resistance at high temperature makes it difficult to join. In addition, the versatility of the system could foster the study for better techniques to characterise the weld evolution, allowing researchers to install sensors in proximity of the weld zone, which is not reachable with the default setup;

Correlation between the experimental data and the weld quality

- The approach developed focuses on the machine behaviour rather than on the characteristics of the weld. Linking the data measured by the monitoring system with the macrostructural, microstructural and mechanical properties of the weld would have a great academic and industrial impact. In particular, knowing the runout evolution and the equivalent pressure at the weld interface, it could be possible to obtain the corresponding temperature field and understand its variation in the circumferential direction;

- The monitoring system developed can be extended as an in-process approach and use the data of runout and other complementary parameters to optimise the machine setup in order to minimise the headstock/tailstock misalignment on the final welded assembly and avoid hotspots;

Assessment of the error associated with the axisymmetric assumption in the numerical modelling of IFW

- Several aspects in disagreement with the axisymmetric hypothesis conventionally adopted in the numerical study of IFW were presented. Researchers, starting from these considerations, can quantify the difference between numerical models developed under the axisymmetric assumption and a full 3D representation of the system, taking into account aspects like the compliance of the system and the non-perfect alignment between the two workpieces. This would allow deciding in which cases the simpler axisymmetric formulation is justified and when more realistic results could be obtained with a 3D modelling.

References

[1] *Boeing Reports Record 2018 Results and Provides 2019 Guidance*. Tech. rep. Boeing, Jan. 2019.

[2] *Annual Review 2018*. Tech. rep. IATA, June 2018.

[3] *Vision 2050*. Tech. rep. IATA, Feb. 2011.

[4] B. Smith. "The Boeing 777". In: *Advanced Materials and Processes* (2003).

[5] F.C. Campbell. *Manufacturing Technology for Aerospace Structural Materials*. Aerospace engineering materials science. Elsevier Science, 2011.

[6] S. Zhang and D. Zhao. *Aerospace Materials Handbook*. CRC Press, 2013, p. 781.

[7] M. M. Attallah. "Inertia friction welding (IFW) for aerospace applications". In: *Welding and joining of aerospace materials* (2012), pp. 25–74.

[8] C. J Bennett. "Inertia Friction Welding of High Strength Aerospace Alloys". PhD thesis. University of Nottingham, 2007, p. 205.

[9] A. Z. Sahin et al. "Analysis of the friction welding process in relation to the welding of copper and steel bars". In: *Journal of Materials Processing Technology* 82 (1998), pp. 127–136.

[10] M. Preuss et al. "Inertia Welding Nickel-Based Superalloy: Part II. Residual Stress Characterization". In: *Metallurgical and Materials Transactions A* 33.10 (2002), pp. 3227–3234.

[11] O. N. Senkov, D. W. Mahaffey, and S. L. Semiatin. "Effect of Preheating on the Inertia Friction Welding of the Dissimilar Superalloys Mar-M247 and LSHR". In: *Metallurgical and Materials Transactions A: Physical Metallurgy and Materials Science* 45A (2014), pp. 5545–5561.

[12] A. Chamanfar, M. Jahazi, and J. Cormier. "A Review on Inertia and Linear Friction Welding of Ni-Based Superalloys". In: *Metallurgical and Materials Transactions A* 46 (2015), pp. 1639–1669.

[13] O. N. Senkov, D. W. Mahaffey, and S. L. Semiatin. "A Comparison of the Inertia Friction Welding Behavior of Similar and Dissimilar Ni-Based Superalloys". In: *Metallurgical and Materials Transactions A* 49 (2018), pp. 5428–5444.

[14] A. Francis and R. E. Craine. "On a model for frictioning stage in friction welding of thin tubes". In: *International Journal of Heat and Mass Transfer* 28.9 (1985), pp. 1747–1755.

[15] A. Słżalec and A. Służalec. "Solutions of thermal problems in friction welding—comparative study". In: *International Journal of Heat and Mass Transfer* 36.6 (1993), pp. 1583–1587.

[16] A. Sluzalec. “Thermal effects in friction welding”. In: *International journal of mechanical sciences* 32.6 (1990), pp. 467–478.

[17] K. Wang and P. Nagappan. “Transient temperature distribution in inertia friction welding of steels”. In: *Welding Journal* 49.9 (1970), pp. 419–426.

[18] A. Moal and E. Massoni. “Finite Element Simulation Of The Inertia Welding Of Two Similar Parts”. In: *Engineering Computations* 12.6 (1995), pp. 497–512.

[19] L. D’alvise, E. Massoni, and S. J. Walløe. “Finite element modelling of the inertia friction welding process between dissimilar materials”. In: *Journal of Materials Processing Technology* 126 (2002), pp. 387–391.

[20] V. Balasubramanian et al. “An Energy Balance Method for the Numerical Simulation of Inertia Welding”. In: *Materials and Manufacturing Processes* 4.5 (1999), pp. 755–773.

[21] V.R. Dave, M.J. Cola, and G.N. Hussein. “Heat generation in the inertia welding of dissimilar tubes”. In: *Welding Journal* 80.10 (2001), pp. 246–252.

[22] B. Grant et al. “Finite element process modelling of inertia friction welding advanced nickel-based superalloy”. In: *Materials Science and Engineering A* 513-514.C (2009), pp. 366–375.

[23] L Wang et al. “Energy-Input-Based Finite-Element Process Modeling of Inertia Welding”. In: *Metallurgical and Materials Transactions B* 36.August (2005), pp. 513–523.

[24] C. J. Bennett et al. “Finite element modeling of the inertia friction welding of dissimilar high-strength steels”. In: *Metallurgical and Materials Transactions A: Physical Metallurgy and Materials Science* 44.11 (2013), pp. 5054–5064.

[25] O. N. Senkov et al. “Efficiency of the Inertia Friction Welding Process and Its Dependence on Process Parameters”. In: *Metallurgical and Materials Transactions A* 48 (2017), pp. 3328–3342.

[26] D. J. Tung et al. “Transient behaviour of torque and process efficiency during inertia friction welding”. In: *Science and Technology of Welding and Joining* 1718 (2018), pp. 1–12.

[27] J. Grooms and C. W. Carrier. *Friction weld vibration quality monitoring system and methods*. US Patent 8,196,800. 2011.

[28] K. K. Wang, G. R. Reif, and S K Oh. “In-Process Quality Detection of Friction Welds Using Acoustic Emission Techniques”. In: *Welding Research Supplement* 313 (1982), pp. 1–5.

[29] D. A. Hartman et al. “Nondestructive, in-process inspection of inertia friction welding: an investigation into a new sensing technique”. In: *6th International Conference on Trends in Welding Research*. 2002, pp. 1–4.

[30] D. A. Hartman et al. *Method and apparatus for in-process sensing of manufacturing quality*. US 6857553B1. Feb. 2003.

[31] J. W. L. Pang et al. “Effects of tooling on the residual stress distribution in an inertia weld”. In: *Materials Science and Engineering A* A356 (2003), pp. 405–413.

[32] M. Karadge et al. “Thermal relaxation of residual stresses in nickel-based superalloy inertia friction welds”. In: *Metallurgical and Materials Transactions A: Physical Metallurgy and Materials Science* 42A (2011), pp. 2301–2311.

[33] O. Iracheta, C. J. Bennett, and W. Sun. “A sensitivity study of parameters affecting residual stress predictions in finite element modelling of the inertia friction welding process”. In: *International Journal of Solids and Structures* 71 (2015), pp. 180–193.

[34] E. Bayer and W. Steffen. *Damping device, welding system for rotary friction welding and rotary friction welding method*. EP2173516A2. July 2007.

[35] T. J. Sweeting. *Friction welding vibration damping*. US9884388B2. Mar. 2016.

[36] S. E. Bray and A. R. Walpole. *Rotary Friction Welding*. US 9791075B2. Oct. 2017.

[37] M. Maalekian. “Friction welding – critical assessment of literature”. In: *Science and Technology of Welding and Joining* (2007).

[38] *Welding – Friction welding of metallic materials*. Standard. Geneva, CH: International Organization for Standardization, May 2019.

[39] M. H. Parsa et al. “Thermo-Mechanical Calculations of Hybrid Rotary Friction Welding at Equal Diameter Copper Bars”. In: *AIP Conference Proceedings 908*. AIP Publishing Articles, 2007, pp. 1105–1110.

[40] W. Li et al. “Linear and rotary friction welding review”. In: *International Materials Reviews* 61.2 (2016), pp. 71–100.

[41] H. Ates, M. Turker, and A. Kurt. “Effect of friction pressure on the properties of friction welded MA956 iron-based superalloy”. In: *Materials and Design* 28.3 (2007), pp. 948–953.

[42] M. Sahin. “Evaluation of the joint-interface properties of austenitic-stainless steels (AISI 304) joined by friction welding”. In: *Materials and Design* 28.7 (2007), pp. 2244–2250.

[43] M. Sahin, H. E. Akata, and K. Ozel. “An experimental study on joining of severe plastic deformed aluminium materials with friction welding method”. In: *Materials and Design* 29.1 (2008), pp. 265–274.

[44] H. C. Dey et al. “Joining of titanium to 304L stainless steel by friction welding”. In: *Journal of Materials Processing Technology* 209.18 (2009), pp. 5862–5870.

[45] P. Sammaiah, A. Suresh, and G. R. N. Tagore. “Mechanical properties of friction welded 6063 aluminum alloy and austenitic stainless steel”. In: *Journal of Materials Science* 45.20 (2010), pp. 5512–5521.

[46] M. B Mohammed et al. “The Evaluation of Coefficient of Friction for Representative and Predictive Finite Element Modelling of the Inertia Friction Welding”. In: *Proceedings of the ASME Turbo Expo 2009: Power for Land, Sea, and Air*. ASME, 2009, pp. 829–837.

[47] C. J. Bennett. “Finite element modelling of the inertia friction welding of a CrMoV alloy steel including the effects of solid-state phase transformations”. In: *Journal of Manufacturing Processes* 18 (2015), pp. 84–91.

[48] D. W. Mahaffey et al. “Effect of Process Variables on the Inertia Friction Welding of Superalloys LSHR and Mar-M247”. In: *Metallurgical and Materials Transactions A* 47A (2016), pp. 3981–4000.

[49] V. I. Vill’. *Friction welding of metals*. American Welding Society; trade distributor: Reinhold Pub. Co., 1962.

[50] T. Rich and R. Roberts. “Thermal Analysis for Basic Friction Welding”. In: *Metal Construction and British Welding Journal* 3 (1071), pp. 93–98.

[51] L. Yang. “Modelling of the Inertia Welding of Inconel 718”. PhD thesis. University of Birmingham, 2010, p. 115.

[52] V. Balasubramanian et al. “A new friction law for the modelling of continuous drive friction welding: Applications to 1045 steel welds”. In: *Materials and Manufacturing Processes* 14.6 (1999), pp. 845–860.

[53] C. J. Bennett, T. H. Hyde, and E. J. Williams. “Modelling and simulation of the inertia friction welding of shafts”. In: *Proceedings of the Institution of Mechanical Engineers, Part L: Journal of Materials: Design and Applications* 221.4 (2007), pp. 275–284.

[54] *Friction Welding Brochure*. Tech. rep. Manufacturing Technology, Inc., 1999, p. 60.

[55] T. L. Oberle et al. *Method of bonding metal workpieces*. US Patent 3,273,233. Sept. 1966.

[56] C. E. Lipp et al. *Friction welding machine with storage means for inertial masses*. US Patent 3,349,982. Oct. 1967.

[57] M. B. Hollander. *Friction bonding method and apparatus*. US Patent 3,235,158. Feb. 1966.

[58] M. B. Hollander. *Friction welding*. US Patent 3,235,162. Feb. 1966.

[59] A. Woodall and C. H. Brian. *Friction welding or like machines*. US Patent 3,717,295. 1971.

[60] E. Jones. *Friction welding machine*. US Patent 4,043,496. Aug. 1977.

[61] A. Harnoy. *Bearing Design in Machinery: Engineering Tribology and Lubrication*. Dekker Mechanical Engineering. Taylor & Francis, 2002. ISBN: 9780824744007.

[62] L. Kashchenevsky. *Hydrostatic arrangement for a spin welding machine and method of supporting spindle for the same*. US 2012/0070108A1. 2011.

[63] K. A. Desai, P. K. Agarwal, and P. V. M. Rao. “Process geometry modeling with cutter runout for milling of curved surfaces”. In: *International Journal of Machine Tools and Manufacture* 49.12 (2009), pp. 1015–1028.

[64] G. Urbikain, E. Artetxe, and L. N. López de Lacalle. “Numerical simulation of milling forces with barrel-shaped tools considering runout and tool inclination angles”. In: *Applied Mathematical Modelling* 47 (2017), pp. 619–636.

[65] E. F. Taylor and J. A. Wheeler. *Spacetime Physics*. W. H. Freeman, 1992, p. 312.

[66] C. D. Loyd. *Method of friction welding*. US Patent 3,694,896. Oct. 1972.

[67] J. L. Farley, H. L. Gerecke, and E. S. Nickel. *Collet chuck for inertia welders*. US Patent 3,512,792. 1967.

[68] J. L. Farley, M. R. Eugene, and S. H. Ira. *Dual chuck assembly for inertia welding*. US Patent 3,542,383. Nov. 1970.

[69] Calvin D. Loyd. *Friction welding chuck assembly*. US Patent 3,606,968. Sept. 1971.

[70] A.N. Hunter. *Apparatus for friction welding*. US Patent App. 13/668,605. June 2013.

[71] A. Y. C. Nee, K. Whybrew, and A. S. Kumar. *Advanced Fixture Design for FMS*. Advanced Manufacturing. Springer London, 2012.

[72] D. F. Eary and G. E. Johnson. *Process engineering for manufacturing*. Prentice-Hall, 1962.

[73] G. W. Deemie and I. H. Sage. *Backstop extension for friction welder*. US Patent 3,439,853. Apr. 1969.

[74] M. F. Zaeh and A. Poehler. "Vibrations in friction welding". In: *Production Engineering - Research and Development* 5 (2011), pp. 159–165.

[75] D. A. Hartman and T. J. Lienert. "Process Monitoring and Control of Rotary Friction Welding". In: *Welding Fundamentals and Processes*. ASM International, Oct. 2011.

[76] D. A. Hartman et al. *Method and apparatus for in-process sensing of manufacturing quality*. US Patent 6,857,553. Feb. 2005.

[77] D. A. Hartman et al. "Acoustic Monitoring of Inertia Friction Welded Austenitic Stainless Steels: Initial Studies". In: *FABTECH International & AWS Welding Show*. 2007, pp. 1–4.

[78] J. Grooms, C. W. Carrier, and C. W. Carrier. *Friction weld system and method with vibration quality monitoring means*. CA2748255 C. 2017.

[79] C. Carrier et al. *Method and apparatus for reducing component vibration during inertia welding*. US Patent App. 10/309,855. June 2004.

[80] J. R. Bell and S. J. Rothberg. "Laser Vibrometers and Contacting Transducers, Target Rotation and Six Degree-of-Freedom Vibration: What Do We Really Measure?" In: *Journal of Sound and Vibration* 237.2 (2000), pp. 245–261.

[81] N.A. Halliwell. "The Laser Torsional Vibrometer: A Step Forward in Rotating Machinery Diagnostics". In: *Journal of Sound and Vibration* 190.3 (1996), pp. 399–418.

[82] X. Yao et al. *Device for detecting data of inertia friction welder*. CN201335674Y. 2008.

[83] X. Yao et al. *Data detecting device of inertia friction welding machine*. CN101750003A. 2008.

[84] W. J. Rankine. "On the centrifugal force of rotating shafts". In: *Engineer* 27 (1869), p. 249.

[85] H. Cao et al. "Mechanical model development of rolling bearing-rotor systems: A review". In: *Mechanical Systems and Signal Processing* 102 (Mar. 2018), pp. 37–58.

[86] S. P. Harsha. "Nonlinear dynamic analysis of an unbalanced rotor supported by roller bearing". In: *Chaos, Solitons and Fractals* 26.1 (Oct. 2005), pp. 47–66.

[87] A. Moazen Ahmadi, D. Petersen, and C. Howard. "A nonlinear dynamic vibration model of defective bearings - The importance of modelling the finite size of rolling elements". In: *Mechanical Systems and Signal Processing* 52-53.1 (2015), pp. 309–326.

[88] A. B. Jones. "A general theory for elastically constrained ball and radial roller bearings under arbitrary load and speed conditions". In: *Journal of Fluids Engineering, Transactions of the ASME* 82.2 (1960), pp. 309–320.

[89] J. M. de Mul, J. M. Vree, and D. A. Maas. "Equilibrium and associated load distribution in ball and roller bearings loaded in five degrees of freedom while neglecting friction—Part I: General theory and application to ball bearings". In: *Journal of Tribology* 111.1 (1989), pp. 142–148.

[90] J. M. de Mul, J. M. Vree, and D. A. Maas. "Equilibrium and associated load distribution in ball and roller bearings loaded in five degrees of freedom while neglecting friction - part II: application to roller bearings and experimental verification." In: *Journal of Tribology* 111 (1989), pp. 149–155.

[91] T. A. Harris. *Rolling bearing analysis*. 4th ed. John Wiley & Sons, Inc., 2001, p. 1086.

[92] T. A. Harris and M. H. Mindel. "Rolling element bearing dynamics". In: *Wear* 23.3 (1973), pp. 311–337.

[93] P. K. Gupta. "Dynamics of Rolling-Element Bearings—Part I: Cylindrical Roller Bearing Analysis". In: *Journal of Lubrication Technology* 101.3 (July 1979), pp. 293–302.

[94] P. K. Gupta. "Dynamics of Rolling-Element Bearings—Part II: Cylindrical Roller Bearing Results". In: *Journal of Lubrication Technology* 101.3 (July 1979), pp. 305–311.

[95] P. K. Gupta. "Dynamics of Rolling-Element Bearings—Part III: Ball Bearing Analysis". In: *Journal of Lubrication Technology* 101.3 (July 1979), pp. 312–318.

[96] P. K. Gupta. "Dynamics of Rolling-Element Bearings—Part IV: Ball Bearing Results". In: *Journal of Lubrication Technology* 101.3 (July 1979), pp. 319–326.

[97] Y. Guo and R. G. Parker. "Stiffness matrix calculation of rolling element bearings using a finite element/contact mechanics model". In: *Mechanism and Machine Theory* 51 (2012), pp. 32–45.

[98] A. D. Dimarogonas, S. A. Paipetis, and T. G. Chondros. *Analytical Methods in Rotor Dynamics*. Springer Netherlands, 2013, p. 274.

[99] C. B. Gan et al. "Nonparametric modeling and vibration analysis of uncertain Jeffcott rotor with disc offset". In: *International Journal of Mechanical Sciences* 78 (Jan. 2014), pp. 126–134.

[100] G. Genta. *Dynamics of Rotating Systems (Mechanical Engineering Series)*. 1st ed. Springer-Verlag New York, 2006, pp. 1–674.

[101] C. W. Lin, Y. K. Lin, and C. H. Chu. "Dynamic Models and Design of Spindle-Bearing Systems of Machine Tools: A Review". In: *International Journal of Precision Engineering and Manufacturing* 14.3 (2013), pp. 513–521.

[102] E. Abele, Y. Altintas, and C. Brecher. "Machine tool spindle units". In: *CIRP Annals - Manufacturing Technology* 59.2 (2010), pp. 781–802.

[103] J. G. Bollinger and G. Geiger. "Analysis of the static and dynamic behavior of lathe spindles". In: *International Journal of Machine Tool Design and Research* 3.November 1963 (1964), pp. 193–209.

[104] A. M. Sharan, S. Sankar, and T. S. Sankar. "Dynamic analysis and optimal selection of parameters of a finite element modeled lathe spindle under random cutting forces". In: *Journal of Vibration and Acoustics, Transactions of the ASME* 105.4 (1983), pp. 467–475.

[105] V. R. Reddy and A. M. Sharan. "The finite element modelled design of lathe spindles: The static and dynamic analyses". In: *Journal of Vibration and Acoustics, Transactions of the ASME* 109.4 (1987), pp. 407–415.

[106] S. M. Han, H. Benaroya, and T. Wei. "Dynamics of Transversely Vibrating Beams Using Four Engineering Theories". In: *Journal of sound and vibration* 225.5 (1999), pp. 935–988.

[107] X. Sheng et al. "Calculation of ball bearing speed-varying stiffness". In: *Mechanism and Machine Theory* 81 (2014), pp. 166–180.

[108] Y. Cao and Y. Altintas. "A general method for the modeling of spindle-bearing systems". In: *Journal of Mechanical Design, Transactions of the ASME* 126.6 (2004), pp. 1089–1104.

[109] Y. Cao and Y. Altintas. "Modeling of spindle-bearing and machine tool systems for virtual simulation of milling operations". In: *International Journal of Machine Tools and Manufacture* 47.9 (July 2007), pp. 1342–1350.

[110] Y. Altintas and Y. Cao. "Virtual Design and Optimization of Machine Tool Spindles". In: *CIRP Annals* 54.1 (2005), pp. 379–382.

[111] H. Cao, T. Holkup, and Y. Altintas. "A comparative study on the dynamics of high speed spindles with respect to different preload mechanisms". In: *International Journal of Advanced Manufacturing Technology* 57.9-12 (2011), pp. 871–883.

[112] X. Zhang et al. "A comprehensive dynamic model to investigate the stability problems of the rotor-bearing system due to multiple excitations". In: *Mechanical Systems and Signal Processing* 70-71 (Mar. 2016), pp. 1171–1192.

[113] H. Wang, Q. Han, and D. Zhou. "Nonlinear dynamic modeling of rotor system supported by angular contact ball bearings". In: *Mechanical Systems and Signal Processing* 85 (Feb. 2017), pp. 16–40.

[114] K. Xu et al. "The influence of rolling bearing parameters on the nonlinear dynamic response and cutting stability of high-speed spindle systems". In: *Mechanical Systems and Signal Processing* 136 (Feb. 2020).

[115] M. Namazi et al. "Modeling and identification of tool holder-spindle interface dynamics". In: *International Journal of Machine Tools and Manufacture* 47.9 (July 2007), pp. 1333–1341.

[116] H. Cao, B. Li, and Z. He. "Chatter stability of milling with speed-varying dynamics of spindles". In: *International Journal of Machine Tools and Manufacture* 52.1 (Jan. 2012), pp. 50–58.

[117] M. R. Movahhedy and P. Mosaddegh. "Prediction of chatter in high speed milling including gyroscopic effects". In: *International Journal of Machine Tools and Manufacture* 46.9 (July 2006), pp. 996–1001.

[118] *History of the MTI Welding*. https://www.mtiwelding.com/timeline. Accessed: 2018-06-15. 2018.

[119] F. P. Bowden, A. J.W. Moore, and D. Tabor. "The ploughing and adhesion of sliding metals". In: *Journal of Applied Physics* 14.2 (1943), pp. 80–91.

[120] R. Hill, E. H. Lee, and S. J. Tupper. "The theory of wedge indentation of ductile materials B". In: *Proceedings of the Royal Society A* 188 (1945), pp. 273–290.

[121] D. S. Dugdale. "Wedge indentation experiments with cold-worked metals". In: *Journal of the Mechanics and Physics of Solids* 2 (1953), pp. 14–26.

[122] J. Liu, Q. Zeng, and S. Xu. "The state-of-art in characterizing the micro/nano-structure and mechanical properties of cement-based materials via scratch test". In: *Construction and Building Materials* 254 (2020), p. 119255.

[123] M. E. Merchant. "Mechanics of the metal cutting process. I. Orthogonal cutting and a type 2 chip". In: *Journal of Applied Physics* 16.5 (1945), pp. 267–275.

[124] M. Eugene Merchant. "Mechanics of the metal cutting process. II. Plasticity conditions in orthogonal cutting". In: *Journal of Applied Physics* 16.6 (1945), pp. 318–324.

[125] E. I. Moser. "A Study of the Quasi-Frictional Forces Resulting on Serrated Clamping Elements". PhD thesis. The Rice Institute, 1955, p. 81.

[126] J. Li and W. Beres. "Three-dimensional finite element modelling of the scratch test for a TiN coated titanium alloy substrate". In: *Wear* 260.11 (2006), pp. 1232–1242.

[127] N. Schwarzer et al. "Optimization of the Scratch Test for specific coating designs". In: *Surface and Coatings Technology* 206.6 (2011), pp. 1327–1335.

[128] R. Turner et al. "Linear friction welding of Ti-6Al-4V: Modelling and validation". In: *Acta Materialia* 59 (2011), pp. 3792–3803.

[129] D.L. Martin, A.N. Tabenkin, and F.G. Parsons. "Precision spindle and bearing error analysis". In: *International Journal of Machine Tools and Manufacture* 35.2 (Feb. 1995), pp. 187–193.

[130] S. Xi, H. Cao, and X. Chen. "Dynamic modeling of spindle bearing system and vibration response investigation". In: *Mechanical Systems and Signal Processing* 114 (Jan. 2019), pp. 486–511.

[131] D. A. Stephenson and J. S. Agapiou. *Metal Cutting Theory and Practice*. Manufacturing engineering and materials processing. Taylor & Francis, 2005, p. 864.

[132] V. P. Astakhov. *Drills: Science and Technology of Advanced Operations*. Manufacturing Design and Technology. Taylor & Francis, 2014, p. 888.

[133] G. Henzold. *Geometrical Dimensioning and Tolerancing for Design, Manufacturing and Inspection: A Handbook for Geometrical Product Specification using ISO and ASME standards*. 2nd ed. Elsevier Science, 2006.

[134] K. W. Chase and A. R. Parkinson. "A Survey of Research in the Application of Tolerance Analysis to the Design of Mechanical Assemblies". In: *Research in Engineering Design* 3 (1991), pp. 23–37.

[135] K. W. Chase et al. "Including Geometric Feature Variations in Tolerance Analysis of Mechanical Assemblies". In: *IIE Transactions* 28.10 (1996), pp. 795–807.

[136] H. Yan, X. Wu, and J. Yang. "Application of Monte Carlo method in tolerance analysis". In: *Procedia CIRP* 27 (2015), pp. 281–285.

[137] E. M. Mansoor. "The Application of Probability to Tolerances Used in Engineering Designs". In: *Proceedings of the Institution of Mechanical Engineers* 178.1 (1963), pp. 29–39.

[138] D. B. Parkinson. "Tolerancing of component dimensions in CAD". In: *Computer-Aided Design* 16.1 (1984), pp. 25–32.

[139] R. C. Juvinall and K. M. Marshek. *Fundamentals of Machine Component Design*. 6th ed. Wiley, 2017, p. 742.

[140] British Iron et al. *The Mechanical and Physical Properties of the British Standard En Steels (B. S. 970-1955)*. The Mechanical and Physical Properties of the British Standard En Steels. Pergamon Press, 1966.

[141] A. M. Taylor. "American Institute of Physics Handbook". In: *Physics Bulletin* 15.10 (Oct. 1964), p. 2126.

[142] F. Cverna and Committee. *Worldwide Guide to Equivalent Irons and Steels*. Materials data series. ASM International, 2006, p. 1407.

[143] *Metallic materials – Conversion of hardness values*. Standard. Geneva, CH: International Organization for Standardization, Oct. 2013.

[144] J. Shieh et al. "The selection of sensors". In: *Progress in Materials Science* 46.3 (2001), pp. 461–504.

[145] S. J. Orfanidis. *Introduction to Signal Processing*. Prentice Hall international editions. Prentice Hall, 1996, p. 798.

[146] F. Levinzon. *Piezoelectric Accelerometers with Integral Electronics*. SpringerLink: Bücher. Springer International Publishing, 2014, p. 169.

[147] N. E. Huang et al. "The empirical mode decomposition and the Hilbert spectrum for nonlinear and non-stationary time series analysis". In: *Royal Society of London Proceedings Series A* 454.1 (1996), pp. 903–995.

[148] S. K. Mitra. *Digital Signal Processing: A Computer-based Approach*. 4th ed. Connect, learn, succeed. McGraw-Hill, 2011, p. 940.

[149] I. Daubechies. *Ten Lectures on Wavelets*. Society for Industrial and Applied Mathematics, 1992, p. 350.

[150] J. G. Webster. *The Measurement, Instrumentation, and Sensors: Handbook*. Electrical engineering handbook series. CRC Press, 1999, p. 2506.

[151] R. L. Hannah and S. E. Reed. *Strain Gage Users' Handbook*. Springer Netherlands, 1992, p. 476.

[152] National Instruments. *Connecting Strain Gauges and Shunt Resistors to the NI-9237*. 2020. URL: https://knowledge.ni.com/KnowledgeArticleDetails?id=kA00Z000000PA73SAG&l=en-GB (visited on 02/26/2020).

[153] H. Cao et al. "Mechanical model development of rolling bearing-rotor systems: A review". In: *Mechanical Systems and Signal Processing* 102 (2018), pp. 37–58.

[154] Z. K. Peng, P. W. Tse, and F. L. Chu. "A comparison study of improved Hilbert–Huang transform and wavelet transform: Application to fault diagnosis for rolling bearing". In: *Mechanical Systems and Signal Processing* 19.5 (2005), pp. 974–988.

[155] G. Kerschen et al. "Past, present and future of nonlinear system identification in structural dynamics". In: *Mechanical Systems and Signal Processing* 20.3 (2006), pp. 505–592.

[156] S. C. Olhede and A. T. Walden. "Generalized Morse wavelets". In: *IEEE Transactions on Signal Processing* 50.11 (Nov. 2002), pp. 2661–2670.

[157] J. M. Lilly and S. C. Olhede. "On the Analytic Wavelet Transform". In: *IEEE Transactions on Information Theory* 56.8 (Aug. 2010), pp. 4135–4156.

[158] W. Goldsmith. *Impact: The Theory And Physical Behaviour Of Colliding Solids*. Edward Arnold, 1960, p. 379.

[159] H. M. Lankarani and P. E. Nikravesh. "Continuous contact force models for impact analysis in multibody systems". In: *Nonlinear Dynamics* 5.2 (1994), pp. 193–207.

[160] A. B. Pippard. *The Physics of Vibration*. Cambridge University Press, 1989.

[161] E. I. Butikov. "Spring pendulum with dry and viscous damping". In: *Communications in Nonlinear Science and Numerical Simulations* 20 (Jan. 2015), pp. 298–315.

[162] D. G. Alciatore. *Introduction to Mechatronics and Measurement Systems*. 2nd ed. McGraw-Hill, 2003.

[163] Scientific Forming Technologies Corporation. *DEFORM™-2D, Version 8.1*. 2018.

[164] J. J. Connor and S. Faraji. *Fundamentals of Structural Engineering*. 2nd ed. SpringerLink : Bücher. Springer New York, 2012.

[165] R. Zeillinger, H. Springer, and H. Kottritsch. "Experimental Determination of Damping in Rolling Bearing Joints". In: *Proceedings from the International Gas Turbine and Aeroengine Congress and Exposition* (1994).

[166] D. A. Bompos and P. G. Nikolakopoulos. "Journal Bearing Stiffness and Damping Coefficients Using Nanomagnetorheological Fluids and Stability Analysis". In: *ASME Journal of Tribology* 136.4 (2014).

[167] Y. Ishida and T. Yamamoto. *Linear and Nonlinear Rotordynamics: A Modern Treatment with Applications, Second Edition*. 2012.

[168] B. J. Stone. “The State of the Art in the Measurement of the Stiffness and Damping of Rolling Element Bearings”. In: *CIRP Annals - Manufacturing Technology* 31.2 (1982), pp. 529–538.

[169] W. Jacobs et al. “The influence of the lubricant film on the stiffness and damping characteristics of a deep groove ball bearing”. In: *Mechanical Systems and Signal Processing* 42.1-2 (Jan. 2014), pp. 335–350.

[170] *Multiple Output Linear D.C. Power Supply*. IPS-4303. RS PRO.

[171] *Power Supply - NI PS-14 Power Supply User Manual*. NI PS-14. National Instruments. Oct. 2013.

[172] *Getting Started Guide - NI cRIO-9066 - Embedded Real-Time Controller with Reconfigurable FPGA for C Series Modules*. NI cRIO-9066. National Instruments. Oct. 2015.

[173] *Data Sheet LK-G32 - Sensor Head Spot Type, Laser Class 2*. LK-G32. Keyence.

[174] *Data Sheet LK-031 - Sensor Head , Small Spot*. LK-G32. Keyence.

[175] *LVDT Signal Conditioner*. AD598. Rev. A. Analog Devices.

[176] *Guidance on the safe use of lasers in education and research*. AURPO Guidan ce Note No. 7 - 2018 Revised Edition. Association of University Radiation Protection Officers. Feb. 2018.

[177] *Instruction Manual - Ceramic Shear Triaxial IEPE Accelerometers - Types 8762A..., 8763B..., 8764B...* 8764B050B. Kistler.

[178] M. Bauccio. *ASM Metals Reference Book*. 3rd ed. ASM International, 1993, p. 614.

[179] A. Can, M. Sahin, and M. Kucuk. “Modelling of Friction Welding”. In: *Unitech*. 2010, pp. 135–142.

[180] R. Schroeder et al. “Failure mode in sliding wear of PEEK based composites”. In: *Wear* 301 (2013), pp. 717–726.

[181] A. C. Greco et al. “Effect of reinforcement morphology on high-speed sliding friction and wear of PEEK polymers”. In: *Wear* 271 (2011), pp. 2222–2229.

[182] T. J. Hoskins et al. “The wear of PEEK in rolling-sliding contact - Simulation of polymer gear applications”. In: *Wear* 309 (2014), pp. 35–42.

[183] Z. P. Lu and K. Friedrich. “On sliding friction and wear of PEEK and its composites”. In: *Wear* 181 (1995), pp. 624–631.

[184] H. Unal, M. Kurt, and A. Mimaroglu. “Tribological performance of industrial polyamide-imide and its composite under different cooling conditions”. In: *Journal of Polymer Engineering* 32 (2012), pp. 201–206.

Appendix A

Monitoring system - Health and safety considerations

A.1 Assessment of the instrumentation

Table A.1, A.2, and A.3, summarises the health and safety specifications for the power supplies, the controllers and the sensors installed in the monitoring systems. In addition to what specified in these guidelines, the power supplies and the controllers should be kept stored inside the provided storage rack at any time to minimise the chances of technicians tripping over loose wires while operating the machine and to prevent accidental contacts with dangerous elements of the system.

Table A.1 Health and safety considerations for the power supplies used in the monitoring systems

Power supplies		
Component	**Specifications**	**Considerations**
RS Pro Digital Bench Power Supply (4 Outputs) [170]	• Output Voltage: 0 → 30 V, 0 → 5 V • Output Current: 0 → 1 A, 3 x 0 → 3 A • Power Rating: 195W • Supply Voltage: 100 → 230V AC • Input Connector: IEC 320 • Output Connector: Plug-In Terminal Block	Turn the power off before working on the power supply. Always follow the local and national standards for electrical safety. Do not open, modify, or repair the unit. Use caution to prevent any foreign objects from entering into the power supply. Do not use in wet locations or in areas where moisture or condensation can be expected.
NI PS-14 [171]	• Output Voltage: 24 → 28 V • Output Current: 2.7 → 3.3 A • Power Rating: 80W • Supply Voltage: 100 → 230V AC • Input Connector: Spring connector • Output Connector: Spring connector • Notes: Enclosed in an electrical box	

Table A.2 Health and safety considerations for the controllers used in the monitoring systems

Controllers		
Component	**Specifications**	**Considerations**
NI cRIO-9066 [172]	• Voltage input range: 9 VDC to 30 VDC • Maximum power input, without C Series modules: 17V • Safety voltage terminal to C terminal: 30 VDC max, Measurement Category I	Always operate the cRIO-9066 in agreement to what specified in the manual. If the product is damaged, return it to NI for repair. The cRIO-9066 is suitable for use in Class I, Division 2, Groups A, B, C, D, T4 hazardous locations; Class I, Zone 2, AEx nA IIC T4 and Ex nA IIC T4 hazardous locations and nonhazardous locations only. The product was tested and complies with the regulatory requirements and limits for electromagnetic compatibility (EMC) stated in the product specifications.
LK-G3001P [173] LK3101 [174] (Laser controllers)	• Power voltage: 24 VDC ±10% • Current consumption: 500 mA or less with 1 head • Analog voltage output: $\pm 10V \times 2$ outputs • Ambient temperature: $0°C \leq Ta \leq 50°C$ • Analog current output: 4 to 20 mA x 2 outputs, maximum load resistance: 350ω • Relative humidity: $0\% \leq RH \leq 85\%C$	Do not alter or modify the controller box. In case of damage return the product to Keyence. When the controller is turned on not touch the input and output connectors.
AD598 LVDTs signal conditioner [175]	• Power voltage: $13 \rightarrow 36$ V • Current consumption: $12 \rightarrow 15$ mA • Excitation output voltage: 5V RMS • Excitation output current: 30mA RMS • Frequency: 5kHz • Signal output voltage: $\pm 11V$ • Signal output current: 6mA	The controller is enclosed inside a junction box to prevent damaging or contact with electrified components. Do not open, modify, or repair the unit. When the circuit is powered up do not touch the terminals.

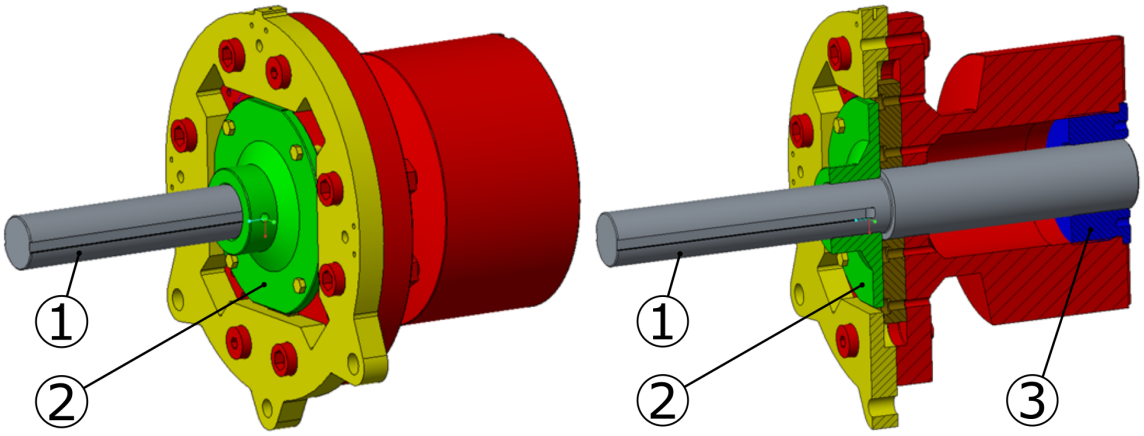
Table A.3 Health and safety considerations for the sensors used in the monitoring systems

Sensors		
Component	**Specifications**	**Considerations**
LK-G32 [173] LK-031 [174] (Laser head)	• Light source type: Red semiconductor laser • Light source wavelength: 650 nm / 670 nm (visible light) • Laser class: Class II (FDA CDRH 21CFR Part 1040.10), Class 2 (IEC60825-1) • Laser output: 0.95 mW • Enclosure rating: IP67 (IEC60529) • Ambient temperature: 0 to $+50°C$ • Relative humidity: 35 to 85 % RH (No condensation) • Reference distance: 30mm ±5mm	Eyes protection is usually guaranteed by the aversion responses (exposure time: approximately 0.25s). This is expected to provide adequate protection under the intended usage conditions (staff trained in the use of laser displacement sensors). [176]
D5/400AG (LVDT)	• Supply Voltage: 0.5 to 7V RMS • Supply Voltage frequency: 5kHz	Low power sensor, safe provided its usage is restricted to what specified in the user manual.
Kistler 8764B050BB (Triaxial accelerometer) [177]	• Supply voltage: 22 → 30 V • Supply voltage: 2 → 18 mA • Output voltage: ±5V • Operating temperature range: -54 → $100°C$	The product complies with current safety regulations (EMC certified). Operate the sensors in accordance to the guidelines described in the user manual.
L2A-06-062WW-350 (Strain gauges)	• Supply voltage: 3V	Low power sensor, safe provided its usage is restricted to what specified in the user manual.

A.2 Handling of the mechanical setup

A.2.1 Prototype system

Considering the manageable dimension and weight of the prototype backstops, it was possible to move the backstop using a trolley cart and install it inside the machine tooling with the manipulator arm that equips the MTI-300T machine. Since clamping directly the backstop could have potentially damaged the sensors, a lifting rod was designed to slide inside the backstop and provide a feature that the manipulator could clamp safely. The same lifting configuration for the two backstops was used, for this reason, the validation for only the tailstock backstop will be shown, having this the highest weight and, therefore, representing worst case scenario. As shown in Fig. A.1, the lifting setup was completed by an adaptor plate (2), designed to connect to the front face of the backstop, and a rear support (3) to be threaded on the backstop used as the second point of contact for the rod (1).



(a) (b)

Fig. A.1 Lifting setup for the backstops of the prototype system designed to be clamped and lifted with a manipulator arm equipped of claw gripper (1: Lifting rod; 2: Adaptor plate; 3: Rear support)

The validation of the configuration was accomplished with the FE model of the system represented in Fig. A.2. To study a worst-case scenario, the rod was constrained at one of the free ends, in fact, the manipulator would clamp the rod along the cylindrical surface, reducing the arm and consequently the bending stress. The Mises stress caused by the weight of the backstop (91 kg) is shown in Fig. A.3, from which it is possible to observe how the stress in all the rod does not exceed 25 MPa, value significantly lower than the yield strength for the EN08 steel used to manufacture the rod (280 MPa [178]).

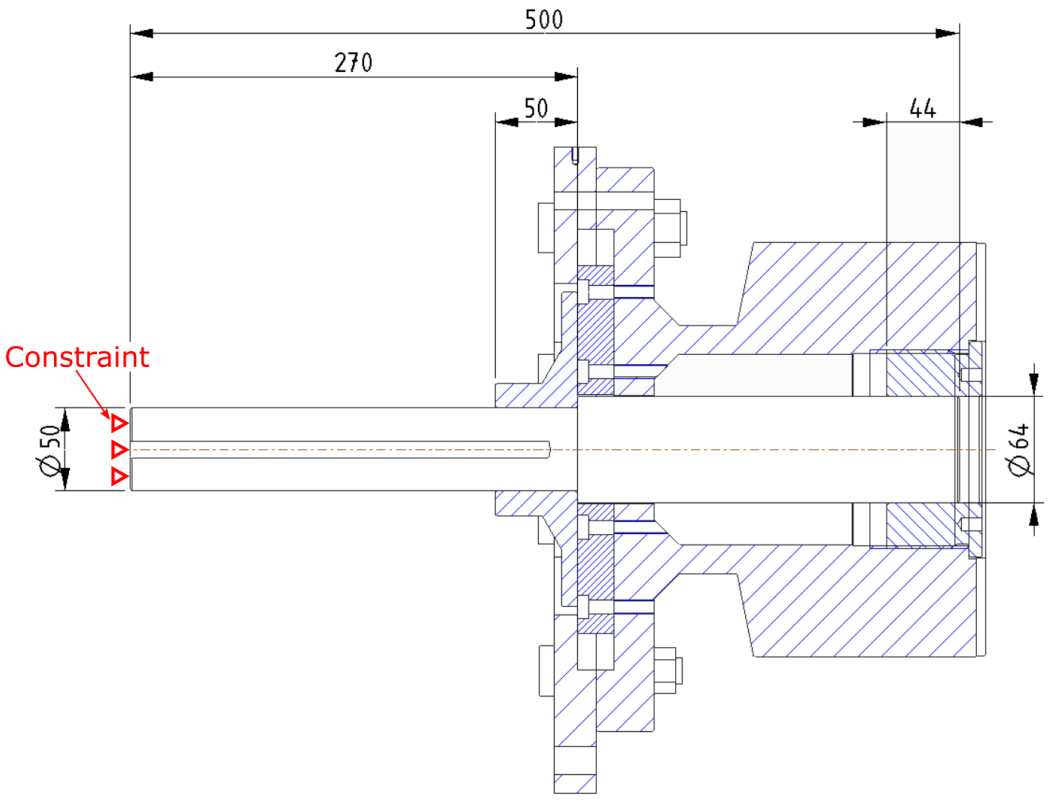


Fig. A.2 Section view of the model analysed in the FE model in which the key dimensions and constraints are shown

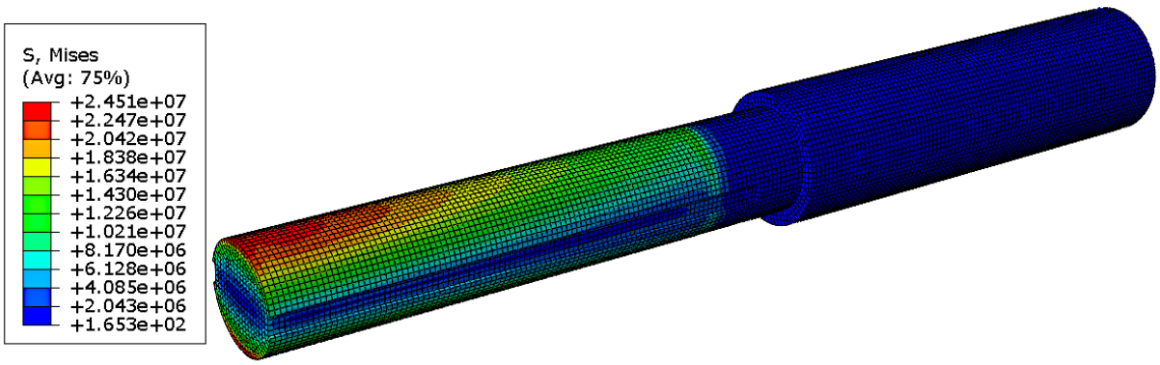
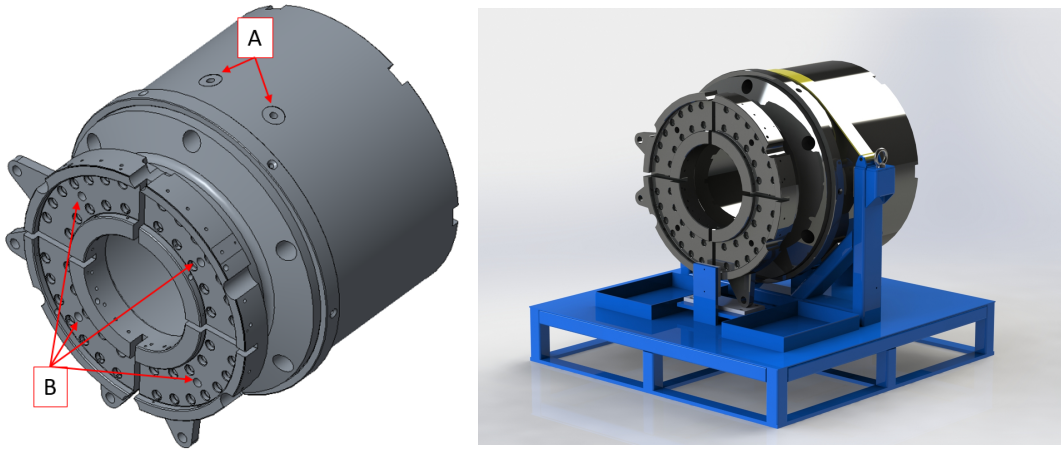


Fig. A.3 Mises stress in the rod caused by the weight of the backstop

A.2.2 Validation system

As shown in Fig. A.4a, the custom backstop could be lifted and manoeuvred using two features: two M16 eye bolts (configuration A) and 4 M20 screws (configuration B).

Configuration A was developed to allow exceptional handling using a crane, while configuration B was designed to use a manipulator arm equipped with a cruciform interface to lift the backstop from the custom storage rack showed in Fig. A.4b into the machine tooling.

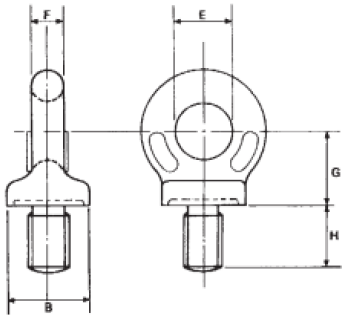


(a) (b)

Fig. A.4 Custom backups lifting and storage details: (a) Detail of the two lifting configurations; (b) Custom pallet (Acres) used to store the backstop when not used.

To validate configuration A, an overall weight backstop equal to 500kg was assumed, for which a safety factor of approximately 2 was obtained considering two M16 eye bolts positioned close to each other and with a lifting angle between the crane ropes smaller than 30°, as shown in Fig. A.5.

PART No.	SWL Tonnes	Thread Size	B mm	E mm	F mm	G mm	H mm	Weight Each Kgs
HW410/1	0.40	M12	22	15	9	20	18	0.07
HW410/2	0.80	M16	29	20	12	26	23	0.16
HW410/4	1.60	M20	40	27	16	36	32	0.44
HW410/6	2.50	M24	52	35	21	46	40	0.85
HW410/8	4.00	M30	65	44	26	58	51	1.66
HW410/10	6.30	M36	81	54	32	72	63	3.17
HW410/12A	10.00	M48	101	68	40	90	79	9.00
HW410/13	12.50	M52	115	76	46	102	89	9.00
HW410/14	16.00	M56	128	86	51	114	100	13.00
HW410/15	20.00	M64	144	96	58	128	112	17.50
HW410/16A	25.00	M72	162	108	65	144	126	31.00



MATERIAL: AS SPECIFIED BY BS 4278 HARDENED & TEMPERED
S.W.L. SHOWN AT 0° (VERTICAL) ANGLE OF LIFT

SAFE WORKING LOAD FOR A SINGLE EYEBOLT IN VERTICAL LIFT	MAXIMUM LOAD 'W' TO BE LIFTED BY A PAIR OF EYEBOLTS WHEN THE ANGLE Ø BETWEEN THE LEGS IS		
	0°<Ø>30°	30°<Ø>60°	60°<Ø>90°
TONNES	TONNES	TONNES	TONNES
0.25	0.32	0.20	0.13
0.40	0.50	0.32	0.20
0.50	0.63	0.40	0.25
0.80	1.00	0.64	0.40
0.90	1.13	0.72	0.45

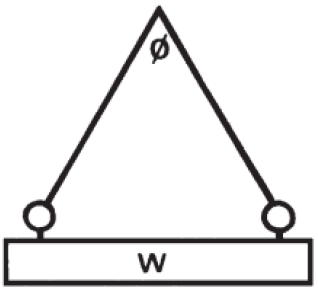


Fig. A.5 Eye bolts specs (Adapted from http://www.iandplifting.co.uk)

To validate configuration B, instead, an FE model of the backstop was developed to make sure the stress caused during the handling with the manipulator arm did not exceed the material yield strength. As shown in Fig. A.6, the geometry of the backstop was simplified removing small features, such as holes. Then, the front face was constrained removing all the 6 DoF, while for the material a density of $8080\frac{kg}{m^3}$, a Young's Modulus of 205 GPa and a Poisson's coefficient of 0.29 were chosen. Restricting the analysis to the neck section, which represents the weakest portion of the backstop, the Mises stress shown in Fig. A.7 were obtained. The stress did not exceed 1.2 MPa in any point of the system that, considering a minimum yield for the material (EN36) of 540 MPa, confirmed the suitability of the design for the lifting.

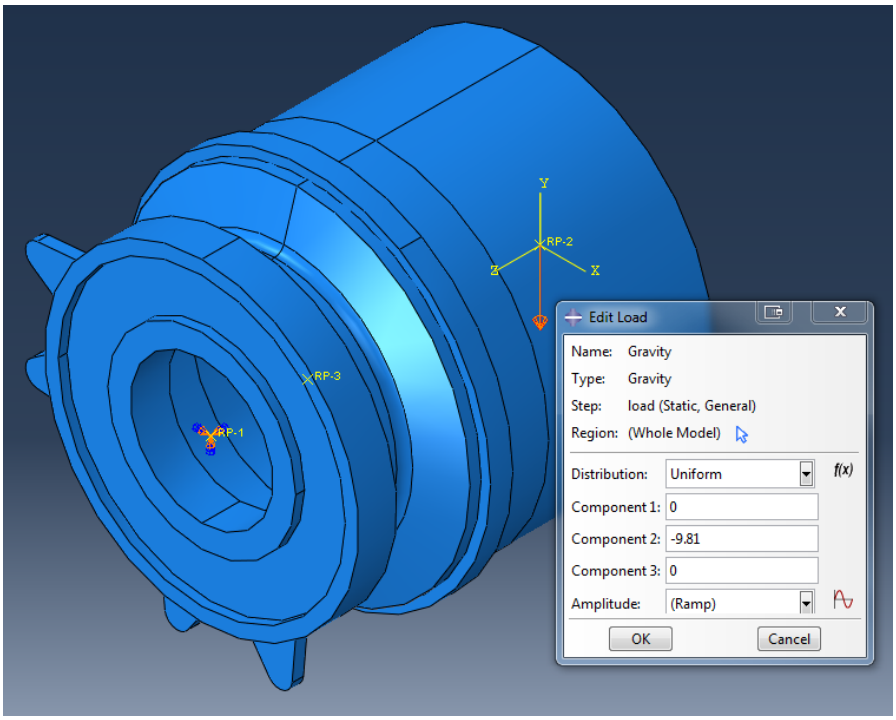


Fig. A.6 FE model developed to calculate the stress induced by the weight of the backstop during lifting with a manipulator arm

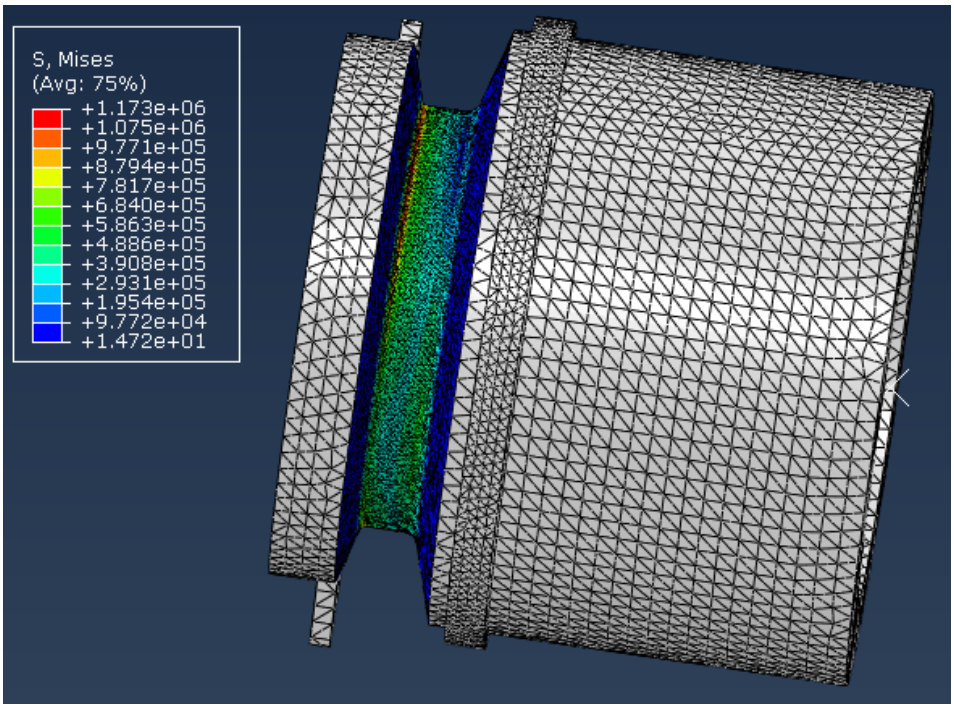


Fig. A.7 Mises stress in the neck section of the backstop during lifting with the manipulator arm

Appendix B

Assessment of plastic suitability in withstanding process loads

As introduced in chapter 4, one of the key steps in the development of the novel approach proposed for the monitoring and characterisation of the IFW system was the choice of the workpieces to be used, including both the geometry and the material. Since the approach proposed aims to characterise the machine behaviour but not the joint itself, unconventional materials like plastic were initially considered. These in fact, compared to high strength-high temperature materials like Nickel-based superalloys, are inexpensive, easy to machine and, because not welding as metals, potentially reusable for multiple tests.

Among the existing plastics, two types were selected since particularly high strength and stiffness, capable to withstand reactively high temperatures (continuous service at over 200°C and discontinuous at over 300°C) and characterised by a low friction coefficient: VICTREX 450CA30, a 30% carbon filled PEEK, and Torlon 7130, a 30% carbon filled PAI.

B.0.1 Setup

To assess the material behaviour at a smaller scale compared to what possible on the IFW machines available (MTI-300T and MTI-2000B), a CNC milling machine (Hermele Machining Centre C 800 U) was used instead. Fig. B.1 shows the setup adopted, plastic testpieces of cylindrical shape were clamped in the spindle collet, while a polished steel plate ($R_a = 0.15\mu$m) was used as a mating surface for the testpieces to simulate the conditions during welding. Two aspects are worth noting, firstly the shape of the steel plate was not important since the test aimed to characterise the behaviour of the plastic for different speed-pressure conditions, secondly, differently from an inertia welder, a CNC milling machine is not able to apply a constant pressure because the axial motion of the spindle is controlled using feed or feed rate. To compensate for this and convert the feed of the spindle into pressure, a four-component Kistler type 9272 dynamometer was positioned below the steel plate and used to capture the axial load corresponding to the applied feed. To complete the material characterisation, the friction torque induced by the relative motion between the plastic testpieces and the steel plate was monitored using the same dynamometer used for the axial load, while thermocouples were used to capture the temperature in close proximity of the contact area of the two elements.

The input values of angular speed and feed for the machine spindle were chosen to simulate the values of tangential speed and contact pressure that a RR1000 workpiece welded on the MTI-2000B machine would experience. Therefore, considering a workpiece with a cylindrical hollow shape with outer diameter ($OD_{MTI-2000B}$) equal to 440 mm and inner diameter ($ID_{MTI-2000B}$) 310 mm, welded with a peak angular speed ($n_{MTI-2000B}$) of 60.6 RPM and thrust ($F_{MTI-2000B}$) of 3774 kN, and a plastic testpiece of outer diameter ($OD_{plastic}$) equal to 12.7 mm and inner diameter ($ID_{plastic}$)

10 mm, the input values for the test are:

$$A_{MTI-2000B} = 76576.3mm^2 \tag{B.1}$$

$$A_{platic} = 48.1mm^2 \tag{B.2}$$

$$n_{plastic} = n_{MTI-2000B} \cdot \frac{OD_{MTI-2000B}}{2} \cdot \frac{1}{OD_{plastic}} \approx 2100RPM \tag{B.3}$$

$$F_{plastic} = \frac{F_{MTI-2000B}}{A_{MTI-2000B}} \cdot A_{platic} \approx 2kN \tag{B.4}$$

where $A_{MTI-2000B}$ ans A_{platic} are the areas of the reference workpiece that can fit on the MTI-2000B and of the plastic testpiece respectively, $n_{plastic}$ the peak input angular speed to use for the test and $F_{plastic}$ the peak thrust.

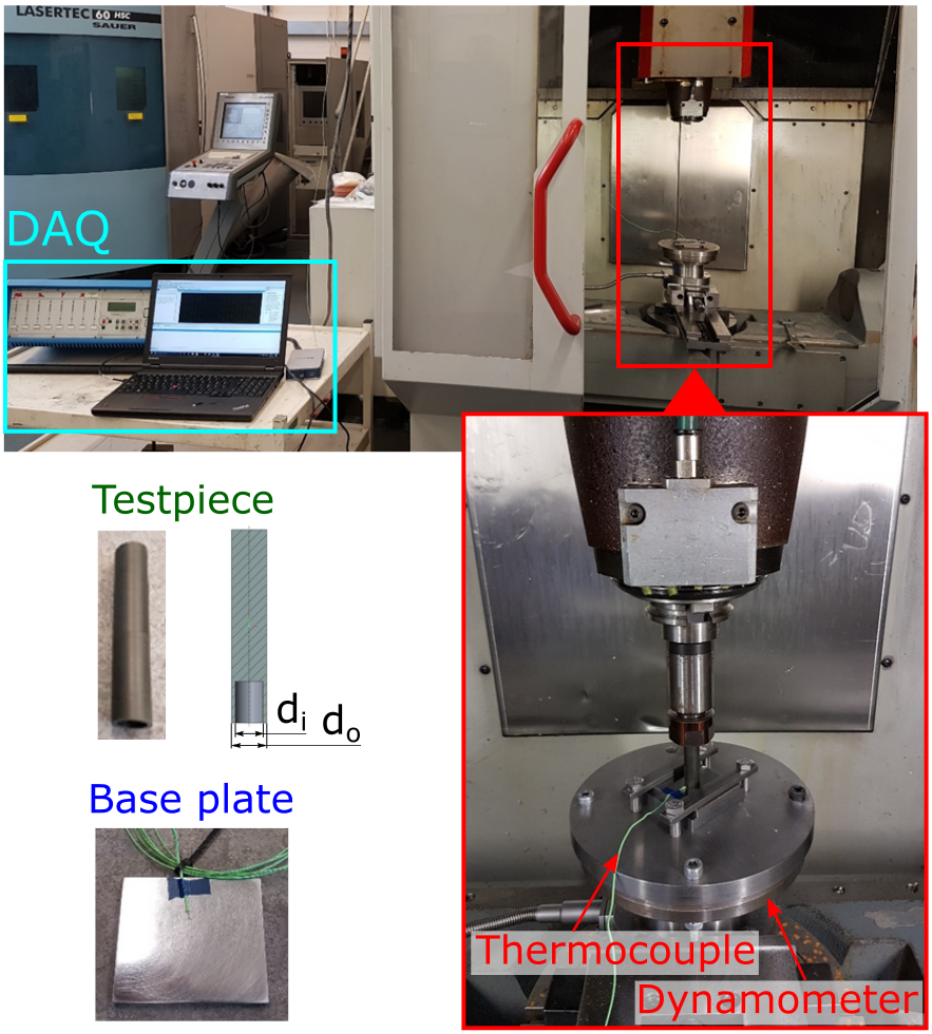


Fig. B.1 Setup used for the characterisation of the plastic testpieces, in which the key elements are the Hermel machining centre, the sensors used to calculate the process loads and temperature (dynamometer and thermocouple), the plastic testpiece and the steel base plate

To have a satisfactory characterisation of the material, several tests at gradually increasing values of feed and angular speed were completed accordingly to the test matrix shown in Fig. B.2. Each step of the test was kept for three seconds, after which system was left to cool down to room temperature before running the successive load case. After each test, values of equivalent Coulomb friction coefficient (μ_{eq}) were calculated from the torque (T_{exp}) and the thrust (F_{exp}) monitored with the dynamometer, using an approach that integrates the contributes of tangential friction load (dF_{fric}) over the testpiece cross section [179] according to the representation in Fig. B.3:

$$dT_{exp} = r \cdot dF_{fric} = r \cdot (p\mu_{eq} 2\pi r dr) \tag{B.5}$$

$$T_{exp} = \int_{r_i}^{r_o} dT = \frac{2}{3}\pi p \mu_{eq}\left(r_o^3 - r_i^3\right) = \frac{2}{3}\pi \frac{F_{exp}}{\pi \cdot \left(r_o^2 - r_i^2\right)} \mu_{eq}\left(r_o^3 - r_i^3\right) \tag{B.6}$$

$$\mu_{eq} = \frac{T_{exp}}{\frac{2}{3} F_{exp} \frac{\left(r_o^3 - r_i^3\right)}{\left(r_o^2 - r_i^2\right)}} \tag{B.7}$$

where r is the radial coordinate, r_i and the r_o the inner and outer radius of the testpiece respectively and p the interface pressure. Finally, the values of friction were correlated to the temperature extracted with the thermocouples.

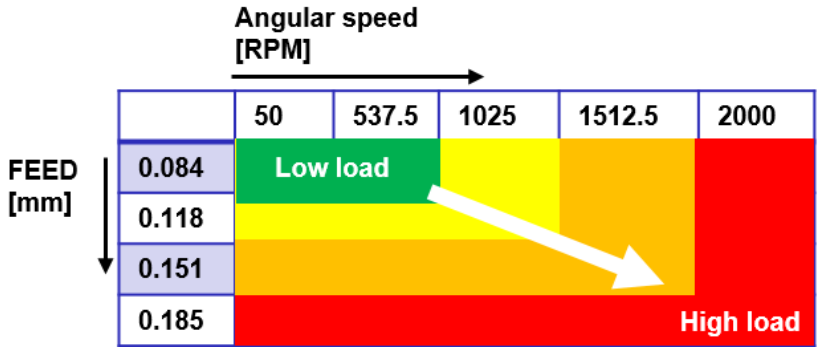


Fig. B.2 Schematic representation of the parameter matrix (feed and angular speed) for the characterisation of the plastic testpieces

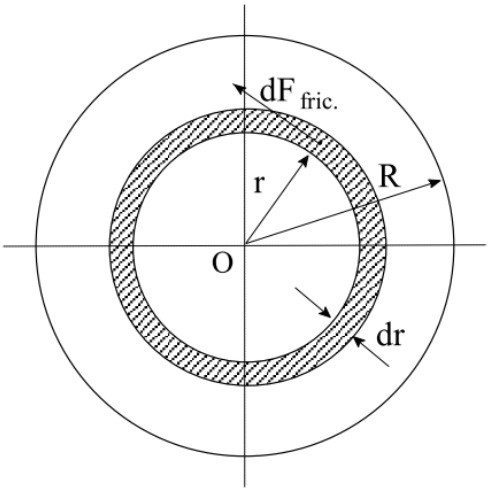


Fig. B.3 Cross section of a cylindrical workpiece showing the infinitesimal tangential friction load contribute (dF_{fric}) over the ring of radius r and thickness dr [179]

B.0.2 Results

The first material analysed was VICTREX 450CA. As shown in Fig. B.4, the material presented limited capabilities to withstand the test conditions and started degrading for values of feed of 0.08 mm and angular speed of 1025 RPM. Before the damaging, the material displayed relatively low values of friction coefficient between 0.18 and 0.23 with temperatures up to 160°C, as summarised in Fig. B.5. After material damaging, the tests were not interrupted and the parameter matrix was completed. In these conditions, however, higher values of friction coefficient between 0.35 and 0.45 were obtained and the rigidity of the testpiece dropped, not allowing to capture results for certain pressure-speed combinations. This is shown by the white areas in the contour plots in Fig. B.5.

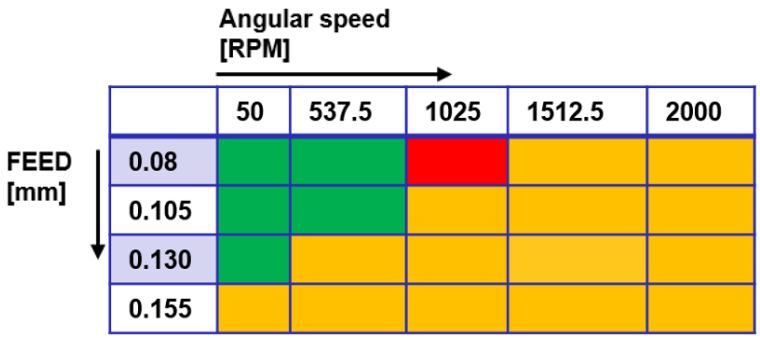
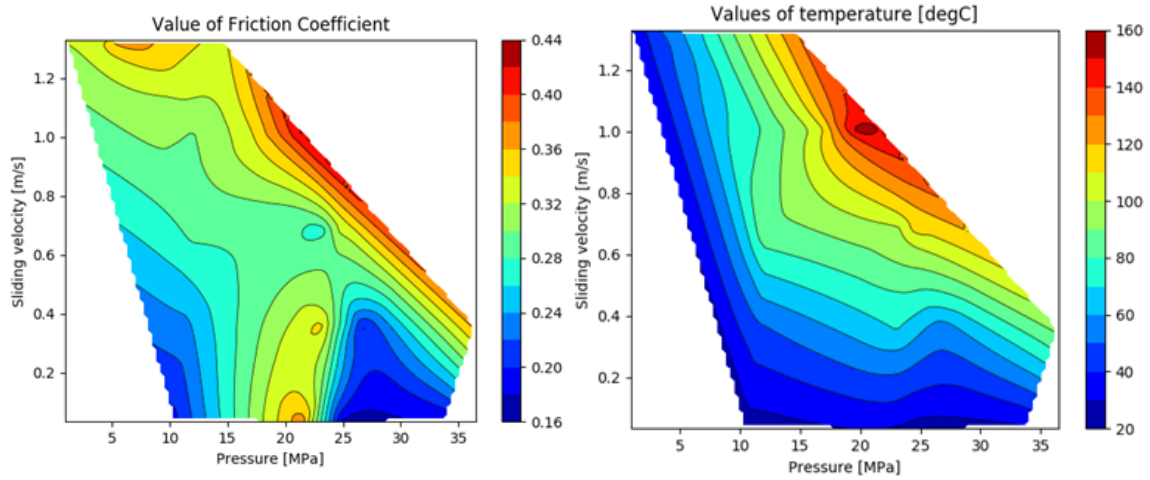


Fig. B.4 Test matrix for VICTREX 450CA, where the green boxes represented parameter combinations successfully completed, red the combination that caused the material damaging and yellow the tests conducted with a damaged testpiece



(a) (b)

Fig. B.5 Results of the characterisation of Victrex 450CA (the white portions in the graph represent combinations pressure-tangential velocity during the tests): (a) Contour plot showing the values of friction coefficient against the tangential speed and the contact pressure; (b) Contour plot showing the values of temperature close to the friction area against the tangential speed and the contact pressure.

A second test was devised to assess the capability of the material to withstand the peak loads in an undamaged testpiece. The material, however, proved not suitable for high pressure-tangential velocity (PV) values and got damaged almost immediately.

The second material studied was Torlon 7130. As shown in Fig. B.6, the material presented a significantly higher resistance compared to Victrex 450CA and failed

for values of feed of 0.151 mm and angular speed of 1512.5 RPM. Fig. B.7a shows that before the damaging, the friction coefficient measured was lower compared to Victrex 450CA, with values ranging between 0.12 and 0.2, while after the damaging the friction coefficient spiked up to 0.36. During the tests, temperatures up to 180°C were observed, as shown in Fig. B.7b. The better performance of the material is confirmed also observing the lower fraction of PV combinations not withstood by the material (white areas in the Fig. B.7) in comparison to Victrex 450CA.

Also in this case, a second test to assess the performance of an undamaged material to the peak PV combinations was completed. Starting from the PV combination that brought to failure the previous testpiece, it was observed that the material managed to withstand the four remaining combinations and failed only when the test duration was extended to five seconds. During this test, values of friction coefficient below 0.1 were measured.

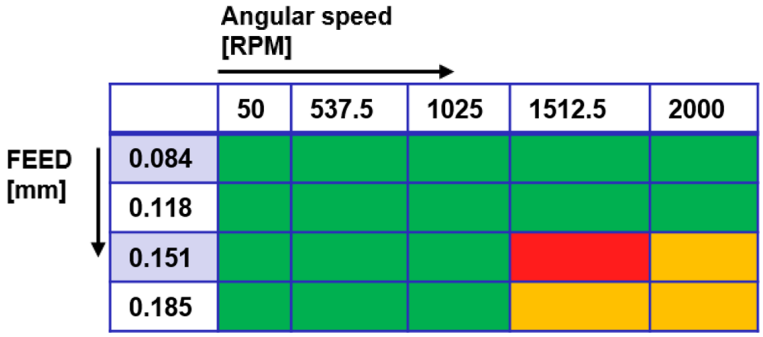
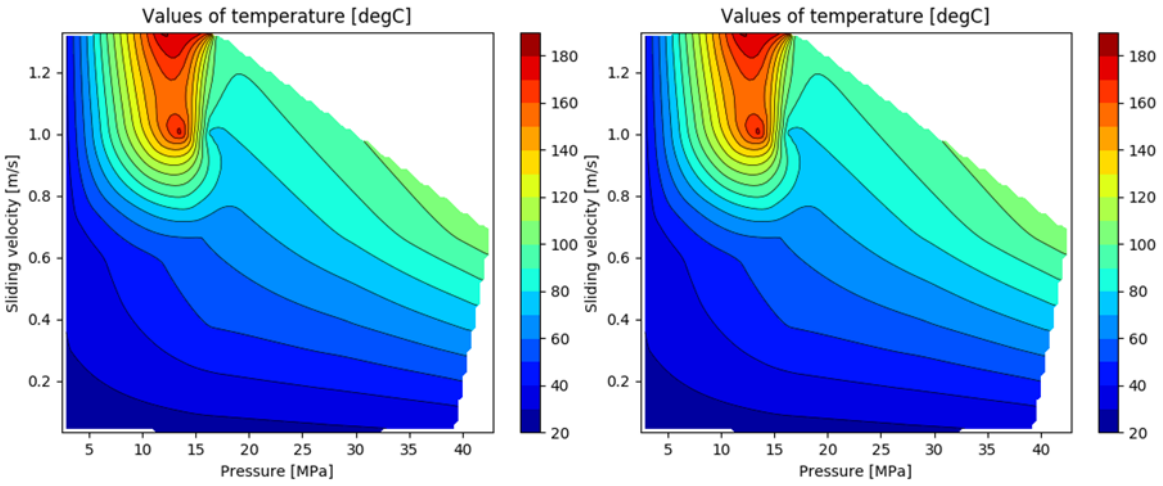


Fig. B.6 Test matrix for Torlon 7130, where the green boxes represented parameter combinations successfully completed, red the combination that caused the material damaging and yellow the tests conducted with a damaged testpiece



(a) (b)

Fig. B.7 Results of the characterisation of Torlon 7130 (the white portions in the graph represent combinations pressure-tangential velocity not reached by the material): (a) Contour plot showing the values of friction coefficient against the tangential speed and the contact pressure; (b) Contour plot showing the values of temperature close to the friction area against the tangential speed and the contact pressure.

B.0.3 Analysis of the morphology of damaging

As mentioned in the previous sections, it was possible to observe clearly during the tests the moment of material failure. This was obtained with an inverse approach that made use of the data of axial load and torque. In fact, as shown in Fig. B.8, the instant of failure was marked by a sudden drop in monitored pressure due to the loss of rigidity of the material and a spike in friction coefficient.

To further investigate the morphology of damage, the testpieces were analysed with visual inspection and optical microscopy. Fig. B.9 shows the results of the visual inspection, from which it is possible to observe that the damaging produced debris and film transfer on the metal base plate. These phenomena have already been observed in several studies about wear mechanisms of polymers [180–184], suggesting that the main cause of failure was wear at high PV values. This was additionally supported by the similarity of the damage morphology for both materials with the results reported by Greco et al. [181] for PEEK specimens tested with a ball-on-disc tribometer, as shown in Fig. B.10c.

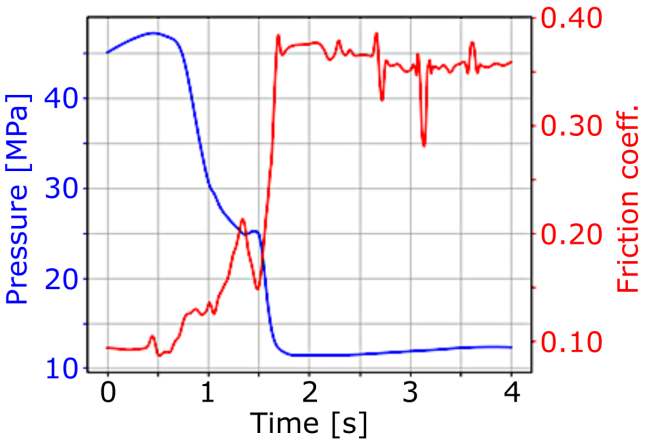


Fig. B.8 Measured values of friction coefficient and axial load at the instant of failure of the testpiece

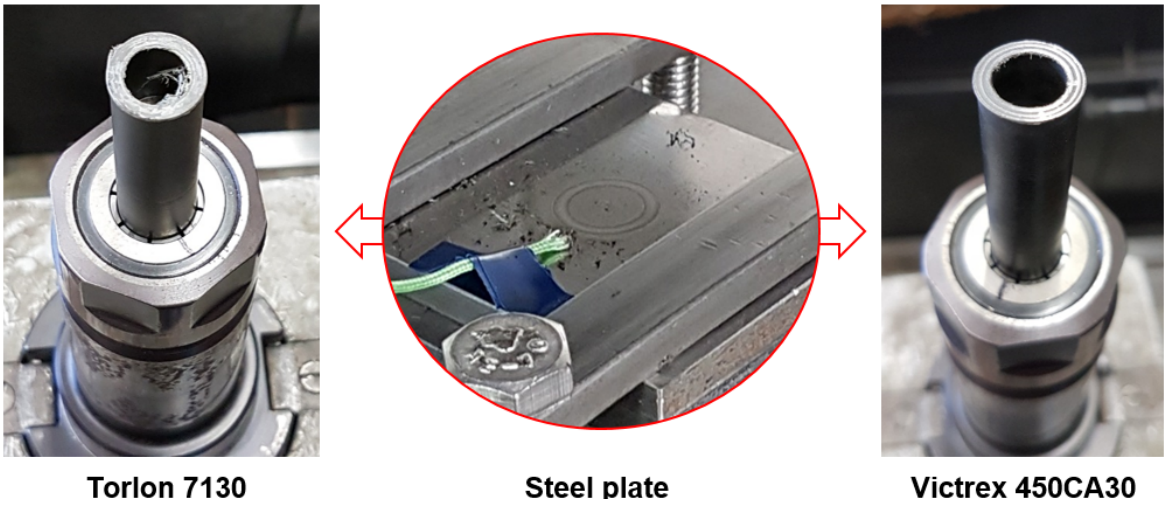
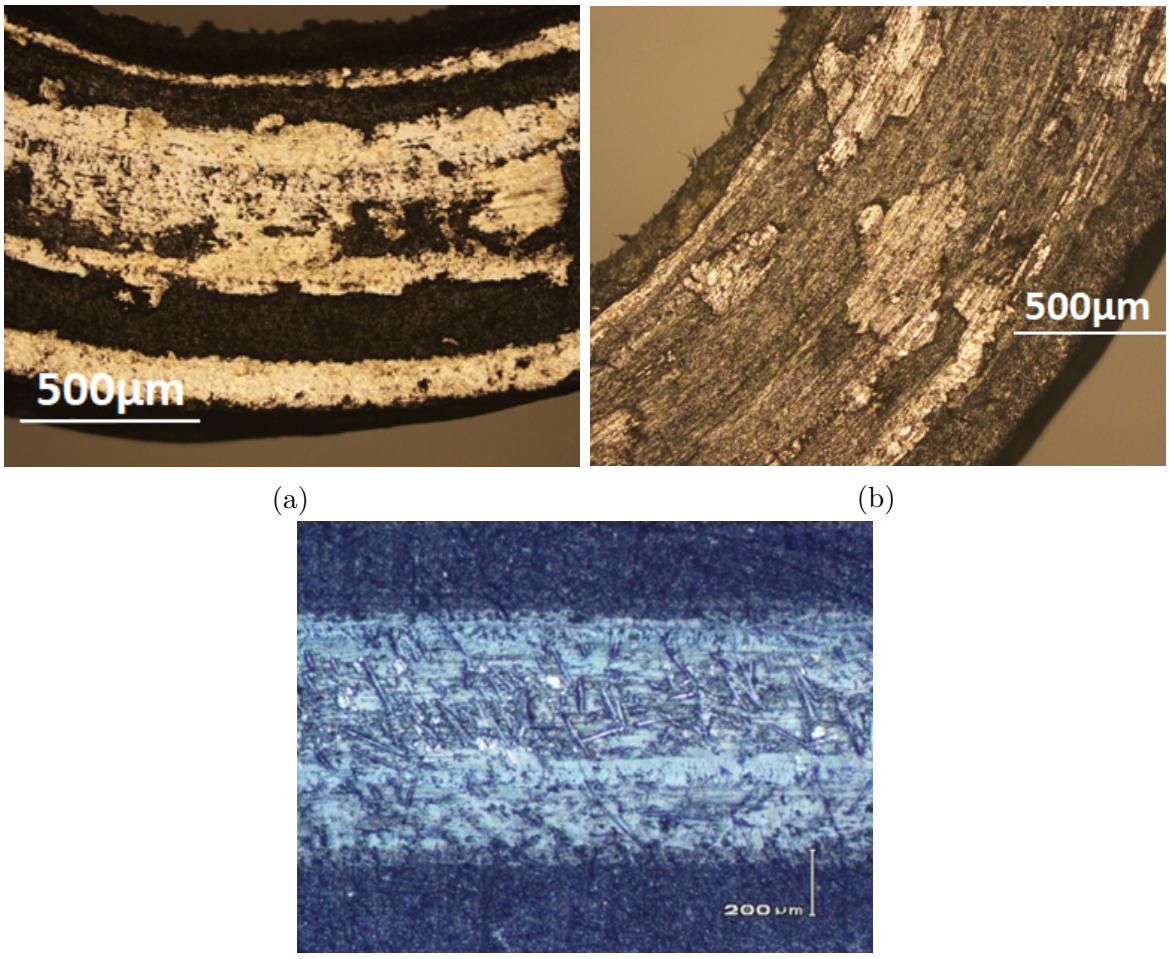


Fig. B.9 Macroscopic damaging for the two types of plastic in which it is possible to observe debris on the metal base plate

The microscopical analysis of the damaged surfaces showed additional details. Firstly, the presence of carbon fibres, beneficial in increasing the mechanical resistance, reducing the micro-ploughing effect at the interface and avoiding stick-slip phenomena, could induce abrasion on the metallic counterpart when get exposed due to the surface abrasion. This phenomenon was observed for both Victrex and Torlon, as shown in Fig. B.10a and B.10b. Secondly, Torlon presented the longitudinal sub-superficial cracks on the side of the testpices shown in Fig. B.11 that, however, did not appear in

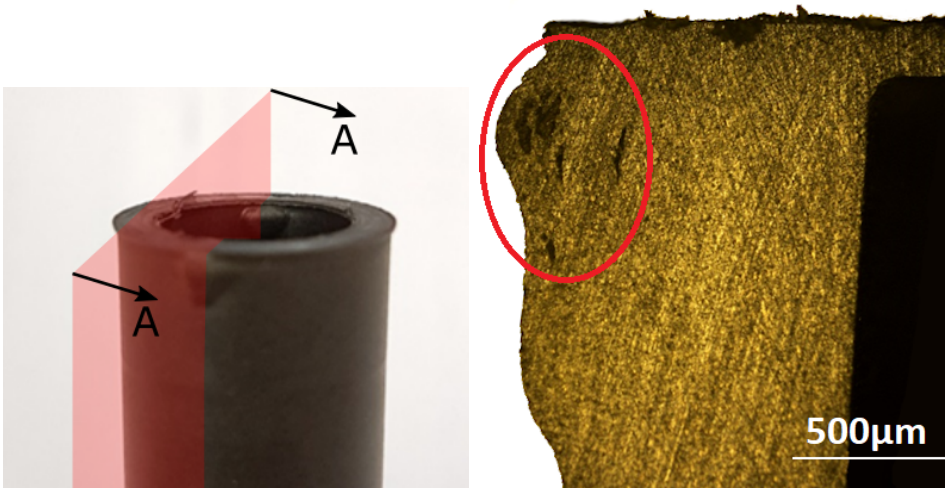
the Victrex testpieces. This difference could be attributed to the different molecular arrangement of the two thermoplastics, amorphous for Torlon while semi-crystalline for Victrex, and the higher load levels to which Torlon was subjected, as suggested by the longitudinal direction of the cracks.



(a) (b)

(c) wear track on PEEK [181]

Fig. B.10 Optical micrographs of the damaged surfaces for the two materials analysed and comparison with a study from literature of PEEK analysed with a ball-on-disc tribometer: (a) Damaged Victrex (PEEK) surface; (b) Damaged Torlon (PAI) surface; (c) Damaged surface generated during a ball-on-disc tribometer study to assess the wear resistance of PEEK Greco et al. [181].



(a) (b)

Fig. B.11 Analysis of the sub-superficial longitudinal cracks in a Torlon testpiece: (a) Damaged Torlon testpiece before being sectioned and analysed; (b) The microscopy analysis revealed how the bulges on the side of the workpiece are sub-superficial longitudinal cracks.

B.1 Conclusions

IFW is conventionally used to weld high strength-high temperature materials like Nickel-based superalloys that, however, are extremely expensive and complex to machine. Since the approach developed aims to characterise the machine behaviour rather than the joint, the only requirement for the material used for the workpieces is the capability to withstand the process conditions. Plastic materials represent an interesting candidate given their relatively low price, good machinability and potential to be reused for several tests.

The first aspect was to choose the plastics more suitable for the application. VICTREX 450CA30 and Torlon 7130 were found as the best candidates given their high strength and rigidity, capability to resist relatively high temperatures and low friction coefficient, important to minimise the surface damaging and frictional heat. A set of tests was devised to replicate the welding conditions in term of tangential speed

and thrust using a CNC machining centre. It was observed that VICTREX 450CA30 was not capable to resist high pressure and tangential velocity combinations. Torlon 7130, instead, showed much more promising results, being capable to withstand even the most demanding test conditions, but even in this case some limitation was found. Firstly Torlon 7130 is an extremely expensive plastic and not of simple machinability due to the presence of carbon filling. Secondly, despite having withstood the peak test conditions, very rapid wear was observed, making it capable to resist to demanding conditions only for few seconds and, consequently, showing limited potential for being reused in multiple tests on an inertia welder.

E quindi uscimmo a riveder le stelle. (Inferno XXXIV, 139)

(Thence we came forth to rebehold the stars. (Inferno XXXIV, 139))